Multichannel Analysis of Intracardiac Electrograms

Supporting Diagnosis and Treatment of Cardiac Arrhythmias

Zur Erlangung des akademischen Grades eines

DOKTOR-INGENIEURS

von der Fakultät für

Elektrotechnik und Informationstechnik

des Karlsruher Instituts für Technologie (KIT)

genehmigte

DISSERTATION

von

Dipl.-Ing. Tobias Oesterlein

geb. in Kronach

Tag der mündlichen Prüfung:	5. Juli 2017
Referent:	Prof. Dr. rer. nat. Olaf Dössel
Korreferent:	Prof. Dr. med. Claus Schmitt

Acknowledgments

This thesis was conducted at the Institute of Biomedical Engineering (IBT), Karlsruhe Institute of Technology (KIT), in close collaboration with the Medizinische Klinik IV from Städtisches Klinikum Karlsruhe. I sincerely thank all persons who contributed to the success of the presented research.

First of all, I want to express my sincere thank to Prof. Dr. Olaf Dössel for supervising this thesis and the possibility to work in his collaborative and inspiring laboratory. I really appreciate the support of my ideas and the freedom he provided me for research. I also want to express my deepest gratitude to Prof. Claus Schmitt for the support he provided throughout the last years, his inspiring guidance, and for refereeing this thesis. Both took the initiative to realize the workshop *Atrial Signals 2015*, whose organization and attendance was a highly valuable experience for me.

I would like to thank all members of institute, who enriched the presented research by stipulating discussions or direct contribution, being simulation results, algorithms or clinical data. A very special thanks goes to my roommate Bhawna for all the intense discussions and the comfortable ambiance we had in our common office during the last two years. I also would like to thank Dr.-Ing. Martin Krüger and Dr.-Ing. Matthias Keller, who greatly supported me when I started my PhD studies at IBT. Familiarization with the clinical environment and analysis of electrogram data would have been much more tricky without the two of you. For excellent discussions and great support in scientific questions I need to thank Dr.-Ing. Gunnar Seemann for his assistance. The presented research was strongly enriched by the ability to analyze simulated data. Gratitude for the generation of these goes to Dr.-Ing. Axel Loewe, who also contributed by critical comments to the evolution my work. It is my honor to have conducted several research projects together with Gustavo 'Goofy' Lenis, who contributed both this professional competence and algorithms for ECG analysis. Several exciting projects have been started with Stefan Pollnow, whom I thank for the possibility to combine simulations with in-vivo and in-vitro measurements. Jochen Schmid deserves thank for his support in all IT related questions and our common project *KaPAVIE*. For great discussions, support and positive mood at the institute, I want to thank Dr.-Ing. Walther Schulze, Dr.-Ing. Thomas 'Fritschí' Fritz, Danila Potyagaylo, Lukas Baron and Michael Kircher. Last but not least I want to thank the administrative staff and technical personal at IBT for their support during the complete duration of my PhD. I guess nothing would work without these guys.

The presented research would not have been possible without the close collaboration with the clinical partners. Above all, my deepest gratitude goes to Dr. Armin Luik from Karlsruhe for his extensive support during the last years. I highly enjoyed discussing our ideas and new developments from both engineering and medical perspective. This teamwork tremendously augmented the relevance of the presented research. I am also very grateful for all the support by the members of the EP-lab in Karlsruhe, who were always patient and collaborative despite their busy schedule. I strongly want to thank Dr. Amir Jadidi from Bad Krozingen for his inspiring thoughts about processing of clinical data and combined computational modeling. An increasing number of projects is realized with Dr. Reza Wakili from Munich, whose dedication I deeply appreciate.

It was my pleasure to supervise a number of students during their theses. By dedicated and inspiring work, they contributed to the research presented in this thesis: Fabian Schenkel, Daniel Frisch, Julia Trächtler, Nazeline Younis, Dan-Timon Rudolph, Johann Jazewitsch, Niko Konrad, Daniela Zöller, Alexander Kramlich, Christian Reich and Salina Huck. In addition, I want to thank Ilia Grygoryev, Silvio Bauer, Niko Gädike, Philipp Müller, Simon Trumph and Sophie An for supporting me in projects apart from their theses.

For comprehensive seminar program and financial support during my undergraduate and graduate studies I want to thank e-fellows.net, the Konrad-Adenauer-Foundation, and the German National Academic Foundation. Studies in the USA were grant-aided by the Baden-Württemberg Program and the Fulbright Commission.

Last but not least, I want to thank my parents and family for supporting me along my way. None of this would have been possible without their assistance and encouragement during the last 30 years. The greatest thanks goes to my girlfriend Sonja, for her understanding patience and backing throughout these busy times.

The research leading to these results has received funding from the German Research Foundation under grant DO637/14-1.
Diese Arbeit entstand mit Unterstützung des Karlsruher House of Young Scientists (KHYS).

Contents

Abbreviations

ACL atrial (basic) cycle length
AFib atrial fibrillation
AFlut atrial flutter
AP action potential
AV atrio-ventricular
BCL basic cycle length
BEGM bipolar electrogram
CC correlation coefficient
CFAE complex fractionated atrial electrograms
CR correct rate
CRN Courtemanche-Ramirez-Nattel (atrial cell model)
CS coronary sinus
CTI cavo-tricuspid isthmus
CV conduction velocity
DF dominant frequency
DP double potential
EAMS electroanatomical mapping system
ECG electrocardiogram
EGM electrogram
EP electro-physiological
FaMaS fast-marching simulator
FDT fuzzy decision tree
FN false negative
FP false positive
GUI graphical user interface
HRA high right atrium
IBT Institute of Biomedical Engineering
IEGM intracardiac electrogram
IVC inferior vena cava
LA left atrium
LAA left atrial appendage
LAT local activation time
LAW local activation wave

LGE late-gadolinium enhancement
LIPV left inferior pulmonary vein
LPV left pulmonary vein
LSPV left superior pulmonary vein
MRI magnetic resonance imaging
MV mitral valve
NLEO non-linear energy operator
NPV negative predictive value
NSR normal sinus rhythm
PC principal component
PCA principal component analysis
PDC partial directed coherence
πCA periodic component analysis
PPV positive predictive value
PSD power spectral density
PV pulmonary vein
PVI pulmonary vein isolation
RA right atrium
RF radio frequency
RPV right pulmonary vein
RSPV right superior pulmonary vein
SD standard deviation
SE sensitivity
SP specificity
SVC superior vena cava
SVES supraventricular extra-systole
SVM support vector machine
TMV transmembrane voltage
TN true negative
TP true positive
TV tricuspid valve
UEGM unipolar electrogram
VFF ventricular far field

CHAPTER 1

Introduction

1.1 Motivation

The treatment of atrial fibrillation (AFib) has received significant attention for several decades, since this arrhythmia still represents the most common sustained heart rhythm disturbance for humans [1]. Considering the European Union, a total of 8.8 million patients were estimated to suffer from AFib in 2010, being projected to about 19.7 million in 2060. Similar values were obtained for the United States of America, indicating a doubling of AFib patients up to 2050 [2]. Both prevalence and associated costs have been subject of several studies. Analysis of a European study group quantified the lifetime risk for developing AFib to 23% for women and even 25% for men [3]. This leads to an immense financial burden on health care systems, estimated up to 26.0 billion US dollar per year for the United States alone [4].

Although AFib is not lethal itself, it is associated with several severe comorbidities. Most importantly, a 34 year follow-up study including 5,070 participants identified AFib to independently increase the risk of cerebral stroke over all age groups up to five times [5]. Stroke associated with AFib was linked to prolonged hospital stay, disability and the need for long term care [1]. This emphasizes the relevance of AFib, both for each individual affected patient and on the socio-economic scale.

But despite intense efforts in research, the mechanisms underlying AFib are still poorly understood, and optimal treatment strategies are lacking. Catheter ablation is typically applied if pharmacological treatment is not effective. But considering the persistent state of AFib, current studies on ablation outcome report a success rate of less than 60% in the 18 month follow up [6, 7]. Even if AFib is successfully terminated by ablation, conversion into atrial flutter (AFlut) was reported in up to 31% of cases [8]. Considering this consecutive tachycardia, it is often reported as very symptomatic and difficult to treat due to a very complex cardiac substrate.

Catheter ablation of both AFib and AFlut is performed in the scope of an electrophysiological (EP) study. During the last years, tremendous advances have been achieved

with respect to the available diagnostic devices, particularly mapping systems and catheters. Common catheters were designed to record up to 20 simultaneous electrograms from within the heart, providing information about the cardiac depolarization. Two additional types were brought to the market, each equipped with 64 electrodes. One model is referred to as *panoramic basket*, as it is configured to acquire electrograms from distributed locations of the complete atrium. A smaller *mini-basket* arrangement is suitable for local high-density mapping. These recording devices can be combined with novel mapping systems, which can be used to generate a virtual cardiac anatomy and allow to acquire thousands of measuring points in the heart within minutes [9].

The resulting amount of data, however, makes simultaneous visual assessment a challenging task for any treating physician. But even in state-of-the-art mapping systems, only few common methods are available for automatic signal analysis, making appropriate data evaluation the bottleneck in the extraction of diagnostically relevant information.

Following the notion, that only joint research of engineers and physicians could tackle the riddle of complex tachycardias, the Städtisches Klinikum Karlsruhe and the Institute of Biomedical Engineering at the Karlsruhe Institute of Technology decided to organize the workshop *Atrial Signals 2015*. Renown experts from both fields were invited, and this very combination contributed to a unique and inspiring atmosphere, to which over 200 international participants were welcomed. The author was part of the organizing committee and had the chance to discuss new ideas with the leading experts of the scientific community. Following two days of intensive discussion, all participants agreed that the analysis of intracardiac electrograms is a fundamental cornerstone in the understanding of cardiac arrhythmias and the design of patient-specific treatment strategies.

The need for corresponding signal analysis techniques motivated the research presented in this thesis. In close collaboration with clinical physicians, cardiac events and parameters were identified which are relevant for treatment. These experience-based ideas from the medical field were reformulated as engineering problems and addressed with the goal of finding a potentially automatic solution. Simulations of cardiac activity were utilized to verify and benchmark new processing techniques, before they were applied to clinical data. All techniques were designed to avoid inappropriate simplification of the analyzed mechanisms. Concluding, a system was developed for the direct clinical application of novel analysis algorithms, allowing to rapidly gain feedback about the diagnostic value of analysis results and their visual representation.

The signal processing techniques presented in this thesis help to comprehend the spatio-temporal relationships in cardiac excitation, and to detect and statistically assess events of diagnostic relevance. They will hopefully provide means to understand the mechanisms of AFib, and aid in designing patient-specific treatment strategies for supraventricular tachycardias like AFlut or AFib with improved success rate.

1.2 Aims of the Thesis

The options to analyze intracardiac mapping data are nearly unlimited. Based on their clinical significance for EP studies, some specific issues were selected as research topics. The joint analysis of several thousand recorded signals was addressed to elucidate the mechanisms behind AFlut. The appropriate assessment of panoramic mapping data was considered due to the unique diagnostic possibilities of simultaneous electrogram acquisition. It was also closely related to the development of methods for statistical analysis of depolarization patterns.

Considering these topics, four major goals were addressed during the presented research:

- Develop algorithms to focus physicians' attention on the critical site of atrial flutter
- Develop techniques which help to identify and analyze the excitation pattern during complex atrial tachycardias as AFib
- Evaluate the diagnostic potential of basket-type catheters
- Bring novel analysis techniques into the clinical environment

1.3 Structure of the Thesis

Part I summarizes the medical and mathematical fundamentals:

- **Chapter 2** recapitulates clinical information about the two atrial arrhythmias AFlut and AFib, their diagnosis, mechanisms, and treatment options. It also provides an overview about diagnostic devices and computational modeling.
- **Chapter 3** outlines basic mathematical concepts for the analysis of intracardiac data and concepts of classification.

Part II outlines the methods for data processing and visualization which were applied or developed during this thesis:

- **Chapter 4** describes the concept of computational catheter models and how their deformation can be simulated.
- **Chapter 5** demonstrates processing steps for the initial filtering of electrogram data.
- **Chapter 6** depicts the preprocessing steps which are required to prepare the geometry of the atrial chamber and to assess spatial information about the catheter position.
- **Chapter 7** discusses special filtering techniques for the removal of ventricular far fields in intracardiac electrogram data.
- **Chapter 8** reflects the concept of activation time assignment, its relation to phase and different interpolation techniques.
- **Chapter 9** demonstrates alternative concepts for visualizing the time-dynamic process of cardiac excitation when annotation of the activation time is not unambiguous.

- **Chapter 10** describes the method which was used to model AFlut. Both the simulation of documented cases of AFlut is addressed, as well as the virtualization of actually measured clinical cases.
- **Chapter 11** continues with an overview of techniques which were developed to aid in the diagnosis of AFlut. They were benchmarked using the simulated flutter scenarios and annotated clinical data.
- **Chapter 12** summarizes different techniques for the analysis of electrograms measured during AFib.
- **Chapter 13** describes the assessment of morphological and temporal patterns in single and multichannel electrogram data.
- **Chapter 14** concludes this part by addressing the requirements of applying the introduced techniques in a clinical context.

Part III demonstrates how the previously outlined means can be used to address diagnostically relevant issues:

- **Chapter 15** presents an evaluation of the coverage of panoramic basket catheters, and assesses the field of view of the mini-basket catheter.
- **Chapter 16** demonstrates the identification of dominant excitation patterns. It is applied in the analysis of ectopic activity observed in biatrial basket catheter mapping data.
- **Chapter 17** subsequently discusses potential advantages as well as pitfalls during mapping with panoramic basket-type catheters.
- **Chapter 18** describes the application of the previously introduced algorithms to extract diagnostically relevant information in the analysis of clinical cases of AFlut.
- **Chapter 19** addresses the region-specific distribution of fractionation before and after pulmonary vein isolation.
- **Chapter 20** provides an example for the analysis of dominant patterns in high-density mapping data acquired during atrial fibrillation.

Chapter 21 summarizes the thesis, draws conclusions from the achieved results and motivates specific fields for future research.

During the last four years, the author contributed to six published journal papers, with two more being currently under review or preparation. He presented his ongoing research at nine conferences, in three invited talks, and co-authored another 18 conference contributions with five additional being currently under review. The author was awarded the first price as young investigator by the International Society of Electrocardiology in 2014. Besides his own research, the author supervised 16 student theses which partly form the basis of the work presented here (compare Chapter *List of Publications and Supervised Theses*).

PART I

FUNDAMENTALS

CHAPTER 2

Clinical Fundamentals

2.1 Anatomy and Physiology of the Heart

Cardiac anatomy and circulatory function The heart is a muscular organ which pumps blood through the human body. Its primary purpose is to supply all organs with oxygen, nutrients, and to deliver and collect various other substances. Located in the middle mediastinum, it is anatomically optimized for this purpose by a division into four chambers, being two atria and two ventricles. The directed flow of blood from the atria to the ventricles and into subsequent vessels is assured by specific unidirectional valves. Right and left side of the heart are separated by the interatrial and interventricular septum, respectively. On either side, the atrium supports the pumping function of the ventricle by passively collecting blood and then actively pressing it into the ventricles [10].

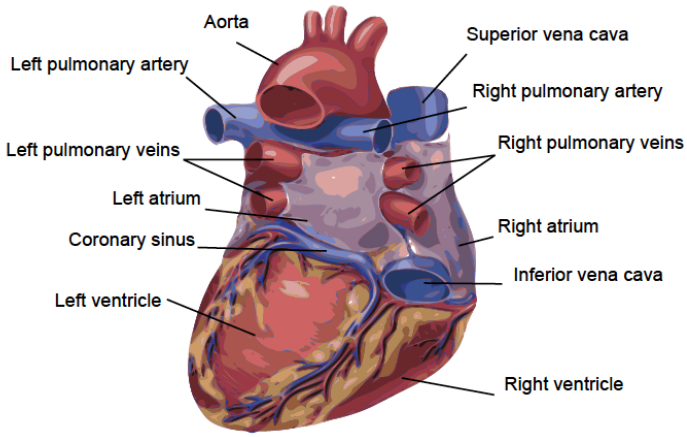

Figure 2.1: Cardiac anatomy. Major atrial structures and vessels are annotated. The heart is shown in posterior view. From [11].

.

Deoxygenated blood from the systemic circuit enters the right atrium (RA) through the superior and inferior venae cavae, and is pumped through the tricuspid valve (TV) into the right ventricle. From there it is injected into the pulmonary circulation, where it is oxygenated again. Coming from the lung, the blood is collected via the pulmonary veins (PVs) in the left atrium (LA), flows through the mitral valve (MV) into the left ventricle and is finally pumped into the systemic circuit towards all organs. Within one cardiac cycle, about 80 ml of blood are transported towards the organs. The cardiac anatomy including major vessels is depicted in Figure 2.1. The coronary sinus (CS) is surrounding the posterior wall of the LA on the level of the valvular plane. This vessel drains the myocardium into the RA and is of particular importance for electrophysiological studies, as a catheter is typically placed in the CS as stable reference for timing and spatial localization [12].

The cardiac wall is formed by myocytes, which can contract and thus perform the actual pumping function. Corresponding to the respective pressures, the wall of the left ventricle is strongest. Myocardium of RA and LA are significantly thinner, ranging about 1 to 3 mm [13]. While the endocardial part of the wall is in contact with the blood, the epicard is surrounded by the pericard. The electrophysiology of mycodardial cells will be addressed in the following.

Cellular electrophysiology The membrane of myocardial cells separates the intracellular and the extracellular space. Specific channels control the transition of ions through this boundary, with particularly Na^+, K^+ and Ca^{2+} being of interest for cellular electrophysiology. At rest, a potential difference of about -80 mV is uphold accross the cellular membrane, being known as transmembrane voltage (TMV) [12].

When cardiac myocytes are excited by an external stimulus, TMV increases slowly until a level of -60 mV is reached. Exceeding this threshold triggers an action potential (AP), as depicted in Figure 2.2. First, a rapid depolarization sets in, caused by an opening of Na^+ channels and subsequent influx of these ions. This results in an overshot of the TMV and an inactivation of the Na^+ channels (phase 1). Subsequently, channels open which permit the influx of Ca^{2+}. This prolongs the depolarized state of the cell (phase 2). Finally, the cell is repolarized again by an outward current of K^+ (phase 3) until the resting TMV is reached (phase 4). During its repolarized state, triggering of a subsequent AP is not possible. This time is referred to as refractory state. Mechanical contraction of the myocard is caused by an increase of Ca^{2+} concentration in the intracellular space, resulting from both the influx from the extracellular space and a release of Ca^{2+} from the sarcoplasmic reticulum [10].

The initial stimulus for depolarization can be generated in four major ways. Some atrial structures, like the sinus node, contain cells which do not have a stable resting potential. Instead they are self-depolarizing, triggering cardiac depolarization in regular intervals. If excitation is originating from the sinus node, this is refered to as normal sinus rhythm (NSR). Also other parts of the heart exhibit this behavior, like the atrio-ventricular node or the Bundle of His. These act as secondary pace makers and set in if the NSR is too slow.

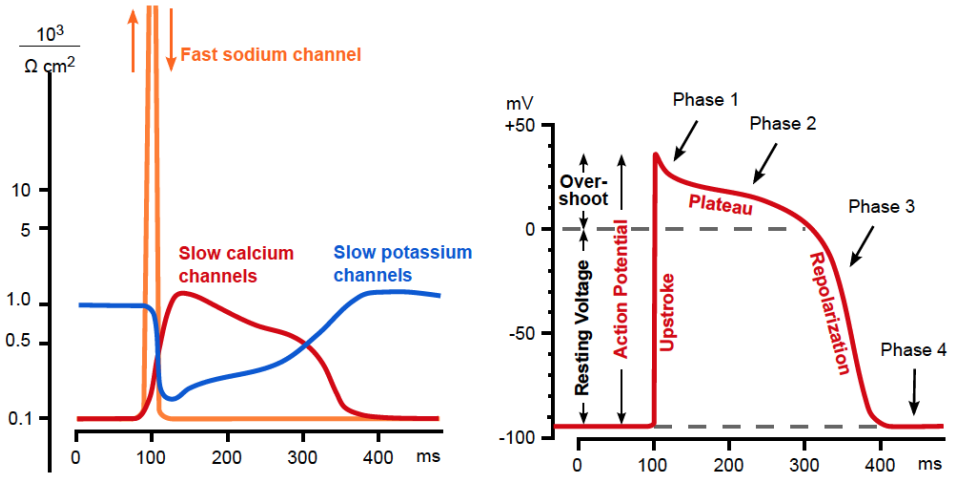

Figure 2.2: Ion channel conductivities and action potential. A schematic of the time-dependent conductivities for the most important ion channels sodium (Na^+), potassium (K^+) and calcium (Ca^{2+}) is shown on the left. The resulting action potential is shown on the right, comprising a rapid upstroke, a plateau, repolarization and rest. From [11].

.

APs of most cells, however, is triggered by the depolarization of neighboring myocytes. This is possible via so-called gap junctions, which form non-specific ion channels and thus provide an intercellular coupling. All cardiac cells are electrically coupled this way, forming an electrical syncytium. Once a stimulus is triggered anywhere in the heart, depolarization is propagated from one cell to the next by intercellular currents via this connection. From a macroscopic point of view, the speed with which the resulting depolarization pattern propagates is termed conduction velocity (CV). During NSR, the earliest point of activation can be found in the RA, next to the superior vena cava (SVC) ostium. This is the location of the sinus node. Subsequently, excitation spreads over both atria and reaches the atrioventricular node. Besides its auto-rhythmicity, this structure also delays the excitation before propagating it to the ventricles in order to optimize hemodynamics. Right and left bundle branches represent fast conducting parts of the ventricular conduction system and forward the excitation to the apex, from which ventricular depolarization begins [10]. The field resulting from the cardiac depolarization and repolarization processes can be measured as electrocardiogram (ECG) on the body surface.

Two further ways of triggering an action potential are common. Some regions exhibit a pathologically unstable resting potential, and thus act as ectopic centers. This can cause cardiac arrhythmias as outlined in the following chapters. Last, also artificial pacing can be performed. On the one hand, it is utilized as therapeutic measure by pace makers, which trigger cardiac activity during bradycardia. On the other hand, it can also be generated by a stimulation catheter during diagnostic procedures. In this case, the reaction on specific pacing sequences is of interest to verify the completeness of electrical isolation or to assess conduction properties.

2.2 Cardiac Arrhythmias

2.2.1 Atrial Fibrillation

Atrial fibrillation (AFib) is the most common heart rhythm disorder with a prevalence of 1 - 2% of the total population. It is a supraventricular tachycardia characterized by a complete loss of regular atrial activity. As it affects morbidity and mortality it is a major growing expense for the health care system [14, 15]. Risk factors are increasing age, male sex, diabetes mellitus, high blood pressure, myopathy and structural heart disease [16]. According to the duration of it's episodes, it is subclassified in paroxysmal, persistent, long standing persistent and permanent AFib [17]. AFib is the primary indication of over 350,000 hospitalizations in the US per year, resulting in total expenses of 26 billion US dollar annually [1].

Pathophysiological mechanisms The pathophysiology of AFib is complex and not yet completely understood. Genetic predisposition, structural modification and fibrotic inclusions, progression of cardiac diseases, inflammation, dysfunction of the autonomic nervous system paired with electrophysiological abnormalities of the atria and PV, favor the initiation and sustaining of fibrillation. Different studies have shown evidence for several (in parts contradicting) theories.

Multiple Wavelet Hypothesis The multiple wavelet hypothesis was introduced by Moe et al. in the late 1980s, stating that AFib is generated by parallel existing microreentry circuits in the atria [18]. The fibrillatory areas are self sustaining depending on CV, shortened refractory periods and increased atrial volume. Based on this model, the maze operation for therapy of AFib was generated [19].

Focal Sources Focal sources triggering episodes of atrial fibrillation could be identified using catheters. Haissaguerre was the first to demonstrate, that focal triggers originating from the PVs could initiate AFib [20]. Ablation of these focal sources terminated AFib [20, 21]. These studies are accepted as proof that AFib can be triggered by focal sources and are the rationale for current ablation strategies like the pulmonary vein isolation (PVI) [22–26] or other strategies targeting triggers outside the PVs [27].

Rotors The concept of rotors generating spiral waves was introduced by Krinsky [28] and Winfree [29] and the first experimental demonstration of a spiral wave was made in a sheep model by Davidenko [30]. The term *rotor* has become a household name and stands for a functional reentrant activity. Once initiated, rotors will spin at very high rates to generate electrical turbulence (fibrillatory conduction) [31]. The localized source hypothesis combines the theory of rotors and focal impulses, that activate rapidly enough to cause disorganized AFib. Recently Narayan et al. [27] could visualize rotors in the human atrium utilizing a computational mapping technique. Their relation to fractionated electrograms, however, is

still a matter of debate [32]. An alternative approach to detect rotors was presented using activation or phase-based analysis of body surface potentials in a non-invasive technique [33]. Both groups could show remarkable success rates in ablating the detected sites in their centers.

Dissociation of Layers and Breakthroughs Epicardial mapping using high-density electrode plagues (244 electrodes with interelectrode distance 2.25 mm) has brought evidence for another rationale of perpetuation of AFib. Allessie and co-workers analyzed the conduction pattern during induced and persistent AFib by means of wave mapping, observing an increased complexity in propagation patterns during persistent AFib when compared to acute AFib. Thus they proposed longitudinal dissociation [34] and breakthroughs [35] as contributing mechanisms. The presence of micro-anatomic intramural re-entry was also recently demonstrated using simultaneous optical mapping of both sides of the heart [36].

Structural and Electrical Remodeling AFib is a progressive disease with a continuous transition from paroxysmal to persistent AFib [37]. Explanations were seen in an increased atrial pressure or volume overload as well as solely electrical phenomena [38–40]. Although the completeness of the electrical remodeling is still unclear, it seems likely, that shortening of the AP, the refractory period, local conduction heterogeneities and zones of slow conduction are playing a major role [37, 41–45].

Fibrotic Tissue Areas of fibrotic tissue may be related to structural or electrical remodeling. In computer models, atrial fibrosis increases the fractionation of the electrograms [46]. Experimental models could show the influence of the excitation dynamics during AFib [47]. However, despite the improvements in detecting fibrosis by late-gadolinium enhancement (LGE)-magnetic resonance imaging (MRI) [48], the correlation to clinically recorded electrograms remains unclear [49, 50].

Autonomic Nervous System of Atria A study conducted by Bettoni et al. demonstrated, that increased sympathetic and parasympathetic tone preceded the onset of paroxysmal atrial fibrillation in a subgroup of patients [51]. Subsequent studies strengthened the theory that sympathetic and parasympathetic influences play a role in AFib [52, 53]. Spontaneous triggering originating from the pulmonary veins followed by electrical stimulation of the ganglionic plexi or the autonomous nerves, which activate the ganglions retrogradely, can induce episodes of AFib [54]. This is the experimental foundation for the hypothesis, that the intrinsic cardiac autonomous system can promote the onset of triggered AFib.

Treatment options After identification of triggers inside the PVs [20], their isolation has become standard first line approach for any catheter ablation. It can be achieved with both radiofrequency ablation or cryoballoon application [55].

Due to limited success rates in the treatment of patients with persistent AFib, additional approaches were suggested. The ablation of complex fractionated atrial electrograms (CFAE)

was suggested as subsequent treatment strategy [56], the initial success rates, however, could not be reproduced in recent large scale randomized studies [6, 7].

Following the hypothesis of rotational sources driving AFib, methods for their identification have been suggested [27]. During this *FIRMap* approach, panoramic mapping catheters are applied to acquire simultaneous multichannel information, which in turn is assessed with a dedicated workstation. However, recent studies also question this approach [57].

Assessing the presence of atrial fibrosis is a cornerstone of alternative strategies. Presuming its role as critical substrate, the identification of fibrotic regions using voltage mapping and the subsequent circumferential isolation was proposed as technique for substrate modification [58]. Also combined evaluation of low voltage areas and the respective activation patterns was investigated [59]. Non-invasive imaging was suggested to quantify the extent of fibrosis and subsequently identify promising candidates for catheter ablation and suitable strategies [60]. Despite this variety of ideas, the optimal treatment strategy for patients suffering from AFib still has to be found. Detection of the mechanisms underlying AFib is one of the most challenging research topics in current electrophysiology.

2.2.2 Atrial Flutter

Atrial flutter (AFlut) is defined as a supraventricular tachycardia with a consistent pattern of excitation. The most common type is typical AFlut which consists of a circuit confined to the RA and involving the cavo-tricuspid isthmus (CTI) bounded by the tricuspid annulus and the inferior vena cava [61]. Therefore, ablation at this critical portion of the path is the first line approach for termination [62].

However, a variety of atypical forms can be located in both RA and LA. In these cases, different anatomical obstacles (like the MV), scars from previous cardiac surgery, regions electrically isolated by ablation (like the pulmonary veins) and arrhythmogenic substrates (like spots subject to substrate modification) can be responsible for the maintanence of the tachycardia [8, 62–66]. Studies reported an incidence rate of 4.7 to 31% of AFlut following an ablation for AFib [8]. Despite the variety of mechanisms, high success rates of AFlut ablation were reported in the range of 88 to 100% [64].

Three categories were suggested to classify the mechanisms of AFlut (compare Figure 2.3) [65]:

- Focal source
- Microreentry
- Macroreentry

The **focal source** is characterized by a centrifugal spread of excitation originating from autorhythmic tissue or a breakthrough. Well-known locations of focal sources are the PVs, and these PV triggers are known to initiate atrial fibrillation [20]. During the tachycardia, individual excitations run over the atria until they are completely depolarized. No excitation can be observed in the atria during repolarization. Electrogram characteristics of the focal

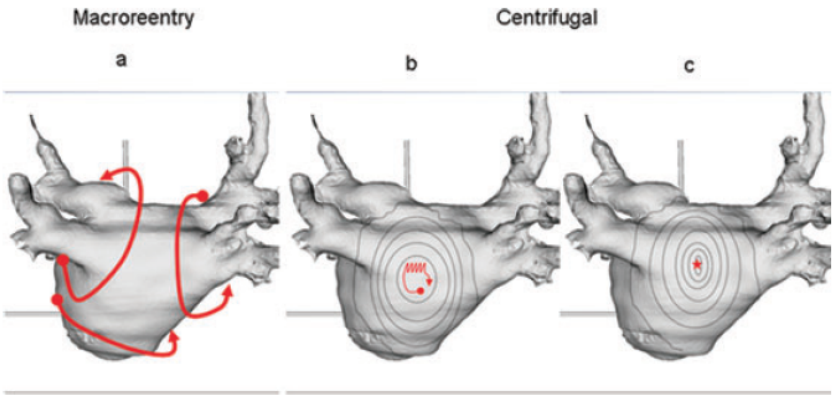

Figure 2.3: Three dominant mechanisms for atrial flutter. In case of macroreentry (a), roof-dependent circuits around the PVs and the perimitral form are observed most frequent. The underlying mechanism for a centrifugal spread of excitation can either be truly focal (c) or based on a microreentry with continuous activity (b). Reprinted from [65] with permission of the publisher.

source exhibit an S peak without R peak in the unipolar signal. However, most tachycardias showing a centrifugal pattern of excitation are actually based on micro reentrant activity, with only about 10 to 26% being truly focal [65, 66].

A **microreentry** is also characterized by a centrifugal spread of excitation. The maintenance mechanism, however, is a continuous propagation of a depolarization wave which passes very slowly through a critical isthmus, like e.g. a previous ablation scar or fibrotic tissue. The resulting centrifugal activation pattern arises from the exit point of the isthmus. In this area, a conduction velocity of <330 mm/s can be observed [63]. Consequently, depolarization can be observed during the complete cycle length, thus the atria are not electrically silent during any point in time. This activation is typically confined by a region of <1-3 cm in diameter, which can be also mapped using a standard multipolar mapping catheter [63, 65, 66]. In contrast to rotational sources assumed during AFib, the microreentry does not meander but harbors stationary at a critical substrate.

Macroreentry is also characterized by a continuous excitation process, in which activity can be observed during the complete cycle length. The complete circuit, however, cannot be mapped simultaneously using a standard multipolar catheter since its minimum diameter of >3 cm [63] exceeds the respective field of view. The flutter cycle typically runs around an anatomical obstacle like mitral or tricuspid valve, or scar isolating ipsilateral PVs. Especially in preablated atria, the flutter path typically is mediated by a gap in an incomplete / revitalized ablation line. Electrogram characteristics of this isthmus frequently exhibit highly fractionated activity covering most of the cycle.

In any case, detection and ablation of the critical point (focal origin, anchor of microreentry, gap for macroreentry) is very likely to terminate the flutter circuit. This is not that easy, however, since the propagation pattern is strongly influenced by existing ablation lines. These can cause fractionation at many sites and slowing of the propagation and activation delay of single regions. Sites showing activity during the diastolic interval of the surface ECG are common ablation targets as they often represent the critical isthmus [8, 66].

Recent studies have demonstrated a significant reduction in overall healthcare utilization by 6% when atrial flutter was treated by catheter ablation. Most dominantly, in-patient hospitalization and emergency department visits were substantially reduced [67].

AFlut has been observed to occur as subsequent tachycardia after ablation of AFib in up to 31% of cases [8]. Although most studies provide an average incidence rate, a strong dependency on the type of ablation could be observed. While only about 1 to 2.9% of AFlut was reported following PVI, linear lesions resulted in a 10 fold higher incidence rate [66]. In any case, diagnosis of post-AFib ablation tachycardias is rather complex due to the modifications done to the atrial substrate by AFib ablation and the subsequent variety of possible maintenance mechanisms [8]. This fact has stipulated various reseach about technqiues for the identification and ablation of post-AFib tachycardias, primarily focusing on step-by-step mapping algorithms based on manual signal assessment [8, 64–66]. Details about the respecitve mapping procedures are presented in section 11.

2.3 Mapping and Ablation

Understanding the patient specific arrhythmia mechanism is an important step in diagnosis. It can be achieved by understanding the propagation pattern of the arrhythmia itself or by assessing its statistical properties. In any case, it is goal of an electro-physiological (EP) study to acquire the required amount of data and simultaneously minimize the risk for the patient. The general workflow of such a procedure is depicted in Figure 2.4. Catheters are inserted via the inferior vena cava (IVC) into the RA and can subsequently be advanced through the septum into the LA. Having entered the desired atrium, mapping can be performed to identify areas in which lesions should be placed with the ablation catheter.

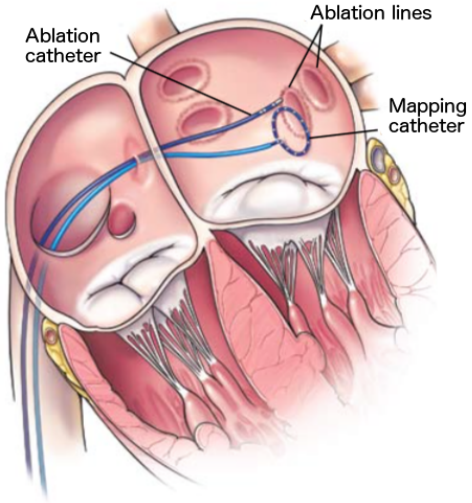

Figure 2.4: Catheters in the heart. After transseptal punction, catheters are advanced into the LA for mapping and ablation. From [68].

.

Different systems have been developed to acquire diagnostical information about the heart. One goal of these systems is to minimize the risk of infection by applying minimally invasive methods instead of open heart surgery. Also the radiation exposure required to localize equipment in the heart should be minimized. Therefore, electroanatomical mapping systems (EAMSs) have been developed, which can localize catheters without the need for X-ray and record all diagnostically relevant data at the same time. Since they are frequently applied in all modern EP labs, developing algorithms and analysis techniques for these kinds of systems is an important step. Different commercially available systems and their concepts are outlined in the following sections.

Other approaches aim to analyze the cardiac excitation pattern without the need for even minimally invasive mapping. These systems solve the so called 'inverse problem', which is a reconstruction of cardiac activity based on the electrogram that can be measured on the body surface. Two companies provide corresponding software: EP-Solutions (Amycard) [69] and CardioInsight (acquired by Medtronic in June 2015) [70]. This problem is mathematically ill-posed and it requires detailed knowledge about the torso and organs, which can be gained using e.g. MRI. A regularization has to be applied, which limits the solution space and focuses on major coarse excitation patterns. For treatment purposes, access to the heart is still required.

Mapping of the arrhythmogenic substrate is also attempted independently from the excitation itself. Therefore, LGE is applied as MRI technique. LGE contrast can be dominantly seen in scar or fibrotic areas. The amount of myocardium which shows strong contrast is e.g. quantified using the Utah scoring system [60]. Centers treating according to this scheme decide the ablation pattern based on the level of Utah score. For patients having score 4 out of 4, ablation has been shown less effective and associated with an increased recurrence rate.

Mapping during open heart surgery is primarily applied for research purposes. It is used to acquire high-density mapping data with epicardial plagues in order to assess complex excitation patterns [34, 35, 71]. Thus, EAMSs are the most common technique to record diagnostically relevant data from the heart and to select regions for ablation.

2.3.1 Electroanatomical Mapping Systems (EAMS)

In the strive to both understanding the electrical excitation pattern of the heart and minimizing radiation during catheter based procedures, electroanatomical mapping systems were developed. These systems should not only acquire the electrical information, but also assess electrogram parameters like voltage or location activation time. To make the excitation pattern comprehendable, the systems were able to generate a virtual cardiac anatomy based on the tracked catheter locations. Thus it was also possible to guide an ablation catheter to a designated spot and apply targeted ablation lesions.

The first system to track catheters in the heart and acquire the desired information was CARTO™ by Biosense Webster [72]. Localization was done using magnetic fields, which were received by three little coils in the catheter tip. Although this allowed for a very precise positioning, the user was limited to catheter with these navigation coils only.

A second system design was introduced to the market by St. Jude Medical, which is currently available in the version EnSite™ Velocity™ [73]. Localization is performed using an impedance based approach, in which a high frequency electrical field is applied through the body. The catheter electrodes subsequently serve as voltage divider, which allows to track all electrodes individually. The field, however, heavily depends on the conductivity value of all traversed organs and thus has to be scaled and adjusted based on a geometrical reference marker in the heart. Therefore the type of CS catheter is usually set prior to the study and subsequently used to adjust the field scaling. The ability to localize all electrodes is a clear advantage, however this comes at the cost of generally decreased accuracy [74], low long-term stability during the procedure and sudden position-changes when ablation current is applied. Thus a remap of the cardiac shell may be required several times throughout the procedures.

The latest mapping system on the market is Rhythmia™ by Boston Scientific. It uses a combined approach for localization, which allows to utilize both techniques. The catheter is initially localized based on electromagnetic tracking, while an impedance field is applied at the same time. During acquisition of the anatomy, the impedance field is recorded for every point in the heart. After the initial mapping, additional catheters can be inserted and localized using the field information. This combines both the long term stability and precision of magnetic tracking, and the ability to use catheters without localization coils. Automatic point acquisition allows to increase the number of points recorded inside the heart [9, 75, 76].

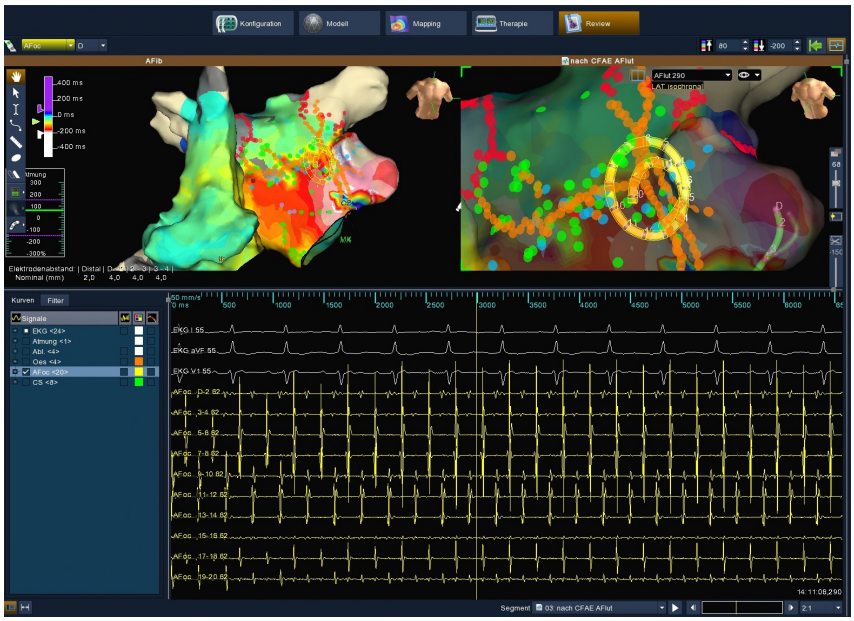

Figure 2.5: Screenshot of the EnSite Velocity EAMS.

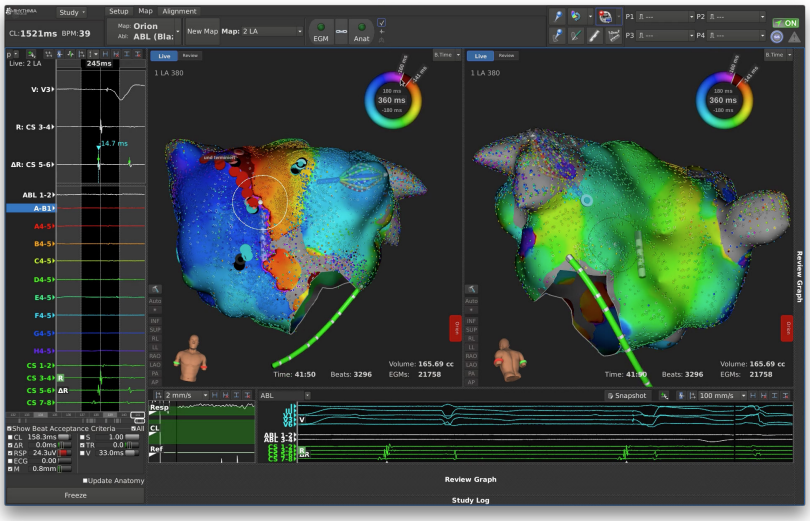

Figure 2.6: Screenshot of the Rhythmia EAMS.

2.3.2 Catheter Designs

The electrical information from within the heart is acquired using catheters, on which small electrodes are mounted. The catheters are composed of three major components: A handle which is used to control curvature and torsion, the electrode arrangement at the catheter tip and a shaft connecting both. The electrodes record the electrical field at their respective position, also causing spatial averaging due to their size and high conductivity. Different

mapping strategies, requirements for maneuverability and cost considerations consequently lead to a variety of designs for diagnostic catheters, which are discussed in the following.

The most simple catheter design consists of four electrodes mounted linearly on a catheter. For all catheters with unbranched design, the distal electrode at the catheter end is referred to by the letter 'D', while following electrodes towards the proximal end are counted using arabic numbering ('2', '3', ...). The distal electrode has a length of 4 mm or 8 mm in this configuration, so that it can be used for both mapping and ablation. Although this simple design is very cost efficient, it provides only limited options for mapping. For several reasons, like e.g. ablation, a certain minimum electrode size is required, increasing spatial averaging effects.

One extension of this concept are longer and curved designs, most often applied as CS catheter. These typically consist of 8 or 10 electrodes, which are arranged in either equal or paired spacing. Respective types are typically indicated in the datasheet using a triplet like 5-5-5 or 2-6-2, respectively, referring to the distances between three consecutive electrodes in mm. Linear arrangements with up to 20 electrodes and more sophisticated electrode spacings are available for interventions targeting typical AFlut, in which the catheter is positioned to cover the right lateral and septal areas simultaneously. This allows to record the excitation pattern during both the AFlut itself and pacing up to a point were conduction block in the CTI is achieved.

In order to understand local excitation patterns, spiral shaped designs were developed (see figure 2.7). Typical catheters comprise 10 to 20 electrodes, arranged on a single or a double loop with either equal or paired spacing (Optima™, Lasso™). In this design, however, the central part of the catheter does not contain electrodes. The star like PentaRay™ (Biosense Webster, diameter 3.2 cm) design has also electrodes rather close to the center, however this comes at the cost of increased interelectrode spacing on the outer circle.

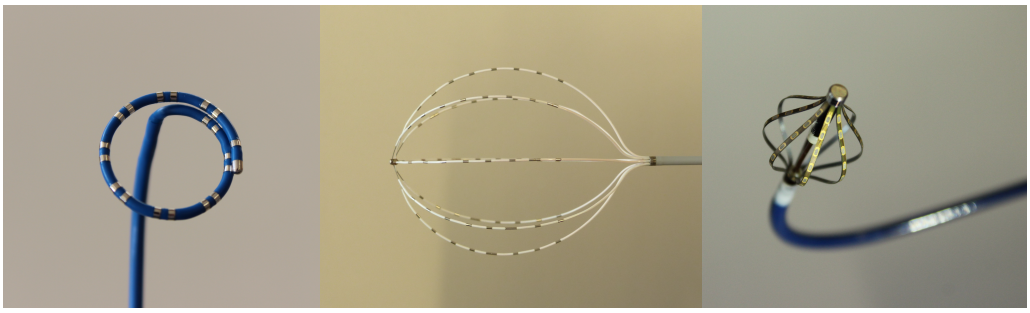

(a) Spiral catheter. **(b)** Constellation™ basket. **(c)** Orion™ mini-basket.

Figure 2.7: Photographs of three common catheter designs. A spiral catheter with 20 electrodes in paired spacing was used to acquire most data analyzed in this thesis. The diameter could be adjusted when areas inside PVs were mapped (a). The Constellation basket allows for simultaneous panoramic mapping with a diameter of up to 75 mm (b). The Orion mini-basket is preferably used for sequential mapping (c).

Since all of these catheters are designed to directly record electrical information from the myocardium while touching the endocard, they rely on good contact. Decrease of contact quality leads to signal averaging effects which compromise signal quality. An alternative approach for non-contact mapping was developed using a dedicated catheter in the heart (EnSite Array™) and solving the inverse problem 'Inside-Out'. This 64-electrode basket shaped catheter was combined with a software to solve the inverse problem and reconstructed 3360 EGMs for the complete endocardial surface [77, 78].

Mapping the complete myocardial activity simultaneously is an important prerequisite of understanding complex excitation patterns like in atrial fibrillation or atypical atrial flutter. The Constellation™ Basket (Boston Scientific) was developed to achieve panoramic contact mapping of cardiac activity. A total of 64 electrodes is mounted on 8 splines, which are designed fully flexible in order not to hurt the endocard when the catheter is deployed. This catheter is available in the diameters 31, 38, 48, 60, and 75 mm, with inter electrode spacings of 2, 3, 4, 5 and 7 mm, respectively. As depicted in Figure 2.7, the electrode arrangement is designed to primarily cover the central part of the atria, with no electrodes positioned in the septal areas. This catheter has been used to rapidly acquire data from AFlut [79–81] and to analyze biatrial propagation dynamics during the onset and perpetuating AFib [27, 82–84].

Application of the Constellation™ Catheter in clinical environment demonstrated two limitations, being first the limited septal coverage and second the tendency to spline bunching. In an attempt to address both issues, Topera Medical (now part of Abbott) developed a new catheter design addressing these two issues. The FIRMap™ basket catheter also has 64 electrodes, with the distal electrode being shifted towards the catheter tip and the proximal one being located closer to the shaft (see Figure 4.3 for comparison). This catheter is available in three different sizes, being 50, 60 and 70 mm. The electrode configuration is designed to cover the septal area better but at the cost of increased interelectrode spacing and thus lower resolution. The issue of spline bunching is addressed by a modification of the design: Splines are not fully flexible but exhibit a rectangular shape on which the electrodes are printed on the outer surface only. This is also expected to reduce far field effects. It is distributed primarily together with the RhythmView™ mapping system, which is the platform providing automatic analysis of intracardiac mapping data with respect of detection of focal sources and rotational activity [85].

Besides the global mapping of activity using non-contact and contact approaches, also new catheters for local high-density mapping were developed. The smaller sized basket Orion™ (Boston Scientific) carries 64 electrodes with an interelectrode spacing of 2.5 mm, and has fully deployed a diameter of 18 to 22 mm [75, 86]. As visualize in Figure 2.7, each electrode has a size of 0.4 mm^2, increasing the sensitivity to record electrical potentials [86]. This catheter is equiped with coils for magnetic tracking, and thus can be used to acquire precise anatomical information. The mapping system Rhythmia™ records both the position and the local impedance field, which can subsequently be used to track standard catheters without coils. The basket-style arrangement has proven helpful for rapid data acquisition using automatic point collection. Studies reported a number of recorded points in the order of 3,236 and 3,566$\pm$1,082, within 9.41$\pm$4.92 min and 5.2$\pm$0.8 min, respectively [9, 75]. The

amount of simultaneously covered area, however, is rather limited and has not been subject to detailed evaluation.

Since the myocardial electrical activity can be mapped much more precisely using the Orion™ catheter with the mini-electrodes, it is possible to detect e.g. vital isthmi in ablation lines. Targeting this position with an ablation catheter precisely can be difficult, however, since the potentials recorded with a 4 mm or 8 mm tip are subject to spatial signal averaging effects. Thus an ablation catheter was developed which included small mini-electrodes embedded in the ablation electrode but isolated both thermically and electrically. The MiFi™ catheter (Boston Scientific) is currently brought into the market as 4 mm irrigated tip catheter. Initial experience indicates, that vital atrial fibers can be identified by sharp potentials on the mini electrodes [87], while the conventional bipole does not detect them. Procedural time, however, seems to be prolonged [88].

2.3.3 Mapping Techniques

Modes of data acquisition Two major concepts of data acquisition can be distinguished during electroanatomical mapping. During sequential mapping, one or more catheters are moved to different endocardial aspects of the atria. They are held in a stable position with contact to the endocard until a specified reference event takes place. Data around (before and after) this event are acquired and then the catheters can be moved to the next location. Using this technique, a map of the atria is acquired point by point. Prerequisite of this technique is first, that the arrhythmia or the evaluted statistical properties must not change during the time required for mapping. Second, a reference is required to synchronize data for certain types of analysis (e.g. determination of local activation time). The collection of these points can be performed either manually or with the help of automatic point collection [9, 89].

For single events of unstable tachycardias like AFib, simultaneous mapping is required. In this approach, synchronization cannot be applied and consequently all data has to be acquired simultaneously. This commonly consists of surface ECG, a stable intracardiac channel for positional reference (e.g. CS) and one or more mapping catheters like single or biatrial positioned panoramic baskets, spiral catheters, etc., depending on the desired type of analysis and the respective field of view. In contrast to sequential mapping, no segmentation or synchronization of the continuous data stream is performed.

Uni- and bipolar electrograms Cardiac mapping catheters are equipped with electrodes which capture the local electrical potential at their respective position. This potential is measured with respect to a reference, for which typically the Wilson Central Terminal is used. Signals which are acquired this way are referred to as unipolar electrograms (UEGMs). Although they very well represent the local activity near the measuring electrode, signal quality is often strongly compromised by various artifacts like power line hum and far fields [90].

For clinical analysis, a high signal quality is desired. Subtraction of the signals measured by two neighboring electrodes is a common technique to eliminate noise components which equally affect both unipolar channels. The resulting bipolar electrogram (BEGM) typically is less affected by artifacts, activity, however, cannot be related to one or the other recorded channel. While the morphology of unipolar signals is very well studied, the morphology of a bipolar measurement depends on the relative orientation between the measuring dipole and the direction of depolarization [90]. The use of an intracardiac reference has been suggested for improved signal quality of unipolar signals. Demonstrative examples of uni- and bipolar EGMs are shown in Figure 2.8.

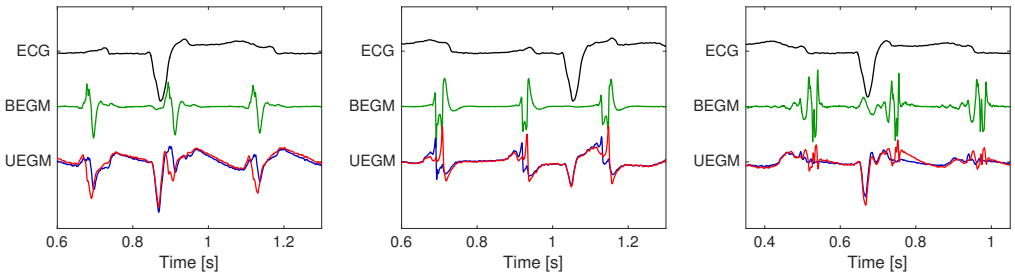

(a) Clear activations. **(b)** Complex morphology. **(c)** Fractionated signal.

Figure 2.8: EGMs in uni- and bipolar configuration. For all three examples, the ECG is shown at the top, a BEGM in the middle and the corresponding two UEGMs in the lower row. The demonstrative signals exhibit clear activations that result in a similar bipolar morphology (a), or a more complex shape of the BEGM (b). The fractionated activity in (c) can clearly be related to one of the unipolar channels. Of note, the influence of ventricular far field is much less in the BEGM.

Common mapping parameters Automatic signal analysis in the EP laboratory comprises three major parameters. First the voltage is assessed, being defined as the maximum peak to peak amplitude which can be measured in a specific window of interest. This time frame is typically set to the duration of one cycle of excitation. Times in which ventricular depolarization may compromise signal analysis can be rejected from analysis.

Second the local activation time (LAT) is assessed, reflecting the point in time at which the cardiac depolarization front passed the catheter. This time is typically also annotated in the window of interest and measured with respect to the activation in a reference channel (typically the CS). Subsequently, LAT information from all measured points is synchronized and visualized in form of color-coded LAT maps. Although this approach is of great help in understanding stable tachycardias with single distinct deflections in all signals, it cannot be used for AFib and can be questioned in case of double potentials and prolonged activations.

In AFib, statistical measures are used to assess the degree of fractionation in the signal. Although all common methods are inspired by early research about CFAE [56], the resulting annotation does not always reflect physicians' assessment [91]. Therefore, usage of CFAE mapping algorithms for fully automatic signal analysis in the clinical context is typically handled with care.

2.3.4 Catheter Ablation

Catheter ablation has emerged to a recommended technique for symptomatic AFlut as well as paroxysmal AFib [16]. For termination of AFlut, successful identification of the mechanism and the critical isthmus is required. Whereas the isolation of the pulmonary veins aims for trigger elimination during AFib, other techniques focus on substrate modification: linear ablation, ablation of CFAE, ablation of ganglionated plexi and recently, panoramic mapping and ablation of rotors. Up to date, all strategies for substrate modification are lacking in defined, reproducible endpoints and the best ablation approach and ablation combinations are discussed controversially [16, 20, 23, 24, 27, 32, 65, 92–97].

For radio frequency (RF) ablation, special catheters are advanced into the heart. These are equipped with both an ablation electrode (typically 4 to 8 mm in length) and additional distal electrodes for bipolar signal acquisition. RF current is delivered from the ablation electrode in a range of about 300 to 1000 kHz, as lower frequencies may stimulate myocardial tissue. Temperature of the surrounding tissue is subsequently increased by resistive heating, which is the dominant mechanism for the generation of myocardial lesions. Lesion formation itself is affected by multiple factors, like catheter tissue contact, transmitted power, time of application, or convective heat dissipation from circulating blood. Additional irrigation with saline has been shown to positively foster lesion growing. The location of ablation lesions can be annotated in all EAMS [89].

An alternative option for lesion generation is provided by cooling [55, 89]. Cryoablation catheters can be inserted in the heart and used to freeze surrounding tissue. Special catheter designs for PVI are available, which provide circumferential RF ablation and simultaneous monitoring of activation inside the PVs.

2.4 Simulation of Cardiac Activity

Algorithms for electrogram analysis have to be designed to process measured data, and thus need to be robust against noise and artifacts. The clinical environment, however, is typically not controlled enough to precisely benchmark the performance of new analysis methods. In addition, the available data for retrospective processing is limited to what was measured during the procedure. Computational modeling provides an important alternative option to clinical data acquisition, as arbitrary scenarios can be simulated. This comprises different tachycardias like AFlut or AFib, mapping with varying catheter designs and positions, and even the assessment of virtual ablation patterns.

All computational models are based on the behavior of single cells, which are described by a set of coupled differential equations. These models typically include ion concentrations, describe the ionic currents and the resulting changes to the TMV. Depending on the application and thus the desired level of detail, cardiac excitation can be simulated on both a biophysical and a phenomenological level. Both approaches will be outlined in the following.

2.4.1 Biophysical Models for Cardiac Electrophysiology

Hodgkin-Huxley Model Biophysical cellular models are based on cellular mechanisms like ion-concentrations and -exchanges. The first cellular model describing the membrane kinetics of an excitable cell was published 1952 [98]. By assessing voltage-clamp experiments from a giant squid neuron, a mathematical formulation of the electric currents across the cell membrane was developed which included Na^+ and K^+ as dominant ions. The equivalent circuit represents this relationship by parallel conductors as shown in Figure 2.9.

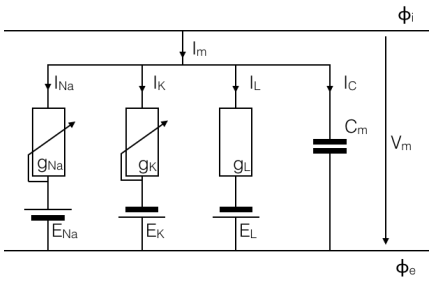

Figure 2.9: Hodgkin-Huxley model as electric circuit presentation. Adapted from [98].

In this circuit, the total current I_m is formed by the sum of four components, representing the capacitive and ionic parts. The ion channels for Na^+ and K^+ are modeled by time dependent conductances g_{Na} and g_K, respectively. The electrochemical gradients E_{Na} and E_K are included to model the driving force for each ion type. The effect of leak channels is modeled by an analog path including the fixed conductance g_L, and the influence of the cell membrane by the capacitance C_m.

Mathematically, the currents I_{Na}, I_K and I_L are given by the product between their respective conductance and the difference between TMV V_m and the ion specific resting voltage E_k, also known as Nernst voltage:

$$I_k = (V_m - E_k) \cdot g_k \qquad E_k = \frac{RT}{z_k F} \cdot \ln \frac{c_{k,i}}{c_{k,0}} \tag{2.1}$$

The Nernst equation describes the potential E_k of an ion k across the cell membrane, depending on its concentration in the intracellular ($c_{k,i}$) and extracellular ($c_{k,j}$) space. It is computed by considering the ideal gas constant R, Faraday's constant F, the temperature T and the charge z_k of the ion.

Thus, I_m can be formulated according to

$$I_m = I_C + I_{Na} + I_K + I_L = C_m \frac{dV_m}{dt} + \sum_k (V_m - E_k) g_k \tag{2.2}$$

The conductivities g_{Na} and g_K depend on the degree of opening of the respective ion channels. Their value is both time and voltage dependent and can be described by gating

variables according to

$$\begin{aligned} g_K &= g_{K,max} n^4 \\ g_{Na} &= g_{Na,max} m^3 h. \end{aligned} \tag{2.3}$$

While the potassium channel can be described by four activating n gates, the sodium channel consists of three gates of type m (activating) and one h gate (inactivating). These gating variables indicate the probability whether a gate and thus the channel is open or not. Differential equations describe the transition between the opened and closed state by utilizing two rate constants α and β. While α describes the probability to get to an opened stated, β reflects the likelihood of closing. The instantaneous values of both rates are functions of V_m, reflecting the TMV dependent behavior of ion channels in the cell membrane:

$$\begin{aligned} \dot{m} &= \alpha_m(1-m) - \beta_m m \\ \dot{h} &= \alpha_h(1-h) - \beta_h h \\ \dot{n} &= \alpha_n(1-n) - \beta_n n \end{aligned} \tag{2.4}$$

Courtemanche-Ramirez-Nattel Model Following Hodgkin and Huxley, more complex cellular models were formulated. These include additional ion channels to better approximate the behavior of single cells or tissue patches, both in physiological and pathological states. The Courtemanche-Ramirez-Nattel (atrial cell model) (CRN) cellular model was designed to describe human atrial myocardium [99, 100]. Building from the Hodgkin-Huxley model, it more precisely reflects different types of Na^+ and K^+ channels, and additionally describes Ca^{2+} concentration. Also the sarcoplasmic reticulum is considered for the intracellular calcium handling.

Resulting time-dependent change of TMV V_m is given by

$$\frac{dV_m}{dt} = \frac{-(I_m + I_{st})}{C_m}, \tag{2.5}$$

in which I_m is given by the sum of all 12 modeled ionic currents. I_{st} further allows to add an external stimulus current.

The CRN model was used for most cardiac simulations described in this thesis. To reflect atrial remodeling, changes to ion channel conductivites were included when required [101]. For simulations of cardiac activity at Institute of Biomedical Engineering (IBT), the solver *acCELLerate* [102] is used.

2.4.2 Conduction of Cardiac Excitation

Individual myocytes are linked by gap-junctions. These provide an electrical coupling of the intracellular space, which in turn causes the spread of excitation from one cell to the next. Having the models for cardiac electrophysiology implemented, the analysis of patches of atrial tissue is the next step. To simulate the process of atrial depolarization in

these patches, different macroscopic models can be applied. The data analyzed within the presented research were generated by either using the detailed bi-/monodomain model or the much faster but simplified Eikonal equations.

Bi- and monodomain models The bidomain model is a very frequently used way to simulate cardiac excitation [102, 103]. Hereby it represents the electrical behavior averaged for a bunch of cells. In this approach, both the intracellular and extracellular space are given by two continuous domains in which the potentials Φ_i and Φ_e are defined. These are linked to the current source densities following Poisson's equation for a stationary electric field

$$\begin{aligned} \nabla(\sigma_e \nabla \Phi_e) &= -\beta \cdot I_m - I_{se} \\ \nabla(\sigma_i \nabla \Phi_i) &= \beta \cdot I_m - I_{si}, \end{aligned} \tag{2.6}$$

in which β represents the surface-to-volume ratio of the cells, σ_i and σ_e the conductivity tensors, I_{si} and I_{se} the stimulus currents applied in the intracellular and extracellular domain, and I_m the total membrane current which links both domains. The corresponding voltage difference between both domains is given by $V_m = \Phi_i - \Phi_e$

Based on these equations, and considering the case in which no external stimulus is applied, the first equation of the bidomain model can be formulated. It relates both the TMV V_m from the cellular model and the extracellular potential Φ_e according to

$$\nabla((\sigma_i + \sigma_e)\nabla \Phi_e) = -\nabla(\sigma_i \nabla V_m). \tag{2.7}$$

The second bidomain equation is given by

$$\nabla(\sigma_i \nabla V_m) + \nabla(\sigma_i \nabla \Phi_e) = \beta \cdot \left(C_m \cdot \frac{dV_m}{dt} + I_m \right) - I_{si}. \tag{2.8}$$

It can be used to determine the intracellular stimulus current, which is used to evaluate the cell models in the next time step.

The bidomain model allows to specify separate conductivity tensors for the intracellular and extracellular domain. This degree of detail is especially useful when the conductive and capacitive effects of large ablation catheters should be integrated. But as this model is very computationally expensive, most cardiac simulations applied in this work were based on the monodomain model. The latter can be derived by assuming a constant anisotropy ratio between the conductivities in the intra- and extracellular domain ($\sigma_i = \kappa \cdot \sigma_e$). This leads to the monodomain equation which is given by

$$\nabla(\sigma_i \nabla V_m) = (\kappa + 1) \cdot \beta \cdot \left(C_m \cdot \frac{dV_m}{dt} + I_m \right). \tag{2.9}$$

Fast Marching approach for Eikonal equations Cardiac excitation of simple rhythms like NSR or AFlut can also be modeled using a phenomenological approach which is even less computationally demanding. Therefore, the Eikonal equations can be used to represent excitation of cardiac tissue in a parameterized approach on macroscopic level [104, 105].

They were derived from the monodomain propagation model and describe the form of activation wavefronts in the domain Ω according to

$$\begin{aligned} ||\mathbf{c}\nabla\tau|| &= 1 + \nabla\cdot(\mathbf{D}\nabla\tau) \qquad \mathbf{x}\in\Omega, \\ \mathbf{n}\cdot\mathbf{D}\nabla\tau &= 0 \qquad \mathbf{x}\in\vartheta\Omega, \end{aligned} \tag{2.10}$$

with $\vartheta\Omega$ representing the boundary of Ω, $\mathbf{c}$ the tensor of scaled propagation velocity, τ the scaled activation time, $\mathbf{D}$ the scaled diffusion tensor, $||\cdot||$ the euclidean norm and $\mathbf{n}$ a unit vector normal to $\vartheta\Omega$ [105]. For $\mathbf{D}\to 0$ in the isotropic case, the velocity of the wavefronts is constant as given by $||\mathbf{c}\nabla\tau|| = 1$. Thus, the wavefront curvature dependent velocity is introduced by the diffusion of activation times.

Solving generally requires several iterations with high complexity (e.g. $O(N^2)$ for grid $N\times N$), however it can be simplified by considering only adjacent nodes for each computation in the fast marching approach. This reduces complexity to $O(N\log(N))$.

Influence of wavefront curvature on CV is considered within this approach. Ionic currents and concentrations, however, are not included. As opposed to a reaction-diffusion model like the monodomain approach, it therefore neglects the source-sink mismatch and should not be applied for complex depolarization processes like AFib.

CHAPTER 3

Mathematical & Signal Processing Fundamentals

3.1 Frequency Domain Analysis

All clinical electrogram data analyzed in this thesis were recorded in time domain, being a continuous signal discretized with a specific sampling rate and quantification for digital signal processing. Although many events can easily be detected in time domain, the frequency content of signals also provides important information about artificial noise components and can be utilized in advanced signal processing algorithms.

3.1.1 Fourier Transform

The Fourier transform is a very common way to assess the frequency content of a time domain signal. Thereby, the signal is decomposed into the trigonometric functions sine and cosine (Fourier analysis), or their exponential analogon. Each component is appropriately weighted to reflect the strength of the respective curve within the signal. By using an infinite sum over all components, signals can be transformed between time and frequency domain.

Considering a time-continuous signal $x(t)$ of infinite length, its Fourier transform $X(f) = \mathscr{F}\{x(t)\}$ at frequency f is defined as

$$x(t) \bullet\!\!-\!\!\circ\, X(f) \tag{3.1}$$

$$X(f) = \langle x(t), \mathrm{e}^{\mathrm{j}2\pi ft} \rangle_t = \int_{-\infty}^{+\infty} x(t)\mathrm{e}^{-\mathrm{j}2\pi ft}\mathrm{d}t. \tag{3.2}$$

The absolute value of $X(f)$ is referred to as frequency spectrum of $x(t)$, as it reflects the energy of individual frequency components in the signal. A filtering effect can be achieved by reducing the strength of specific frequencies. The corresponding time domain signal $x(t)$

can be retrieved by the inverse Fourier transform given by

$$X(f) \circ\!\!-\!\!\bullet\, x(t) \tag{3.3}$$

$$x(t) = \langle X(f), \mathrm{e}^{-\mathrm{j}2\pi ft} \rangle_f = \int_{-\infty}^{+\infty} X(f)\mathrm{e}^{\mathrm{j}2\pi ft}\mathrm{d}f. \tag{3.4}$$

For digital processing, both time and values of recorded signals have to be discretized. Given the sampling frequency f_A, values are available at each multiple of the sampling time $T_\mathrm{A} = 1/f_\mathrm{A}$. Accordingly, values of $x(t)$ are discretized to

$$x_n := x(nT_\mathrm{A}) = x(t)|_{t=nT_\mathrm{A}}, \quad n \in \mathbb{Z}. \tag{3.5}$$

Considering the N available sample values of the signal after discretation, the analoga for the Fourier transform X_k and its inverse are calculated by

$$x_n \bullet\!\!-\!\!\circ\, X_k \tag{3.6}$$

$$X_k = \sum_{n=0}^{N-1} x_n \mathrm{e}^{-\mathrm{j}2\pi\frac{kn}{N}} \tag{3.7}$$

and

$$X_k \circ\!\!-\!\!\bullet\, x_n \tag{3.8}$$

$$x_n = \frac{1}{N}\sum_{k=0}^{N-1} X_k \mathrm{e}^{\mathrm{j}2\pi\frac{kn}{N}}. \tag{3.9}$$

The direct implementation of this transform is dependent to the number of sample points N with a computational complexity of $O(N^2)$. By utilizing its symmetry and periodicity, the Fast Fourier transform was developed as efficient algorithm [106, 107].

Although the Fourier transform does indicate the presence of a frequency component within a signal, it does not allow to obtain information during which time it was observed. The short time Fourier transform was developed to address this issue. The signal $x(t)$ is therefore multiplied with a window function $w(t)$, which is non-zero only within the evaluated time frame. Its transform $S(f,t)$ subsequently reflects the components in a time-frequency domain [108]:

$$S(f,t) = \int_{-\infty}^{+\infty} x(\tau)w(\tau - t)\mathrm{e}^{-\mathrm{j}2\pi f\tau}\mathrm{d}\tau \tag{3.10}$$

The resolution in time and frequency domain can be controlled by selecting an appropriate windowing function. However, due to their uncertainty relation, resolution of both quantities cannot be increased arbitrarily [108].

3.1.2 Wavelet Transform

An alternative strategy to assess the frequency content of a signal is provided by means of the wavelet transform. While complex exponentials are used as kernel function in the Fourier transform, different types of wavelets can be chosen as kernel in the wavelet transform.

A wavelet $\psi(t)$ with its Fourier transform $\Psi(f)$ must fulfill the admissibility condition of being a continuous zero-mean function as expressed in

$$C^{\psi} = \int_{-\infty}^{+\infty} \frac{|\Psi(af)|^2}{|f|} \mathrm{d}f < \infty \tag{3.11}$$

The transformation is then given in dependency of both ψ and the scaling parameters a and b to be [108]

$$W^{\psi}(a,b) = \langle x(t), \psi_{a,b}(t) \rangle_t = \frac{1}{\sqrt{|a|}} \int_{-\infty}^{+\infty} x(t) \psi^* \left(\frac{t-b}{a} \right) \mathrm{d}t. \tag{3.12}$$

A major advantage of the wavelet transform is its capability to adapt the time-frequency resolution. For high frequencies, temporal resolution is improved, with spectral resolution being increased for low frequencies. This is depicted and in Figure 3.1 and put into comparison with the other outlined frequency domain representations.

To adapt the time-frequency resolution, the mother wavelet is scaled by a and time shifted by b. The factor $1/\sqrt{|a|}$ is inserted to ensure that signal energy is not changed during scaling.

The inverse transformation is given by [108]

$$\hat{x}(t) = \frac{1}{C^{\psi\tilde{\psi}}} \int_{-\infty}^{+\infty} \int_{-\infty}^{+\infty} W^{\psi}(a,b) \tilde{\psi} \left(\frac{t-b}{a} \right) \frac{\mathrm{d}a\mathrm{d}b}{a^2}, \tag{3.13}$$

for which both analysis wavelet $\Psi(f)$ and the synthesis wavelet $\tilde{\Psi}(f)$ need to fulfill the admissibility condition

$$C^{\Psi\tilde{\Psi}} = \int_{-\infty}^{+\infty} \frac{\left| \Psi^*(f) \cdot \tilde{\Psi}(f) \right|^2}{|f|} \mathrm{d}f < \infty. \tag{3.14}$$

For the discrete wavelet transform, parameters are computed by dyadic scaling $a_k = 2^k$ and $b_{m,k} = m \cdot 2^k \cdot T_{\mathrm{A}}$. This allows to use multirate filter banks for the rapid computation of the discrete wavelet transform. Corresponding, the frequency domain is divided by a factor of 2 of each level of decomposition, with the approximation coefficients reflecting the spectrum up to 0.5 times the Nyquist frequency f_N, and the detail coefficients representing the remaining frequencies.

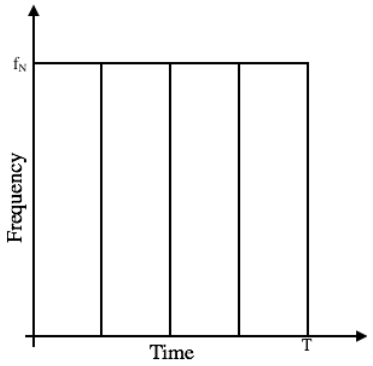

(a) Signal in time-frequency domain.

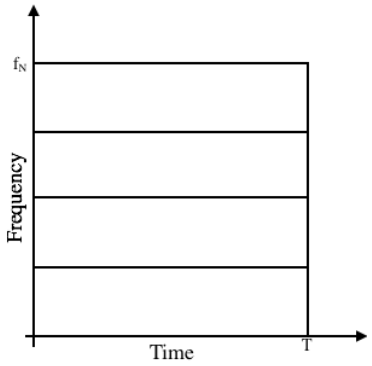

(b) Time-frequency domain (FFT).

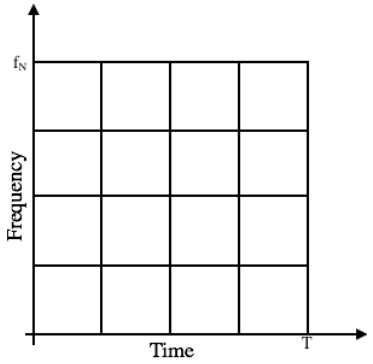

(c) Time-frequency domain (STFT).

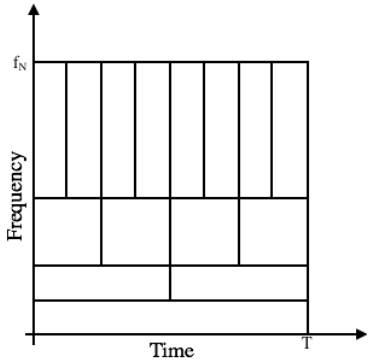

(d) Time-frequency domain (WT).

Figure 3.1: Time and frequency resolution for different transforms. The time resolution of the measured signal depends on its sampling frequency (a). Frequency components cannot be localized in time when the FFT is applied (b). A fixed resolution in both domains is applied in the STFT (c). The resolution is adapted in the WT to achieve high spectral resolution for low frequencies and improved temporal resolution for high frequencies.

3.2 Signal Processing Techniques

3.2.1 Non-Linear Energy Operator

The presence of activity within a signal is reflected by an increase of instantaneous energy. While typically the total energy of the signal is of interest, an expression for its time dependent value has been derived following considerations about an ideal spring-mass-system [109].

The samples x_n of a time-discrete simple harmonic oscillation with amplitude A, digital frequency Ω and phase ϕ can be described according to

$$x_n = A\cos(\Omega n + \phi). \tag{3.15}$$

The resulting expression for the energy of the harmonic oscillator can be formulated by

$$E_{\mathrm{NLEO}} = A^2\sin^2(\Omega) \approx A^2\Omega^2, \tag{3.16}$$

with the approximation $sin(\Omega) \approx \Omega$ considered valid for frequencies below 1/8 of the sampling frequency [109]. In this case, the relative error is smaller than 11%.

Transferring this concept to discrete time domain signals, the instantaneous energy E_n for time step n can be derived by utilizing trigonometric identities to

$$E_n = x_n^2 - x_{n-1} \cdot x_{n+1}, \tag{3.17}$$

thus being computed with three successive samples of the signal [109]. This operation is termed non-linear energy operator (NLEO). It is proportional to both the squared amplitude and the squared frequency of the signal. To obtain a more robust estimate in presence of noise, the resulting NLEO value was typically low-pass filtered as described in literature [110] to evaluate electrogram signals in this thesis.

3.2.2 Hilbert Transform and Phase Determination

The Hilbert transform can be used to generate a real-valued signal with shifted frequency components. This is an important step to obtain either the signal envelope or the phase for periodic processes.

Hilbert transform The Hilbert transform can be formally denoted by the Cauchy principal value (p.v.) of the improper integral

$$\tilde{x}(t) = \mathscr{H}\{x(t)\} = \frac{1}{\pi} \text{ p.v.} \int_{-\infty}^{+\infty} \frac{x(\tau)}{t-\tau} \mathrm{d}\tau. \tag{3.18}$$

Another more intuitive expression can be formulated as multiplication in the frequency domain by considering the Fourier transforms of both the signal $X(f)$ and the Hilbert transform as given by

$$\mathscr{F}\{\mathscr{H}\{x(t)\}\} = \tilde{H}(f) \cdot X(f) \tag{3.19}$$

with

$$\tilde{h}(t) = \begin{cases} \dfrac{1}{\pi t}, & \text{for } t \neq 0, \\ 0, & \text{for } t = 0. \end{cases} \tag{3.20}$$

$$\tilde{H}(f) = \begin{cases} -\mathrm{j}, & \text{for } f > 0, \\ 0, & \text{for } f = 0, \\ +\mathrm{j}, & \text{for } f < 0. \end{cases} \tag{3.21}$$

As indicated by equation (3.21), positive and negative frequencies are shifted by -90° and $+90^\circ$, respectively [111].

Analytic signal Given a time domain signal $x(t)$, its analytic signal is defined as

$$x_a(t) = x(t) + \mathrm{j}\mathscr{H}\{x(t)\} = x(t) + \mathrm{j}\tilde{x}(t), \tag{3.22}$$

with $\tilde{x}(t)$ denoting the Hilbert transform of the signal. According to the definition above, the analytic signal only has positive spectral components.

Thus $x_a(t)$ is a complex-valued time signal, whose absolute value represents the envelope $A(t)$ of $x(t)$ as given by

$$A(t) = |x_a(t)| = \sqrt{x^2(t) + \tilde{x}^2(t)}. \tag{3.23}$$

Phase The trajectory of a variable in state space representation can be analyzed to assess the dynamics of the underlying process. For repetitive processes, the current state within the period can be described by the phase $\phi(t)$. It can be measured with respect to an origin, which has to be located inside the (non-overlapping) trajectory to obtain unique results.

To obtain a state space plot if only one single variable x is available, it can be plotted against a time-delayed version of itself $x(t+\tau)$. The appropriate time lag τ can be defined as first zero crossing of the autocorrelation of $x(t)$, or based on the duration of rapid changes of the observed process [112]. Subsequently, $\phi(t)$ can be determined based on the trigonometrical relations according to

$$\phi(t) = \arctan\left(\frac{(x(t+\tau) - x^*)}{x(t) - x^*}\right), \tag{3.24}$$

in which x^* defines the origin of the state space trajectory [112]. This origin can be approximated by the mean of $x(t)$.

In order to avoid the issue of finding an appropriate value for τ, a method based on the Hilbert transform was suggested [113]. Using this approach, $\phi(t)$ can be expressed using

$$\phi(t) = \arctan\left(\frac{-(x(t) - x^*)}{\tilde{x}(t) - x^*}\right), \tag{3.25}$$

in which x^* defines the origin of the phase plane [114].

In applications considering cardiac data, phase values are typically computed for all acquired electrograms. Subsequently, the detection of phase singularities is of interest, as it reflects the center of a rotational depolarization pattern. Following the concept of topologic charge, phase singularities can be defined by evaluating ϕ at a specific instance of time t_0

$$n_{t_0} = \frac{1}{2\pi} \oint_c \nabla\phi(t_0)\mathrm{d}l, \tag{3.26}$$

in which the line integral is evaluated over path l on a closed curve c. This integral will yield zero if the path contains no phase singularity, otherwise its value will be $\pm 2\pi$ (depending on the chirality of reentry and orientation of integration). Studies have addressed the detection of phase singularities as filaments in space [115, 116] or on triangular meshes [117].

3.2.3 Principal Component Analysis

The principal component analysis (PCA) is an important method in the field of statistical data analysis. It is a widely applied approach for dimensionality reduction of measurement data, and can be applied to simplify the structure of a dataset before e.g. feature extraction is performed.

Primary objective is to transform a number D of potentially correlated variables into a smaller number M of linearly uncorrelated variables, preserving the desired amount ($M < D$) or all ($M = D$) information. Therefore, a new orthonormal base is generated, which can be used to project the data into a subspace with decreasing variance in each component.

Consider a set of N observations $\mathbf{X} = [\underline{x}_0, \underline{x}_1, ..., \underline{x}_N]$ of the D-dimensional measurement vector $\underline{x}_n$, forming an $N \times D$ matrix. This data shall correspond to the $N = 20$ measurement points in the $D = 2$ dimensional space shown in Figure 3.2. For demonstration purposes, data points in this figure were annotated using two different classes, whose separation is a common task.

Goal of the PCA is to find a new base $\mathbf{A}$ for expressing $\mathbf{X}$ according to

$$\mathbf{X} = \mathbf{Z}\mathbf{A}^T. \tag{3.27}$$

Therefore, a version $\mathbf{X}_Z$ of zero empirical mean is constructed from the data matrix $\mathbf{X}$, allowing to assess the variability from the origin. Subsequently, the observation covariance matrix $\mathbf{R}$ is computed as

$$\mathbf{R} = \mathbf{X}_Z^T \mathbf{X}_Z \tag{3.28}$$

and its eigenvectors and eigenvalues are determined. Eigenvectors are sorted by decreasing values of the respective eigenvalues, leading to $\lambda_1, ..., \lambda_D$. The cumulative sum up to a certain number of eigenvalues M hereby reflects the amount of explained variance when reconstruction is performed using only the corresponding first M eigenvectors.

The resulting transformation is given by

$$\mathbf{Z}_{PCA} = \mathbf{X}_Z \mathbf{A} \tag{3.29}$$

with $\mathbf{Z}_{PCA}$ containing the principal component (PC) scores representing transformed data, and $\mathbf{A}$ being formed by the M eigenvectors of $\mathbf{R}$ which are used for reconstruction. If all eigenvectors are used, data is reconstructed perfectly. The dimensionality is reduced if only a number $M < D$ of eigenvectors is used.

Considering the example demonstrated in Figure 3.2, reduction to $M = 1$ seems reasonable. Projection onto the first principal component allows for linear separation of both classes using a single threshold. Its value could for example be determined using Fisher's Linear Discriminant [118, 119].

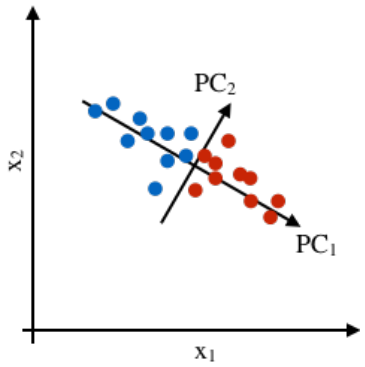

Figure 3.2: Example demonstrating the concept of PCA. 20 data points in the two-dimensional space are plotted, together with the principal components found by PCA. Data points were labeled using two different classes, which became linearly separable in the first dimension of the transformed space.

3.3 Classification

3.3.1 Decision Tree

Decision trees are classifiers in which the assigned label is determined based on a sequence of decisions. Starting from the root node, specific properties of class features are assessed, and successive branches are followed based on the outcome. For each node, decisions may be based on attributes of different types, like continuous values (size, weight) or categorical variables (gender). The corresponding links must be mutually distinct and exhaustive. Following the branches, finally a leaf node will be reached, which assigns the resulting label [118].

This type of classifier brings several advantages, like automatic selection of features. During growing of the tree, most significant attributes are located in the upper levels, least significant features may be neglected. Each feature is analyzed individually, so that scale differences are not a problem. Both linear and non-linear features can be used, as the tree is not based on any underlying model. Last but not least, interpretation of the resulting tree is very intuitive. However, over-fitting to the training data may occur if growing of the tree is not limited. This can be avoided by subsequent pruning, being the removal of branches which do not classify strongly.

Several ways exist to generate or grow a tree, like ID3, C4.5 or CART (classification and regression tree) [118]. In general, the complete training set is split into subsets by evaluating every single feature. Considering a previously defined metric, the best feature is selected and the dataset partitioned accordingly. On each subset the process is repeated until a stopping criterion is reached.

The resulting subset after a decision should be as pure as possible. Following the concept, but reflecting that the variability of classes is more easy to measure, several criteria have been designed which assess the impurity of the resulting outcome. One possibility is to determine

the entropy $H(S)$ of the set of objects S according to

$$\mathrm{H}(S) = -\sum_{x \in X} p(x) \log_2 (p(x)), \tag{3.30}$$

in which $p(x)$ denotes the relative frequency of objects of class x among all existing classes X in S. Goal during growing the tree is to reduce the cumulative entropy of the resulting subsets.

Another frequently applied criterion is the Gini diversity index, defined by

$$\mathrm{GDI}(S) = 1 - \sum_{x \in X} p(x)^2. \tag{3.31}$$

For sets with objects of just one class, the Gini diversity index is zero [118].

3.3.2 Support Vector Machine

The support vector machine (SVM) is a kernel-based classifier with the favorable property of having sparse solutions, meaning that the classification of new inputs only depends on the evaluation of the kernel function on a subset of training data points. Although it was designed for binary linear separation, the usage of kernel functions and the combination of multiple SVMs allows to tackle also multiclass problems which do not exhibit a linear border.

Hard margin SVM The fundamental SVM classification statement of a hard margin SVM is linear and given by

$$y(\mathbf{x}) = \mathbf{w}^T \Phi(\mathbf{x}) + b, \tag{3.32}$$

with $\Phi(\mathbf{x})$ being the transformed features of the input data, $\mathbf{w}$ the weight vectors and b the bias paramter [119]. Depending on the binary class membership of input samples $\mathbf{x}$, the output $y(\mathbf{x})$ will result in values higher or smaller than 0. Corresponding target values $t_1, ..., t_N$ with $t_n \in \{-1, 1\}$ shall be defined so that $t_n y(\mathbf{x}_n) > 0$ for all training data points.

The decision boundary that separates both classes with a maximum margin can be found by optimizing the following expression with respect to $\mathbf{w}$ and b, i.e. maximizing the minimum distance between all points $\mathbf{x}_n$ and the boundary (compare Figure 3.3):

$$\max_{w,b} \left\{ \frac{1}{||\mathbf{w}||} \min_n \left[t_n \left(\mathbf{w}^T \Phi(\mathbf{x}_n) + b \right) \right] \right\} \tag{3.33}$$

Optimization can be achieved by reformulating equation (3.33) with Lagrange multipliers $a_n \geq 0$. Additional boundary conditions can be introduced by calculating the derivatives subject to $\mathbf{w}$ and b, leading to the dual representation of the maximum margin problem as given by

$$\max_{\mathbf{a}} \tilde{L}(\mathbf{a}) = \max_{\mathbf{a}} \left\{ \sum_{n=1}^{N} a_n - \frac{1}{2} \sum_{n=1}^{N} \sum_{m=1}^{N} a_n a_m t_n t_m k(\mathbf{x}_n, \mathbf{x}_m) \right\} \tag{3.34}$$

with the kernel function being defined by $k(\mathbf{x}_n, \mathbf{x}_m) = \Phi(\mathbf{x}_n)^T \Phi(\mathbf{x}_m)$ and respecting the constraints

$$a_n \geq 0 \quad \text{for } n = 1, \ldots, N \tag{3.35}$$

$$\sum_{n=1}^{N} a_n t_n = 0. \tag{3.36}$$

Having determined the parameters a_n, new data points can be classified according to

$$y(\mathbf{x}) = \sum_{n=1}^{N} a_n t_n k(\mathbf{x}, \mathbf{x}_n) + b, \tag{3.37}$$

with the sign of $y(\mathbf{x})$ representing the resulting class label. Computation is hereby simplified as only the resulting support vectors of the training dataset will have $a_n > 0$, with all other points being not considered for the classification of new data due to $a_n = 0$.

Using nonlinear kernel functions allows to transform the input feature vectors $\mathbf{x}_n$ into a higher dimensional feature space in which perfect linear separation may be possible. Further enhancement is possible to relevance vector machines, which can be extended to multiclass problems more comprehensively and also return direct posterior probabilities [119].

Soft margin SVM In the case that classes are not perfectly separable, misclassification of some training data has to be accepted to train an SVM model which is of reasonable generalization capability. Therefore, slack variables $\xi_n > 0$ are introduced which penalize misclassification and modify the optimization problem (compared Figure 3.3). To balance both margin size and slack variable penalty, a second parameter C is used. The resulting optimization problem reflects the "soft margin SVM" [119] and can be formulated as

$$\min_{\mathbf{w},b} \left\{ \frac{1}{2} \|\mathbf{w}\|^2 + C \sum_{n=1}^{N} \xi_n \right\}. \tag{3.38}$$

Application of Lagrangian multipliers leads to the same form as shown in equation (3.37), however under different constraints

$$0 \leq a_n \leq C \tag{3.39}$$

$$\sum_{n=1}^{N} a_n t_n = 0. \tag{3.40}$$

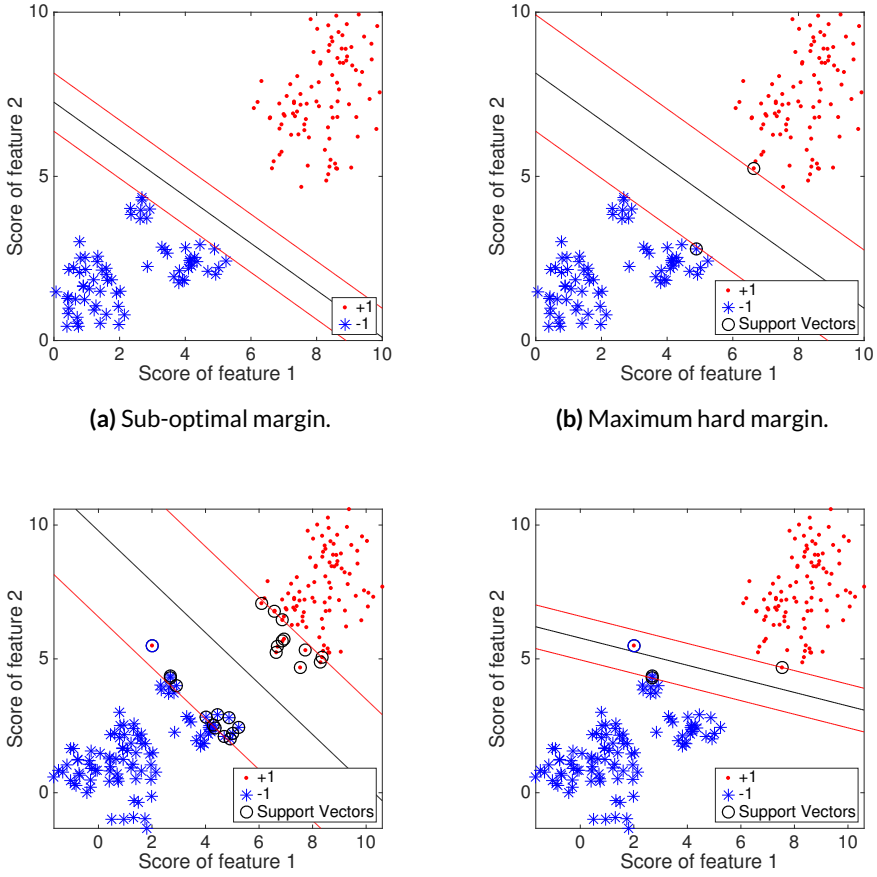

(a) Sub-optimal margin.

(b) Maximum hard margin.

(c) Soft margin ($C = 10^{-2}$).

(d) Soft margin ($C = 10^{-0}$).

Figure 3.3: Example demonstrating the SVM-based classification. Data from a binary decision problem is plotted in a two-dimensional feature space. While a separation boundary could be placed anywhere in the domain, it would most likely not provide optimal margin for the decision (a). Using the hard margin SVM finds the margin with maximum distance to the support vectors (b). The soft margin SVM allows to relax the boundary condition in order to achieve a higher generalizability. The corresponding trade-off between penalization of outliers and margin width can be adjusted using the parameter C (c, d).

PART II

QUANTITATIVE ANALYSIS OF ATRIAL ELECTROGRAMS

CHAPTER 4

Computational Catheter Models

As presented in Chapter 2.3.2, various catheter configurations are available and designed for specific purposes during diagnosis and treatment. Although all modern catheters are steerable and thus allow to control curvature and torsion, they are also designed flexible enough to avoid perforation of the myocardium. Thus the resulting form of the catheter in the heart frequently does not match its state ex-vivo. In fact, the shape of the catheter is determined by its rigidity and an interplay of forces applied by the atrial wall and steering maneuvers of the physician. Consequently, the true positions of all electrodes need to be respected when assessing the spatio-temporal relations in EGM recordings.

In clinical practice, the use of EAM systems allows to localize the electrodes during mapping and relate their position to the cardiac anatomy. During the simulation-based development of novel algorithms, however, the deformation of virtual catheters is not given. One way to deal with this issue is to directly transfer the position of electrodes from the clinical measurement into the simulation. This, however, requires to use the clinical anatomy also for the simulation, and inhibits the use of other mapping positions than in the clinic [120]. Previous research from our group suggested a projection method to include a catheter at arbitrary positions into simulated geometries. Therefore a temporary set of electrodes was determined within the blood pool. These initial positions were defined according to the specification of the catheter, and demonstrated at a single-loop spiral. Each of the initial electrodes was subsequently projected along the normal onto the tissue (when the catheter should lie e.g. on the posterior wall) or radially (if the catheter should be placed e.g. in a PV) [121]. This approach, however, does not allow to model the deformation of splines, which can result in electrodes lying in the blood pool without wall contact.

In this chapter, the development of a computational catheter model is described, as it was part of a supervised student thesis [122]. The shape of the model can be adapted to a given cardiac anatomy and thus allows to include more realistic recording sites in virtual diagnostic studies. In addition, it allows to evaluate the effect of catheter size and its electrode arrangement on mapping data acquisition.

4.1 Simulation of Catheter Deformation

Description of the Catheter Shape In order to gain a virtual representation of a catheter shape, its form was modeled by a parameterized curve $\mathbf{r}(s)$. Considering its tangent $\mathbf{T}$, normal $\mathbf{N}$ and binormal $\mathbf{B}$, $\mathbf{r}(s)$ can be described in matrix notation according to the Frenet-Serret formulas [123]

$$\begin{pmatrix} \dot{\mathbf{T}}(s) \\ \dot{\mathbf{N}}(s) \\ \dot{\mathbf{B}}(s) \end{pmatrix} = \begin{pmatrix} 0 & \kappa(s) & 0 \\ -\kappa(s) & 0 & \tau(s) \\ 0 & -\tau(s) & 0 \end{pmatrix} \begin{pmatrix} \mathbf{T}(s) \\ \mathbf{N}(s) \\ \mathbf{B}(s) \end{pmatrix}, \tag{4.1}$$

in which κ and τ represent curvature and torsion, respectively. Equation 4.1 provides a set of linear homogeneous ordinary differential equations (ODE) with arclength-dependent coefficients. In order to compute the absolute coordinates of the splines in space, $\mathbf{r}(s)$ was incorporated into equation 4.1 and integration was performed using the trapezoidal rule. This technique was chosen after assessing the rectangle rule forward, rectangle rule backward, trapezoidal rule, and the analytical solution for constant curvature and torsion, and comparing their result to a reference example solved by the Runge-Kutta method which could assess arbitrary values of κ and τ for any s. Despite improved accuracy, the latter could not be applied due to its computational cost during the optimization process of shape adaption. The catheter splines were modeled by line segments having piece-wise constant curvature and torsion defined at the supporting points along the curve.

The undeformed shape of the catheter curve was determined according to considerations about the equilibrium of an elastic rod [124, pp. 91–101]. Given boundary constraints for the start and end point of the curve, its form is consistent with a stationary minimum of its potential bending energy E_{pot}. For a rod with length l, E_{pot} is given by

$$E_{pot} = \frac{1}{2}\int_0^l A \cdot \kappa^2(s) + C \cdot \tau^2(s)\,\mathrm{d}s, \tag{4.2}$$

where $\kappa\,[\mathrm{m}^{-1}]$ is the curvature, $\tau\,[\mathrm{m}^{-1}]$ is the torsion, $A\,[\mathrm{Nm}^2]$ is the bending stiffness and $C\,[\mathrm{Nm}^2]$ is the torsional stiffness of the material [124, pp. 11-12].

Computing the undeformed state of a catheter spline consequently meant to find values for κ and τ which minimize the objective function E_{pot} and fulfill the boundary constraints like positions and angles at start and end of the curve. This was done by applying a MATLAB built-in optimization function for multidimensional non-linear constrained problems.

Modeling Catheter Deformation The presented approach for designing computational catheter models could be used to precisely model the electrode positions of complex catheter geometries. In addition, it was designed to handle the deformation of the catheter shape caused by the interaction of splines and the atrial wall. Therefore the position of supporting points along the curve was incorporated as boundary constraint into the solver: All points have to be located inside the anatomy. The required density of supporting points is related

to the complexity of the surface mesh. Since the endocardial surface as acquired during intracardiac mapping is generally rather smooth, an adequate density of supporting points was already given by the approximation of the catheter curve. Although the adaption of shape is possible with this approach, certain mechanical effects, like friction at the atrial wall, and dynamic processes like the permanent motion of the atrium or the deformation of the atrium by the catheter were not considered.

4.2 Implemented Basket Catheter Models

Although all types of catheters are affected by the deformation of shape, whole-chamber mapping catheters like the Constellation™ basket (Boston Scientific, USA) are of special interest. They are manufactured using super-elastic alloy splines, well-known to cause spline bunching in MV and roof of the LA [125]. A clinical example of a deformed catheter can be seen in Figure 4.1. The screenshot from the Velocity mapping system shows the basket catheter located in postero-superior position in the left atrium. Bunching of splines in the MV area and at the roof can be observed in both anterior (left) and lateral (right) view.

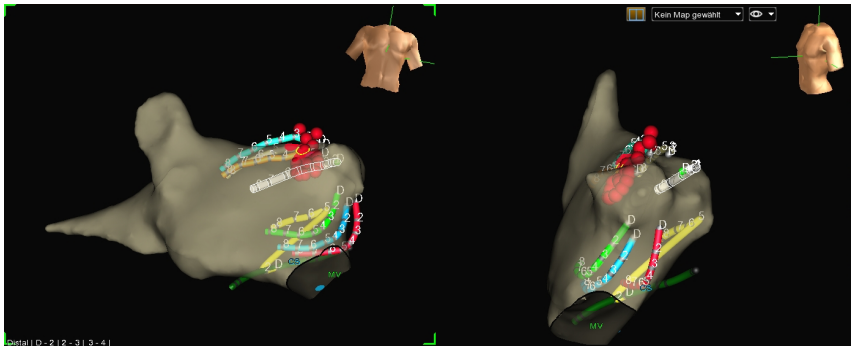

Figure 4.1: Screenshot of the Velocity mapping system demonstrating the deformation of a basket catheter. The basket is placed in postero-superior position in the LA. Individual splines of the basket are shown in different colors. Besides the basket, also the CS catheter (green) and the ablation catheter (white) can be recognized. The LA is shown in antero-posterior (left) and latero-septal view (right). While several splines are located in the roof and the MV, a lack of coverage can be observed at the anterior wall.

Following the above mentioned approach, individual splines of the basket catheter were modeled. The basket size was defined by the length of the splines. Geometrical constraints about the connection between splines at the distal catheter tip and the proximal end of splines was given by the assembly. Since the eight splines are uniformly distributed around the longitudinal axes, the interspline angle results to 45 °. The clamping angle between the longitudinal axes and the splines was adapted to match a fully deployed catheter in an undeformed state ex-vivo. The position of electrodes along each spline was given by their distances along the parameterized curve. This information was directly available from data sheets and product specifications.

Constellation EA For the topics addressed in the presented studies, two catheter designs with their respective electrode arrangements (EA) were focused upon. First, a catheter designed according to the Constellation™ basket product specifications was modeled, being referred to as *Constellation EA*. This catheter is available in the market for over 15 years now and was applied in multiple studies addressing atrial flutter (AFlut) [79, 80, 126] and atrial fibrillation (AFib) [82–84, 127]. It was not only used during panoramic approaches, but also for local mapping of the PVs [128, 129]. When basket catheter mapping is performed for diagnostic purposes, selecting the best possible catheter size and mapping position are of interest. These have to be balanced with potential disadvantages like bunching of catheter splines [125] and a lack of coverage in the proximal spline area [80].

FIRMap EA In order to cope with these issues, a novel catheter design was recently developed. The FIRMap™ (Abbott Medical, USA) basket is manufactured with more rigid splines to reduce spline bunching. In addition, the electrode arrangement was modified to allow for EGM acquisition in proximal areas [130]. In this configuration, the catheter is frequently used during FIRM-based mapping strategies targeting rotors and focal sources [85]. Since the number of electrodes was kept constant, however, the resulting interelectrode distance along the individual splines had to be increased and led to a reduced mapping density. This catheter was the second to be modeled, referred to as *FIRMap EA*.

Both electrode arrangement (EA) and clamping angle were adapted for each computational baskets as indicated by specifications or specimen. With respect to spline rigidity, the properties of both catheters were set highly flexible. The resulting basket models are depicted in Figures 4.2 and 4.3. An agreement between both the images and the overlays can be observed. Using these techniques, the shape of spiral catheters or individual splines of PentaRay could also be computed.

Basket in the Atrial Anatomy After implementation of the basket catheter models, the computational catheters were applied during several studies as described in Chapters 15.2.2 and 17.1. Therefore, different catheter sizes and EAs were assessed with respect to interspline distances and resulting coverage. The basket catheters were placed in the atrium and the algorithm for shape adaption was applied.

An example of the basket catheter model in the LA can be seen in Figure 4.4. Considering the LA size of 51 mm (lateral to septal), a catheter diameter of 48 mm was selected. Two splines near the posterior wall show towards roof and inferior posterior wall, respectively, as can be clearly seen in part (a).

In order to position the basket conveniently, a user interface was developed as depicted in Figure 4.5. The interface allows to select different catheter types, vary the catheter size, and change its position and orientation. Also different atrial geometries can be imported. Images can be chosen as background and used to visually inspect the agreement between implemented catheter designs and their respective photograph or data sheet. The resulting

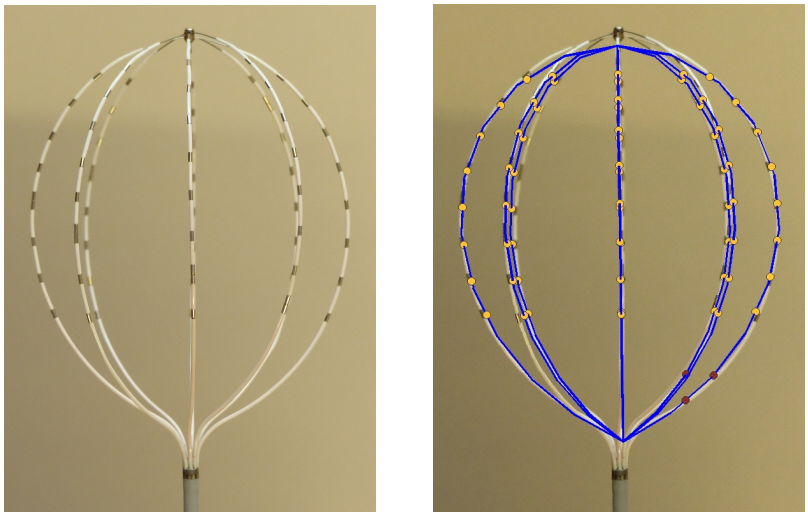

(a) Constellation catheter. **(b)** Overlay with simulated catheter.

Figure 4.2: Constellation catheter photographs, overlaid with the undeformed simulated catheter model. Yellow dots indicate the positions of the electrodes. Note the agreement between these simulated positions and the silver electrodes on the images. From [122].

catheter shape and its electrode positions can be exported to perform subsequent analysis of spatio-temporal patterns in diagnostic algorithms.

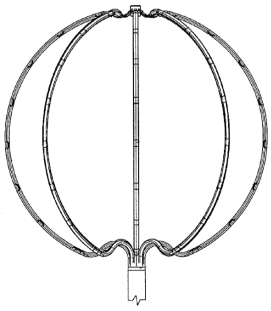

(a) FIRMmap catheter.

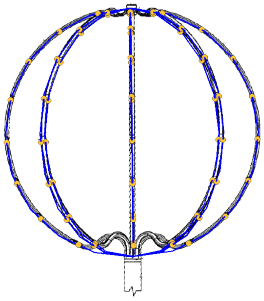

(b) Overlay with simulated catheter.

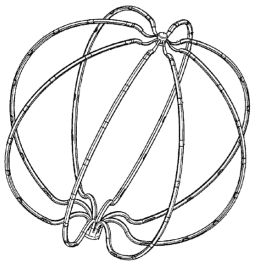

(c) FIRMmap catheter.

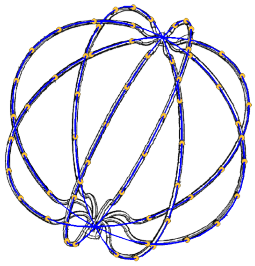

(d) Overlay with simulated catheter.

Figure 4.3: Image of the FIRMap specification sheet, overlaid with the undeformed FIRMap EA basket. Yellow dots indicate the positions of the electrodes. Note the agreement between these simulated positions and the silver electrodes on the images. Figures from [122] and adapted from [130].

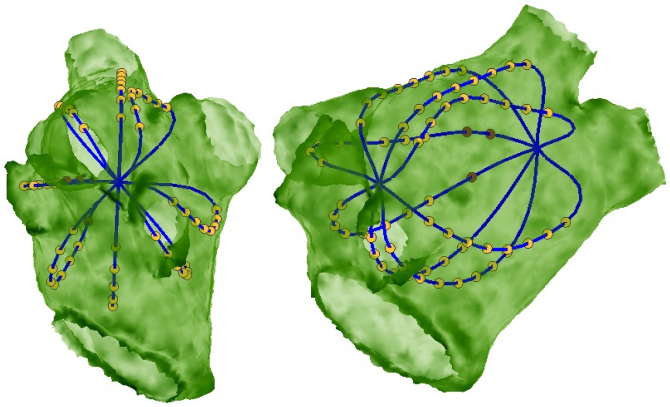

(a) Lateral view **(b)** Postero-lateral view

Figure 4.4: Constellation catheter of size 48 mm in postero-superior position. The catheter size was selected based on the atrial size of 51 mm. Spline separation can be observed at the posterior wall.

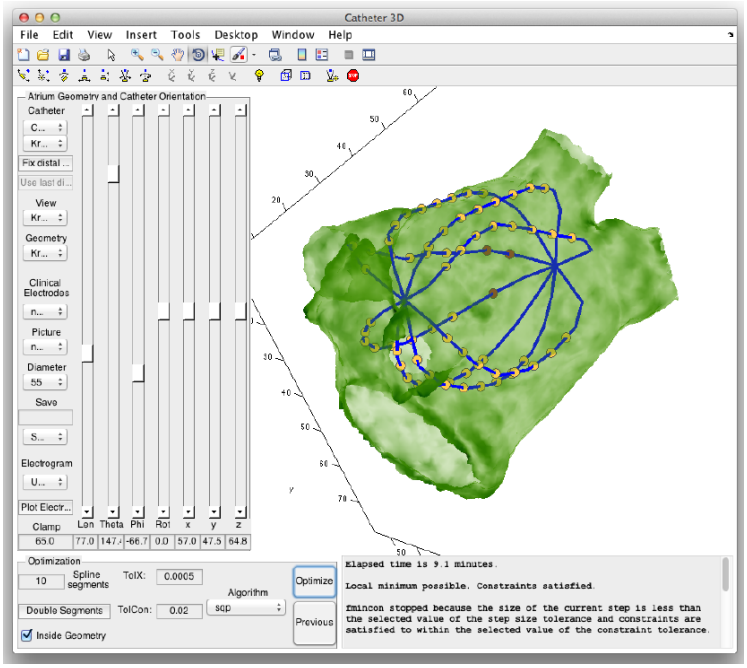

Figure 4.5: Graphical user interface (GUI) for the placement of catheters. The GUI allows full control over catheter type, size, position and orientation. The resulting electrode positions can be exported after optimization and used for subsequent analysis or algorithm development. Figure from [122].

.

CHAPTER 5

Preprocessing of Electrograms

Two major preprocessing steps were mandatory prior to electrogram analysis. First, filtering was required to remove high frequency noise and low frequency components. Second, ventricular activity had to be detected. This could be done based on the surface ECG, in which ventricular components could be easily distinguished from atrial activity. The techniques used for these tasks were developed during previous research projects [11, 131–133]. They were optimized and extended in close collaboration with Gustavo Lenis, who is conducting research in the field of ECG processing [134, 135].

5.1 Filtering Specific Frequency Components

All electrograms initially represent extracellular potentials, recorded in unipolar configuration with reference to an indifferent electrode. For the latter, frequently the Wilson terminal crest is used. These signals are typically corrupted by low frequency components, like baseline wander or respiratory effects. Power line hum of 50 Hz as well as other discrete and artificial frequency components also compromise signal quality, combined with general high frequency noise. An example of unfiltered unipolar electrograms (EGMs) is visualized in Figure 5.1. The electrograms were recorded by a Constellation™ basket catheter during atrial flutter (AFlut) on electrodes B3 and G1, respectively. The presented data were 5 s long and chosen due to the presence of clear atrial activity. The surface ECG lead V6 was plotted additionally to ease differentiation between atrial and ventricular activity. For each of the following plots, signals were scaled to emphasize the relative strength of signal and noise components. The filtering techniques used for the processing of clinical data will be outlined in the subsequent paragraphs.

Removal of baseline wander Slow processes like respiration or capacitive effects at the electrodes can cause baseline wander in the low frequency domain. While spectral components as little as 1 Hz are of interest during the processing for unipolar EGMs, the

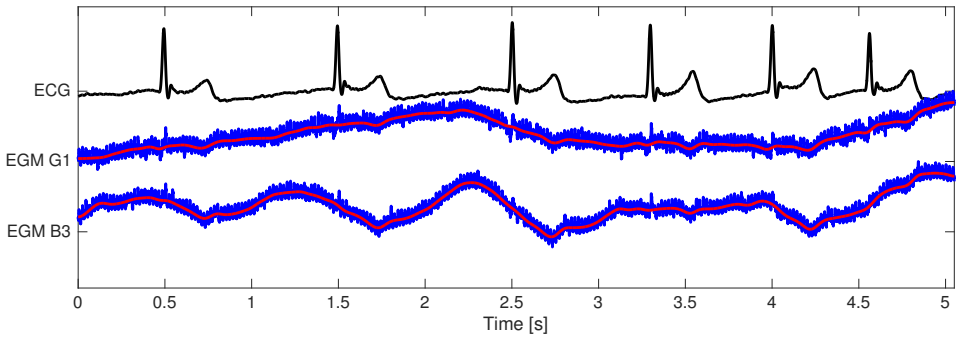

Figure 5.1: Exported unipolar EGM without additional filtering. Note strong 50 Hz power line hum and baseline wander, compromising the identification of atrial activity. The baseline was estimated (red) and removed in subsequent steps.

ventricular repolarization (T wave) has been shown to contain frequency content of up to 7 Hz [136]. This overlap hampers the application of standard high-pass filter techniques in baseline wander removal.

Therefore, the following preprocessing method was developed and presented [137]. First, the raw signal $x_r(t)$ was split into segments of 40 ms. The median values of every segment were interpolated using cubic splines. As this initial baseline estimate could contain undesired high frequency components, a Gaussian low-pass filter with a width of 7 Hz in frequency domain was subsequently applied. This value was chosen consistently with the center frequency of the T wave of the ECG [136]. The resulting baseline estimate is visualized in Figure 5.1. Based on visual assessment, it closely followed the baseline wander and reduced the component of ventricular repolarization. Subsequently, the baseline estimate was removed from the initial signal, as demonstrated in Figure 5.2.

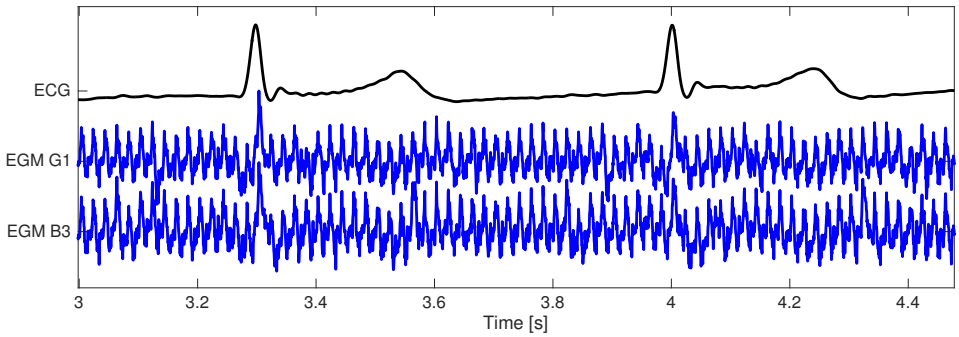

Figure 5.2: Removal of the baseline in unipolar EGMs. The baseline was estimated in time domain by median filtering and spline interpolation (compare Figure 5.1). It was subsequently subtracted from the original signal.

Clinical filter settings Certain cut-off frequencies are typically applied for the different signal types in the clinical context. As these values are based on year long clinical experience and strongly effect the morphology of the filtered signal, it is generally adviceable to use comparable values in automatic signal analysis. For surface ECG, and depending on the

application, the high-pass is frequently set to 0.5 Hz, with the low-pass set to 50 Hz [138]. For bipolar signals, cut-off values of 30 and 300 Hz are typically applied [139]. As low frequency components are of increased importance in the analysis of unipolar EGMs, the high-pass cut-off frequency is set to about 0.1 Hz [137].

The exact type of filters which are used in clinical electroanatomical mapping system (EAMS) and their order are not known. For the specific case of the electrogram recording system EP Labsystem Pro of Bard, previous research has indicated that Butterworth filters of first order were used as both high-pass and low-pass, respectively [140].

Application of these filters is demonstrated in Figure 5.3. The unipolar EGMs were filtered with a low-pass at cut-off frequency 300 Hz and a high-pass with 0.1 Hz. Due to their improved suppression of high frequency noise, filters of order 4 were applied. The 50 Hz component still dominated the signals.

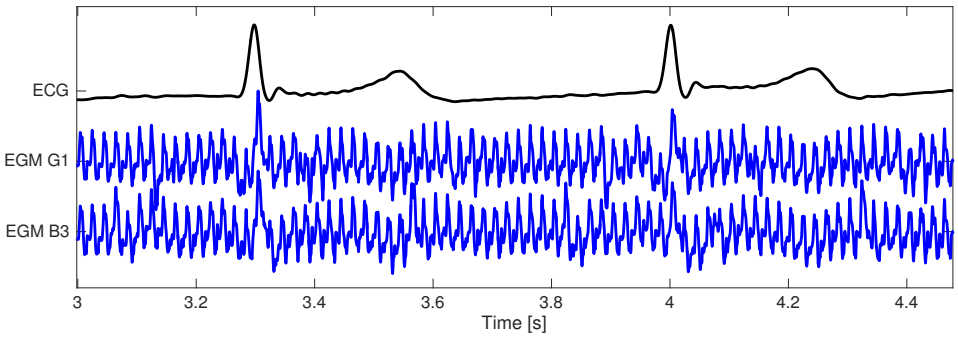

Figure 5.3: Unipolar EGMs filtered with clinical cut-off frequencies (0.1 - 300 Hz). The signal is dominated by 50 Hz power line hum.

Removal of specific frequency components Power line interference at 50 Hz is the most dominant artifact in unipolar signals, and peaks in the spectrum can also be observed at harmonics of this frequency. Frequently, additional discrete spectral components can be located at frequencies higher than 70 Hz, which cannot originate from a physiological source.

Spectral analysis of clinical data revealed, that the frequencies of these interferences varied when data was acquired at different clinical centers and using different recording systems. The exact source of the artificial components could not be located, as they may be caused from both the utilized mapping system (i.e. while using impedance based localization) or various equipment also present in the electro-physiological (EP) lab (pumps, ablation generator, ...). This indicates the need for algorithms to automatically detect artificial frequency components.

A corresponding detection and filtering technique was developed within the scope of a student project [141] and is currently under review for publication. In short, the power spectral density (PSD) was determined for each recorded EGM. Based on the assumption, that artificial components would affect all channels, the resulting PSDs were averaged. A sliding window of width 2 Hz was used to analyze the spectrum, with maximum and median

of the spectral values calculated at each step and their quotient computed. If this value exceeded a certain signal specific threshold, a peak was annotated. A subsequent iterative algorithm was used to determine the fundamental frequency, as it was generally located below 100 Hz and thus more hardly to be discerned from physiological components. The resulting list of frequency peaks was subsequently handed over to a filtering algorithm for removal of these artificial components [141].

In order to remove discrete spectral components, a notch filter with a Gaussian kernel was designed [137]. This form was chosen due to its small time band-width product. The width of the Gaussian in frequency domain was set to 2 Hz, and copies of this bell were added to attenuate each harmonic. The filter was multiplied with the spectrum in frequency domain. After transformation back into time domain, the resulting signal did not show oszillations at these frequencies any more.

The application of the 50 Hz notch filter on the example signals is shown in Figure 5.4. Atrial activity can be recognized with a cycle length of 253 ms.

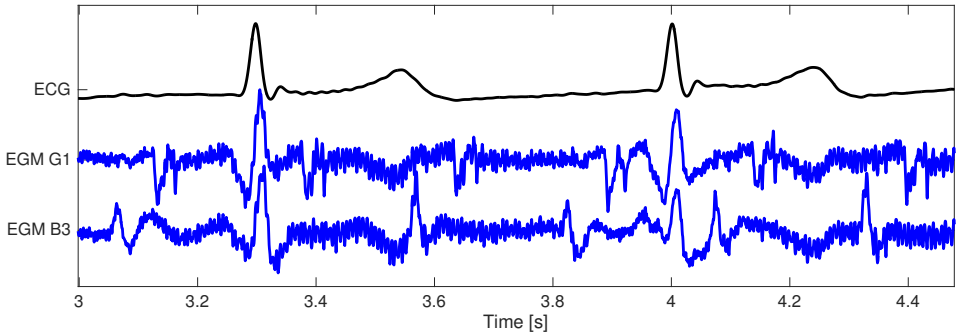

Figure 5.4: Removal of power line hum. A notch filter was applied in frequency domain to remove the 50 Hz component. The Gaussian bell was chosen as kernel for the filter function due to its optimal time-bandwidth product. Atrial activity can be recognized at this step.

After additional removal of other discrete frequencies at 142.5, 144, 195.5 and 203.5 Hz, different atrial and ventricular components could be identified in the signal (see Figure 5.5). Atrial activity was now clearly visible, and fractionation could be observed in EGM G1. A comparison with the original unfiltered signal in Figure 5.1 emphasizes the need of careful preprocessing prior to signal analysis.

However, ventricular components could still be recognized synchronously to the QRS complexes in the surface ECG. An additional far field could also be observed simultaneous to the T wave, although it was weakened by previous baseline filtering. As these components overlap with the atrial activity in the frequency domain, they have to be addressed using sophisticated methods in time domain (compare Chapter 7).

Preprocessing of bipolar signals For comparison, the respective preprocessing steps are also shown for bipolar signals. Bipolar EGMs were constructed from the electrode pairs G1/G2 and B3/B4, respectively, thus involving the unipolar EGMs used in the previous

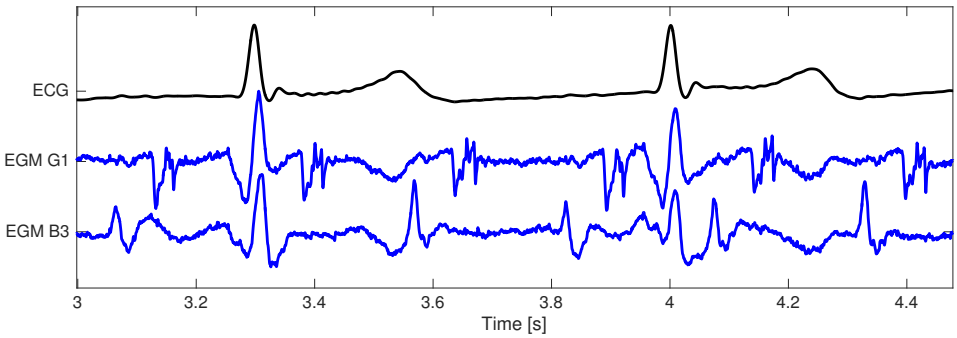

Figure 5.5: Removal of additional interferences at discrete frequencies. After identification of four undesired frequency components, a notch filter was applied in frequency domain to remove them. Atrial activity can be seen more clearly.

paragraphs. The difference between both EGMs is plotted in Figure 5.6, in which a strong baseline wander can be observed. But neither power line noise nor other high frequency components were present.

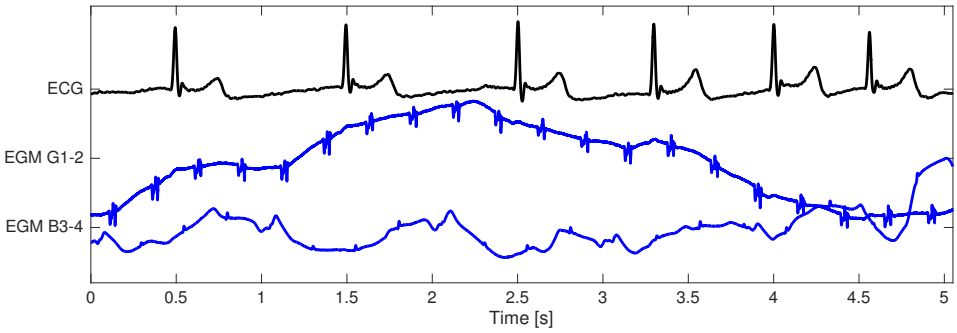

Figure 5.6: Bipolar EGMs without filtering. In contrast to unipolar EGMs, common components of the noise like synchronized artificial high frequency components or power line hum are canceled out by subtraction and do not require additional filtering.

Figure 5.7 reflects the result of applying forth-order high- and low-pass filters with the common cut-off values for bipolar signals of 30 and 300 Hz, respectively. Baseline wander was strongly attenuated and atrial activation complexes were clearly visible. The ventricular activity does hardly affect the measured EGM, as it similarly affected both unipolar channels. This result was in agreement with clinical observations, that the application of high- and low-pass filters is sufficient in most cases to achieve sufficient signal quality for bipolar EGMs. Note that this is in contrast to unipolar signals, for which the presence of discrete frequency components strongly affected signal quality (compare Figure 5.3).

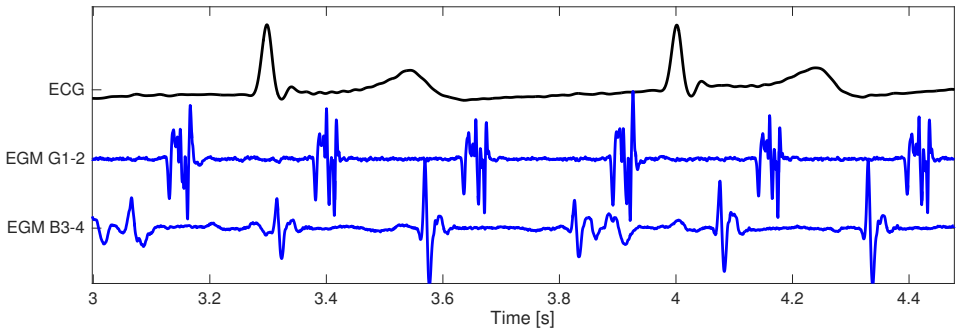

Figure 5.7: Bipolar EGMs after application of high-pass and low-pass. Filtering with cut-off values of 30 Hz (high-pass) and 300 Hz (low-pass) removed the baseline wander.

5.2 Detection of QRS Complexes

As demonstrated above, an undesired component within atrial EGMs is caused by ventricular activity. The so called ventricular far field (VFF) can most clearly be observed in unipolar EGMs, as this component is often canceled out in bipolar signals. It is caused by the depolarization of the ventricles, and is also present as QRS complex in the surface ECG. As the ventricular activity causes larger electrical potentials than the atrial one, QRS complexes are more easy to identify in the ECG than P waves.

Techniques for the removal of VFFs will be presented in Chapter 7. Alternatively, analysis of atrial electrograms can also be restricted to the time between QRS complexes, as no ventricular depolarization takes place within the RR interval (compare Chapter 11.1). For both approaches, information about the time of ventricular contraction is required.

In this chapter, a technique for the detection of QRS complexes is outlined. It is part of the IBT biosig toolbox for ECG processing, which allows the annotation of various interesting events from onset of the P wave up to end of the T wave. This is an important tool for the analysis of parameters related to ventricular depolarization or repolarization, effects of pharmacological treatment or risk statification [135, 142]. A benchmarking of the presented technique follows in Chapter 11.1, in which manual annotations and automatic QRS complex detection were compared in a database of 503 ECG traces, with all 810 QRS complexes being identified correctly.

Annotation of QRS complexes in single lead ECG signals First, QRS complexes were detected in each individual channel of the surface ECG. The band-pass filtered ECG was down-sampled to 400 Hz to allow for rapid processing. The stationary wavelet decomposition was performed up to a frequency of 50 Hz [135]. By default, the Haar wavelet was used, and the detail coefficients of the frequency band around 50 Hz were analyzed. Both wavelet and frequency range could be modified by the user. The energy of the transformed signal was normalized and an adaptive threshold computed by a moving average. Times exceeding the threshold were labeled as QRS complex [135, 142].

In a second processing step, the largest peak within the QRS complexes was annotated as R peak and adjacent extrema as Q and S peaks, respectively. Additional processing methods were available to reliably detect events like the beginning of the P wave [135].

Multichannel approach If multichannel data were available, first the QRS detection was performed independently in all leads. Then the R peaks were assigned to individual ventricular depolarizations by a voting algorithm. Within this algorithm, R peaks closer than 100 ms are merged and a minimum time between ventricular activities of 250 ms is assured by discarding inconsistently annotated R peaks.

If required, the algorithm also allowed to compute a QRS template of normal beats for each lead and correlate it to every occurrence. This could be used to determine the ECG channel with best signal quality.

Assessment of signals with 1 s duration Most signal processing methods for ECG analysis were developed for the assessment of parameters in Holter ECG. Respective signals frequently have durations lasting up to several days, making long-term changes of QRS morphology or statistical evaluation of ectopic activity most important tasks.

Within the field of intracardiac signal analysis, continuous signals are typically in the order of minutes. Therefore, the correct detection of ventricular activity itself is sufficient in most cases as supportive information for EGM analysis. Focusing on data recorded during LAT mapping, exported signals have a fixed duration of 1 s (Velocity EAMS) or 2.5 s (CARTO EAMS). In these cases, the detection of QRS complexes using an adaptive threshold is not possible.

Therefore, the QRS detection algorithm was adapted within the scope of this research project. After the detail coefficients of wavelet decomposition were computed, the 99% quantile was used to determine a saturation value thr_{sat} for the energy level. The minimum threshold for QRS detection was adapted based on two ideas inspired by physiology: As the morphology of QRS complexes was expected to be constant during the short period of the addressed tachycardias, the threshold was set to a fixed but individual value thr_{minAmp} for each signal. Following the assumption that the atrio-ventricular (AV) node refractory properties limit the heart rate to about 180 beats per minute, a maximum corresponding number N_{QRS} of QRS complexes was computed according to the signal duration. Subsequently, peak detection was applied with a minimum inter-peak distance of 50 ms and a minimum height $thr_{minAmp} = 0.5 \times thr_{sat}$. If the resulting peak number N_{peaks} exceeded N_{QRS}, most likely only atrial activity was detected and consequently all detections were discarded.

Using these modifications to threshold computation, the QRS detection could be successfully applied also to signals as short as 1 s. Besides the detection of ventricular activity, information about the atrial activity can also be extracted from the surface ECG. During some projects of the presented research, a close collaboration between the fields of ECG and EGM processing proved very promising. One example was the study of P wave onset, for which intracardac electrograms could be used as reference (compare Chapter 17.2) [135].

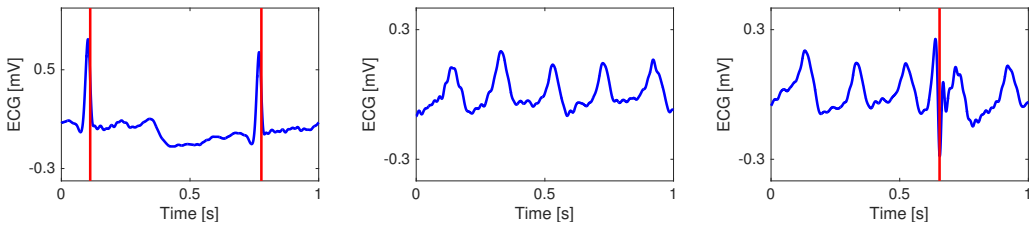

(a) 2 QRS complexes. **(b)** No QRS complex. **(c)** 1 QRS complex.

Figure 5.8: ECGs of short duration with annotated QRS complexes. Due to their short duration of 1 s, the adaptive threshold approach used for typical ECG recordings could not be applied to these ECGs. An adapted method was implemented and used to identify the presence of ventricular activity (red lines). A variable number of QRS complexes was observed within the signals.

CHAPTER 6

Atrial Geometry and Catheter Position

In order to comprehend the spatio-temporal patterns in multichannel mapping data, knowledge about the position of measuring electrodes and the cardiac anatomy is essential. Although the data format used for export in different EAM systems varies significantly (see Chapter 14.2), different preprocessing steps with respect to geometrical data are common.

When cardiac information was acquired in form of maps, the available clinical data usually comprised the spatial coordinates of each measurement. For time-continuous data, however, monitoring the position of each electrode and the subsequent identification of representative catheter locations was an important step during preprocessing. Also the acquired atrial geometries required certain preprocessing for subsequent analysis, as outlined in the next chapters. All steps were developed and optimized for processing speed during this thesis, as they were considered an important cornerstone to the goal of performing an automatic analysis during the procedure.

6.1 Preprocessing of Atrial Geometries

The cardiac anatomy, which is displayed as virtual representation of the heart during the electro-physiological (EP) study, is typically generated based on the catheter positions reached during mapping. Each location acquired outside of the current model extends the point cloud that represents the anatomy, comparable to inflating a balloon. Invalid points can be excluded manually within the mapping system during the procedure while the anatomy is generated. This can be due to unintended moving of the catheter (e.g. from through the MV into the left ventricle), or caused by computational merging of adjacent structures (e.g. LSPV and LAA). In any case, the resulting anatomy is a closed triangulated surface mesh, as shown in Figure 6.1 (a). Including the openings for vessels and valves into the model was the first step in the analysis workflow. In order to optimize up this process, a combination of

user-interaction (annotation of cardiac structures) and automatic processing (modifying the cardiac mesh) was designed during the research for this thesis.

Annotation of Anatomical Structures In order to open the valves, they first have to be identified. One possible method is to annotate a representative template of the atrium, which subsequently could be registered with the patient-specific geometry. A statistical atrial model has been created based on computed tomography data from 138 subjects [143]. However, the patient-specific anatomical variations from the standard model with two PVs on each side were shown to be quite large, like a common ostium of ipsilateral PVs or three PVs entering the atrium on one side. This complicates model-based approaches for the automatic annotation of patient-specific anatomies, although corresponding segmentation algorithms have been proposed which directly address this challenge [144].

Since the intra-procedural acquisition of the anatomy is based on sequential scanning of the endocardial aspect over several minutes, the supporting technician has a sufficient amount of time to annotate atrial structures as instructed by the physician. Annotation can be done by placing labels along the border of the structures using the electroanatomical mapping system (EAMS). A minimum number of three labels was required to define the path around a structure, each one marked with an abbreviation of the corresponding component. For complex structures, like the transition between atrium and ventricle, the physician can additionally utilize his tactile sensation when guiding the catheter or monitor the amplitude of atrial and ventricular signal components. Combined with his experience, these features allow for a precise annotation of the patient-specific geometry prior to the signal analysis without prolonging the procedure.

Extracting the Atrial Body After the anatomy has been annotated, it was exported from the EAMS together with the respective labels. An algorithm was developed to automatically extract the atrial body based on this information. For one atrial structure after the other, all respective labels were located. Since all considered structures had a circular shape, it was decided to fit a plane through these points and subsequently sort them by their angle around the mean of all coordinates. The individual supporting points were connected in circular order using a dedicated implementation of the Dijkstra algorithm, leading to a boundary between the atrial body and the processed component of the atrial anatomy. A line was drawn from the center of the atrium through the mean coordinate of the boundary, intersecting the structure to be removed. Region growing was started from this intersection point and continued until the complete boundary was included. All encompassed area was removed from the atrial mesh, leaving boundary intact and saving its mean coordinate as reference for latter visualization. In case that no annotation was available, an option of a manual mode was also included. Therefore, the atrial mesh was shown to the user as point cloud in a dialog window. The dialog allowed to rotate and zoom the view. For each structure after the other, the user was asked to mark all corresponding points. These were subsequently removed, leaving just the atrial body remaining.

The result of automatic processing can be seen in Figure 6.1, which is a plot comparing the LA prior and after opening. The required time for processing a biatrial anatomy of about 25.000 vertices and 50.600 facesvertices was about 17 s.

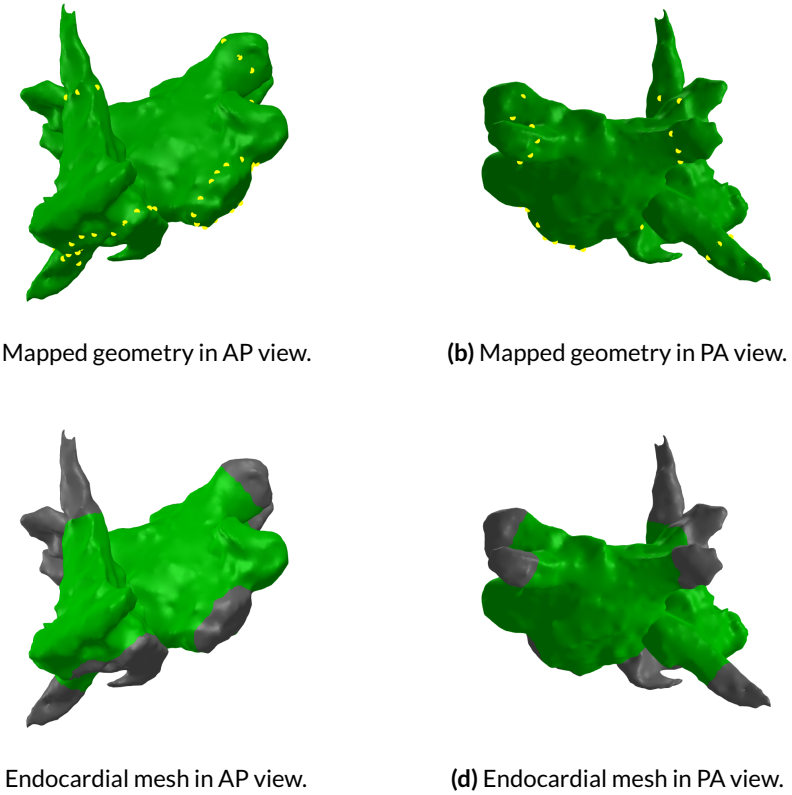

(a) Mapped geometry in AP view. **(b)** Mapped geometry in PA view.

(c) Endocardial mesh in AP view. **(d)** Endocardial mesh in PA view.

Figure 6.1: Extracting the atrial body from the acquired anatomy. The geometry was acquired as triangulated surface mesh during clinical mapping and subsequently exported (a, b). Annotations (yellow dots) were placed on the anatomy under guidance of the physician and indicated the boundary between regions. Usage of specific labels for each structure allowed for automatic processing (not shown). The resulting endocardial mesh was generated within seconds (c, d).

6.2 Detection of Segments with Stable Catheter Positions

In order to identify stable catheter positions within continuous mapping data, a parameterizable algorithm was developed. It was originally implemented within the scope of a student thesis for the morphology based analysis of atrial fibrillation data [145] and subsequently reformulated. Based on the three-dimensional coordinates of N electrodes sampled with frequency fs_{Loc} over time T, it computes the time intervals during which the catheter position can be considered stable.

Therefore, the position vector is analyzed using sliding windows of length w_L and shift w_S. For each window, median position and standard deviation along each individual dimension is computed. Hereby, the median was chosen instead of the mean since it is more robust to sudden shifts caused by contractions of the adjacent myocard. Beginning from the start of the recording, successive windows were merged to a stable interval as long as the euclidean distance of all electrodes to their position in the first window was below a given threshold t_p. If any electrode exceeded this threshold, a new stable interval was begun. Existing intervals of stable median position were subsequently reanalyzed considering the standard deviation. Since huge values of this parameter indicate a strong movement of the catheter around a stable location, the interval was split again if the threshold t_s was exceeded. Finally, all stable intervals were returned for consecutive analysis (e.g. catheter contact, electrogram morphology, excitation pattern, ...) that exceeded a minimum duration.

The sampling frequency of the electrode tracking is a technical property of the utilized mapping system. For the Velocity EAMS, fs_{Loc} is 100 Hz, and for Rhythmia it is 20 Hz. Common values for the analysis include a window of $w_L = 1\,s$ which is shifted by $w_S = 0.5\,s$, and thresholds of $3\,mm$ for median position and its standard deviation, respectively. Increase of these values was required if the respiratory compensation was not engaged during the recording.

The application of this approach using above's values to a segment of mapping data can be observed in Figure 6.2. Data from a 20 pole spiral catheter were recorded for a period of 30 s. The algorithm was set to return only segments which were stable for more than 3 s. The resulting three catheter positions are visualized in parts (b) and (c), indicating a mapping of the anterior wall.

Although a threshold of $3\,mm$ may be considered a rather conservative estimate, it has to be noted that absolute stability can be hardly achieved by the physician during mapping. Several effects contribute to this, like breathing (although when respiratory compensation is engaged), pulsatile blood flow caused by ventricular activity, and deformation of the myocardium during atrial excitation. These effects have to be distinguished from voluntary catheter re-positioning.

6.3 Coverage Maps

A high spatial density of intracardiac measurements is helpful for understanding a tachycardia mechanism or gain information about the atrial substrate. One part of the processing workflow was the assessment of the atrial coverage, being the amount of endocardial area from which electrograms data were acquired [146].

Therefore two distance thresholds were defined, indicating the immediate proximity d_i and medium distances d_m between measurement positions and surface vertices. To be consistent with the remaining analysis workflow, the locations of the electrodes were previously projected onto the closest vertex of the geometry. The resulting error was considered ac-

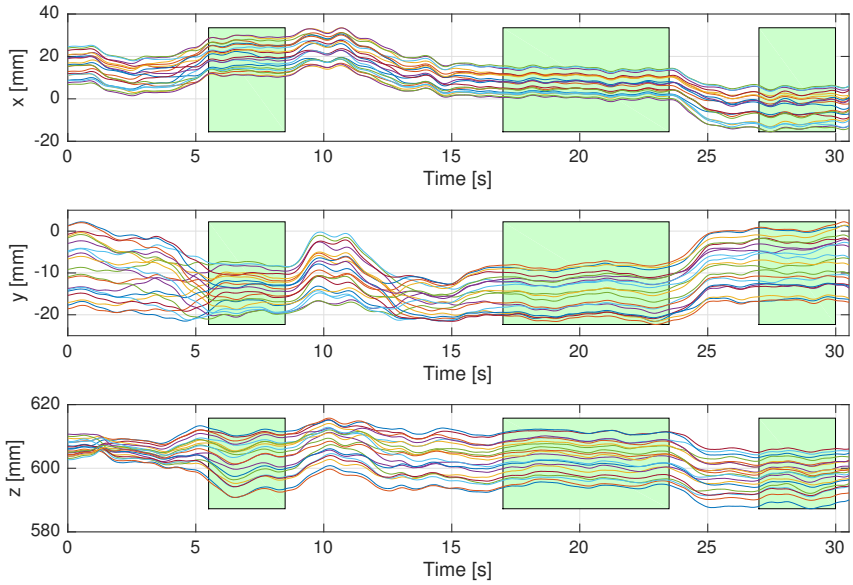

(a) Position time series with annotation of automatically detected stable segments.

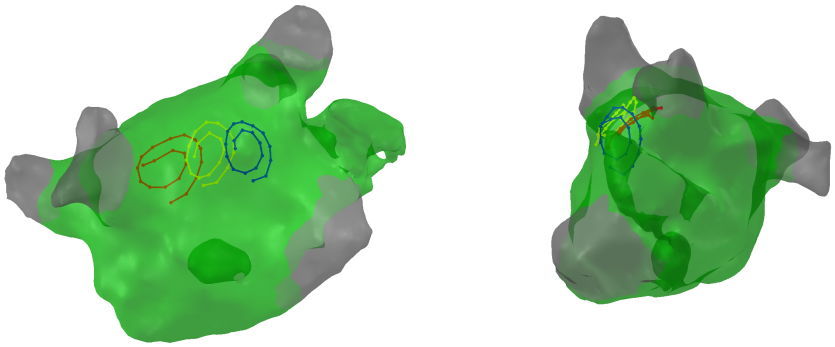

(b) Catheter positions in RAO view. **(c)** Catheter positions in lateral view.

Figure 6.2: Detection of stable catheter positions. A segment of length 30 s was analyzed and three stable positions were identified in the position time series (a). The corresponding catheter locations were plotted in the atrial shell (b, c).

ceptable, due to the small distance between neighboring vertices (mean 1.7 ± 0.6 mm in the example outlined in Figure 6.1) on the one hand, and the expected error in catheter position tracking and its relation to the contracting atrial wall on the other hand.

Vertices of the endocardial mesh with an Euclidian distance less than d_i or d_m to any acquired point were determined. Although a distance measure following the surface curvature would be more exact than the Euclidian distance, the latter was chosen as it could be computed rapidly and the effect of curvature was considered neglectable for the atrial structure and the small distances. The covered area was subsequently defined as the region included by d_m. For statistical purposes, its relation to the total atrial surface was computed.

For visualization using the atrial surface mesh, areas within d_i and d_m were colored green and yellow, respectively, with all remaining geometry colored red. An example for this technique is presented in Figure 6.3. Unmapped areas can easily be identified by their red

color, allowing the physician to judge whether remapping is appropriate. The total number of points used for analysis in RA and LA were 288 and 384, respectively.

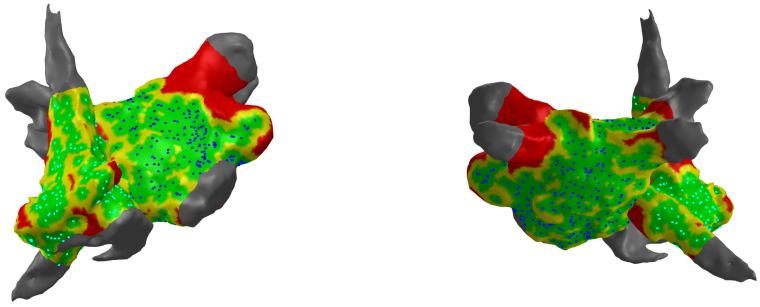

(a) Endocardial coverage in AP view. **(b)** Endocardial coverage in PA view.

Figure 6.3: Typical coverage of the endocardial surface by intracardiac measurements. Surface areas closer than a distance threshold d_m=10 mm to any recording position were considered covered (colored yellow). The immediate proximity to measurement points is indicated green (d_i=5 mm), while uncovered regions are indicated red. Dots mark the position of recordings in the RA (cyan) and LA (blue), respectively.

CHAPTER 7

Removal of Ventricular Far Field

The possibility to interpret intracardiac electrograms (IEGMs) can be compromised by various artifacts that obscure the atrial activity as represented by the local activation wave (LAW). Considering unipolar electrograms (EGMs), baseline wander, high frequency noise and powerline hum are the most frequent undesired components. As these are well-defined in the frequency domain, filters like high-pass, low-pass and notch filter can be used to reduce the power of these undesired spectral components (see Section 5.1).

Another, and usually undesired component of IEGMs, represents the electrical activity of the ventricles and is known as ventricular far field (VFF). The spectral components of VFF are located in the same frequency range as atrial activity, because of which frequency-domain filters cannot be applied without compromising the morphologies of LAWs as well. While the atrial excitation typically takes place prior to the ventricular contraction in sinus rhythm, this assumption is not valid during atrial tachycardias with stable basic cycle length (BCL). Consequently, separating both components in time-domain is not possible as well.

One solution was proposed by the usage of bipolar or pseudo-unipolar EGMs: As the noise affects the intracardiac channels with a comparable phase and magnitude, it can be reduced by substracting two channels. This is the rationale for computing bipolar electrograms (BEGMs) or applying an intracardiac reference to compute pseudo-unipolar EGMs (compare Chapter 2.3.3).

For all kinds of unipolar signals and bipolar signals recorded close to the mitral valve, however, special filtering techniques need to be applied to reduce the VFF. Several techniques are commonly suggested, like template matching and subtraction, adaptive ventricular cancellation or independent component analysis [147]. In previous work, our group and others evaluated the applicability of the principal component analysis (PCA) [148, 149] to remove VFF components. Results indicated that PCA is a powerfull technique for VFF cancellation. Its applicability, however, relies on the decoupling of atrial and ventricular activity. Although this can very well be assumed during atrial fibrillation (AFib), it is in question during atrial flutter (AFlut) with stable conduction from the atria to the ventricles.

Therefore we sought to develop a new technique for the removal of VFF, which is optimized for cases with stable temporal coupling of atrial LAWs and ventricular activity.

This technique is based on the periodic component analysis (πCA), which was initially developed in the field of speech processing [150]. Within the student project of Dan-Timon Rudolph, this technique was benchmarked [151] and subsequently published [137, 139, 152]. For all these techniques, the time of ventricular contraction needs to be known. This information, however, can reliably extracted from the surface electrocardiogram (ECG). Corresponding algorithms and methods for multichannel detection of QRS complexes are described in Section 5.2.

7.1 Principal Component Analysis

PCA is a method frequently applied to reduce the dimensionality of data for clustering purposes. It has also been applied in different fields of EGM processing [148].

From the mathematical point of view, it is a linear transformation which projects given data (e.g. N properties of S subjects) into a new orthogonal subspace given by the eigenvectors of the covariance matrix. This also removes the correlation between the N properties. In addition, the eigenvectors are sorted by descending variance. Eigenvectors which belong to the largest eigenvalues are expected to explain the most variance of the data. Thus for similar measurements, the first eigenvector approximates the general shape of the data, while the eigenvectors of smaller eigenvalues describe the details of each respective subject. When the data is projected using only a limited number M (with $M < N$) of eigenvectors, this allows to approximate either the general shape of the properties or to focus on individual deviations.

When PCA is applied to remove VFF in IEGMs, typically N channels of electrograms with each having a duration of S samples are subject to analysis. These signal snippets contain data from one intracardiac channel and their timing is given by windows around each detected QRS complex. Accordingly, all signals are synchronized with respect to the ventricular depolarization. In case of AFib, a rather chaotic atrial excitation can be expected and the atrial component in the resulting EGM snippets will exhibit different morphologies. With respect to the ventricular activity, however, all signals are expected to have a similar shape due to synchronization.

Given the $N \times S$ matrix X of EGM data, first an inverse version of X is added to obtain the zero mean data matrix X^* of size $2N \times S$. Next the PCA is applied on X^*. After this step, the eigenvectors which explain the most of total variance are expected to primarily contain the shape of the ventricular component. Consequently, eigenvectors accounting for at least thr_{PCA} of total variance are rejected and the remaining ones were used to reconstruct the EGM without VFF. Linear interpolation of the baseline was performed to ensure continuity of the signal after removal of the VFF component.

The threshold was suggested as $thr_{PCA} = 0.8$, comparable to values applied in previous work [149]. When compared to Adaptive Template Subtraction, the PCA based approach leads to an individually estimated VFF component for each ventricular depolarization, and thus is expected to perform better [148].

7.2 Periodic Component Analysis

While the PCA can be used to separate sources based on statistical independence, other properties like different periodicity also provide suitable features to detect underlying patterns in a composition of signals. The πCA is a mathematical transformation which was designed to separate repetitive structures in signals based on their cycle duration. Previous work utilizing this approach included the frequency detection in multiple channels [150] or the separation of maternal and fetal ECG [153]. In further fields of ECG signal processing, it was used to estimate AFib activity [154, 155] or analyze T wave alternans [156].

Within the scope of this thesis, the concept of πCA was adapted to be applicable for VFF removal during AFlut. Due to the well organized and stable underlying excitation process, the cycle length of AFlut remains nearly constant over time. Since the conduction of excitation to the ventricles is not random but rather deterministically based on the restitutional properties of the AV node, stable patterns of 2:1 or 3:1 conduction can frequently be observed during intracardiac mapping (compare Figure 7.1). This observation motivated the application of a periodicity-based technique for the separation of atrial and ventricular activity.

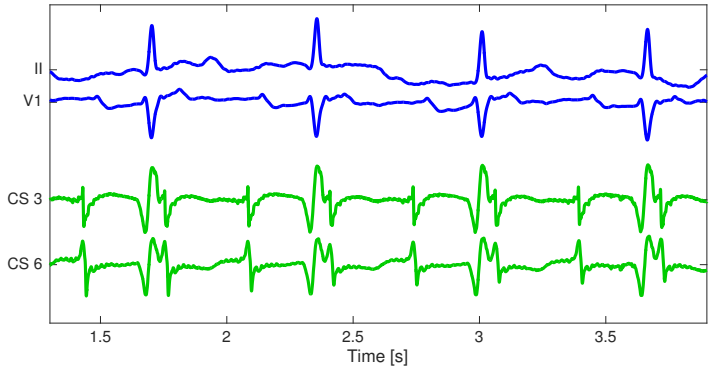

Figure 7.1: Example of stable 2:1 conduction between atria and ventricles. Two channels of surface ECG clearly show monomorphic and periodic QRS complexes (blue). Both unipolar CS channels show more rapid but regular atrial activity (green), indicated by the steep negative gradient in the signal. At a BCL of 320 ms every second atrial excitation was conducted to the ventricles. Note the stable temporal relation between atrial and ventricular activity. Data from patient C4 according to Table 7.1.

In above mentioned research, simultaneously recorded multichannel data had been subject of analysis [150, 153–156]. The data was provided as matrix $X(t)$ with each row representing one channel $x_i(t)$. The πCA is applied to determine a linear mixing vector w which maximizes the periodicity of the transformed signal $s(t) = \mathbf{w}^T * X(t)$ for a given period τ. To solve this problem, a formulation is chosen in which the goal is to minimize a measure of non-periodicity ε. This optimization can be formulated as [153]

$$\varepsilon(\mathbf{w},\tau) = \frac{\sum_t |s(t+\tau) - s(t)|^2}{\sum_t |s(t)|^2} = 2\left(1 - \frac{\mathbf{w}^T C_{xx}(\tau)\mathbf{w}}{\mathbf{w}^T C_{xx}(0)\mathbf{w}}\right), \tag{7.1}$$

in which $C_{xx}(\tau)$ is given by the covariance matrix of $X(t)$ according to

$$C_{xx}(\tau) = E_t \left\{ X(t+\tau) X(t)^T \right\}. \tag{7.2}$$

The vector w_{opt} of optimal transformation weights to minimize ε can be easily computed with help of the Rayleigh-Ritz theorem [150]. It is given by the eigenvector of the biggest generalized eigenvalue of the matrix pair $(C_{xx}(\tau), C_{xx}(0))$. The linear transformation $s(t) = w_{opt}^T * X(t)$ thus results in the signal with optimized periodicity τ. No constraints, however, are imposed on signal morphology.

When simply applied to a set of IEGMs, the respective morphologies would be mixed by πCA to optimize periodicity, but the resulting signals could not be used for diagnostic purposes. Consequently, modifications were required to this original πCA approach to make it usable as artifact removal technique which reduces the VFF component but preserves the morphology of LAWs.

The respective changes to the application of πCA were investigated during this thesis. In agreement with the desire to focus on the atrial activity, the period τ was set to the BCL. One single IEGM was used as first channel in the data matrix X. A total of N_c additional channels in X were generated by signals that contained pulses for samples of the IEGM which may be corrupted by VFF (compare Figure 7.2).

Subsequently, the πCA was utilized to assign weights to all channels with pulse trains. As no Dirac pulses were placed at times outside the VFF, the morphology of pure atrial activity could not be changed when computing a linear combination. To optimize the periodicity of LAW morphology, the πCA thus approximated the VFF. For an optimal mixing vector w_{opt}, an inverse template VFF_{est} would be formed by all N_c additional channels, matching the original VFF_{org}. When added to the original IEGM in the first channel of X, VFF_{est} would be removed from the signal. The amplitude of the initial EGM was preserved by scaling w so that its first component was equal to 1.

In summary, first the position of QRS complexes was determined in the surface ECG. Subsequently the BCL was determined using e.g. a coronary sinus (CS) channel without artifacts. Due to the stable location of the CS catheter, this channel had to be chosen only once for a procedure. For each IEGM channel after the other, the artificial channels were generated and the data matrix $X(t)$ composed. The weight vector w_{opt} was computed using the πCA and normalized. Finally the reconstructed electrogram could be computed as $AA_{final} = w_{opt}^T * X(t)$.

Having this general concept in mind, two alternative options were suggested. First, it would be possible to reduce the number of additional artificial channels if e.g. Mexican hat wavelets were used as basis functions instead of Dirac pulses [137]. However, both the spacing and the width of the corresponding Gaussian curves would have to be chosen appropriately to resemble the morphology of the ventricular component. Second, an improved estimate of each respective VFF could be generated when artificial channels would be estimated for each QRS complex individually instead of using periodically spaced Dirac

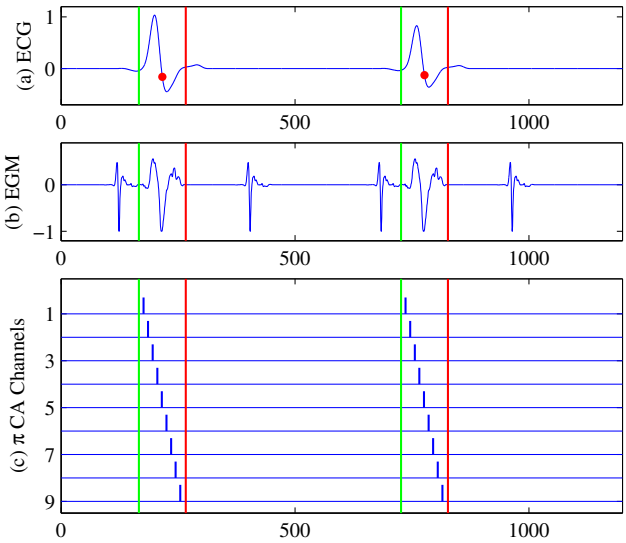

Figure 7.2: Concept of the πCA. (a) QRS complexes are detected in the surface electrocardiogram, and the time window which might be compromised is annotated. (b) The respective window is marked in the IEGM. (c) Artificial channels are generated and appended to the EGM. Each artificial channel contains a sequence of Dirac impulses, with a fixed relative position to the ventricular activity. Goal of πCA is to find a linear combination of these channels to resemble the morphology of the VFF component and subsequently remove it. The number of channels is chosen to provide a pulse for each sample within the window of interest. Reprinted from [137] with permission of the publisher.

pulses synchronous to the QRS complexes. This, however, would increase the number of required artificial channels by a factor given by the number of QRS complexes.

7.3 Application of PCA and πCA

Having provided motivation and theoretical background of both artifact removal techniques, their application is the central part of the following chapter. First clinical and synthetic data are introduced, which were used to demonstrate and benchmark these techniques. The results of performance analysis and application to clinical data conclude this section.

Clinical Data Clinical data from routine ablation of stable AFlut were retrospectively exported to demonstrate the applicability of both artifact removal techniques. The database comprised three patients which were mapped using the electroanatomical mapping system (EAMS) EnSite Velocity™ (St. Jude Medical, St. Paul, MN, USA) and provided written informed consent. Table 7.1 provides an overview about the most important properties of the exported data and patient details.

Data from patient PtA was acquired using a basket catheter (Ba, Constellation, Boston Scientific), while patients PtB and PtC were mapped using a 10 pole circular mapping catheter (Opt, Optima, St. Jude Medical). The stability of the atrial rhythm was monitored using a CS catheter. Surface ECG, intracardiac electrograms and catheter positions were exported for continuous traces of mean duration 5.6 s. Bipolar EGMs were filtered by the

	Age, sex	Cath	Seg	Dur [s]	RR [ms], $\mu \pm$SD (nR)	BCL [ms] $\mu \pm$SD (nA)
PtA	54, m	Ba	C1	4.8	672 $\pm$79 (7)	253 $\pm$2 (19)
		Ba	C2	5.1	814 $\pm$193 (6)	252 $\pm$2 (20)
		Ba	C3	4.8	706 $\pm$157 (7)	253 $\pm$2 (19)
PtB	64, m	Opt	C4	7.5	654 $\pm$1 (11)	327 $\pm$2 (23)
PtC	65, f	Opt	C5	7.6	538 $\pm$5 (14)	269 $\pm$7 (28)
			C6	4.0	534 $\pm$5 (8)	266 $\pm$8 (15)
			C7	5.6	654 $\pm$196 (9)	264 $\pm$7 (21)

Table 7.1: Details of patient and electrogram data. Duration (Dur), catheter (Cath), mean and SD of RR intervals and atrial basic cycle length (BCL) are given for each EGM segment (Seg) C1-C7. Numbers of R peaks (nR) and atrial activations (nA) are noted in parenthesis. Note that the SD of atrial BCL is 2 ms for patients PtA and PtB, indicating very high periodicity of the atrial rhythm. While a SD of 1 for the ventricular rate also indicates a stable AV conduction in patient PtB, the higher values for patient PtA indicate a variability in the AV coupling.

clinical system with a high-pass of 30 Hz and a low-pass of 300 Hz. Unipolar EGMs were filtered during processing, using a high-pass of 1 Hz, a low-pass of 250 Hz and a notch filter to remove 50 Hz powerline hum and non-physiological discrete high-frequency components. Both unipolar electrograms (UEGMs) and BEGMs were subject to analysis.

The ventricular rate was determined based on the timing of detected QRS complexes. LAWs in CS signals were assessed to compute the atrial rate. For all available and simultaneously recorded channels, first active parts of the signal were detected using an energy-based approach [157]. Second the LAW morphologies were aligned in time based on correlation. The channel showing best correlation was selected to compute the final measures for the atrial rate.

As outlined in Table 7.1, the atrial BCL was very stable for patients PtA and PtB, with a standard deviation (SD) of about 2 ms and relatively stable for patient PtC (about 7 ms). The ventricular rate was also very stable for patient PtB (SD=1 ms) and some episodes of patient PtC (C5 and C6, each with SD=5 ms). In these cases, AV conduction shows a clear 2:1 pattern. For segments C1-C3 (patient PtA) and C7 (patient PtC), high values of the SD RR can be observed (80-200 ms), indicating a variable AV conduction.

Synthetic Electrograms Besides the clinical dataset, also a database of synthetic EGMs was compiled to quantitively assess the performance of both signal processing algorithms. In order to resemble the measured data as closely as possible, templates of atrial activity and ventricular far-fields were generated from the clinical data. The templates were constructed from manual annotations and comprised windows of duration 100 ms, ensuring to capture all related activity. At least four individual complexes were used to construct the templates and the mean correlation coefficient (CC) betwen the template and each single annotated morphology was monitored to verify a sufficient match. The mean CC over all templates was 0.94, being considered to represent sufficient agreement. To ensure the comparability in subsequent analysis, the maximum peak amplitudes of all templates were normalized to 1 mV. This procedure resulted in a total of 7 templates of atrial activity and 4 templates of ventricular activity [139].

	Cond	ACL [ms]	Jitter RR	Jitter AA	Amp AA/VFF
PA	2:1	280	No	No	1/1
PB	3:1	200	No	No	1/1
PC	Varying	240	No	No	1/1
PD	Varying	240	No	No	Fixed
PE	Varying	240	Yes	No	Breath
PF	Varying	240	Yes	No	1/1
PG	Varying	240	No	Yes	1/1
PH	Varying	240	Yes	Yes	1/1

Table 7.2: Populations of synthetic electrograms PA-PH. Conduction pattern (Cond), ACL, jitter and amplitudes (Amp) were varied to generate datasets mimicking clinical data.

The templates were combined to generate 8 different populations of synthetic electrograms. The properties of these EGMs were specified to mimic clinical examples as closely as possible. Details of the parameters used in each population are summarized in Table 7.2. Since atrial activity could be recorded during any phase of the flutter circuit during clinical mapping, six equally spaced shifts between atrial and ventricular activity were reproduced. Thus each compiled population included 28 template combinations with 6 different phase shifts, resulting in 168 individual traces in each population. Simultaneous occurences of atrial and ventricular components were refered to using Sim and Non-Sim, respectively.

According to clinical observations documented in literature, atrial (basic) cycle length (ACL) was set to 200, 240 or 280 ms. The simulated conduction ratios between atria and ventricles were chosen as 2:1, 3:1 and alternating patterns of both values. In order to resemble variability in the AV node conduction (AVC) time, the positions of R peaks were varied (populations PE, PF and PH) by adding a random jitter (uniform distribution, half-width 5, 10, 20 or 30 ms). Variability in ACL was modeled by a jitter of 5 or 10 ms in the atrial excitation rate of populations PG and PH.

For populations PD and PE, the same timing of atrial and ventricular components was used as in PA. Their amplitude, however, was modified so that either the LAW or the VFF was multiplied by a fixed value of 0.5 (PD) or modulated by $1 + 0.5 * sin(x)$ (PE). For the latter, x was chosen to represent a breathing frequency of 0.3 Hz within physiological range [158].

Each signal was compromised by additive White Gaussian noise ($\Sigma = 0.04\,mV$). Neither powerline hum nor baseline wander were modeled since the data was expected to represent filtered bipolar EGMs. Examples of five different signals are depicted in Figure 7.3.

Demonstrative Examples The practical implications of the theoretical considerations about constant temporal relation of atrial and ventricular activity on artifact removal are depicted in Figure 7.4. A synthetic electrogram from population PA is analyzed using both PCA and πCA. The templates for both the atrial and ventricular component are visualized in parts (a) and (b), respectively. At about 1250 ms of simulated data, both atrial and ventricular activity concur simultaneously (c). Due to the fixed temporal relation between atrial and ventricular activity, this overlap is consistent for each ventricular contraction. This is also

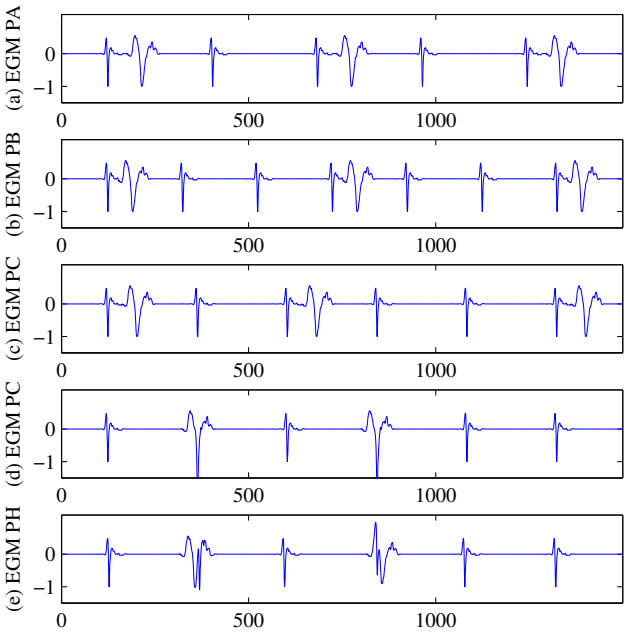

Figure 7.3: Demonstrative examples of different populations. Atrial cycle length and relative timing between atrial and ventricular depolarization were varied in the synthetic signals to mimic clinical data. Reprinted from [137] with permission of the publisher.

reflected by the PCA-based estimate of VFF morphology, containing a superposition of the atrial and the ventricular component. When the πCA is used to retrieve the undisturbed atrial LAW, the VFF morphology is correctly estimated since the atrial component within the VFF can already be explained by the periodic occurrence of the atrial activity.

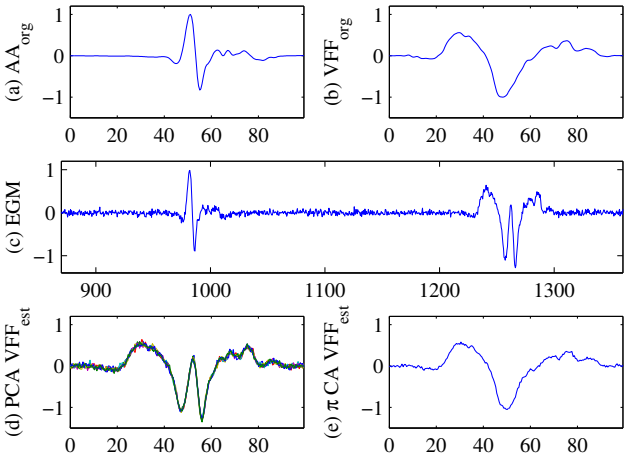

Figure 7.4: Comparison of the VFF estimates generated using PCA and πCA. Both atrial activity (a) and VFF occured simultaneously in the EGM at 1250 ms (c). The estimates for the VFF as generated using the PCA contained both the atrial and the ventricular component, since both were synchronized (d). The πCA correctly estimated the VFF (e). Although the estimated did not contain the atrial morphology, note that only one single estimate was generated for all QRS complexes. Reprinted from [137] with permission of the publisher.

The effect on the resulting signal after VFF removal can be observed in Figure 7.5. Since the atrial component is considered a part of the morphology including the artifact, it is removed by the PCA from the signal (compare part (b)). The πCA was able to separate ventricular and atrial components when the inverse template of ventricular activity was determined, and thus successfully retains the morphology of the atrial LAW.

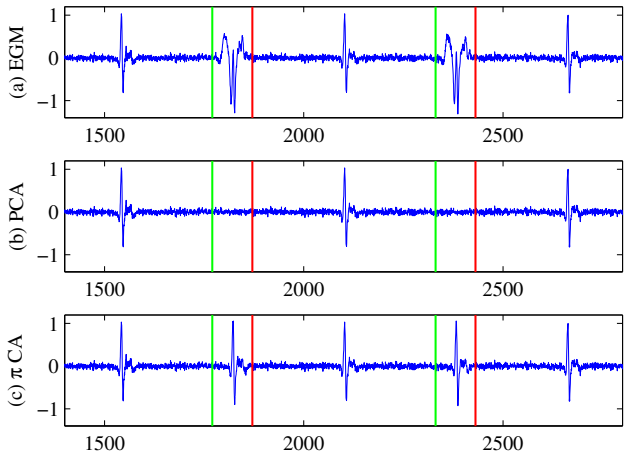

Figure 7.5: Demonstration of both VFF removal techniques on a synthetic atrial signal. An EGM with stable atrial rate and fixed conduction rate 2:1 was filtered (a). When reconstruction was performed using PCA, both AA and VFF were removed (b). Application of πCA retained the morphology of the atrial component (c). Vertical lines indicate beginning and end of the VFF component. Time given in ms, amplitudes in mV. Reprinted from [137] with permission of the publisher.

Performance Benchmark The synthetic populations of EGM data were used to assess the performance of both PCA and πCA. Two measures were chosen for a quantitative benchmark, based on correlation and residual far-field energy. If at least 40 % of the timespan of the ventricular component showed overlap with the atrial LAW, reconstructing the morphology of the atrial component was considered the major goal. For this case, the CC was computed between the original LAW and the signal after artifact removal. For little or no overlap between VFF and atrial component, measuring the diminution of ventricular activity was selected as performance criterion instead of the CC between both baselines. This was measured by the fraction of initial energy of the VFF which was still present after filtering ($relEn$). While a value of 1 was the best case for CC, $relEn = 0$ represented the best case for Non-Sim signals. The respective results are depicted in the following, using mean and standard deviation as statistical measures, and boxplots for visual representation.

The performance of both reconstruction techniques during stable AFlut with stable AV conduction time was evaluated using the three populations showing these respective properties (PA, PB, PC). The results are visualized in Figure 7.6, in which the data for population PA is indicated by *2:1*, PB by *3:1* and PC by *Var*. For an overlap of LAW and VFF (part a)), the correlation showed very high values (CC = 0.98 ± 0.00, PA-PC) when πCA was applied, while this dropped strongly (CC = 0.03 ± 0.08) for PCA. This is in

perfect agreement with the demonstrative example depicted in Figure 7.5, in which the PCA diminished all activity. Both techniques, however, were able to remove the ventricular component when there was no overlap (NonSim signals, b)). This is indicated by the low values of *relEn*.

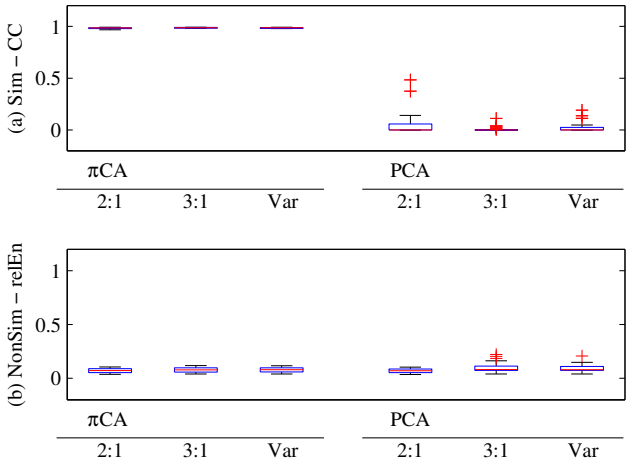

Figure 7.6: Statistics of filtering performance for stable conduction. (a) For simultaneous signals, AA morphology was nearly perfectly reconstructed using πCA (CC = 0.98 ± 0.00) but showed little correlation when PCA was used (CC = 0.03 ± 0.08). (b) For non-simultaneous signals, both PCA and πCA removed energy from the signal, which is the desired reconstruction of the noised baseline without VFF activity. Reprinted from [137] with permission of the publisher.

The effect of changes in the relative amplitude between LAWs and the ventricular component was assessed by evaluating the reconstructed signals of population PD. Other properties, like atrial BCL and AV conduction time, were kept stable as in the previously analyzed PA. The relation of both is indicated by *1:1*, *2:1* and *1:2* in Figure 7.7. Although the amplitudes were reduced to half of their initial value, no trend could be observed in the reconstruction result for neither PCA nor πCA. This was in agreement with out expectations, since the stability of amplitude was considered to play an important role during reconstruction but not its value itself.

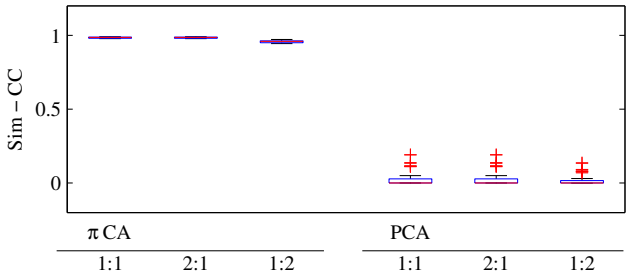

Figure 7.7: Reconstruction performance depending on the ratio of amplitudes of AA and VFF. Similar mean CC was observed for all scenarios (AA/VFF: 1:1/2:1/1:2; πCA: CC = $0.99 \pm 0.00/0.99 \pm 0.00/0.96 \pm 0.01$; (PCA: CC = $0.03 \pm 0.05/0.03 \pm 0.05/0.02 \pm 0.04$). Reprinted from [137] with permission of the publisher.

The stable coupling between atrial and ventricular activity was initially predicted to be responsible for the poor performance of PCA and motivated the development of πCA. To evaluate this effect, different levels of dissociation between atrial and ventricular activity were mimicked in dataset PF. While the increasing aperiodicity of RR intervals showed little effect on the performance of πCA (CC > 0.98), the outcome quality of PCA increased considerably. Without jitter, CC of 0.03 ± 0.05 was observed. Already for a half-width of 5 ms this value increased to 0.63 ± 0.18. For 10, 20 and 30 ms, the CC changed to 0.70 ± 0.17, 0.75 ± 0.16 and 0.77 ± 0.14, respectively.

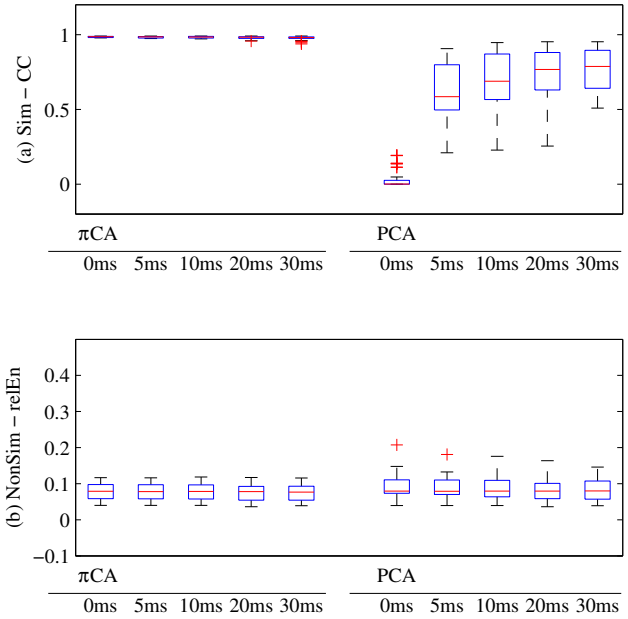

Figure 7.8: Filtering performance with respect to variations in AVC. Performance of πCA remained nearly constant for increasing aperiodicity while performance of PCA improved. Reprinted from [137] with permission of the publisher.

As demonstrated in Figure 7.7, the relative strength of LAW and VFF as reflected by amplitude does not play an important role for the filtering performance of PCA and πCA. However, dynamic alterations in the amplitude can also be present in the signals, e.g. caused by breathing. This was reflected by population PE, in which the amplitudes were either kept stable (*const*) or one component was modulated (*VFF / AA*). Variability of AV conduction time was introduced to achieve comparable results for PCA as well. Considering this technique for reconstruction, its performance was comparable over all scenarios (CC for const/VFF/AA: 0.70 ± 0.17 / 0.71 ± 0.16 / 0.69 ± 0.17). Changes in the amplitude of the atrial component did not affect the reconstruction performance of πCA (1.00 ± 0.00), while a reduction of performance could be observed when the amplitude of the ventricular component was modulated (0.85 ± 0.06). This can be explained by the fact, that one single estimate for the VFF is computed using πCA, which is not adapted for each individual occurrence. To confirm this, $\pi\text{CA}_{\text{ind}}$ was also applied to this dataset, generating an individual

estimate of the VFF for each QRS complex. Indeed, the resulting CC shows high values independent of modulation (0.99 ± 0.00 / 0.99 ± 0.00 / 0.94 ± 0.01).

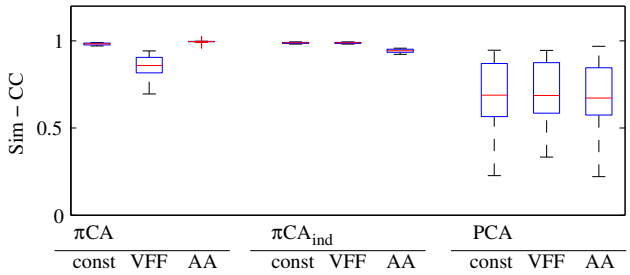

Figure 7.9: Reconstruction performance with respect to amplitude variations over time. The varied component is noted under each boxplot. Modulating VFF amplitude deteriorated πCA performance (CC = 0.98 to CC = 0.85) while πCA$_{\text{ind}}$ was not affected. Reprinted from [137] with permission of the publisher.

Since the πCA was designed as novel filtering technique to overcome existing limitations in the special case of periodic atrial activity, a violation of this assumption can be expected to strongly compromise filtering performance. To confirm and quantify this effect, dataset PG was compiled which included aperiodicity of the atrial rate but with stable coupling time to the ventricles. The performance of both PCA and πCA in case of simultaneous and non-simultaneous signals is depicted in Figure 7.10. Results demonstrated poor performance of the PCA during *Sim* signals, indicated by the CC (0.03 ± 0.05 / 0.25 ± 0.32 / 0.27 ± 0.34) with considerable intra-population variability. Performance of the πCA was reduced when the aperiodicity of ACL became stronger (mean CC 0.99 ± 0.00 / 0.64 ± 0.31 / 0.39 ± 0.33).

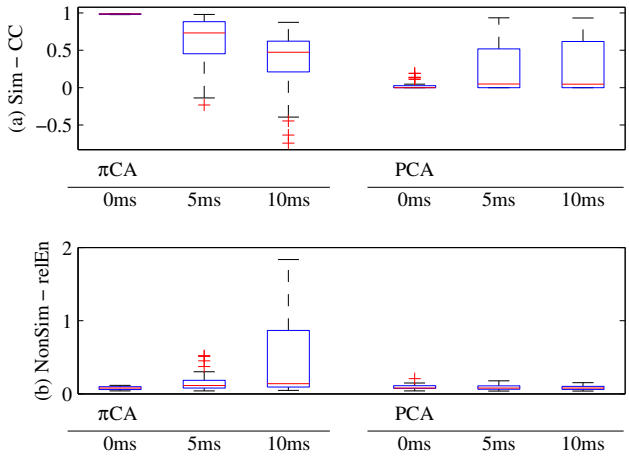

Figure 7.10: Influence of ACL variability on performance. Filtering with the πCA was deteriorated when ACL became more irregular. Reprinted from [137] with permission of the publisher.

Concluding, the combined effect of aperiodicity in atrial cycle length and the AV conduction time was evaluated using population PH. The resulting CCs are shown in Figure 7.11 and

are consistent with the conclusions drawn earlier: πCA showed very good results for stable atrial BCL, independent of variation in the ventricular rate. Its performance, however, was strongly affected by aperiodicity in the atrial rate. Contrastingly, the well-known technique PCA was hardly affected by an irregularity in the atrial rate, and performed increasingly better when a decoupling of atrial and ventricular activity took place. For a stable coupling between both, performance of PCA was poor. More details about this benchmark were published in [137].

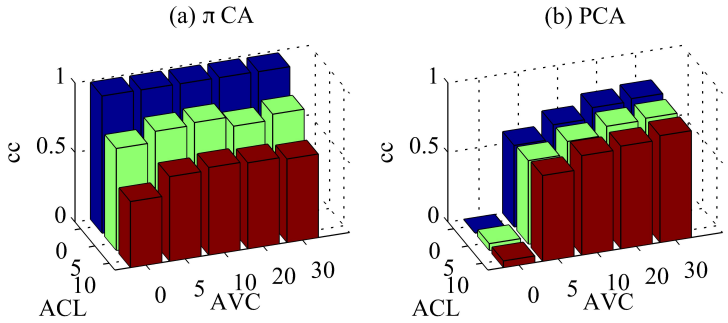

Figure 7.11: Combined effect of ACL and AVC time variability on performance. Median values of CC are plotted for both variables. (a) πCA performance deteriorated for increasing ACL variability. (b) PCA shows increasing performance when RR intervals become increasingly irregular. Bars colored by irregularity of ACL. Reprinted from [137] with permission of the publisher.

Application on Clinical Data After benchmarking using synthetic data, both algorithms were applied to different sets of clinical data. An example of artifact removal in a bipolar signal with periodic atrial and ventricular activity (C4) is depicted in Figure 7.12. As shown in the unfiltered EGM (part (b)), the VFF slightly preceeds the LAW, compromising its diagnostical interpretation. Application of PCA for artifact removal attenuates both components to nearly baseline values. If the πCA is used, however, the morphology of the atrial LAW remains unaltered.

For comparison, the filtering algorithms were applied on a second EGM with a more variable ventricular rhythm (C3). With an SD of 157 ms, its ventricular activity can be considered decoupled from the atrial one (compare Table 7.1). The result of filtering can be observed in Figure 7.13. In this case, also PCA was able to reconstruct the atrial LAW correctly.

Considerations for usage It has been demonstrated, that the πCA can be used to remove undesired ventricular components from IEGMs when the atrial BCL is stable. This is especially useful in cases of a fixed coupling between atrial and ventricular activity, since common techniques like Template Matching and Subtraction or PCA cannot be used in this

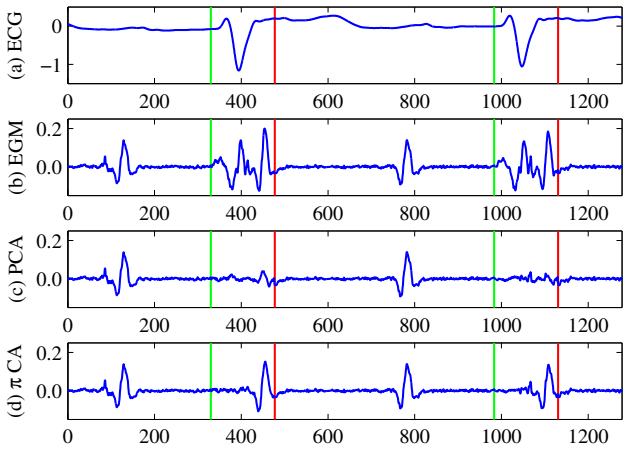

Figure 7.12: Demonstration on clinical data with stable conduction properties and highly periodic atrial and ventricular rate (C4). (a) Surface ECG. (b) Measured EGM with VFF. (c) PCA removes both AA and VFF. (d) Morphology of AA is retained using πCA. Time given in [ms], amplitudes in [mV]. Reprinted from [137] with permission of the publisher.

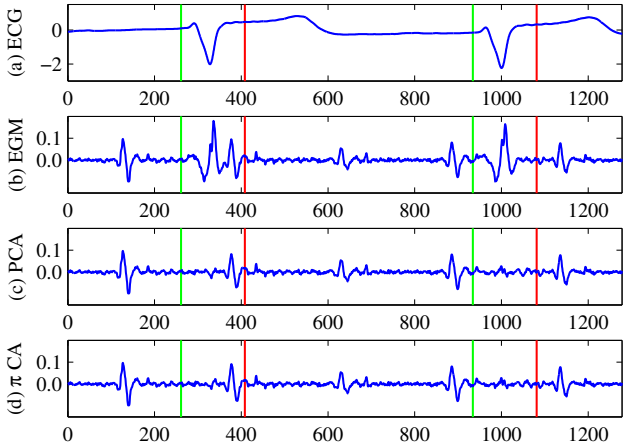

Figure 7.13: Demonstration on clinical data with stable atrial rate but decoupling of atrial and ventricular activity (C3). (a) Surface ECG. (b) Changes of relative timing between AA and VFF can be observed in the measured EGM. Both PCA and πCA preserve AA morphology and remove the VFF component (c and d). Time given in [ms], amplitudes in [mV]. Reprinted from [137] with permission of the publisher.

case. If atrial excitation pattern and rate are constant, but the AV conduction is variable, PCA can in general be applied.

The periodicity of atrial LAWs is an important prerequisite to the applicability of the πCA. Slight variations in the BCL can be expected and are documented in the order of 5 ms [158], they could be, however, accounted for using phase-wrapping as suggested by Sameni et al. [153]. For rather short signals of duration in the order of 1 to 2.5 s, it may be more appropriate to simply select data from the undisturbed cycle for analysis purposes (compare Section 11).

Recently, the Orthogonal Component Analysis was developed and implemented in our lab. This is an advanced version of the PCA, which reconstructs the atrial activity by a transformation of statistical moments in the PCA-space [159]. One major advantage of

this method is its ability to work with non-periodic signals, as periodicity is not part of this processing technique. It requires, however, knowledge of the position of LAWs in uncompromised time windows during the initialization, and the timing of all potentially compromised LAWs during processing. The database generated during this research can be used to benchmark this new technique in a next step.

CHAPTER 8

Determination of the Local Activation Time

8.1 Annotation of LAT

Local Activation Time (LAT) maps have become a valuable diagnostical aid during electrophysiological studies. They are used to visualize the electrical excitation on a three dimensional cardiac geometry, allowing to easily comprehend the propagation pattern. Therefore, intracardiac electrograms are measured at multiple positions, the LAT is assigned in each individual signal and subsequently a complete map is interpolated. This map can in turn be used to detect lines of block, compute parameters like the local conduction velocity (CV). Since even small errors in the determination of the timing can cause huge errors during CV computation, the best possible LAT assignment is highly important.

8.1.1 Criteria to Define the LAT

It has been demonstrated in experimental animal data, that the time of the steepest negative slope in the unipolar electrogram coincides with the electrical excitation passing the measuring electrode [90]. Although this is a very favorable marker, the determination of this point can be compromized by powerline noise, other high frequency noise and far-fields. The effect of these interferences is much less for bipolar signals. For these, however, the shape of the signal heavily depends on the relative orientation between the wavefront and the measuring dipole [90]. Thus no characteristic point in the electrogram can be used as marker for the LAT. Due to its well understood nature, unipolar electrograms (UEGMs) are considered the gold standard for LAT annotation in clinical signals [90]. In case of noise or fractionation, bipolar electrograms (BEGMs) or hybrid approaches are frequently utilized which detect the atrial activation first in the bipolar signal and then annotate the LAT in the unipolar EGM [160].

Since feature detection in bipolar EMs can be performed automatically in a more robust way, BEGMs are commonly used for processing in EAM systems. Characteristic points which can be detected in the signal are its maximum and minimum value, as well as the maximum positive or negative derivative. Although these points may or may not concur with the exact moment of the depolarization passing, they can reliably indicate an activation complex.

Common to all methods is the annotation of LAT related to the intrinsic deflection, either due to the high amplitude or the change in polarity of the EGM. Both concur to a local maximum of the energy in the signal, and thus also the use of an energy-based algorithm was proposed [161]. Therefore, the non-linear energy operator was applied to the signal, followed by rectification and low-pass filtering at about 24 Hz. The maximum of the resulting signal was used as surrogate for the LAT. The performance of this approach is analyzed in the following chapter. It was first assessed using simulated data and subsequently applied to clinical data. The results have been presented to the scientific community previously [162].

8.1.2 Benchmarking with Simulated Data

Simulations Simulations were performed on a regular grid of cubical voxels with a spatial resolution of 0.2 mm. The setup included a tissue patch (42.2 x 15 x 4.4 mm) and a 7F ablation catheter with two electrodes (compare Figure 8.1). Simulations were performed using the human atrial cell model by Courtemanche et al. [99] and solved using the bidomain approach implemented in the *acCELLerate* simulation environment [102]. The sampling rate for simulations was set to 10 kHz and clinical filter settings were applied (second order Butterworth filter, high-pass at 5 Hz or 30 Hz, low-pass at 250 Hz). This simulation setup has been validated against clinical electrograms previously [140]. Angles α and β were varied to evaluate the effect of catheter orientation, covering a total of 49 different settings. Unipolar signals were calculated using the mean of the extracellular field in the upmost blood layer as reference. Bipolar signals were defined as the potential difference of the proximal and distal electrodes. Setup and simulations were part of a student project supervised by Matthias Keller.

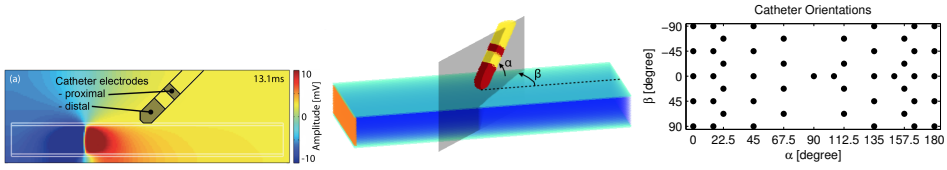

(a) Extracellular potential. **(b)** Coordinate system for catheter position. **(c)** Simulated catheter orientations.

Figure 8.1: Simulation setup used for LAT studies. (a) Extracellular potentials. (b) Simulation setup. Planar stimulation was performed on the left side of the tissue patch. The excitation wavefront passed the catheter as a nearly planar wave. Angles α and β were varied, covering 49 orientations as depicted in (c).

Methods to determine the LAT The LAT t_{True} in patch simulations was defined as the time of maximum upstroke velocity of the transmembrane voltage (TMV) in the most endocardial tissue layer and considered as reference ground truth for benchmarking. For unipolar measurements, the computational node underneath the center of each electrode was considered. The geometric mean of both electrode centers was used for the bipolar case.

Six morphological landmarks of the simulated EGMs were analyzed as criteria to annotate the LAT t_{Cri} within this study, being the maximum and minimum value (t_{Max} and t_{Min}), the maximum and minimum derivative ($t_{+dV/dt}$ and $t_{-dV/dt}$), as well as the maximum absolute values (t_{Abs} and $t_{|dV/dt|}$). In addition, the maximum value of the filtered NLEO and its baro-center was used (t_{NLEO} and t_{baro}).

Impact of catheter orientation and filtering on signal morphology Simulated unipolar signals showed a biphasic morphology as depicted in Figure 8.2 (a). High-pass filtering with increasing cut-off frequency removed the low frequency components leading to a more dominant negative peak.

Morphology of bipolar signals varied strongly depending on the catheter orientation. Both monophasic (in (anti-)parallel alignment) and biphasic (orthogonal tilt) signals were observed. Filtering caused further changes to this morphological variety as can be seen in Figures 8.2 (b-d).

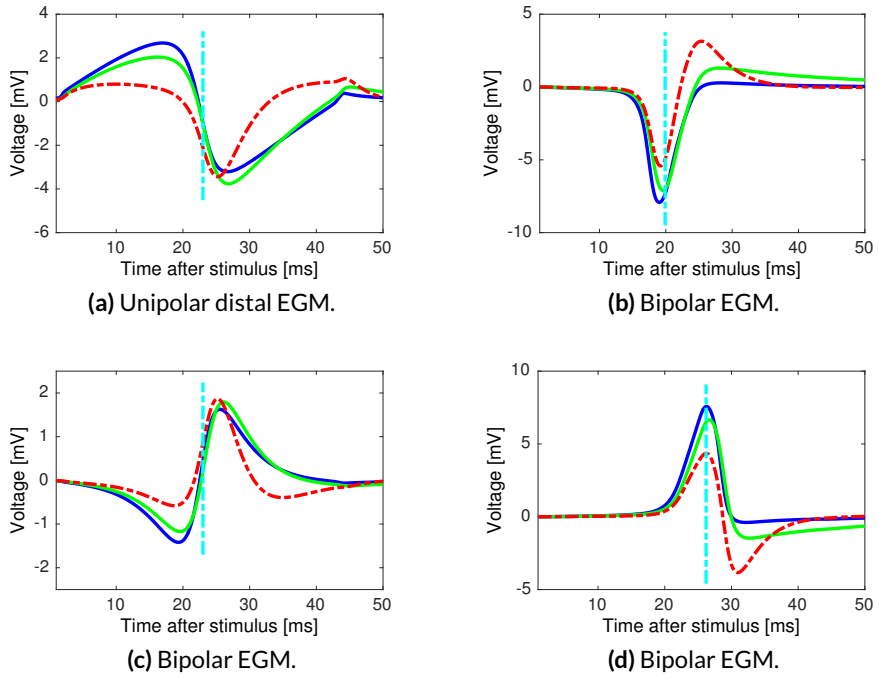

(a) Unipolar distal EGM. **(b)** Bipolar EGM.

(c) Bipolar EGM. **(d)** Bipolar EGM.

Figure 8.2: Effect of catheter orientation and filtering on electrogram morphology. Raw signals (blue) were filtered using a high-pass at 5 Hz (green) and 30 Hz (red, dashed). Corresponding t_{True} is plotted as vertical dashed line and coincides with different characteristic points of EGM morphology. (a) Unipolar electrogram of the distal electrode ($\alpha = 90°$, $\beta = 0°$). Bipolar electrograms for $\beta = 0°$ and $\alpha = 180°$ (b), $\alpha = 90°$ (c), and $\alpha = 0°$ (d).

LAT determination in simulated signals The performance of the criteria was evaluated by comparing t_{True} with the respective t_{Cri} in simulated EGMs which were filtered at a high-pass of 30 Hz. The absolute time difference $|\Delta t_{MaxMin}| = |t_{Max} - t_{Min}|$ between maximum and minimum of bipolar signals was computed as 6.6 ± 1.5 ms.

Boxplots of the difference $\Delta t_{CriTrue} = t_{Cri} - t_{True}$ are visualized in Figure 8.3. For unipolar signals, -dV/dt demonstrated the smallest deviation of all common criteria with 0.8 ± 0.9 ms. All methods showed mean errors of more than 1 ms for bipolar signals. Both energy-based approaches resulted in mean differences of less than 0.5 ms in unipolar and bipolar configurations. A high standard deviation can be noted for bipolar analysis using common criteria.

8.1.3 Impact of Criteria on Clinical Values

Clinical data Four LAT maps recorded from three paroxysmal AF patients (age 59.3 ± 12.7 years) in sinus rhythm were analyzed retrospectively. Data was acquired for 1 s using a 10 polar circular mapping catheter (Optima, St. Jude Medical) in pair-wise bipolar configuration, in connection with the Ensite NavX electroanatomical mapping system (EAMS) (St. Jude

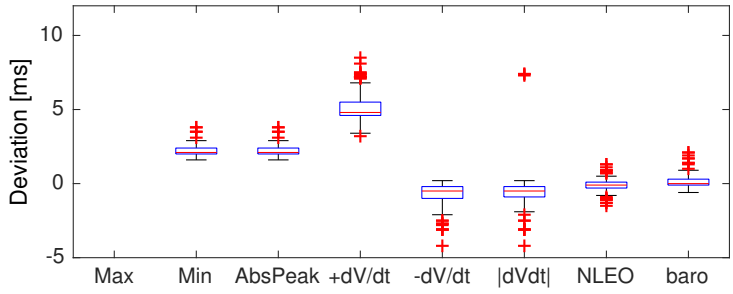

(a) Error in LAT annotation for unipolar signals.

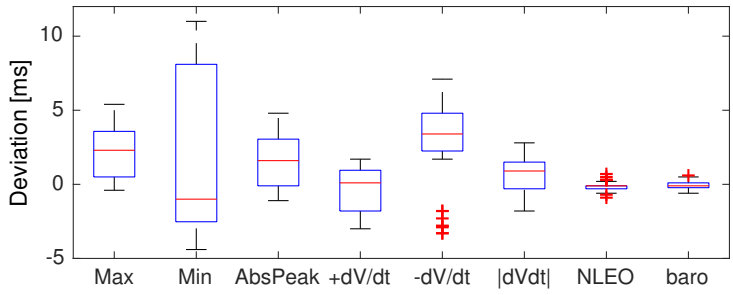

(b) Error in LAT annotation for bipolar signals.

Figure 8.3: Statistical error of annotated LATs. Boxplots of $\Delta_{tCriTrue}$ for simulated unipolar (a) and bipolar (b) electrograms. In agreement with literature, -dV/dt demonstrated the best match for unipolar signals. Performance of common criteria varied strongly depending on catheter orientation for bipolar EGMs. Values of $\Delta_{tMaxTrue}$ were out of range for unipolar signals (median 21.2 ms), as the maximum of the filtered signal was not related to the local depolarization.

Medical). Sample rate was 1200 Hz and signals were filtered by the mapping system with cut-off frequencies of 32 Hz and 250 Hz, respectively. Signals which met at least one of the following criteria were not incorporated: Excluded by the physician, peak to peak amplitude below the noise level of 0.08 mV, or at least one t_{Cri} deviating more than 120 ms from the reference catheter activation time. Thus 489 out of 999 signals were used for analysis.

Generation of LAT maps using different criteria To demonstrate the consequences for clinical signal processing, LAT maps were generated using the same recorded electrograms but different LAT criteria. For all these clinical signals, the absolute time difference $|\Delta t_{MaxMin}| = |t_{Max} - t_{Min}|$ was 9.4±5.8 ms. An antero-septal part of the resulting maps for one exemplary subject is shown in Figure 8.4, using signal maximum (a), minimum (b) and NLEO (c). In addition, the distribution of Δt_{MaxMin} on the complete left atrium is plotted in RAO view (d). All maps showed a propagation originating close to the right superior pulmonary vein. Changes at markings I and II demonstrate the impact of algorithm selection on the resulting map, causing early or late activation. The pattern was observed to be more smooth when the NLEO was applied.

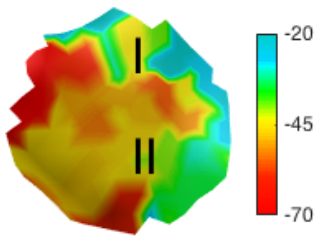

(a) Maximum signal value.

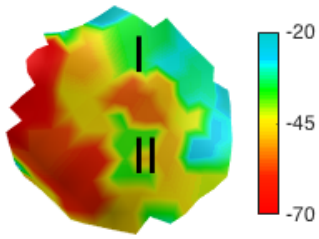

(b) Minimum signal value.

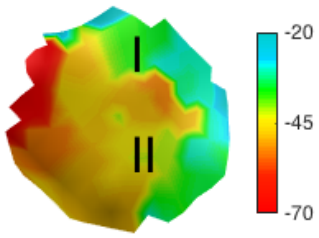

(c) Annotation using NLEO.

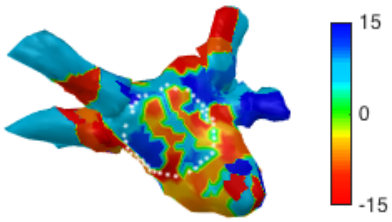

(d) Differences between annotations.

Figure 8.4: Impact of annotation method on clinical data. LAT maps generated from the same clinical signals using three different criteria Max (a), Min (b) and NLEO (c). The complete LA geometry including the selected area for demonstration (white dots) and the distribution of $\Delta_{tMaxMin}$ is shown last (d). All values given in ms.

8.1.4 Discussion and Conclusion

Unipolar signals For unipolar signals, the smallest error of -dV/dt was consistent with the classical criterion of using the steepest negative gradient of the signal to define the LAT. The remaining deviation of 0.8±0.9 ms was reduced to 0.4±0.6 ms if the high pass was set to 0.05 Hz, and to 0.2±0.2 ms if only the distal electrode was considered (which was always in contact). Annotation using the NLEO resulted in 0.2±0.1 ms for the distal electrode. Since information about tissue contact is not known in clinical practice, both electrodes were incorporated for the statistics. Both Min and -dV/dt showed low standard deviation and a bias of 2.2 and -0.8 ms, respectively, which could be corrected by an additive value.

Bipolar signals In case of bipolar EGMs, all common LAT criteria showed mean errors greater than 1 ms, with the best value 1.2±0.7 ms for |dV/dt|. Considering parallel alignment regarding the wave propagation only, AbsPeak performed best ($|\Delta t_{Abs}|$=0.45 ms), which was in agreement with literature [90] and corresponding to Figures 8.2 (b, d). The inconsistent performance when considering different orientations might be caused by the varying mor-

phology of bipolar signals. Both energy-based criteria performed better with mean errors below 0.3 ms.

Clinical implications With respect to the clinical data, selection of different annotation criteria was shown to affect the resulting LAT maps. Although the general excitation pattern was consistent in all three maps of Figure 8.4, zones of early or late activation were present at locations I and II depending on the annotation criterion. Using the NLEO provided a relatively continuous activation pattern. Quantitative analysis showed a mean $|\Delta t_{MaxMin}|$ of 9.4 ms for clinical EGMs, representing the range of jitter which can be expected in LAT map annotation. Although this does not affect the global pattern, it may compromise evaluation of local data during conduction velocity (CV) estimation.

Limitations of this study All simulations were performed using a homogeneous tissue patch and a planar wavefront. Thus the model did not account for the heterogeneities present in real anatomy [101] and curved wavefronts. However, the simulation setup resembled locally homogeneous scenarios described in literature [90]. Although not outlined here, simulations were also compromised by noise and subsequently analyzed.

Conclusion Different criteria are used in clinical practice to define the LAT. This is the first work known to the author to compare the performance of these criteria based on detailed simulations. The results indicated that the maximum negative derivative of the signal (-dV/dt) was the most appropriate indicator of LAT using unipolar signals. For bipolar signals, the maximum of the absolute derivative |dV/dt| could be used with a good performance in signals. The clinical importance of criterion selection was demonstrated by examples of resulting LAT maps. Best performance was achieved using two energy-based algorithms, which showed to be robust against changes in catheter orientation. Since they do not rely on morphological landmarks, they might also be used to define the LAT for fractionated signals. Therefore the energy-based criteria were used frequently during the presented research to achieve a reliable automated local activation time (LAT) detection.

8.2 Determination of Atrial Activation Rate

During sinus rhythm and without any major disturbance in AV conduction, each atrial depolarization is followed by a contraction of the ventricles. Thus an analysis of the RR intervals generally reflects the frequency of atrial activity. During more rapid atrial tachycardia, however, the refractory period of the AV node does not allow every single activation to be passed to the ventricles. Consequently, the direct analysis of atrial signals is required to extract diagnostically relevant information about the atrial excitation. This information can be retrieved in both time and frequency domain.

Selection of an appropriate channel Electrograms recorded in the coronary sinus (CS) are commonly used to assess the stability of atrial excitation. Since the CS catheter remains at a stable position during the complete procedure, it cannot only be used as positional reference, but also to observe the stability of timing and morphology of local activation waves (LAWs). As unipolar electrograms (EGMs) are frequently compromised by powerline hum and ventricular far-fields (compare Chapter 7), bipolar EGMs are typically chosen for analysis. Although BEGMs are generally less affected by ventricular far field (VFF), the recording position very close to the ventricles has to be considered to be within the near-field of the source, and thus ventricular components can frequently be observed in some of the CS channels. Typical CS catheters have 8 or 10 electrodes, providing 4 or 5 bipolar channels. In order to determine the atrial cycle length for a stable tachycardia, analysis of one reliable channel is sufficient. Due to the patient-specific position of the CS, however, it cannot be stated in general, if the proximal or the distal bipolar leads are less affected by the ventricular activity.

Usually, a suitable channel is selected by visual inspection prior to the clinical mapping procedure. Consequently it is used for temporal alignment during mapping and its data is included as sole reference in the exported data. If data from several CS leads was available (e.g. CARTO maps, Rhythmia study files), selection of the channel most suited for analysis was helpful. Therefore, a semi-automatic method was developed during this thesis to automatically rank BEGMs according to their suitability for atrial rate computation. As suggested for the selection of a channel in QRS detection, the kurtosis was applied during this context. The kurtosis of a data vector X represents its fourth central moment, divided by the fourth power of its standard deviation. For signals with long segments of baseline and strong and discrete LAWs, a high value for the kurtosis of the amplitude histogram is expected. Its value will be low, contrastingly, if the signal contains prolonged atrial activity with low amplitude. Based on these considerations, two copies of each BEGM were generated, one with the time of QRS complexes blanked and one with all remaining data removed. For both signals, the kurtosis was computed and its quotient assessed to identify the most suitable channel. If the position of QRS complexes was not available for channel selection, the quality measure was based on the kurtosis of the complete signal only. The CS channels were sorted according to their expected suitability for atrial rate detection and displayed to the user for verification purposes.

In case of dominant frequency (DF)-based ablation procedures of atrial fibrillation (AFib), maps of EGM data are acquired on multiple points of the atrial surface (compare Section 2.3.3). In this case, each individual EGM is subject to analysis of the atrial rate [163–166].

Determination of the basic cycle length in atrial flutter The basic cycle length is one of the most important parameters of an atrial flutter (AFlut) circuit. It can be determined if at least two consecutive LAWs can be detected in the reference channel and their time difference can be computed. Typical basic cycle length (BCL) values for AFlut lie between 180 and 400 ms (compare Table 10.2 in Chapter 10.1). As the duration of exported reference

EGMs for LAT maps recorded with the Velocity EAMS is 1 s (and up to 2.5 s when CARTO is used), three to five atrial LAWs can be expected in each EGM. The LAW which was found most appropriate and thus used for synchronization of LAT data is located in the center of the exported segment.

Although the BCL of AFlut is very stable, small fluctuations have been documented in the order of 5 ms standard deviation [158]. These are not random but periodicity can be found in the respective time series. Several factors influence the instantaneous BCL, like the respiratory state and ventricular state, both causing changes in the atrial volume which in turn change conduction properties according to the mechano-electrical feedback hypothesis [158]. In order to appropriately analyse sequential mapping data recorded during atrial flutter, variations of the BCL need to be detected and accounted for. Within this thesis, an algorithm was developed to automatically assess and monitor the atrial BCL in the reference channel throughout the recorded data.

First, several measures were computed for each individual reference EGM. All active segments of the signal were detected using an energy-based approach [157]. The peak of the energy signal was used to determine the LAT. The central LAT within the segment and its first preceeding and succeeding LAW were used for further analysis, providing information about a prior and a subsequent cycle. Snippets of duration 50 ms were extracted around each LAT, and subsequently used to compute the precise duration of the preceeding and succeeding cycle based on correlation between the respective LAWs. In addition to the cycle length, also the correlation coefficient of the best temporal alignment itself was computed. Second, a mean template of the central LAW over all reference channels was determined, and correlated with each individual reference EGM again.

In the third step, information about BCL and correlation was evaluated to reject measurements which were not consistent with the mapped excitation pattern. Determined BCL values were provided to the user as boxplot and as plot over time. The median BCL was shown as initial estimate for the final BCL. Electrogram data acquired during the sequential mapping process were subsequently rejected, when the LAW correlation of any of the two inspected cycles was below 0.6, or if the BCL deviated more than 10 % from the final BCL measurement. Data were also discarded if the correlation with the mean template was below 0.6.

An example for this process is depicted in the following figures. The initial data from 610 sequential measurements is plotted in Figure 8.5. All reference EGMs are shown in the top row. While the central LAWs exhibit similar morphologies, also signals with varying morphology (e.g. including a strong negative deflection) or different cycle length can be observed. This is in agreement with both boxplot and time-series visualization in the lower row. The median BCL was determined 303 ms. After rejection of low quality signals, the remaining reference EGMs exhibited similar morpholgy and cycle length (Figure 8.6).

Also a multichannel analysis would be possible to monitor the atrial rhythm more closely. The correlation between the central segments does provide information about the stability

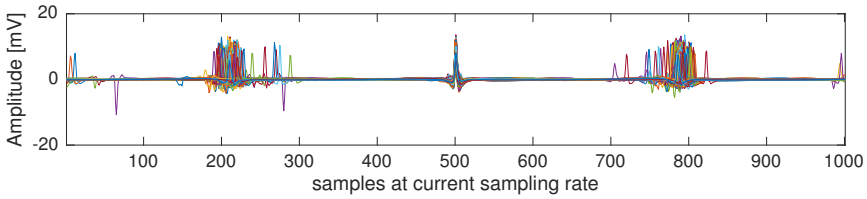

(a) CS signals as imported (610 EGMs).

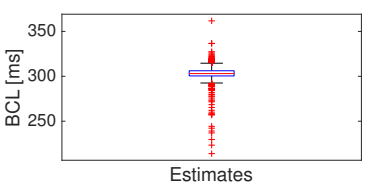

(b) BCL estimate (303 ms).

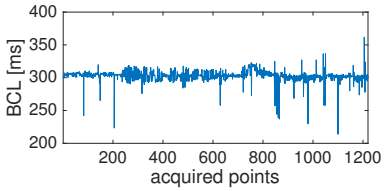

(c) BCL over time.

Figure 8.5: Estimation of AFlut BCL considering all signals (a). The BCL is visualized as boxplot (b) and as continuous value over time (c). Deviations from the median BCL could be observed, which may be caused by alterations in the arrhythmia itself or by misdetections in the CS channel.

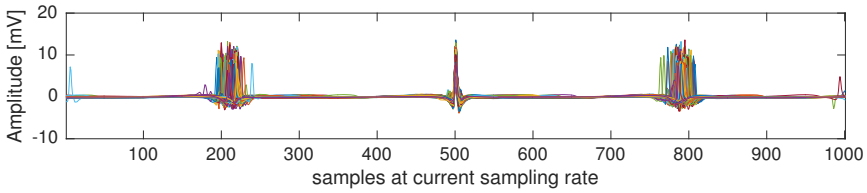

(a) CS signals after assessment of consistency (571 EGMs).

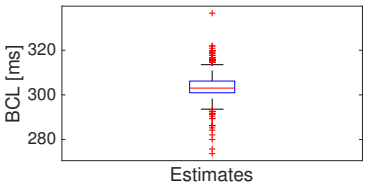

(b) BCL estimate (303 ms).

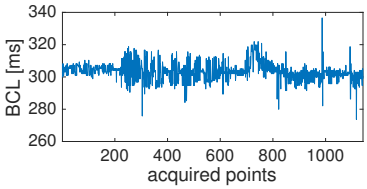

(c) BCL over time.

Figure 8.6: Estimation of AFlut BCL considering only consistent signals (a). CS EGMs were rejected if their BCL deviated for more than 10% of the median value or if the similarity of the synchronization activation complex was too low. Both boxplot (b) and values over time (c) became more consistent.

of the underlying excitation pattern (see section 13.2). However, monitoring all CS leads simultaneously would allow to observe their sequence of activation (LAT pattern). Thus it would also be possible to reject data from cardiac patterns which show similar cycle length but a deviating excitation sequence. This approach, however, was not utilized during this research due to two major reasons. First, the clinical data exported from the EAMS Velocity did only contain one intracardiac reference channel, making multichannel approaches for lead selection not applicable. This issue could be overcome in the future by assigning additional intracardiac channels to the three traces actually reserved for the surface electrocardiogram

(ECG). Second, it was found rarely that stable atrial tachycardias changed into different forms of tachycardias during clinical mapping and without any ablation being performed. Intermediate episodes of sinus rhythm may take place, but can easily be identified by the sudden increase of cycle length. Conversion into other forms of flutter typically took place during ablation and were accompanied by an increase of cycle length.

Activation rate and dominant frequency during atrial fibrillation A more complex case is given by atrial fibrillation, in which the constantly changing depolarization pattern compromises the ability to determine a specific excitation rate. On the one hand, this is due to more fractionated activity, in which the annotation of LAT may not be unambiguous. Additionally, the morphology of LAWs may change from one cycle to the next, excluding the possibility of precise correlation based alignment. Due to the dynamic excitation during fibrillation, the activation rate observed in one channel may not be constant, but also vary over time. Nevertheless, different approaches have been developed to estimate the atrial activation rate or its inverse, the DF. Although both values are expected to be consistent, studies have shown a correlation of only 0.21 between both values [167]. The dynamics of amplitude and cycle length within the analyzed EGM were suggested as possible limitation of DF determination in that study. However, also the annotation of LAT in time domain usually is not obvious, thus may compromise the estimation of cycle length and was not excluded as reason by the authors.

The activation rate is frequently used to assess the regularization of atrial excitation during an ablation procedure, in which an increase by at least 10 % indicates that the tachycardia gets more regularized and thus the correct point for ablation was chosen [27]. The DF is also used to identify AFib sources, in anticipation that areas with a high DF and a gradient towards smaller values in surrounding tissue may represent drivers of AFib [163–166].

An approach to compute the DF was implemented within a student project [168], following a concept published previously. The corresponding algorithm consisted of the following steps [163]:

1. Band-pass filtering at 40-250 Hz
2. Calculate absolute value (i.e. rectification)
3. Low-pass filtering at 20 Hz
4. Windowing (Hanning)
5. Zero padding
6. Fast Fourier transform (FFT)
7. Search for maximum of power spectrum

This technique was discussed intensively within previous work, addressing signal processing fundamentals [169] as well as the application on uni- or bipolar signals, the influence of SNR, VFF and the duration of the signal [163]. In order to focus on the physiological values, the search range for the maximum of the power spectrum is frequently limited to values of about 2.5 to 16 Hz [167]. Of note, the typical threshold for continuously fractionated signals is an activation cycle length of 120 ms, equivalent to a DF of 8.3 Hz.

An example of DF computation and the corresponding time domain EGMs is shown in Figure 8.7. Both unipolar signals were recorded simultaneously on spiral catheter electrodes 8 and 14, respectively. While EGM 8 shows clear deflections and one distinct peak in the PSD, signal 14 is more fractionated in time domain and also less concentrated in frequency domain.

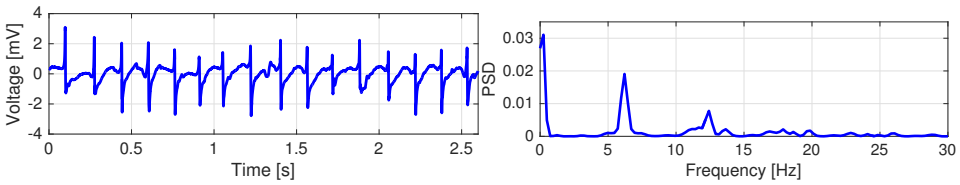

(a) EGM 8 with clear deflections. **(b)** PSD of EGM 8 showed clear peaks.

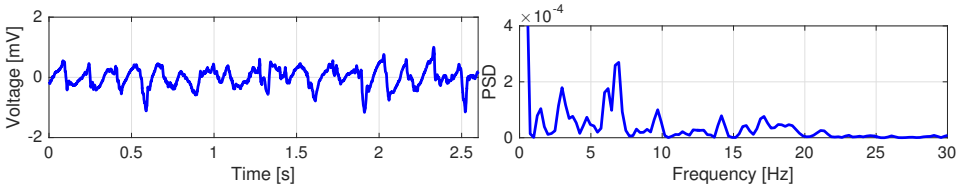

(c) EGM 14 with less consistent activation. **(d)** PSD of EGM 14 was less concentrated.

Figure 8.7: Dominant frequency calculation for unipolar EGMs. While one distinct peak clearly indicated the DF for signals with consistent periodic activity (a, b), the method was less reliable for fractionated activity (c, d).

8.3 Relationship of LAT and Phase

LAT maps are typically used to comprehend the pattern of cardiac excitation during atrial flutter [65]. For focal tachycardias, the point of earliest activation is considered the source and consequently target for ablation. For reentrant tachycardias, the location of the isthmus is of special interest, as ablation at this point is expected to terminate the arrhythmia. It can be identified by observing the excitation pattern and searching for a moment at which the excitation slowly propagates through a narrow region (crowding of isochrones). The third type of reentrant mechanism (microreentry) is characterized by an area in which all isochrones meet, and thus the LAT cannot be defined.

This specific scenario, namely the identification of rotational activity, can also be addressed using a physics-based approach: The concept of phase. Instead of representing the activation in terms of time within the excitation cycle, it is represented by the phase from $-\pi$ to $+\pi$. Following the concept of topological charge, a microreentry results in a singularity point [112].

As outlined in Chapter 3.2.2, a common method to determine the phase is based on the Hilbert Transform. Segments of baseline values, however, can compromise the phase computation. Since the presence of baseline is commonly observed in filtered bipolar electrograms, a preprocessing step termed *Sinusoidal Recomposition* was developed in order to overcome this issue [114]: The input signal v is reconstructed using sinusoidal wavelets, which are scaled proportionally to the negative derivative of the signal. The duration of the wavelet T is given by the cycle length of the observed process and can be determined using the methods outlined above:

$$w(t) = \int_{t-T/2}^{t+T/2} \sin(t-\tau) \left| \frac{\mathrm{d}v}{\mathrm{d}\tau} \right| \frac{1 - \operatorname{sign}\left(\frac{\mathrm{d}v}{\mathrm{d}\tau}\right)}{2} \mathrm{d}\tau \tag{8.1}$$

This technique can be applied to both unipolar and bipolar signals. Although the negative gradient in bipolar signals does not reflect a physiological process like in unipolar EGMs, it can be used very well to indicate the presence of an activation complex. An example for this technique can be seen in Figure 8.8. The phase of a filtered unipolar EGM is computed using both the Hilbert transform directly and after sinusoidal recomposition. In this case, the same signal as in Figure 8.7 (a) was used, and its period T determined using its DF. As the signal was recorded using an intracardiac reference, the amplitude of ventricular far field was low when compared to e.g. the data presented in Figure 5.5. However, both this far field and segments of baseline compromise the reliability of phase determination.

8.4 Interpolation Techniques

The number of points sequentially acquired during mapping is typically in the order of several hundreds, which is much lower than the number of vertices used to represent the

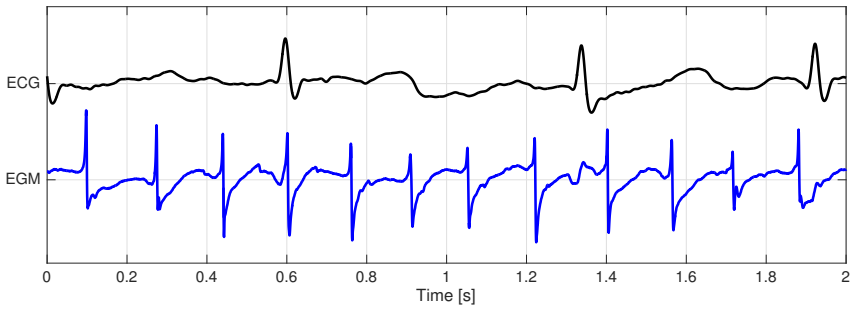

(a) Filtered unipolar EGM with clear deflections.

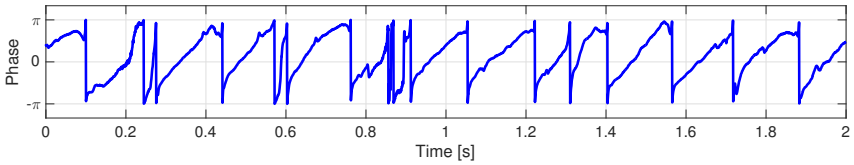

(b) Phase of the signal as computed by Hilbert transform.

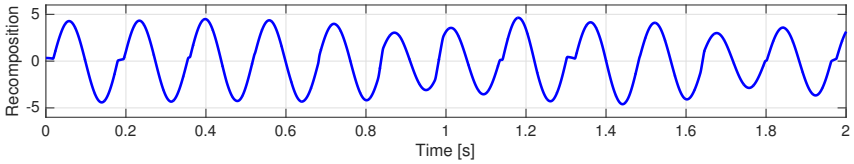

(c) Sinusoidal recomposition.

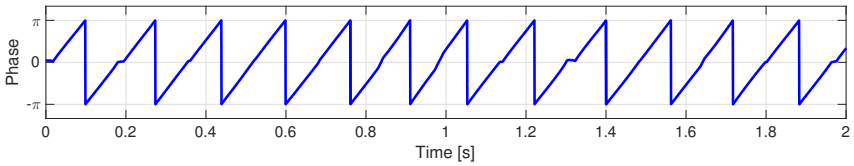

(d) Computed phase after sinusoidal recomposition.

Figure 8.8: Computation of phase with and without sinusoidal recomposition. The phase of a filtered unipolar EGM (a) was computed using the Hilbert transform (b). The result is compromised by far field effects (0.6 s) and baseline values (0.9 s). Transformation of the recomposed signal (c) reduced erroneous phase jumps (d). The phase transition from $-\pi$ to π coincides with the steepest negative gradient of the unipolar EGM.

atrial geometry. Consequently, interpolation between the points has to be performed for visualization and some processing techniques. In the following, the different techniques will be summarized and demonstrated.

Interpolation techniques Three major techniques were used to perform the interpolation step:

- **Nearest Neighbor**
  To merely visualize scalar analysis results like the LAT of a measured EGM, this value was directly assigned to the atrial region surrounding the recording position. For each vertex of the anatomy, data from the closest electrode was taken, without interpolation of values between measurement points. Therefore no other than the acquired values

were used for visual representation. This technique was generally applied to interpolate information about voltage or the presence of activity in the EGMs.

- **Laplacian-Interpolation**
  For continuous processes like the cardiac depolarization, however, interpolation with constant values is not appropriate. For this case, a second technique was implemented which minimized the Laplacian for getting a smooth interpolation. It was originally introduced to interpolate the surface potential distribution of an electrical volume conductor [170].
  Consider the interpolation of k known values onto N vertices of the geometry. Let the vector of data values be $\mathbf{f}$, which can be rearranged to

$$\mathbf{f} = \begin{pmatrix} \mathbf{f}_1 \\ \mathbf{f}_2 \end{pmatrix}, \tag{8.2}$$

  with $\mathbf{f}_1$ being the vector of unknown values for points 1 to k and $\mathbf{f}_2$ be the vector of all known values for points $k+1$ to N.
  Based on the formulation of the Laplacian in a triangular mesh [170], the Laplacian can be expressed as matrix L with elements

$$\begin{aligned} l_{ii} &= -\frac{4}{\overline{h_i}}\overline{\left(\frac{1}{h_i}\right)}, \\ l_{ij} &= -\frac{4}{\overline{h_i}}\frac{1}{n_i}\frac{1}{h_{ij}} \qquad \text{for } i \neq j,\ p_j \text{ direct neighbor of } p_i, \\ l_{ij} &= 0 \qquad \text{for } i \neq j,\ p_j \text{ no direct neighbor of } p_i, \end{aligned}$$

  with h_{ij} being the distance between p_i and p_j, n_i the number of neighbors of p_i, $\overline{h_i}$ the average of h_{ij} over the neighbors of p_i, and $\overline{(1/h_i)}$ being the average of $1/h_{ij}$ over the neighbors of p_i.
  Similar to $\mathbf{f}$, L can be partitioned according to

$$L = \begin{pmatrix} L_{11} & L_{12} \\ L_{21} & L_{22} \end{pmatrix} \tag{8.3}$$

  Based on these considerations, two interpolation techniques were generated. First, the Laplacian was set to 0 for all points for which no function value was known. This resulted in methods I, the *linear Laplacian* given by

$$\mathbf{f}_1 = -L_{11}^{-1} L_{12} \mathbf{f}_2 \tag{8.4}$$

  As extrema only occurred at points with given values, the interpolated values did not exceed this boundary. Thus this technique could be used to visualize NLEO and amplitude values as these were bounded.
  For interpolation of LAT times, however, a second method was required that allowed values which were not restricted by the mapping field. Instead, a depolarization with constant speed should be assumed if measurements did not indicate otherwise. This

was reflected in method II *minimization*, the Laplacian of all points was minimized resulting in the least squares solution

$$\mathbf{f}_1 = -\left(\begin{pmatrix} L_{11} \\ L_{21} \end{pmatrix}^t \begin{pmatrix} L_{11} \\ L_{21} \end{pmatrix}\right)^{-1} \begin{pmatrix} L_{11} \\ L_{21} \end{pmatrix}^t \begin{pmatrix} L_{12} \\ L_{22} \end{pmatrix} \mathbf{f}_2 \tag{8.5}$$

- **Eikonal Diffusion Solver**
  Although the *minimizing Laplacian* already provided a continuous interpolation pattern very useful for a single cardiac depolarization process, it was not able to handle the phase jump present for reentrant tachycardias. Therefore a third method was considered and implemented as described in literature [105] as part of a student project supervised by Axel Loewe [171] (compare also Chapter 2.4.2). This technique was based on an eikonal-diffusion solver, that estimated phase values instead of LATs and also considered wavefront curvature. In addition it utilized sparse matrix formulation for a memory efficient handling of data.
  The respective interpolation scheme consisted of a two step approach, in which first an initial estimate was computed by considering only the diffusion process. This reduced to a Laplacian interpolation capable of handling reentrant patterns. In a second step, the complete eikonal-diffusion process was solved iteratively. It also allowed to consider the wavefront curvature dependent CV and anisotropic conduction by specifying appropriate tensors $\mathbf{c}$ and $\mathbf{D}$. These parameters could also be related to the parameters required for monodomain simulations, allowing the method to specifiy an initial condition of consecutive simulations. For interpolation, however, isotropic conduction was assumed. LAT values also had to be converted from time to phase space by dividing through the BCL.

Sinus rhythm activation on a 3D geometry In order to demonstrate these interpolation techniques, data from an in silico approach was used. Atrial excitation during one beat of sinus rhythm was simulated using a bi-atrial anatomical model, which was previously generated from segmented magnetic resonance imaging (MRI) data of a healthy male subject [172]. The model consisted of 1.1 million tissue voxels with a resolution of 0.33 mm in each spatial direction. It also included anisotropic conduction and tissue heterogeneities [173]. Cardiac depolarization was computed using the monodomain solver *acCELLerate* [102] and a bi-atrial voxel model. Extracellular potentials were determined using field calculation [174] (compared Chapter 2.4).

For each endocardial tissue voxel, the LAT was determined using the upstroke of the TMV, being the time of maximum positive derivative. Rapid depolarization could be observed along the crista terminalis on the right atrial posterior wall (compare Figure 8.9).

Subsequently, a triangulated surface mesh was generated which represented the endocardial wall. Virtual electrodes were located in the blood pool within 1.5 mm of the tissue surface, with a bipolar spacing of approximately 2 mm. Measurements were determined by randomly positioning 500 bipoles in the RA and 600 in the LA. Extracellular potentials

were extracted from the simulation at each electrode position at 2000 Hz sampling rate. The bipolar signal was computed as difference between both electrodes and their mean position used as location of acquisition. LATs were assigned to each bipolar signal using the NLEO as described in Chapter 8.1. Subsequently the LATs were interpolated on the atrial shell.

The resulting interpolation schemes can be seen in Figure 8.9. Using the *Nearest Neighbor* technique, discrete areas of simultaneous activation could be observed (b). Application of the *minimizing Laplacian* resulted in a qualitatively more smooth pattern of activation.

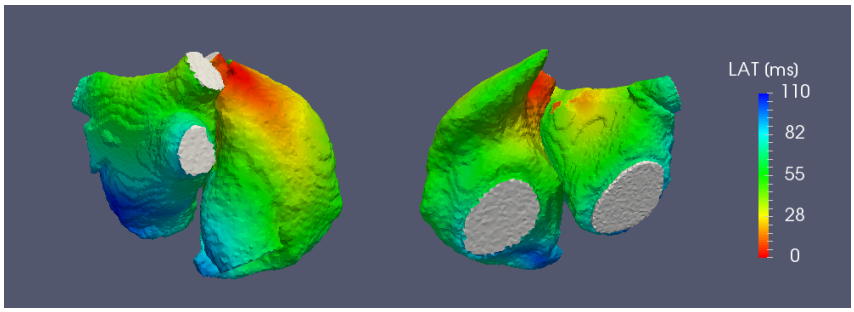

(a) LATs extracted from the simulated tissue.

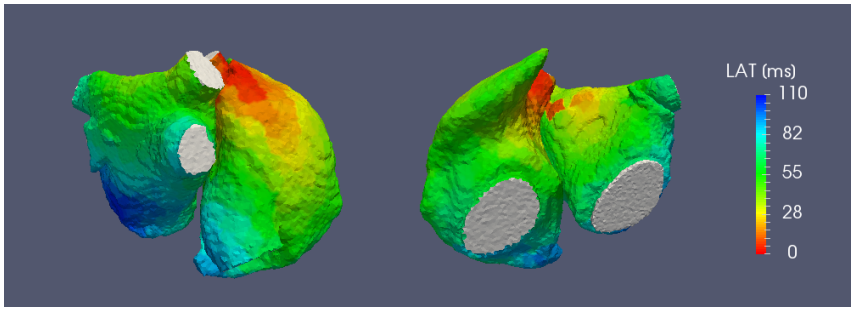

(b) LATs interpolated using *Nearest Neighbor*.

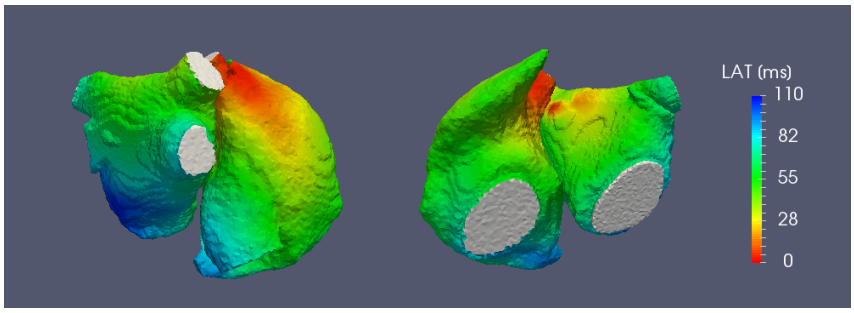

(c) LATs interpolated by minimizing *Laplacian*.

Figure 8.9: Interpolation of LATs using different techniques. The reference LATs were determined directly from the maximum upstroke of transmembrane voltage of the simulated tissue (a). Bipolar electrograms were computed at 500 right and 600 left atrial positions. The NLEO was used to assign the measured LATs, which were subsequently interpolated on the atrial shell using the *Nearest Neighbor* (b) and the *minimizing Laplacian* (c) approach.

Method	RA	LA
NN	0.82±4.13	0.58±3.98
	-4.50 / -1.50 / 0.50 / 2.50 / 6.00	-4.00 / 1.50 / 0.50 / 2.00 / 5.00
Laplacian	0.73±3.17	0.64±2.83
	-2.15 / -0.50 / 0.38 / 1.30 / 3.96	-1.91 / 0.51 / 0.32 / 1.28 / 3.70

Table 8.1: Deviation between simulated and interpolated LAT. Laplacian interpolation exhibited a lower standard deviation and more compact quantile ranges. All value in ms, quantile ranges 5%, 25%, 50%, 75% and 95%.

For quantitative analysis, the LAT assigned to each vertex by the interpolation techniques was compared to the ground truth extracted from the simulation. The results are summarized in Table 8.1. Both methods showed a mean error of less than 1 ms, indicating the absence of a systematic offset. Comparison of standard deviations between both methods demonstrated smaller values for the *Laplacian*-based technique. In addition, the quantiles were computed for 5%, 25%, 50%, 75% and 95% of deviations. Assessment of the 25% and 75% quantiles indicate that the errors using *Laplacian* interpolation were about 1 ms smaller. This was also shown by the 5% and 95% quantiles.

Excitation during reentrant mechanisms To demonstrate the interpolation of LATs during reentrant activations, a simplified model of ventricular slice was used as suggested in literature [105]. LATs were specified as phase values at predefined locations. Subsequently, both *Nearest Neighbor* interpolation and the eikonal-diffusion solver were applied.

A comparison of these techniques can be seen in Figure 8.10. The given measurement positions are indicated by white dots in (a). The corresponding phase values were assigned as constant values surrounding each point, clearly indicating the borders between interpolation regions. The initial estimate of eikonal interpolation is shown in part (b). A continuous change of phase can be observed, the wavefront as indicated by the phase jump, however, does not exhibit any curvature. After iterative optimization of the eikonal-diffusion solver converged, the final result additionally demonstrated curvature of the circulating wavefront (c).

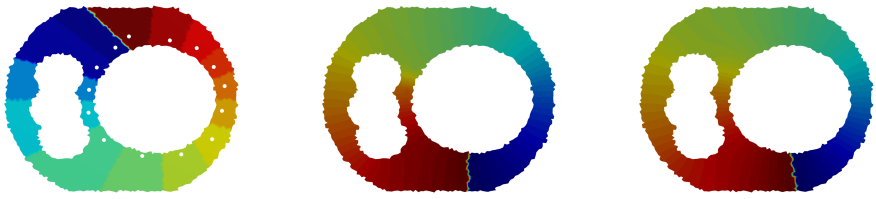

(a) Nearest neighbor. **(b)** Laplacian diffusion. **(c)** Eikonal-diffusion.

Figure 8.10: Interpolation of a reentrant LAT pattern. Phase values were assigned to 14 positions (white dots) and interpolated using *Nearest Neighbor*, leading to constant phase values without smooth transition (a). The *eikonal-diffusion* solver first initialized using only diffusion (b) and then iteratively optimized the solution (c).

CHAPTER 9

Dynamic Visualization of Cardiac Activity

Although the concept of LAT maps is widely used, it has two major limitations. For generation of a map, one continuous time span in each electrogram is selected, which is expected to contain exactly one cardiac excitation pattern. The latter can be for example one SR activation or one cycle of a cardiac tachycardia. If several electrograms are used to construct the map, a synchronization needs to be performed. Within the chosen time span, the LAT of each electrogram is determined as a scalar value according to Chapter 8.1.

Consequently, the annotation of the LAT is not reasonable if there is fractionated activity without a clear intrinsic complex or if there are two distinct deflections in the electrogram (double potentials at lines of block). Three examplary electrograms can be seen in Figure 9.1. In order to cope with the previously mentioned issues, new techniques for the visualization of cardiac activity for diagnosis were developed in this thesis and presented to the cardiological community [175].

It has to be mentioned that the drawbacks of required LAT annotation were independently recognized and addressed by another group, who suggested the technique of *Ripple Mapping* for signal visualization [176, 177]. In this approach, bars were placed at each measurement location, pointing outwards perpendicular to the surface mesh. The length of the bars was variable and indicated the absolute value of the measured voltage at each time instant. The rapid change of voltage amplitude caused equivalent changes in bar length, given the rationale for the name of the new technique.

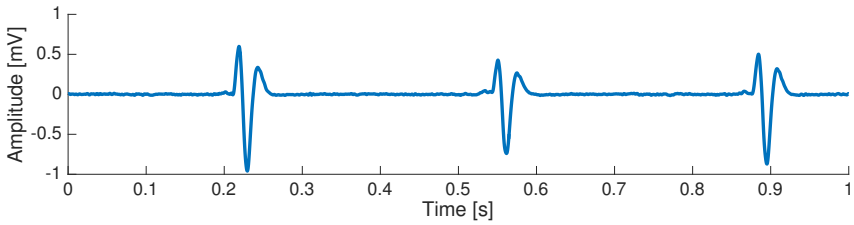

(a) Clear deflections.

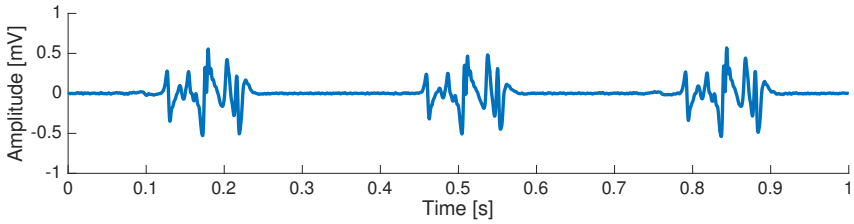

(b) Fractionated EGM.

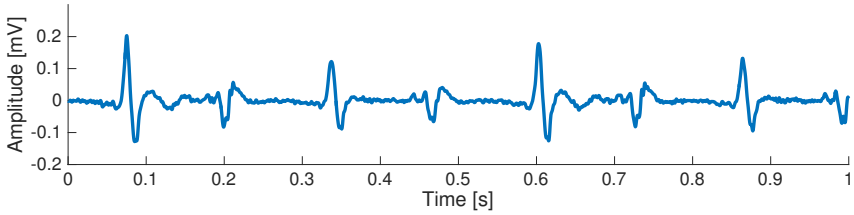

(c) Double potential.

Figure 9.1: Signals demonstrating morphologies of different complexity. In case of single deflections, annotation of the LAT is reasonable (a). In case of fractionated signals (b) and double potentials (c), the concept of annotating a LAT reaches its limitations and other techniques should be considered.

9.1 Time-Continuous Representation of Atrial Activity

For LAT maps, the complete information which is comprised in the electrogram (EGM) is reduced to one single value. Instead of annotating an LAT in the signal, the goal of the new approach was to transform the signal and maintain its temporal information. Certain requirements needed to be fulfilled by the resulting signal. Primarily, it should allow a clear differentiation between episodes in which no activity was present (baseline) and those containing activity (activity complexes). Second, a smooth course seemed favorable, since it eased the interpolation between measurement points. Third, the resulting signal should reflect the amount of activity in the signal.

Two concepts were developed which satisfy these expectations. Using the non-linear energy operator allowed to generate a transformed signal that also reflects the amount of activity in the signal over time. As suggested by physicians, an approach based on binarization was also developed, since the clear discrimination between active and inactive

areas eases visualization. At first, the concept of phase movies is shortly reviewed, as it is commonly used to represent data during atrial fibrillation (AFib).

9.1.1 Phase Movies

As demonstrated in Chapter 8.3, EGMs can be transformed into phase space by the Hilbert transform. Although this is more often done with unipolar signals, it can be applied to bipolar EGMs as well. As bipolar electrograms (BEGMs) signals typically contain prolonged segments of baseline, sinusoidal recomposition was applied as preprocessing technique to more reliably determine the instantaneous phase. The period T for this technique was set to the BCL of the underlying flutter mechanism. The resulting signals in phase space are plotted in Figure 9.2.

Both the signal with single clear deflections and the one with prolonged activation were accurately represented in phase domain. For both, phase jumps indicate the presence of activation complexes. Information about the actual duration of the fractionated complexes, however, is lost. Similarly, only the dominant deflection is indicated by the transition from π to $-\pi$ for the double potential.

Concluding, all EGMs were transformed into a more continuous signal in phase space. The increase of phase indicated the progress between different cardiac cycles, making phase mapping an interesting tool to visualize propagation of depolarization. It can very well be interpolated on the atrial anatomy as it will be demonstrated in Chapter 17.4. But neither prolonged activity nor double potentials were accurately represented, posing the demand for new techniques as outlined in the following chapters.

9.1.2 Energy-based Representation

As outlined in Chapter 3.2.1, the NLEO can be used to determine a surrogate for the instantaneous energy of a signal. If the prerequisite is fullfilled (highest frequency component is below 1/8 of the sampling frequency), its value is proportional to the squared values of both the amplitude and the frequency of the signal. Postprocessing includes rectification and low-pass filtering, which is a very favorable property of the transformation, since the excitation pattern is smoothed.

The cut-off frequency of the low-pass was suggested to be 24 Hz [161], which proved to be a reasonable setting. Selecting a lower value was found to cause smearing of the activation complexes. A second challenge was the variability of electrogram amplitudes: Since the electrogram amplitude heavily depends on various factors like tissue contact, catheter orientation and wavefront propagation, the resulting NLEO value also depends on these parameters. In order to visualize the dynamic activity, a normalization of the NLEO signal at each measurement point was required. Therefore the area under the curve of the signal was normalized to 1. This was performed in sliding windows, since the tissue contact

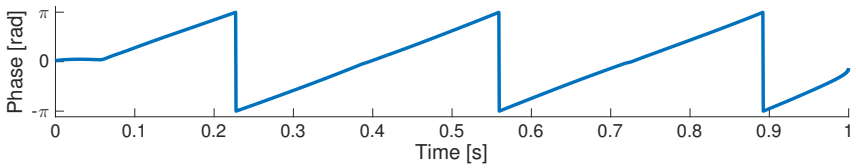

(a) Clear deflections.

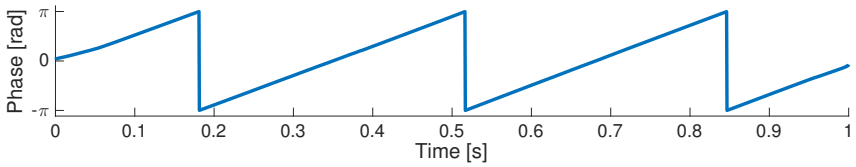

(b) Fractionated EGM.

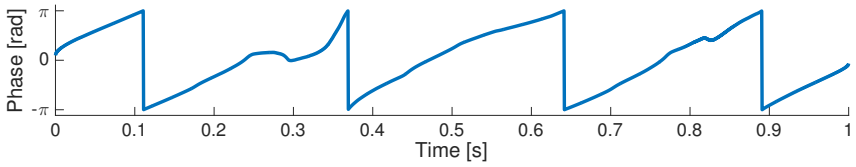

(c) Double potential.

Figure 9.2: Phase of the signals from Figure 9.1. The instantaneous phase was determined by sinusoidal recomposition and Hilbert transform. Fractionation is not reflected by the resulting signal, and only the dominant deflection of the DP can be recognized.

and thus the amplitude of each activation complex may vary over time. The window duration was suggested as 0.9% of the cycle length of the observed activity. In case of discrete complexes, this results in a normalization of the amplitude of each excitation. If prolonged complexes are present in the signal, these will exhibit a smaller maximum amplitude after normalization.

The result of this transformation to the signals shown in Figure 9.1 is visualized in Figure 9.3. While clear deflections are represented by a single peak in the energy-domain, fractionated activity shows activity over a longer period in time, during which distinct deflections of the original EGM are pronounced. Double potentials in turn can be recognized by the presence of two peaks of increased energy within one cycle.

Monitoring the instantaneous energy over time allows to relate the spatio-temporal excitation pattern based on the activity in each EGM, without the need for annotating the LAT. Potential issues arise, however, by the selection of the low-pass filter cut-off frequency. While too high values may cause a lack of sufficient smoothing, small frequencies may cause a smearing of distinct deflections.

9.1.3 Description using Binarized Activity

A second approach for dynamic visualization was focusing on the differentiation between the active and inactive parts of the signal (compare also Chapter 11.1.2 for a more comprehensive

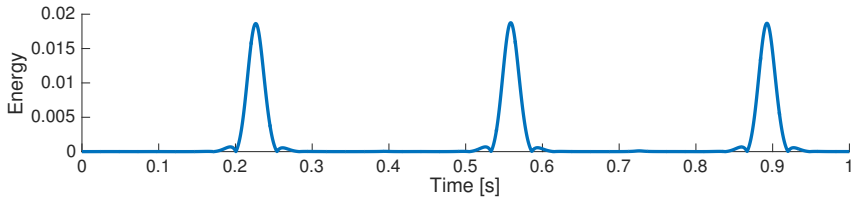

(a) Clear deflections.

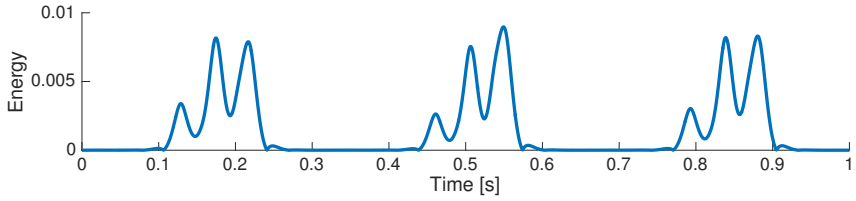

(b) Fractionated EGM.

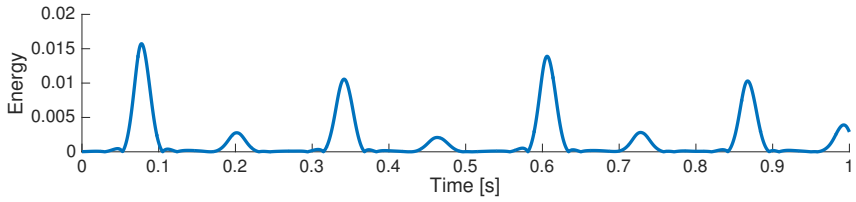

(c) Double potential.

Figure 9.3: Normalized energy of the signals from Figure 9.1. The energy was computed using the NLEO, low-pass filtered and subsequently normalized for the area under the curve for each cycle. Both fractionation and DPs are reflected by the resulting values.

discussion of related issues). The EGM was transformed into an activity signal, which could only have the binary states active and inactive. Following this approach, an EGM was generally considered inactive during the complete measurement time. If the measured voltage indicated the presence of an activity complex (e.g. based on the voltage, energy-measures, ...), the corresponding time was set to active. Initially, an approach based on the postprocessing of the non-linear energy operator (NLEO) was applied [157].

Compared to the energy-based representation, the resulting activity signal only contained two discrete values, making the need for normalization unnecessary. An example for this approach can be seen in Figure 9.4. While distinct activities are characterized by short active segments, fractionated activity were reflected by prolonged periods of activity. Two distinct active segments indicated the presence of double potentials.

However, the outcome of this technique highly depended on the detection of active parts, and thus the applied method and its parameterization. Since amplitude and morphology of signals depend on multiple parameters like electrode size, tissue contact etc., the implementation of an activity detection algorithm seemed reasonable in a semi-automatic way. See Chapter 11.1 for a detailed discussion of activity detection.

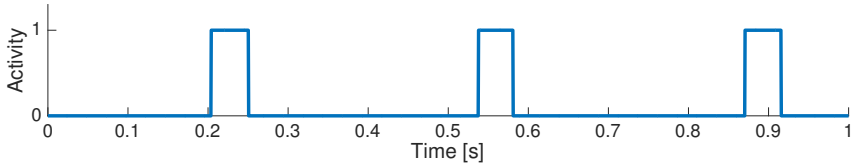

(a) Clear deflections.

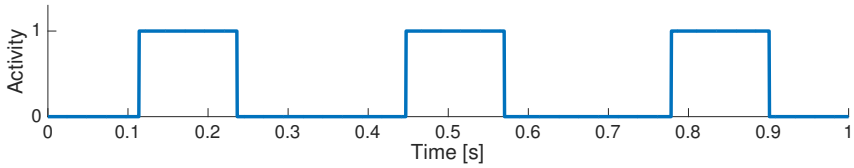

(b) Fractionated EGM.

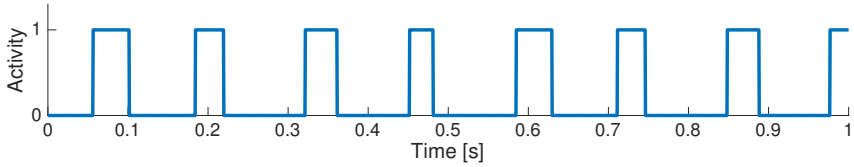

(c) Double potential.

Figure 9.4: Activity of the signals from Figure 9.1. Active samples were annotated within each signal. Both fractionation and DPs are reflected by the resulting values.

9.2 3D Visualization

After the time-dependent activity signal was computed for each electrode, the resulting excitation pattern needed to be visualized. One approach developed during this research was based on projecting the activity information on the atrial anatomy. This approach was especially designed for the analysis of atrial maps, in which a multitude of data was available from various atrial positions. The information of each electrode was assigned to the vertex of the geometry, which was closest to the measurement point. If several measurements were acquired within a very small surface area, only the data with the highest EGM amplitude was used for analysis since it was expected to enable a map with best quality. After all information was assigned to surface vertices, interpolation to the remaining surface points was performed. Therefore either the NN or the Laplacian interpolation approach was used (compare Chapter 8.4). For Laplacian interpolation, the linear approach was used which did not exceed the given value range. Since interpolation was not reasonable for areas too far from measurement points, these were discarded for visualization. The usage of interpolation for smoothed representation and the different processing steps are the two major differences between the presented technique and *Ripple Mapping*.

A second approach was developed in case that data from individual catheters was subject to analysis. In this case, data was not projected on the atrial anatomy. Instead a triangular surface mesh of the catheter geometry was computed, reflecting its shape and potentially including deformation. Projection and interpolation were then applied to the catheter mesh, without the need for discarding electrodes. It was found useful to simultaneously display the

catheter model with the activity information and the atrial geometry for orientation during final visualization.

Excitation during sinus rhythm A simulated excitation during normal sinus rhythm (NSR) was used to demonstrate these approaches. As outlined in Chapter 8.4, cardiac depolarization of a biatrial voxel model was computed using *acCELLerate*. The time of upstroke of transmembrane voltage (TMV) was assessed in the tissue, providing a reference LAT map (compare Figure 9.5). Extracellular potentials were calculated and acquired using virtual electrodes located within 1.5 mm of the tissue surface. From these, extracellular potentials were extracted with 2000 Hz sampling rate, resulting in 500 right and 600 left atrial bipolar signals. In agreement with clinical processing, signals were filtered with a high-pass cut-off frequency of 30 Hz and a low-pass with a cut-off frequency 300 Hz.

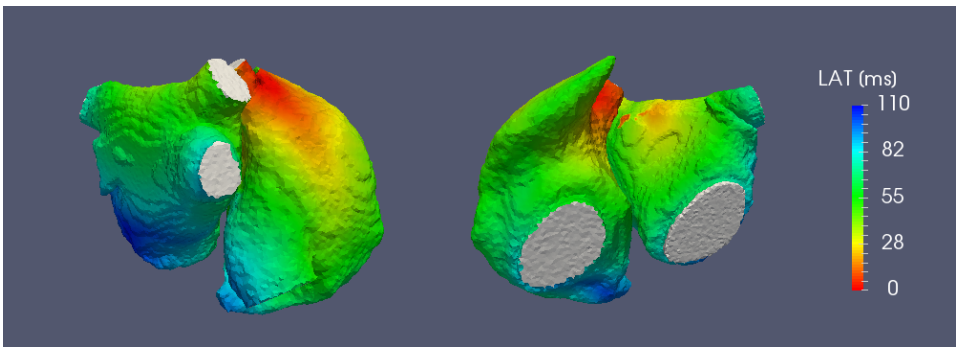

Figure 9.5: LAT of the simulated excitation pattern

The energy-based representation of each bipolar signal was computed as outlined above, normalized and subsequently interpolated on the atrial shell. For demonstration purposes, this was done using *Nearest Neighbor* and the *Laplacian* interpolation. Both results can be seen on the left and in the middle of Figure 9.6, respectively. The binary representation of activity is visualized on the right of Figure 9.6. It can be seen that depolarizing regions are indicated as active in this binary representation. While the local maximum of energy indicates the current position of the depolarizing wavefront at each time instance, this information cannot be inferred from the discretized view.

All three time-continuous visualization techniques allowed to understand the cardiac excitation pattern without the need of annotating LATs. In contrast to the LAT map shown in Figure 9.5, they are not displayed as static image. While the assessment of the cardiac excitation patterns using static LAT maps can typically be done more quickly, the usage of dynamic movies allows to comprehend temporal relationships like dyssynchronicity between regions more easily. It can also handle prolonged or fractionated activity, or double potentials.

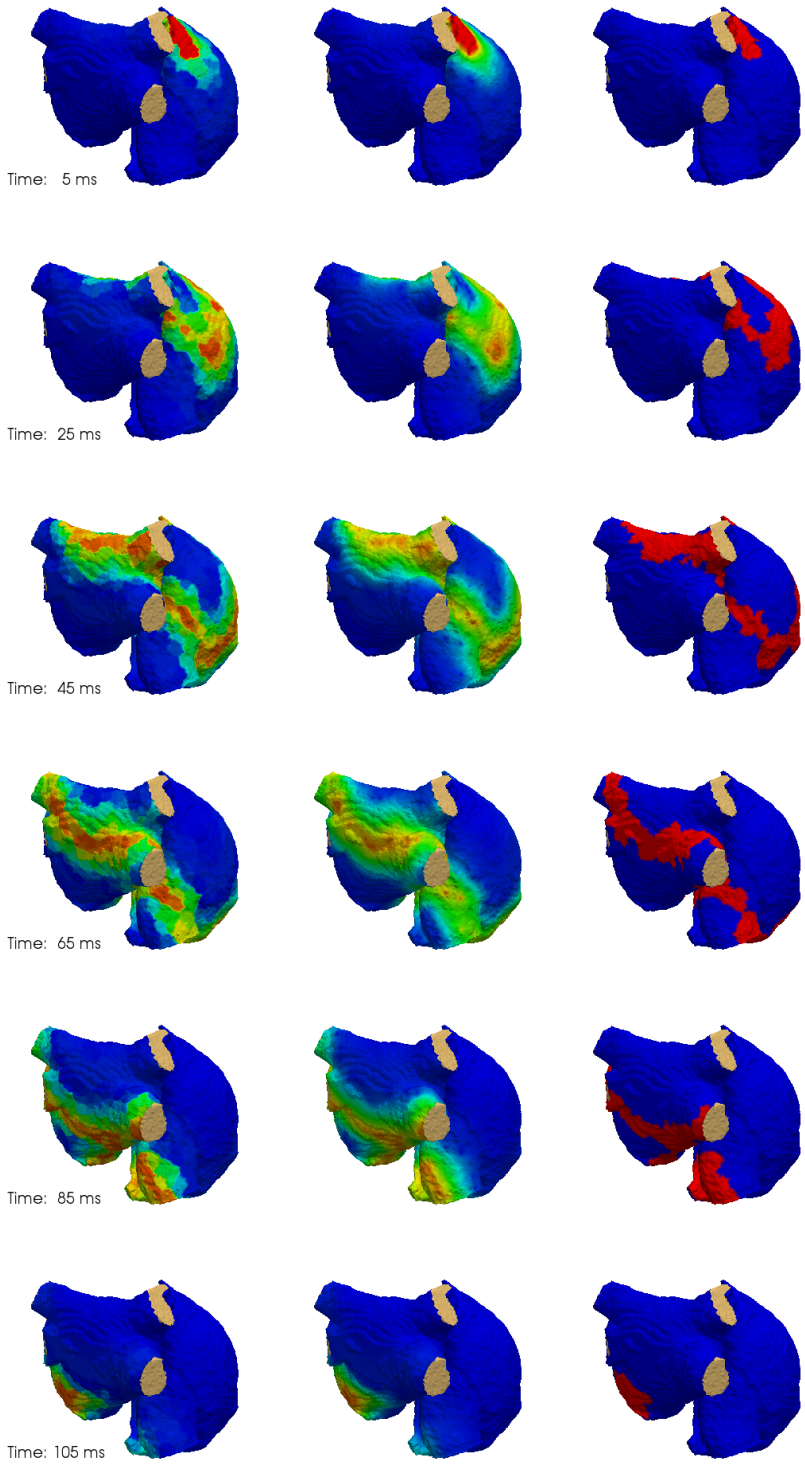

Figure 9.6: Time-continuous visualization of cardiac excitation during NSR. The pattern of depolarization corresponds to the LAT map shown in Figure 9.5. The energy-based activities of each electrode are interpolated onto the atrial shell using the *Nearest Neighbor* (left) and the *Laplacian* approach (middle). For these, the color indicates the energy values ranging from rest (blue) to highly active regions (orange). The binarized activity is plotted using the *Nearest Neighbor* (right). Note that the maximum energy indicates the current position of the depolarization front, while this information is not contained in the binarized activity.

Rotor on Patch Rotational activity is of significant interest as mechanism maintaining atrial fibrillation. To demonstrate the ability of activity movies to visualize these kind of phenomena, it was utilized to analyze data from a simulated rotor which was provided by Markus Rottmann.

Rotational activity was simulated in a flat patch of size 10×10 cm, consisting of cubical voxels with isotropic edge length of 0.1 mm. The myocardium was modeled by a layer of 5 voxel thickness and covered by a blood layer of equivalent dimensions. Electrophysiological characteristics of the Nygren et al. [178] cell model were adapted to represent chronic atrial fibrillation as presented previously [179]. Extra-cellular potentials were computed inside the blood and acquired in the most endocardial layer by an array of 43×43 equally spaced electrodes with a sampling rate of 1 kHz.

Subsequently, a triangular mesh was generated which represented the surface of the patch with over 11,000 points. In agreement with the previously outlined work flow, the virtual electrodes were projected on this anatomy. The energy-based representation of activity was subsequently computed and interpolated on the surface mesh using *Nearest Neighbor*. The resulting energy movie is plotted in Figure 9.7, showing equidistant snapshots every 50 ms over approximately 1.5 cycles of rotation. The visualization of more than one cycle is an important advantage of the continuous representation, as LAT maps are naturally limited to the visualization of the maximum duration of one cycle.

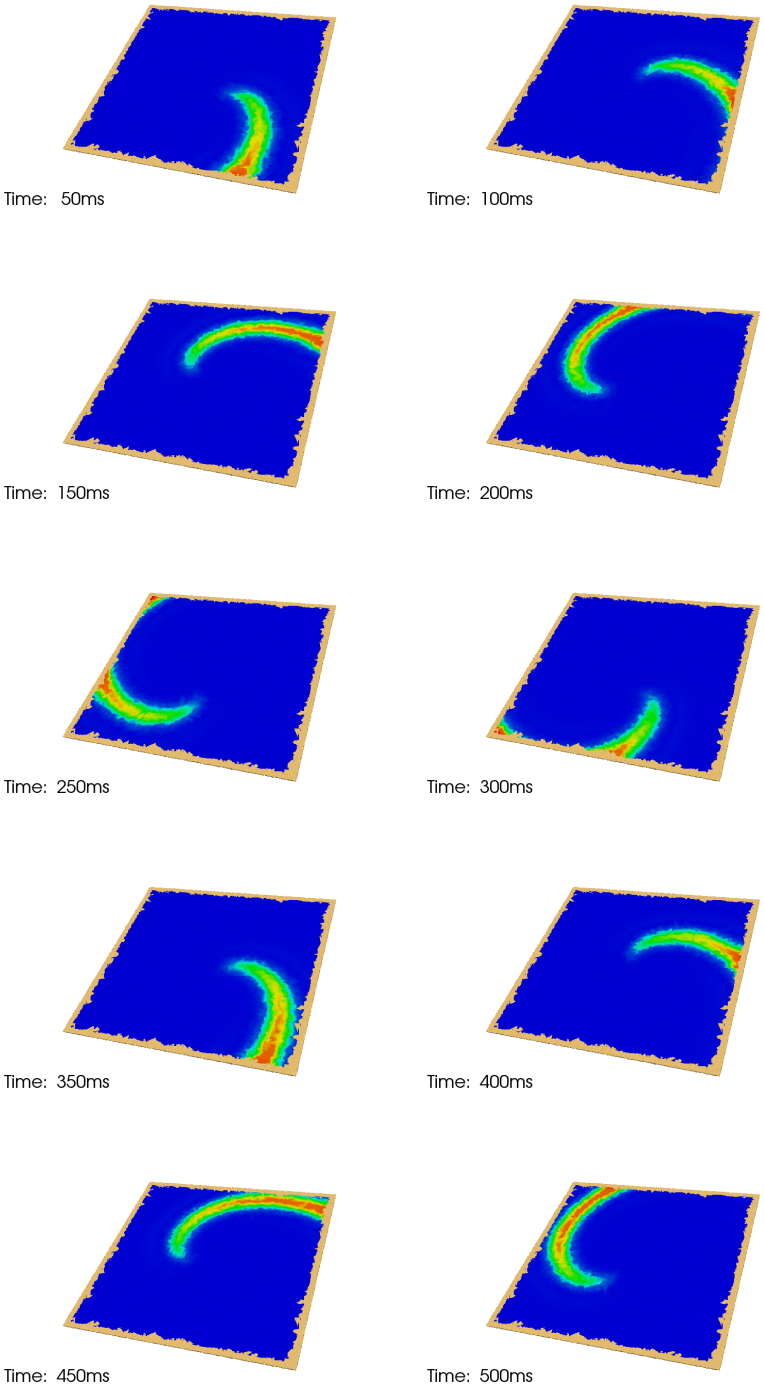

Figure 9.7: Energy movie of rotational activity. The extracellular potential caused by a rotational activity was acquired on a surface directly over the patch and visualized as time-continuous process without annotation of the LAT. This allowed to visualize dynamics for more than one BCL.

CHAPTER 10

Simulation of Atrial Flutter

A huge number of text books, review papers and case-reports is availabe to physicians when it comes to the diagnosis and treatment of atrial flutter (AFlut). All of them provide a consistent view on this well understood atrial tachycardia, elucidating underlying mechanisms and proposing treatment options. Diagnosis of the patient at hand, however, can become quite complex. This especially concerns patients which develop AFlut after index or repeat ablation of atrial fibrillation (AFib), since the atrial substrate already shows complex patterns of isolating lines and ablation spots [64].

As will be outlined in Chapter 11, diagnosis of the presented mechanism is currently based primarily on the experience of the physician. Despite an increasing amount of available and diagnostically useful data, the number of engineering-based algorithms for automated signal processing is rather limited. This also concerns the subsequent decision for a treatment option, which aims for termination of the arrhythmia but hardly considers activation during normal sinus rhythm (NSR) or reinducibility.

Due to its organized and well-understood form, the atrial activity during AFlut can be very well simulated. Biophysical cellular models have been applied for this, but require significant computational resources due to their ion-channel based approach. For AFlut, however, simulation can also be performed on the macroscopic level using the Fast-Marching approach on Eikonal Equations [180, 181]. This allows to simulate the excitation process faster than real time, theoretically enabling to assess the impact of ablation lines on the tachycardia during an ongoing intervention. A corresponding approach was previously implemented in a virtual reality ablation simulator which was designed for the training of cardiologists [181]. The fast-marching simulator (FaMaS) used at Institute of Biomedical Engineering (IBT) was implemented within a student research project [171], supervised by Axel Loewe and used in several research projects [182–184].

One goal of the presented research was to develop algorithms to support physicians in diagnosis and treatment of AFlut using multichannel data analysis. In this context, simulation of the tachycardia offers the unique possibility to develop and benchmark algorithms in a laboratory environment before they are applied clinically. Therefore, however, the simulations should be as realistic as possible.

Two approaches were followed during the presented research project to achieve this goal. On the one hand, a database of virtual AFlut scenarios was generated based on documented cases of clinical tachycardias. For this purpose, a system was set up to be able to manually parameterize simulations easily. On the other hand, an algorithm was designed to automatically parameterize the simulation according to clinical mapping data (see Chapter 10.2). This could also be considered a fundamental step for patient-specific ablation planing during the procedure. Both will be outlined in the following sections.

10.1 Database of Documented Atrial Flutter Forms

The mechanisms underlying AFlut are very well described in literature. This applies to right atrium (RA) tachycardias [61, 62, 185] as well as left atrium (LA) forms [63, 186, 187], occurences after ablation for AFib [64, 65, 186] and macro reentrant mechanisms [188]. Based on these descriptions, a database of virtual AFlut forms was set up. These comprised scenarios which precisely resembled documented clinical cases and ones which were implemented based on loose descriptions. A graphical user interface was implemented for the realization of the simulations.

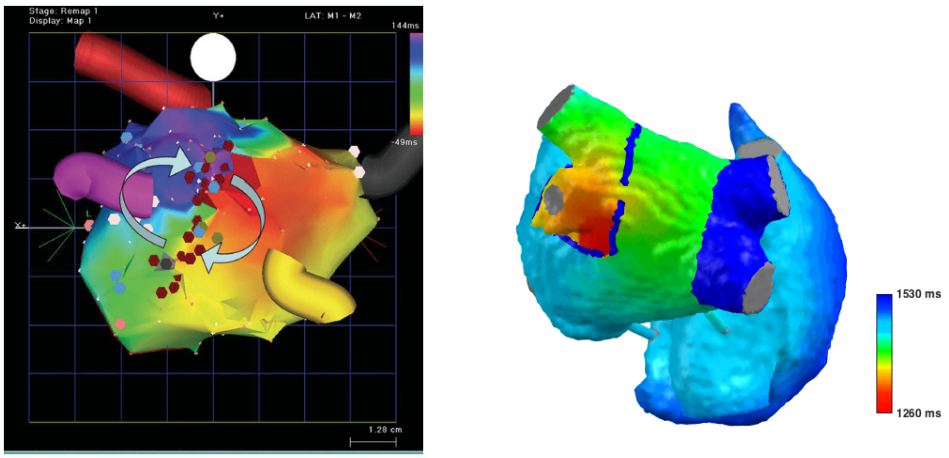

(a) Result of clinical mapping. **(b)** Simulation outcome.

Figure 10.1: Simulating a clinical case of AFlut. Activation time mapping indicated two gaps in the isolation lesion surrounding the LPVs (a). The simulated excitation matched well with the clinical LAT pattern after personalization of the model (b). (a) is reprinted from [186] with permission from the publisher.

One example for a simulated clinical case is depicted in Figure 10.1. A left atrial tachycardia was observed and documented following the circumferential ablation of pulmonary veins (PVs) [186]. local activation time (LAT) mapping indicated a small-loop reentry with a basic cycle length (BCL) of 190 ms passing gaps in the ablation line encircling the left PVs. The corresponding simulation can be seen on the right hand side. After parameterization, both the excitation pattern and the cycle length were in agreement with the clinical pattern.

This provided an excellent scenario to test an algorithm for the detection of micro reentrant circuits (compare Chapter 11.2).

Properties adjusted for the simulation All simulations were performed using a bi-atrial anatomy to be able to study both left and right atrial excitation patterns. The model included heterogeneities in tissue classes and anisotropic conduction. Tissue classes and interatrial bridges were generated according to a rule-based algorithm developed and published previously for voxel geometries [173]. The algorithm was modified to work on a triangular surface mesh and applied to this model within a diploma thesis [189, 190]. The bridges included the most common interatrial connections like Bachmann's Bundle (present in nearly the complete population), posterior connections (67-93%) [191] and a coronary sinus bridge (compare Figure 10.2).

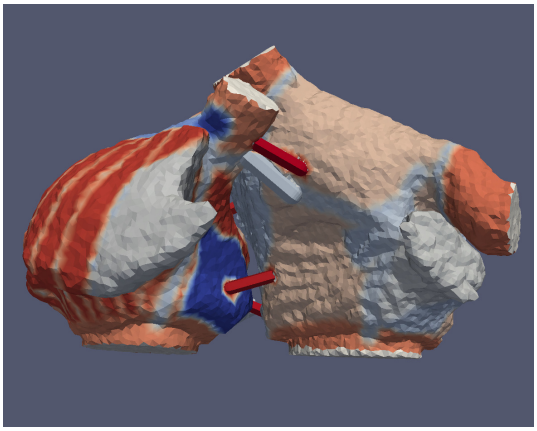

Figure 10.2: Atrial geometry used for the simulation of AFlut scenarios. The bi-atrial geometry is colored by the respective material classes. 6 inter-atrial bridges provide the electrical connection between both atria as defined by a rule-based algorithm [173, 189]. From [192].

Literature specifications for the conduction velocity (CV) of atrial myocardium cover a wide range of values. Studies of paced excitations with inter-beat-intervals down to 300 ms showed CVs of 770±200 mm/s with a range of 470 to 1070 mm/s in the LA [193]. Measurements during ongoing RA flutter demonstrated mean values of 610±210 mm/s [62]. Conduction velocities along the macroreentry circuit of ongoing right and left AFlut were assessed in a study focusing on the identification and the properties of the critical isthmus. For the isthmus itself, values of 270±130 mm/s were found, while the mean values of CV outside this critical area were found statistically significantly different with about 800 mm/s [188]. Contrastingly, in a study using noncontact mapping to evaluate RA flutter [61], CV of the CTI was found to be 740±360 mm/s (ranging from 310 to 1700 mm/s). For the smooth and trabeculated RA, values of 1160±480 and 1220±650 mm/s were found, respectively, with a range from 330 to 2090 mm/s. Besides certain anatomical areas like the cavo-tricuspid isthmus (CTI) [194], also regions surrounding previous ablation scar are known to reduce the local CV [8]. Using an electroanatomical mapping system (EAMS), CVs of less than

330 mm/s were observed [195]. In general, data about the CV of slow conducting zones in the clinical context are limited, since the presence of strongly fractionated and continuous electrograms hamper precise measurements.

For simulated scenarios, first the bi-atrial anatomy was initialized with a standardized myocardium (tissue class 32). Its CV was specified in the value range 450 to 800 mm/s, as indicated by previous clinical measurement studies. For the ease of parameterization of a specific flutter scenario, isotropic conduction was generally set to a fix value of 1 for the atrium.

Areas critical to the simulated flutter circuit were subsequently annotated on the atrial geometry. Their conduction properties were adjusted to permit the perpetuation of a stable tachycardia. Thus the CV values used for simulation were adapted in the range of 40 to 400 mm/s in order to achieve the required cycle length for a stable mechanism.

Lines of scar were manually inserted circumferentially around ipsilateral PVs to represent ablation scar from previous pulmonary vein isolation (PVI). For scar-related reentry mechanisms, gaps were included in the ablation line to resemble surviving atrial fibers, representing the critical isthmus of a flutter circuit [8].

In order to induce each respective mechanism, one instance of the ongoing tachycardia was resembled as starting point of the simulation. Already depolarized tissue was set to a refractory state, and a triggering stimulus was located in the desired direction of propagation. This approach bounded the excited wavefront and allowed for a directed excitation pattern. Simulations of reentrant mechanisms were performed for at least 5 s to ensure that the resulting pattern was stable and matched with the desired flutter mechanism.

User interface to parameterize flutter forms A graphical user interface (GUI) was designed in MATLAB to be able to parameterize and verify the simulated AFlut scenarios more conveniently. It was initially developed during a master thesis [192] and subsequently extended. A screenshot of the GUI can be seen in Figure 10.3. Different conduction properties can be assigned to atrial regions to resemble heterogeneities encountered during clinical mapping. The simulation can directly be started to assess the resulting propagation pattern.

Files used for simulation The FaMaS system was used to simulate cardiac excitation (compare Chapter 2.4.2). All required files were generated by the parameterization GUI. These comprised the file (*.vtk) containing the anatomy used for the simulation and including atrial regions with varying refractory and CV properties. Also the heterogeneity of fiber orientation, the position of scar, and the location of triggers and refractive tissue were provided. Second, the configuration file (*.famas) was written including all parameters to specify tissue properties and the simulation itself like duration, temporal resolution and parallelization.

An example for these data can be seen in Figure 10.4, which shows the state of the tissue vertices. Sinus node and ectopic trigger are indicated by stars, respectively, to clearly indicate

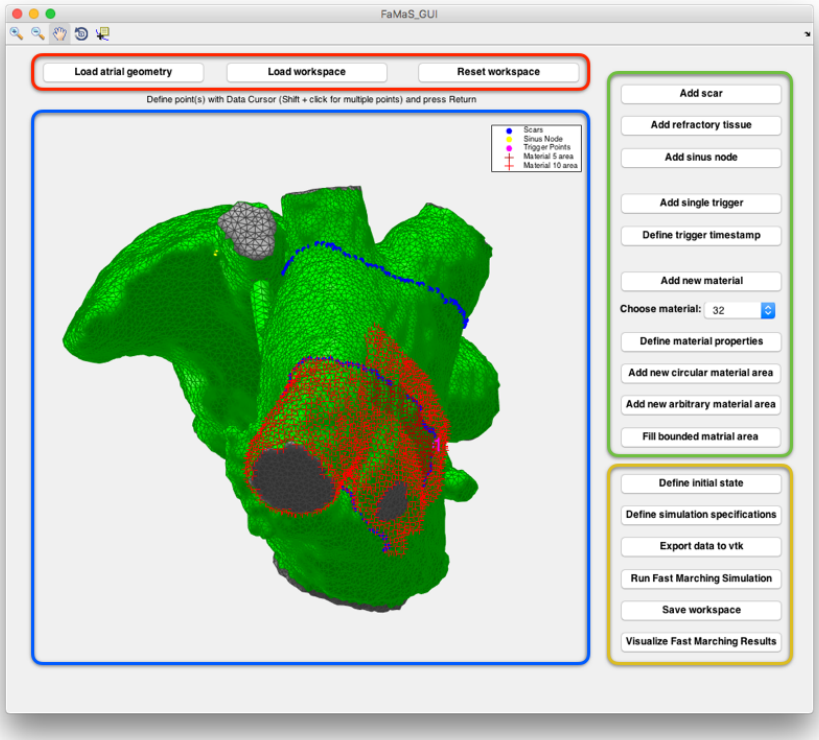

Figure 10.3: GUI to manually parameterize AFlut. It allowed to load existing data (red box), and the imported anatomy was visualized in the central part of the figure (blue box). While normal atrial tissue was indicated in green, areas with altered conduction properties were labeled in red. Sinus node, scar and additional triggers could be added and their tissue properties adjusted (green box). Buttons allowed to directly start the simulation (yellow box). The demonstrated data reflects the tissue properties used to simulate the scenario depicted in the introductory Figure 10.1.

their position on the mesh. Scar from a previous ablation was located around both ipsilateral PVs, showing gaps in the scar at the posterior LIPV. This was in agreement with the clinical documentation of the case (compare Figure 10.1 and source [186].)

The corresponding tissue classes are visualized in Figure 10.5. The areas close to the scar-related reentry path were adjusted to have reduced CV and refractory period (see Table 10.1). This allowed to induce a stable AFlut during the vulnerable phase of NSR with only one ectopic trigger in the LIPV region.

Tissue class	CV [mm/s]	Refractory period [ms]
32	700	200
10	300	170
5	150	100

Table 10.1: Parameters of the tissue used to simulate scenario 20. The myocardial CV was set to 700 mm/s. The regions perpetuating the micro-reentrant circuit showed reduced CV of 300 mm/s and 150 mm/s, respectively. The reduced refractory period within the PV area allowed to initiate the flutter with just one ectopic beat originating in the PV ostial region.

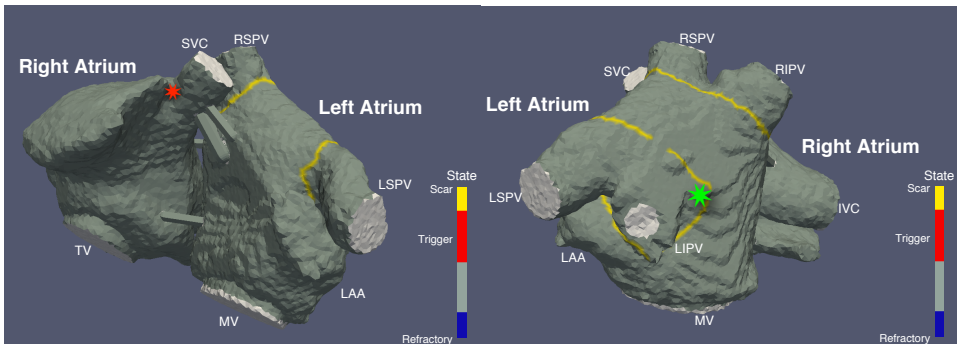

(a) Anterior view. **(b)** Posterior view.

Figure 10.4: Initial states of the personalized tissue. Scar was introduced to resemble prior PV isolation. Refractory tissue could be included to direct stimulated excitations. Stars indicate the positions of the sinus node (red) and a pulmonary vein trigger (green). From [192].

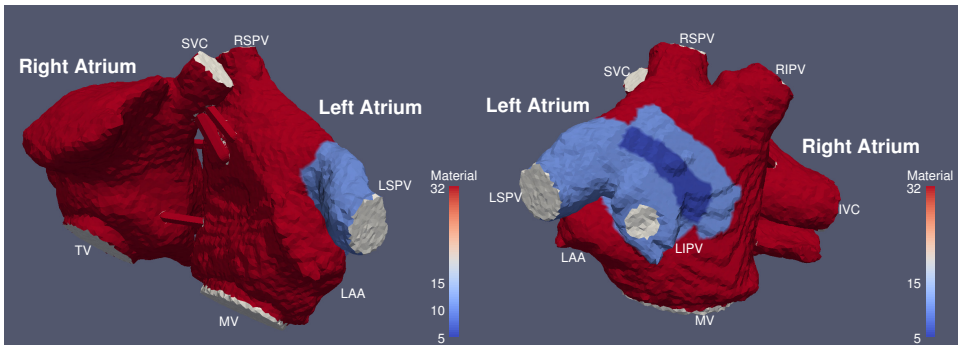

(a) Anterior view. **(b)** Posterior view.

Figure 10.5: Tissue classes used to personalize conduction parameters. The different types of myocardium were defined to assign varying electrophysiological properties like CV and refractory period to specific atrial regions. From [192].

Implemented flutter forms With respect to clinical occurrence after ablation for AFib, different studies found consistent results for different types of flutter mechanisms. In a study considering 17 patients, the most common form involved the mitral isthmus (33%), with roof-dependent flutter in 27% and focal origin in 22% of cases. Of note, termination of the tachycardias was achieved in 96% [64]. In a study focusing on discrimination between truly focal and micro reentrant sources, 128 patients were analyzed. While macroreentry was found in 109 mapped tachycardias, localized microreentry was found in 95, with truly focal activity present in only 34 cases [65]. Note that these numbers already indicate that several tachycardias frequently occur in one single patient, as the flutter circuit is continuously modified during ablation. Depending on the population, about 3.4 ± 2.4 tachycardias were observed per patient [186]. In a review article about AFlut occurrence after AFib ablation, macro reentrant circuits were found most often around the MV (28%), and roof-dependent in 12% [66].

Besides various information about the occurrence frequency of flutter mechanisms, also common values for BCL can be found in literature (compare Table 10.2). While mean values range from 228 to 325 ms within these studies, individual cycles were found with durations as short as 175 ms.

Study	Characteristics	Addressed	BCL [ms]
Ammar et al.	77 patients	Perimitral	271±65
(2015) [187]	(66±9, 56 men)		
De Ponti et al.	65 patients	Macro reentrant	308±68 (200-515)
(2007) [188]	(56.7±16.7, 41 men)		
Deisenhofer et al.	16 patients	LA flutter after PVI	264±41 (180-330)
(2006) [186]	(57±7.7, 11 men)		
Itoh et al.	26 patients	RA flutter	246 (201-376)
(2013) [62]	(64±14, 18 men)		
Jais et al.	22 patients	LA flutter	303±78 (190-450)
(2000) [63]	(60±14, 15 men)		
Jais et al.	14 patients	Source anterior LA	325±125 (220-550)
(2006) [195]	(65±13, 3 men)		
Jais et al.	128 patients	AFlut after AFib	34 focal: 341±115
(2009) [65]	(58±11, 109 men)		95 micro: 278±85
			109 macro: 269±67
Ndrepepa et al.	12 patients	RA flutter ccw	228±27 (182-260)
(2001) [185]	(61±13, 10 men)	RA flutter cw	240±32 (202-278)
Mesas et al.	13 patients	AFlut after PVI	3 focal: 266±35.9
(2004) [196]	(57.4±8.9, 8 men)		11 macro: 275±75
Patel et al.	17 patients	AFlut after AFib	288±77 (175-550)
(2008) [64]	(62±10, 14 men)		
Schilling et al.	13 patients	RA Flutter	241±35
(2001) [61]	(mean 60, 11 men)		

Table 10.2: Studies providing information about the occurrence of flutter mechanisms and their respective cycle lengths. Patient characteristics are indicated as number of patients, mean age in years and number of male patients.

Data from the scar-related reentry at the LPV was already presented in the previous figures of this chapter. A counter-clockwise perimitral circuit is demonstrated as a second example in Figure 10.6.

The final database included a total of 20 scenarios of AFlut and is depicted in Table 10.3. It included clockwise and counter-clockwise macro reentries around tricuspid valve (TV) and mitral valve (MV), macro reentries around the PVs, focal sources originating close to the PVs, and also micro reentries located at revitalized ablation lines or slow conducting tissue. These scenarios were subsequently used to verify diagnostic algorithms as outlined in Chapter 11.2. Six simulations are based on clinically documented cases and were initially implemented within the scope of a student project [192]. They are summarized in the following listing, together with the respective BCL (given by direct clinical documentation and resulting simulation):

- *sc12*: Ccw macroreentry around MV [186] (BCL 180 and 177 ms)
- *sc20*: Scar-related reentry at left pulmonary vein (LPV) [186]: (BCL 190 and 175 ms)
- *sc23*: Scar-related reentry at right pulmonary vein (RPV) [196]: (BCL 235 and 224 ms)

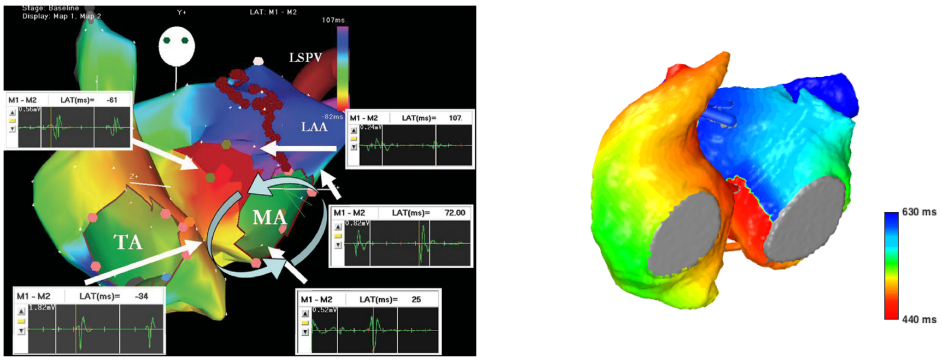

(a) Result of clinical mapping. **(b)** Simulation outcome.

Figure 10.6: Comparison of clinical and simulated perimitral flutter. Information from a clinically documented tachycardia (a) was used to personalize the model and simulate cardiac excitation during the arrhythmia (b). (a) reprinted from [186] with permission from the publisher.

- *sc40*: Focal Source at anterior right superior pulmonary vein (RSPV) [196]: (BCL 307 and 295 ms)
- *sc50*: Microreentry at anterior MV annulus [195]: (BCL 286 and 172 ms)
- *sc51*: Microreentry at anterior left atrial appendage (LAA) [186]: (BCL 280 and 270 ms)

Mechanism	Atrium	Position	Direction	ID	BCL [ms]
Macroreentry	RA	Tricuspid Valve	ccw	sc10	205
Macroreentry	RA	Tricuspid Valve	cw	sc11	184
Macroreentry	LA	Mitral Valve	ccw	sc12	177
Macroreentry	LA	Mitral Valve	cw	sc13	180
Scar-related Reentry	LA	LPV	post	sc20	172
Scar-related Reentry	LA	LPV	ant	sc21	226
Scar-related Reentry	LA	RPV	post	sc22	233
Scar-related Reentry	LA	RPV	ant	sc23	224
Figure-8 Macroreentry	LA	Both PVs	ant	sc30	228
Figure-8 Macroreentry	LA	Both PVs	post	sc31	227
Figure-8 Macroreentry	LA	RPVs	ant	sc32	228
Focal Source	LA	RSPV anterior		sc40	285
Focal Source	LA	RSPV posterior		sc41	246
Focal Source	LA	LSPV anterior		sc42	297
Focal Source	LA	LSPV posterior		sc43	296
Microreentry	LA	ant MV annulus		sc50	172
Microreentry	LA	ant LAA		sc51	227
Microreentry	LA	ant RSPV		sc52	186
Figure-8 Microreentry	LA	ant		sc53	159
Microreentry	LA	post wall		sc54	186

Table 10.3: Database of manually parameterized AFlut forms. 20 different scenarios were parameterized to cover a variety of clinically relevant forms. These included typical RA flutter as well as atypical LA forms like macroreentry, focal soures and scar-related micro reentries. Directions of macro reentries around valves are indicated by cw (clockwise) and ccw (counter-clockwise), roof dependent forms by ant (roof excited from posterior to anterior), and post (anterior to posterior), and scar related forms by the corresponding direction of excitation outside the PV region.

10.2 Personalization of a Computer Model

The database of flutter scenarios can be very well used to develop and benchmark diagnostic algorithms. In order to optimize the treatment of individual patients using computational models, however, virtualization of the patient-specific flutter circuit is required. Due to its high simulation speed, the FaMaS is a valuable tool to evaluate for example the effect of different lesion patterns on termination and vulnerability to recurrence before ablation is performed.

In the quest to find an optimal treatment strategy for ablation of AFib, computational models have been widely used to assess the effect of different lesion patterns [197–200] or signal guided ablation strategies [200, 201]. Recent work has demonstrated the personalization of models based on late-gadolinium enhancement (LGE)-magnetic resonance imaging (MRI). AFlut was subsequently introduced by pacing, and the resulting flutter cycle assessed for ablation planning [202]. No electrical information from the clinical mapping, however, was incorporated in this method. All of these approaches have in common, however, that detailed biophysical cellular models were applied to resemble the complex excitation dynamics during AFib. Frequently, ion-based cellular models like Luo-Rudy [197–199] or Courtemanche-Ramirez-Natell [200, 201] were used, always with changes to ion-channel conductivity representing the remodelled state with shortened action potential (AP) duration. With respect to their applicability in the clinical environment, computational time is in the order of hours, and thus a significant limiting factor.

An approach to exploit the rapid computational time of the FaMaS in order to generate a personalized ventricular model based on electroanatomical mapping data was described in literature [180]. Non-contact mapping using the EnSite balloon catheter was applied to determine the local activation times on a ventricular geometry. The apparent CV of the model was subsequently modified in order to approximate the clinical measurement. Therefore, the global conductivity was adapted first, and then an iterative strategy was proposed to subdivide the ventricular mesh into different zones and process these one by one. In short, the CVs were adapted or the zones subdivided for improved approximation, starting with zones showing largest error in activation times and being activated first. The optimization of CV adaption was terminated when the number of zones reached 64 or the simulation converged. After application to simulated and clinical data, a correlation could be demonstrated between regions identified as slow conducting after CV adaption and scar as shown on LGE-MRI images. This method was extended to a statistical approach which could also incorporate potential measurement errors using Bayesian inference [203]. Parameterization of a patient-specific model using an Eikonal-approach was also suggested on the ventricular level to determine vulnerability to tachycardia and fibrillation [204], as well as to assess the effects of pacing during resynchronization therapy [205].

Part of this thesis was the development of a workflow that can be used to virtualize clinical and thus patient-specific cases of AFlut. In a first step, intracardiac electrograms were evaluated in order to determine characteristics which indicate the presence of scar or

conduction block. Based on this information and visual assessment, the corresponding model was set up and combined with information about the excitation pattern. Last, an iterative strategy was used to adapt the region specific CV. The first evaluation of electrogram (EGM) characteristics and the implementation of the CV adaption strategy into the FaMaS was done within a student project [206] and published subsequently [184].

10.2.1 Generation of Initial Models

Before the conduction properties could be adapted, an initial model had to be set up. This model included the atrial anatomy itself, the location of scarring, and the position at which the excitation for the evaluated cycle began. Also the position of electrodes was included.

Clinical data Two sets of clinical data were available for initial algorithm development. Both were acquired using the EAMS EnSite Velocity™ at Städtisches Klinikum Karlsruhe and exported for further analysis. Patient 1 was male, 54 years old, and presented with persistent atypical roof-dependent LA flutter around the right PVs (BCL=253 ms). He was pre-ablated several times due to persistent AFib and AFlut. Prior ablation also included PVI and a roof line. The critical isthmus was determined to be a gap on the left side of the roof line (compare Figure 10.7). Ablation at this spot confirmed its role in the presenting circuit and converted the tachycardia into a second form.

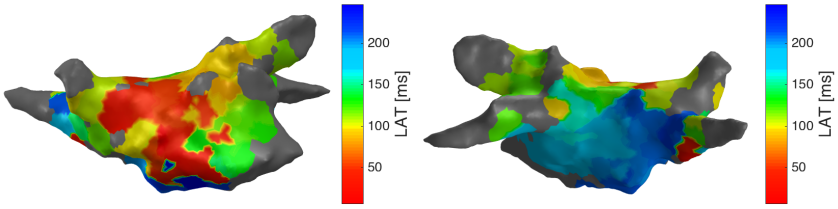

(a) Anterior view. **(b)** Posterior view.

Figure 10.7: Clinical LAT map of patient 1. Excitation passed through an isthmus on the lateral side of a previously ablated roof line. Depolarization subsequently crossed the posterior wall and entered the anterior wall from the lower septal region.

Patient 2 (male, 56 years) was initially treated for persistent AFib. Substrate modification was performed (CFAE ablation) after successful isolation of the PVs. During defractionation, AFib converted into counter-clockwise perimitral AFlut, diagnosed by sequential LAT mapping with a 10 pole single loop spiral catheter. The LAT map showed an anterior line of block, causing a delayed activation of the superior anterior wall when compared to its inferior aspect (compare Figure 10.8).

After successful implementation and benchmarking, the algorithm was also applied to a third patient.

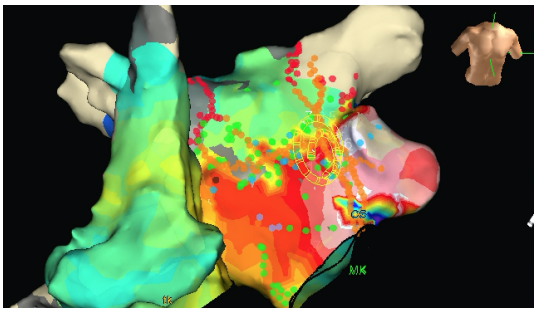

Figure 10.8: Clinical LAT map of patient 2. A line of block can be seen on anterior wall, indicated by the large delay of activation inferior and superior of the line.

Visual assessment of excitation patterns Based on visual evaluation of LAT maps and activity movies (compare Section 9), the distribution of conduction block was assessed for each patient. This conduction block was assumed to represent scar, since there was no second paced rhythm available to differentiate between functional and persistent blocks [207]. The presence of ablation scar at PV ostia was hereby indicated by electrical isolation between the veins and the LA (see the left superior pulmonary vein (LSPV) in Figure 10.8 for example). Scarring on the atrial myocardium was assumed if the LAT indicated that conduction did not propagate on a direct path between atrial regions but instead traveled around an imaginary obstacle (compare the anterior wall in Figure 10.8).

Since AFlut is characterized by a continuous excitation process, the beginning of a cycle can be set arbitrarily. In the clinical environment, however, it is common to select the window of interest for LAT analysis in such a way, that the earliest excitation within the cycle represents the exit site of the isthmus. As the color red is assigned to the earliest LAT in standard clinical color maps, moving the time window and looking for a red spot helps to easily identify the isthmus as potential ablation target. In order to simulate the excitation pattern using FaMaS, a trigger was required which initiated the spread of depolarization. The position of this stimulus was selected to match the location of the isthmus, so that the size of the trigger could be kept minimal. As the simulated stimulus itself caused a centrifugal spread of excitation, the tissue in reverse direction was additionally set to a refractory i.e. unexciteable state. This channelized the excitation process into the desired direction. The duration of this initial refractory period was chosen sufficiently large to stop the excitation in reverse direction, but short enough not to interfere with the ongoing tachycardia after the first complete cycle. The corresponding setup for patient 1 is depicted in Figure 10.9. Besides the scar (*Dead nodes*), the images also show both the *Trigger node* and the *Initial refractory nodes*.

The annotation also included regions in which a collision of wavefronts was observed (posterior wall of patient 2) or in which the propagation passed through a narrow isthmus (roof of patient 1). Subsequently, all recording positions which were close to the annotated regions were compiled to form a database of signals indicating

- normal conduction
- scar

Figure 10.9: LA roof of patient 1. The atrial anatomy is colored by the status of the nodes of the surface mesh. Scar is shown in black while normal vertices are colored gray. The trigger (red) was located at the isthmus, being enclosed by scar (isolation of left PVs and roof line) and refractory tissue in reverse direction. This is expected to cause a depolarization pattern which excites the posterior wall in inferior direction. Modified from [206].

- wavefront collision
- critical isthmus.

The spatial distribution on the atrial geometries is visualized in Figure 10.10. The scar is indicated by black dots, and measurement positions surrounding it were termed *Scar electrodes* (red crosses). The threshold for the maximum distance to the scar was set to 10 mm. After *Isthmus electrodes* and *Collision electrodes* were annotated (blue circles), respectively, all remaining electrodes were labeled *Normal* (green dots).

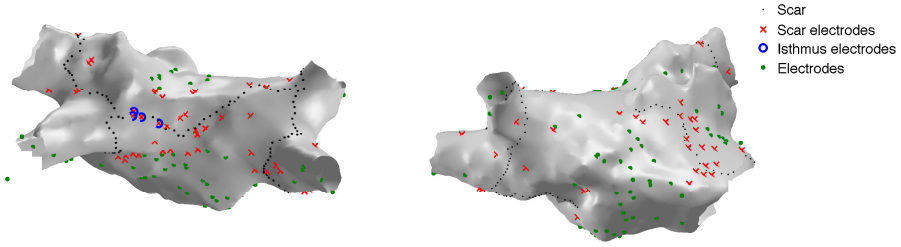

(a) Patient 1 PA view. **(b)** Patient 1 RAO view.

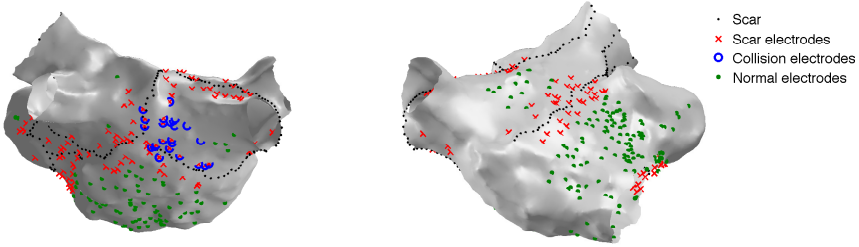

(c) Patient 2 PA view. **(d)** Patient 2 RAO view.

Figure 10.10: Classification of electrodes by recorded phenomena. After manual annotation of scar, isthums and collision, the adjacent electrodes up to a distance of 10 mm were assigned the respective label. *PA=postero-anterior; RAO=right anterior oblique.* From [206].

Preprocessing of excitation maps The cardiac excitation pattern was indicated by the clinical LAT map. Although this map provides information for each vertex of the anatomy, information was actually only available at the electrode locations and subsequently interpolated on the atrial surface. In order to generate an excitation which was consistent with the annotated position of scar, the interpolation step was repeated on the anatomy that actually included the conduction block. Therefore the Laplacian interpolation scheme (see Chapter 8.4) was used to provide a smooth and continuous excitation pattern.

Visual inspection of the results, however, revealed inconsistencies in the LAT map. Since the excitation is governed by a causal process, these inconsistencies were most likely due to incorrect annotations of the EGM, inaccurate synchronization with the reference channel or erroneous localization of the mapping catheter. Due to the limited number of mapping points and thus sparse information about the excitation process, there was no redundancy to clarify the inconsistent activation pattern. Therefore, the annotations were corrected manually to assure the causality of the depolarization pattern. Thereby neither the dominant flutter mechanism nor its cycle length were altered.

An example for this process can be seen in Figure 10.11, with the re-interpolated map on the left and the corrected map on the right. Note the correction of inconsistencies like the orange spot prior to the isthmus. After the causality of the process was verified, the LAT information for each electrode was exported together with the state information since this is import for the FaMaS algorithm

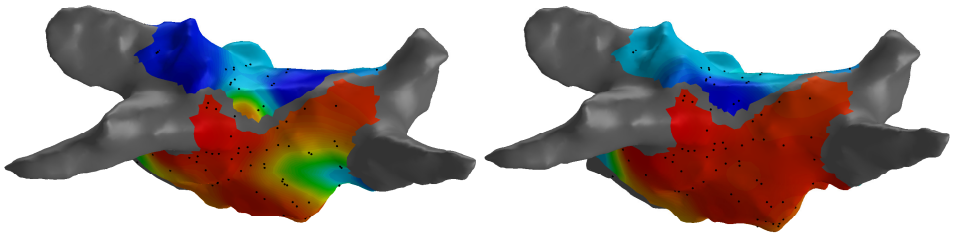

(a) Re-interpolated map including scar. **(b)** Interpolation ensuring causality.

Figure 10.11: Preprocessing steps of LAT maps for CV estimation. The original clinical map can be seen in Figure 10.7. It was interpolated by the Laplacian interpolation method considering the location of scar (a). Subsequently, inhomogeneities in the excitation pattern were adapted to ensure causality of the depolariztion process. From [206].

Initial assessment of electrogram characteristics The morphology of EGMs is known to reflect certain properties of the underlying conduction pattern. Most importantly, signals containing short activation complexes of large amplitude indicate the undisturbed and rapid propagation of a depolarization wavefront over vital tissue, while signals with prolonged and fractionated activation complexes with low amplitude indicate the presence of fibrotic critical substrate [62, 195]. Moreover, double potentials in a signal (e.g. two activation complexes

within one flutter cycle) indicate the presence of conduction block [207]. Sophisticated approaches to determine and utilize corresponding measures from intracardiac electrograms (IEGMs) will be presented in Chapter 11.

As first attempt to assess the possibility to differentiate between signals recorded at vital tissue, at scar or at the isthmus / collision sites, the annotations shown in Figure 10.10 were used. The respective signals were compiled into a database of electrograms, of which subsequently measures like peak-to-peak amplitude, and skewness and kurtosis of the amplitude histogram were evaluated [208]. Contrasting to expected outcome, only minor differences were observed between the different groups of electrograms. Although the signals recorded close to scar were expected to have strongly diminished amplitude, their values also covered the range expected for vital tissue. Assessment was also done for a reduced distance threshold of 5 mm, but did not lead to different results.

Several possible explanations can be found for this outcome. First, the position of the acquired points may be compromised by inaccuracies of the mapping system. If an atrial region was mapped at the beginning of the procedure and then a slightly distant point was re-mapped at some later point in time, a lack of long term stability may have caused these to be projected in very close locations of the atrial shell. Second, only bipolar signals were considered, being actually the difference between two signals. If one measuring electrode is located on the scar, and the other one is not, this may also cause a large bipolar amplitude. Third, both patients had a history of AFib, which may have caused the atria to be fibrotic to some extend. This would reduce the amplitude of signals measured in locations remote from scar to be reduced as well. Forth, the map was generated with a rather limited resolution and using 1 mm electrodes. Usage of higher density of points and a smaller electrode size (e.g. Orion catheter with Rhythmia mapping system) may allow to more precisely evaluate the substrate.

In conclusion, the information gained from individual electrograms was not meaningful enough at this stage to automatically and reliably annotate scar or the isthmus on the atrial geometry. Therefore the visual assessment of the spatio-temporal excitation process as outlined above was kept as expert-guided part of the workflow.

10.2.2 Personalization of Conduction Properties

After the patient specific geometry was prepared and the LATs were preprocessed, the local CV could be estimated. Therefore an iterative algorithm was developed and implemented. This algorithm first determined a global CV which matched the clinical BCL. Subsequently, local homogeneities were included to better approximate the LAT of each electrode individually. Therefore the atrial surface mesh was subdivided into regions surrounding each measurement position. A simulated dataset with known properties was generated to verify correct functionality during algorithm development.

Inspired by a previously published algorithm [180], an iterative procedure was chosen to estimate local heterogeneities of conduction. Since this technique was originally designed to

parameterize a ventricular model based on non-contact mapping data during NSR or pacing, several modifications were required during the initial design phase.

These changes affected some fundamental steps, as AFlut represents a continuous propagation pattern for which the stability over time without repetitive stimulation has to be achieved. In addition, the contact mapping provided detailed LAT information for several hundred measurement positions on the atrial surface. These were selected to represent the centers of zonal division, meaning that the conduction properties around each measurement point could be adjusted by the algorithm.

With respect to estimating the regional CVs, first one global CV was determined which matched to the clinically observed cycle length $BCL_{clinical}$. Therefore the simulation was started with an initial guess of CV_k (e.g. 900 mm/s for iteration step $k = 0$). For each surface vertex which was part of the flutter circuit and measured by an electrode, the time between its third and fourth excitation was computed to avoid initial delays due to the refractory tissue. The mean of all these values was considered the initial $BCL_{FaMaS,k}$ and compared to $BCL_{clinical}$. If the absolute value of the difference between both values was below a certain threshold (here 1 ms), CV_k was set as global CV. Otherwise, the CV for the next iteration CV_{k+1} was adapted by the proportion between both BCLs as given by

$$CV_{k+1} = CV_k \cdot \frac{BCL_{FaMaS,k}}{BCL_{clinical}}, \tag{10.1}$$

resulting in a one step approach to estimate the global CV.

After the initial value of the global CV was set, adjustment of the local CV began. Therefore the atrial surface was subdivided into areas around each electrode as given by a Voronoi diagram. These areas were combined to zones for joint analysis. The zones were processed iteratively according to their clinical activation time. The causality as verified previously was an important aspect at this point. If the difference of activation times as given clinically ($LAT_{clinical}$) and computed by the FaMaS (LAT_{FaMaS}) exceeded a user defined threshold thr_{LAT}, the CV of all vertices of the current zone was decreased or increased by 50 %. Zones were split into subzones if required for more detailed adaption. When one zone was successfully adapted, the next zone was processed.

In order to avoid extreme changes in conduction along the excitation pattern, thresholds were introduced for a maximal (thr_{maxCV}) and minimal (thr_{minCV}) CV, as well as for a maximum difference between adjacent regions ($thr_{interCV}$). Discarding these thresholds led to fibrillation while the CV was adapted. During benchmarking of the algorithm, a variety of combinations was evaluated on both clinical cases (see Table 10.4). Statistical analysis of the analyzed cases revealed, however, that the computational time and accuracy of the outcome hardly depended on the exact setting of these parameters. Therefore the most loose parameter combination was chosen for future analysis.

This complete approximation process was implemented as alternative computational strategy into the FaMaS and could be enabled by specific commands in the FaMaS configuration files. The resulting output included information about the anatomical location of regions with varying CV and a list containing their individual conduction properties. This allowed to

Threshold parameter				
Minimal CV (mm/s)	thr_{minCV}	10	50	100
Maximal CV (mm/s)	thr_{maxCV}	1000	1500	2000
Maximal CV difference (mm/s)	$thr_{interCV}$	200	500	800
Acceptable error (ms)	thr_{LAT}	1	5	

Table 10.4: Parameter thresholds for which the CV estimation was benchmarked.

directly call the FaMaS again to execute the parameterized simulation. As a consequence, this simulation could in turn be used to test ablation patterns.

10.2.3 Application to Clinical Data

After successful development of the procedure to virtualize clinical flutter forms using the data from patients 1 and 2, it was applied to a set of high-density mapping data recorded by the Rhythmia EAMS.

Clinical mapping data A 70 year old female patient was mapped during routine catheter ablation of persistent LA AFlut using the Rhythmia EAMS at Städtisches Klinikum Karlsruhe. During mapping of the initial form (counter-clockwise perimitral flutter, BCL 330 ms), the tachycardia converted to a second form (roof dependent macroreentry, BCL 430 ms). LAT maps were acquired for both mechanisms and showed concordant information about the underlying substrate. The roof-dependent form was selected for virtualization and processed accordingly.

Figure 10.12 represents a screenshot of the mapping system. In the selected instance, the depolarization wavefront just exits a region of slow conduction towards the roof. The slow conducting region was located in the center of the anterior wall. Due to the large difference in activation time compared to its surrounding regions, it can be clearly identified by its purple color in the LAT map. Of note, this region was also observed during the index tachycardia. Both the posterior wall and the septum were activated by broad wavefronts. The lateral part of the anterior wall was activated by a depolarization wave coming from the posterior wall, traveling around the left PVs, and passing the LAA. This wavefront excited the zone of slow conduction after one BCL again and sustained the tachycardia. Both left and right PVs were isolated by prior ablation, indicated by the grey coloring of low voltage. A total of over 12,000 EGMs was acquired in about 22 min to construct the electrical propagation pattern for this map.

Generation of the initial model An initial model was generated from the imported clinical data and provided the basis for personalization of conduction properties and thus virtualization of the presented arrhythmia. Scar was added to the anatomy to reproduce PV isolation and inserted between regions that did not show an ongoing propagation in the LAT map. To allow for precise annotation of these conduction blocks, the LAT map was plotted as background for the manipulated mesh.

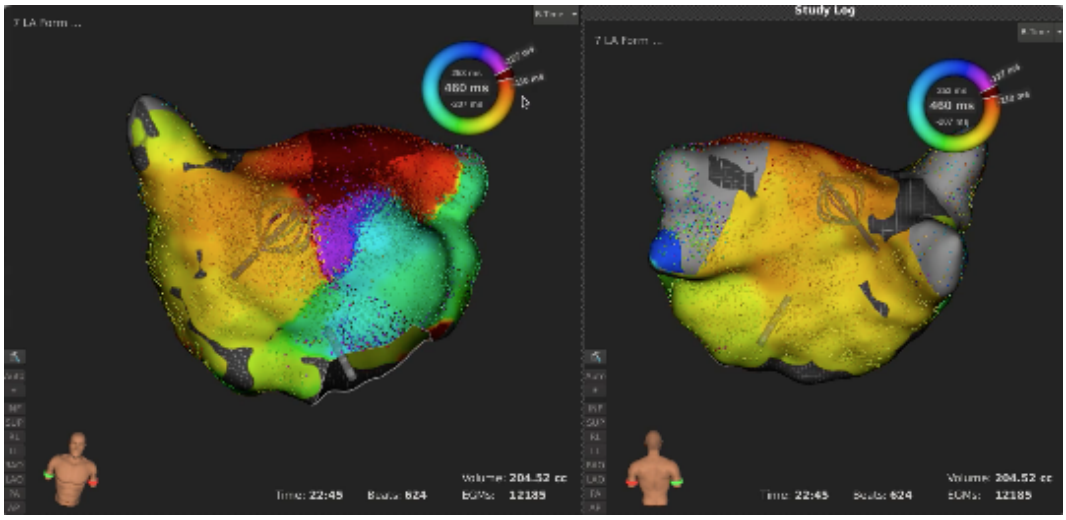

Figure 10.12: Clinical LAT map of an example case.

The exit point of the zone of slow conduction was defined as trigger and surrounded by refractory tissue, ensuring propagation towards the roof. Initial global CV was set to 600 mm/s and $BCL_{clinical}$ to 436 ms. Limits for velocity estimation were chosen as previously benchmarked: $thr_{minCV} = 10\,mm/s$, $thr_{maxCV} = 2000\,mm/s$, $thr_{interCV} = 800\,mm/s$ and $thr_{LAT} = 5\,ms$.

In contrast to the previously available mapping data form EnSite Velocity, no raw electrical information was contained in the maps exported from the Rhythmia EAMS. As neither the measurement points nor the acquired EGMs were available at that time, 500 randomly selected vertices of the excitable endocardium were used as virtual electrodes. Their LATs were extracted from the LAT map. Also in this case, some electrodes were manually removed after visual inspection as their LATs were contradicting to other neighboring values and violated causality.

Result of conduction velocity estimation Simulation using the initial $CV_0 = 900\,mm/s$ resulted in an initial BCL of 291 ms. Therefore the global CV was rescaled using equation 10.1 to 400 mm/s.

In the second step the local CVs were computed. This process took below 20 s, and the resulting CVs are plotted in Figure 10.13. Low values for the estimated CV could be observed at the central anterior wall, which was in agreement with the zone of slow conduction observed during clinical mapping. Although the mean global CV was initially estimated to 400 mm/s, nearly the complete posterior wall exhibited CVs of 800 mm/s and higher.

Subsequently the flutter was initialized using the personalized conduction properties. The depolarization wavefront followed a stable pattern that matched to the clinically observed tachycardia mechanism in path and BCL. LAT maps of both the clinical mapping and the simulated flutter are plotted in Figure 10.14. For the simulated arrhythmia in (b), one cycle

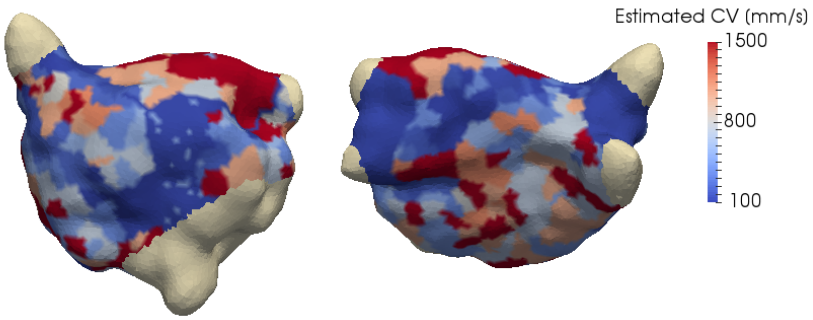

Figure 10.13: Estimated CV map of the example case. A zone of slow conduction can be seen on the central anterior wall, being in agreement with clinical observations. Conduction is also reduced at the lateral roof PV ostia, close to the PV isolation line. While the global CV estimate was 400 mm/s, local values for the CV in most regions were estimated to exceed 800 mm/s.

of the continuous simulation was plotted with the beginning of the cycle set to the exit point. No depolarization was simulated for the electrically isolated atrial regions located at the PVs and the anterior wall. Visual comparison of both the clinical map and the simulation result demonstrated certain analogies: First, the roof was depolarized rapidly once the activation passed the zone of slow conduction. Second, septum and posterior wall were activated nearly simultaneously during the orange phase of the cycle by two different wavefronts. Third, a first conduction delay could be observed at the inferior anterior wall close to the MV annulus, which was present in both maps (green). Concluding, a strong delay in activation could be observed around by crowding of the isochrones around the zone of slow conduction in the central anterior wall. Based on these observations, it was concluded that the virtual flutter qualitatively resembled its clinical prototype.

Limitations Although the CV estimation was performed automatically in a short amount of time, manual preprocessing was required to generate the initial model. This included the insertion of scar, which was visually assessed from the propagation map and by considering the voltage map if available. While placement of scar at previous ablation lines can be justified, conduction block in atrial regions without prior ablation may also be functional. Currently it is not possible to differentiate between these mechanisms without interrupting the ongoing tachycardia.

Also the anisotropy cannot be estimated based on one single flutter form. Thus it could only be deducted model-based [189]. If paced data would be available, this may allow to both delineate functional and anatomical scar, and allow to infer information about tissue anisotropy.

It has to be noted that the algorithm does require the depolarization process to comply with causality. Clinical LAT maps in general describe the excitation pattern very well on a global scale. Within small regions, however, changes of the BCL during mapping (compare Chapter 7.3) may cause inconsistencies in the temporal sequence of excitation. These had to be corrected for a reasonable CV estimate.

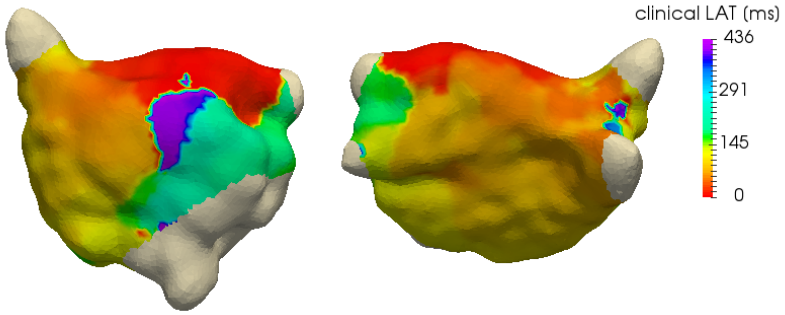

(a) Clinically presenting tachycardia (compare Figure 10.12).

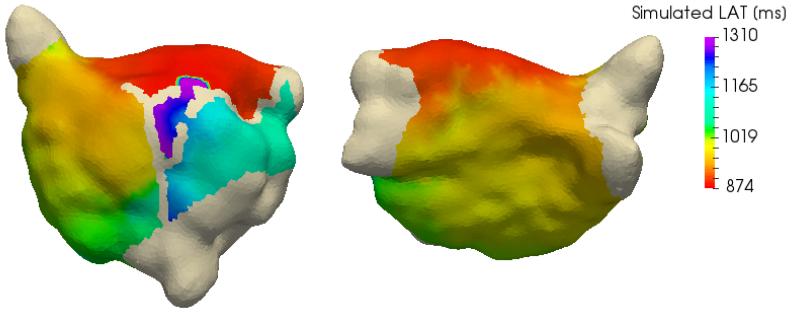

(b) Simulated flutter circuit (one cycle chosen for visualization).

Figure 10.14: Propagation pattern of the virtualized flutter. LAT maps of the original clinical data (a) and one cycle of the simulated tachycardia (b) are shown. Both exhibit a high qualitative similarity and presented equal BCL of 436 ms.

Conclusion and outlook As demonstrated in this example, the tachycardia induced in the personalized model closely resembled its clinical original form. Therefore the flutter was considered to be successfully *virtualized*. On the one hand, this approach allows to extend the database listed in table 10.3 by real clinical cases. Thus diagnostic algorithms can be applied to more data. One the other hand, virtualization is the fundamental step to admit testing sets of ablation lesions in the computational model before applying these to the patient. It will be able to identify those which terminate the arrhythmia. Due to the fast processing speed of the FaMaS, this approach can be well applied in the clinical workflow.

However, up to now preprocessing steps are required which are time consuming and rely on visual inspection. From a theoretical point of view, a combination of LAT and voltage maps should contain all data which are required to automatically place scar, trigger and refractory tissue on the anatomy. An initial attempt to evaluate these characteristics based on EGM characteristics was conducted during this research project but did not provide convincing results. However, the density of acquired EGMs, their localization precision and signal quality was improved by the use of a novel mapping system. Thus it is envisaged to newly execute a corresponding analysis, aiming for a complete automation of the workflow.

Not only the termination is of interest when effects of different ablation patterns are evaluated. In addition, both reinducibility and resulting ejection fraction are of clinical relevance. Two steps have to be accomplished before these goals can be reached. First information about anisotropy should be included in the mode. This could be achieved by applying a rule-based approach as demonstrated earlier [189]. It could also be assessed in clinical data, if information about depolarization from different directions was available for each endocardial region. This, however, would require additional high-density maps during sinus rhythm or paced excitations.

As ejection fraction is a mechanical property, the FaMaS is not an appropriate tool to assess this parameter. However, once the model is parameterized, it could be transferred into a more complex computational environment that could estimate the mechanical properties like force and pumping function during sinus rhythm [105, 205].

CHAPTER 11

Algorithms to Support Diagnosis of Atrial Flutter

Atrial flutter can frequently be observed as either index arrhythmia or as organized tachycardia following the ablation of atrial fibrillation (AFib). In the latter case, atrial flutter (AFlut) often is resistant to pharmacological treatment and cardioversion, but as well seen as intermediate step before SR ist achieved [64]. In both cases, however, numerous studies have already demonstrated consistent results with respect to the underlying mechanisms and their anatomical locations [8, 209]. This understanding and the resulting treatment decisions have led to success rates in the order of 80 to 100 % when catheter ablation is applied to terminate AFlut. The understanding of the patient-specific variant, however, is the central prerequisite of successful ablation.

Currently, this diagnostic process is primarily based on the experience of the physician. Although comprehensive electrogram data can be acquired from the complete atrium using an electroanatomical mapping system (EAMS) with multi-polar mapping catheters ([75]), there are currently only two automatic analysis techniques. First, the maximum bipolar voltage of electrograms (EGMs) is evaluated within one cycle. Regions which exhibit voltage values below a certain threshold are considered scar, potentially being part of an anatomical obstacle. Typical threshold values for atrial myocardium are in the range of 0.5 mV for zones of low voltage and 0.05 mV for dense scar [188, 210]. Second, the local activation time (LAT) is annotated in each signal. After all signals are synchronized (compare section 8.2), the LAT reflects the global excitation pattern. This static image allows to gain a first impression of the course of atrial activation [64].

However, a number of additional features are applied by physicians in the diagnostic process and typically evaluated manually by visual inspection. Considering the analysis of individual signals, these comprise the presence of double potentials, and evaluation of fractionation and duration of activity in each signal [207]. From a multichannel point of view, additional features can be determined, like the mid-diastolic activity, area-based cycle length coverage and the critical isthmus [64]. Goal of this research was to develop algorithms

which can help to assess these parameters automatically in order to support the physician in understanding the flutter circuit for successful ablation.

Clinical mapping strategies Several mapping strategies have been suggested to systematically determine the presenting form of AFlut. One deductive mapping scheme applicable to left atrium (LA) flutter incorporates following steps [65]:

1. *Assess cycle length regularity* Macro reentrant tachycardias are known to exhibit a high stability in basic cycle length (BCL), while focal sources may show strong variations in cycle length (see also section 7). Thus it was suggested to first evaluate the BCL based e.g. on coronary sinus (CS) recordings. If BCL deviations of more than 15% were observed, the mapping strategy was directly adapted to search for a focal source as in step three. Otherwise mapping of the macroreentry was attempted.
2. *Search for macroreentry* Two macro reentrant forms of flutter are dominantly observed in the LA: Perimitral and roof-dependent. By recording points sequentially around the mitral valve, the perimitral form could be confirmed or rejected. Acquiring points from the posterior wall over the roof to the anterior wall allowed to assess the presence of a roof-dependent form. If either one was confirmed, linear lesions were drawn at the mitral isthmus line (mitral valve (MV) to left inferior pulmonary vein (LIPV)) or the roof (left superior pulmonary vein (LSPV) to right superior pulmonary vein (RSPV)), respectively.
3. *Search for origin of centrifugal activation* If none of these forms was confirmed, additional points were mapped in order to find the origin of the focal source. Also electrograms with activity lasting for more of 50% BCL were annotated. Subsequently, entrainment mapping was used to either confirm the reentry circuit or determine the focal origin.

This mapping strategy was developed to be applicable without the use of an EAMS, and thus concentrated on sequences of individual collected points. Especially in the context of micro reentrant mechanisms, the limited signal processing techniques provided by state-of-the art EAMSs hamper the assessment of signals which are active for over half the BCL, since annotation of the LAT is disputable in this case [65]. The critical isthmi were shown to exhibit low voltages and concur with the isoelectric line between flutter waves in the surface electrocardiogram (ECG) [66]. An example for this behaviour can be seen in Figure 11.1, in which the EGMs measured by a PentaRay catheter on a microreentry can be observed.

In the search for the optimal spot to terminate macro reentrant circuits, a strategy was proposed to easily identify the isthmus based on the relative timing between surface and intracardiac electrograms [188]. First, tachycardia BCL was determined using activation of the CS reference channel. Second, AV conduction was suppressed by carotid sinus massage or an intravenous bolus of adenosine, allowing to clearly identifiy the P wave morphology in the ECG. The window of interest was subsequently set to cover 90-95% of the BCL, with the P wave centered in the analyzed window. Consequently, mid-diastolic potentials were

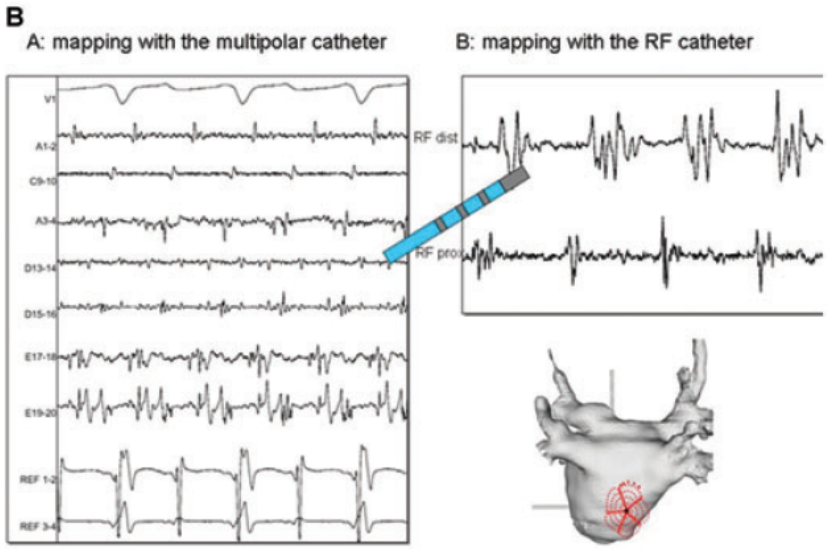

Figure 11.1: EGMs measured on a microreentry during atrial flutter. Continuous activity was observed on splines D and E, covering the complete BCL. Reprinted from [65] with permission from the publisher.

identified as sites at which the activation time was determined at or outside the boundary of the window of interest. Given the colormap used for activation mapping in the clinical context, this corresponds to the head-meets-tail region identified in purple-to-red (compare Figure 11.2). The imporance of the mid-diastolic potentials was also demonstrated by other groups [195].

If the patient was pre-ablated, conduction recovery of previously isolated regions like the pulmonary veins or the cavo-tricuspid isthmus (CTI) could be considered first [65]. Based on statistical analysis of 140 patients, evaluation of activation pattern and timing of the CS activity was suggested as initial stratification criteria to differentiate AFlut mechanisms at the beginning of a multi step diagnostic process [211]. Especially in the context of extensive low-voltage zones, identification of an optimal ablation spot is considered a challenging task [212].

Clinical Criteria and Engineering Pendants The clinical mapping strategies outlined above incorporate many steps based on visual analysis. In order to find appropriate and automatic signal processing techniques, an understanding of the observed phenomena and their interrelation is required.

From a macroscopic point of view, the cardiac excitation wavefront propagates along the myocardium. The moment at which it passes a measuring electrode is termed LAT, and the resulting excitation pattern is referred to as LAT map. In microscopic view, cells depolarize, which is accompanied with currents causing a change in extracellular potential. The morphology of an unipolar EGM has been very well studied, and the moment of maximum negative gradient of the unipolar electrogram (UEGM) was shown to coincide with the passing of the wave. Some time prior and after this moment, however, often a deviation

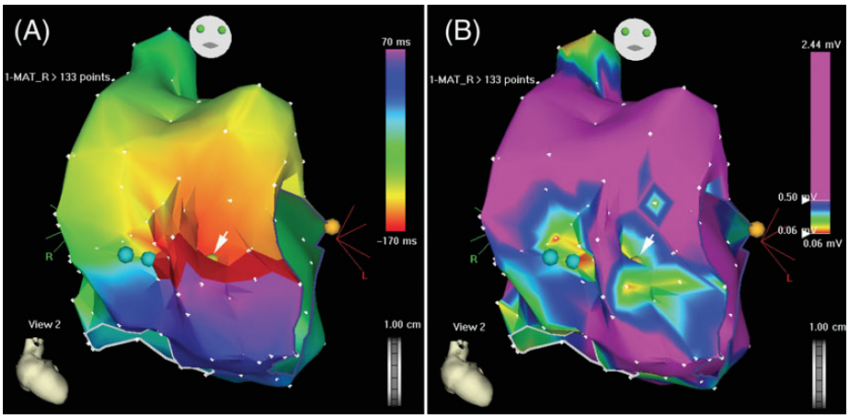

(a) RA flutter, BCL 240 ms.

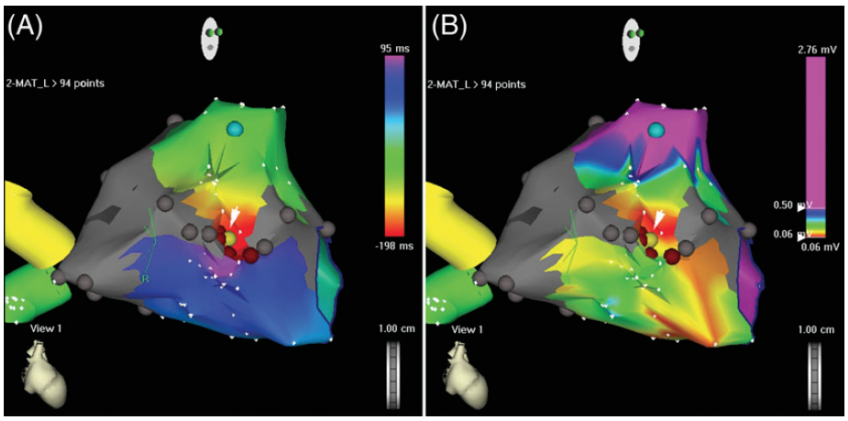

(b) LA flutter, BCL 300 ms

Figure 11.2: Localization of the mid-diastolic isthmus based on its relative timing to the P wave in surface ECG. The technique is demonstrated in two examples from a right and left atrial macroreentry, respectively. The window of interest for LAT analysis is centered on the P wave and its length set to about 90 % of the respective BCL. The transition purple-red indicates the location of the critical isthmus (left side). Bipolar electrogram at this site exhibited low voltage, coinciding with the isthmus location (right side). Reprinted with permission from the publisher [188].

from baseline can be observed in the EGM. For bipolar signals, the local depolarization can be related to one dominant deflection in the bipolar electrogram (BEGM), being the atrial activation complex. In clinical practice, however, fractionation can frequently be observed in uni- and bipolar EGMs. This is considered to be related to the presence of fibrosis or scar [46], both causing reduced and inhomogeneous inter-cell coupling and a reduction of conduction velocity. Besides the fractionated morphology, also reduced amplitudes and a prolonged duration of the atrial activation complex were observed in the clinical context.

Several studies focusing on AFlut demonstrated the importance of respective sites, as one single ablation point was sufficient to terminate the tachycardia. For micro reentrant mechanisms after pulmonary vein isolation (PVI), electrograms with activations lasting up to 140 ms were observerd [186]. Other studies found mid-diastolic potentials of 200±80 ms duration (range 110 to 360 ms) in unablated LA regions, occupying 63±22% of cycle

length [195]. In the analysis of a cohort including 246 LA flutter cases, a prolonged activation complex was found at the critical substrate in each of 95 focal micro-reentries, with a duration of 256±74 ms and amplitudes of 0.15±0.12 mV. This emphasizes the need for a tool to identify the active parts of an EGM, being deflections from baseline which are stronger than noise. After the detection of active parts, further analysis allows to assess their individual characteristics, like duration, or adjunctive properties.

On example of the latter is the detection of micro reentrant sources. Using LAT maps, these mechanism are identified by visual inspection of the LATs that are present in a bounded area not bigger than 2 cm. If LAT values can be found that cover at least 75% of the BCL, a microreentry is assumed [65]. As each electrogram is assigned one single LAT value only, while prolonged activity on average extends over 200 ms, the usage of LAT values in this context may cause problematic annotations. The usage of activity may represent a powerful alternative option, since it represents a time-continuous measure for each EGM without simplification to one scalar value. From an engineering point of view, the detection of micro reentrant sources can be considered equivalent to finding regions that exhibit 100% of BCL coverage by OR conjunction of adjacent measurements.

The P wave in surface ECG reflects the depolarization of atrial myocardium. Strong and clear P waves which are isolated by an isoelectric line in the surface ECG indicate a rapid and complete depolarization of both atria. This can be observed during sinus rhythm and may be indicative for a truly focal mechanism during AFlut. Inversely, a complete lack of isoelectric intervals can be expected during macro reentrant tachycardias. From this point of view, approaches that concentrate on the identification of mid-diastolic potentials [188] actually identify tissue which is depolarizing at a moment in time during which no activity is present in the remaining atrial tissue.

Identification of P waves may be hampered when the isoelectric baseline is not visible due to the presence of a reentrant mechanism. In addition, P waves do represent the atrial activity but rather electric field caused by the depolarizing tissue, projected onto the measuring dipole. Since intracardiac measurement data are available during electrophysiological studies anyway, an alternative strategy was developed during this thesis. Instead of focusing on the P waves, the activity of EGMs is directly assessed to compute the amount of depolarizing atrial tissue. This measure is able to differentiate the contribution of both atria to the resulting P wave surrogate, is independent from the surface lead and is highly sensitive due to the close proximity to the source which minimizes spatial averaging effects. Details and its application will be outlined in Chapter 11.2.

11.1 Measures Describing Activity of Individual Electrograms

In agreement with these considerations, algorithms were developed to compute two measures for each single electrogram: Their activity and the presence of double potentials. Although

their diagnostic relevance is widely accepted in cardiology, neither one is currently assessed in commercial clinical mapping systems. The algorithms developed during this thesis are considered a fundamental step towards improved mapping strategies of complex atrial flutter scenarios.

Bipolar electrograms recorded by a catheter inside the atrial volume and not in contact to the endocard exhibit an isoelectric baseline. This value is typically compromised by measurement noise in the order of ± 0.05 mV and may also be disturbed by artifacts like sudden peaks of up to 50 mV due to a contact between two electrodes. If measured close to the ventricles, these signals may also contain far fields caused by the ventricular depolarization. When the catheter approximates the endocardial wall, additional deflections can be observed which are caused by the depolarization of adjacent cardiac cells. As depicted in the previous paragraph, the morphology of the corresponding atrial activity complex can be used to derive information about the substrate. The maximum bipolar voltage of the deflection indicates the conduction velocity [62] and the presence of scar or fibrotic tissue [195, 213]. The duration of the activation complex indicates the presence of a critical isthmus [65, 186, 195].

Intracardiac electrograms are usually defined as double potentials when two discrete atrial complexes per reentry circuit can be observed, separated by either an isoelectric baseline or a low amplitude interval [61, 214]. These EGMs are of diagnostic interest since the twofold occurrence indicates a conduction disturbance, typically consisting of a functional or anatomical line of block [61]. Since the two components represent the left and right handed activation of the line of block, respectively, the duration of the isoelectric interval indicates the conduction delay. This duration will decrease while the mapping catheter is guided towards the pivot point of electrical excitation along a line of double potentials. This pivot point may in turn represent a critical isthmus for ablation, making knowledge about double potentials a diagnostically relevant tool.

11.1.1 Database of Annotated Atrial Activity

Within the presented research project, a database of annotated atrial activity was set up for the development and benchmarking of various processing techniques. It incorporated a total of 2863 bipolar intracardiac electrograms, which were acquired during LAT mapping of stable sustained atrial flutter using the Velocity EAMS at Städtisches Klinikum Karlsruhe. Duration of each electrogram was 1 s, and simultaneously recorded surface ECG and intracardiac CS reference was also available. Each signal was sampled at 2034.5 Hz. Data were acquired from eight different patients (358 ± 238 recordings per patient), whose characteristics are summarized in table 11.1. All provided written informed consent.

Result of manual annotation All 2863 EGMs were subsequently annotated by a scientist with more than 2 years experience in the field of intracardiac electrogram (IEGM) processing. The surface ECG and the inspected intracardiac EGM were shown synchronously using a custom-made MATLAB-based GUI, allowing to clearly identify R peaks and the

Patient ID	Age	Gender	Mechanism	Atrium	Points	Catheters
PtAFlut1	71	m	focal	LA	269	Inquiry Optima (10)
PtAFlut2	71	f	microreentry	LA	320	Inquiry Optima (10)
PtAFlut3	54	m	anterior roof dependent	LA	249	Inquiry Optima (10)
PtAFlut4	71	m	macroreentry unknown	LA	34	Constellation Basket, Inquiry Optima (10)
PtAFlut5	64	m	microreentry	RA, LA	461	Inquiry Optima (10)
PtAFlut6	65	f	RIPV unknown	LA	228	Inquiry Optima (10)
PtAFlut7	61	m	unknown	RA, LA	461	Inquiry Optima (10)
PtAFlut8	56	m	ccw perimitral	RA, LA	841	Inquiry AFocus II (20)

Table 11.1: Patient characteristics for the database of AFlut EGMs. Clinical data from eight patients (age 64±6.8 years) were included in the database. All data was recorded during stable tachycardia.

corresponding ventricular far field components. The sweep speed was set to 175 mm/s, allowing a precise annotation of all events. The magnification of signal amplitude was adjusted automatically to the strength of the electrogram components. The complete duration of data was displayed at once for each measured point, allowing to comprehend the excitation process. A list of all signals was provided and allowed to skip ambiguous signals. Buttons allowed to mark individual EGMs as noise, ventricular far field (VFF) or artifact.

Following rules were set up to obtain a clear annotation procedure:

1. If no significant activity was observed (typically less than 0.1 mV peak-to-peak values), the signal was considered *noise*
2. If the only significant activity was synchronous to the QRS complex, the signal was considered *VFF*
3. If the signal did neither show periodic activity of constant morphology and consistent BCL, nor a dominant VFF, it was considered compromised by an *artifact*
4. All remaining signals were considered *usable* for further analysis

For every signal, the position of the R peak in the surface ECG was annotated by clicking with the mouse. In all *usable* signals, the beginning and the end of each atrial activity complex were marked. If VFF activity was observed simultaneously to an atrial activity, care was taken to only annotate the time window of atrial activity as good as possible. The initial deflection from the isoelectric and the final return to its level was considered the beginning and the end of the atrial activity.

Usable signals were additionally marked as *double potentials*, if at least two distinct deflections could be identified within one cycle, separated by a nearly isoelectric baseline.

After annotation, 1981 of 2863 EGMs were identified as *usable* signals showing a periodic activity pattern. The remaining 882 EGMs were considered drowned out by the noise (187 signals), dominated by ventricular far field (207 signals) or inconsistent in activation (488 signals). 154 of the 1981 annotated EGMs presented double potentials.

Examples for *usable* signals are shown in figure 11.3. In every figure, the surface ECG is plotted at the top, the intracardiac CS reference in the middle, and the annotated EGM at the bottom. The examples were chosen for presentation as they cover a variety of different morphologies: While a clean signal with strong single deflections is plotted in (a), a highly

fractionated signal is depicted in (b). The annoated activity within the latter covered a huge percentage of the cycle length. Regular P waves (i.e. flutter waves) can be seen in the ECG. The EGM shown in (c) contained a far-field component which occurred only simultaneous to the R peak. This VFF exhibited a morphology which was comparable to the atrial activity in terms of amplitude and complexity. An example for double potentials is plotted in (d).

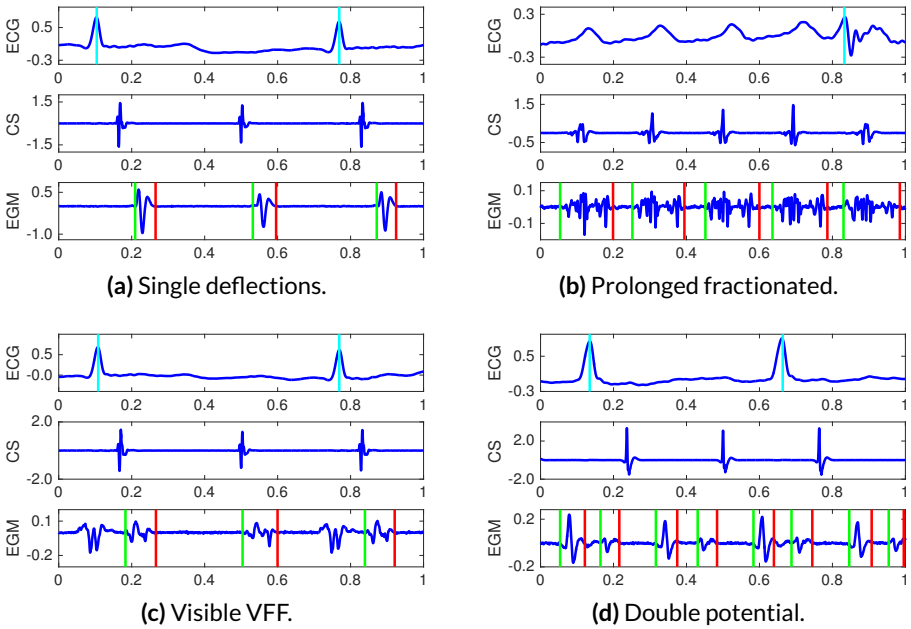

Figure 11.3: Example signals from the flutter EGM database. Surface ECG with annotated R peaks (cyan) are shown at the top. Coronary sinus EGMs are plotted in the middle, centered on the activation complex which was used to synchronize sequential measurements during clinical LAT mapping. The inspected EGM is shown at the bottom, with beginning and end of atrial activity indicated by vertical green and red lines, respectively. All annotations were done manually. Amplitudes as given in mV, time in s.

The degree of fractionation within each signal was not assessed. However, the database could easily be extended in this regard. The dataset compiled during this thesis is the first atrial flutter database at IBT. Although an extension of the database is desirable, data already showed a certain degree of variability since it included eight patients and was recorded using several catheter types.

Result of automatic preprocessing After manual annotation was completed, automatic processing was applied to determine BCL and the position of R peaks. Since the required intracardiac reference and the surface ECG were manually selected during the procedure, a good quality of these signals was assumed and therefore no additional artifact removal technique was applied.

The BCL was determined using the approach presented in Chapter 8.2. Briefly, each intracardiac reference electrogram was inspected individually. All activities were annotated using an energy-based approach. The central activity was used by the clinical system for

Patient ID	Traces	Doc BCL [ms]	Comp BCL [ms]	R peak pos
PtAFlut1	55	290	294.9±4.4	-10.2±1.8
PtAFlut2	64	190	198.6±18.2	-15.9±2.9
PtAFlut3	50	250	253.1±2.5	-17.9±2.4
PtAFlut4	1	260	260.0±0.5	-15.4±0.0
PtAFlut5	98	330	330.8±3.4	-7.0±2.5
PtAFlut6	46	240	253.6±8.9	10.5±3.4
PtAFlut7	103	266	268.4±2.0	-11.2±1.4
PtAFlut8	86	280	267.4±2.5	-8.4±2.2

Table 11.2: Evaluation of reference traces for the database of AFlut EGMs. *Traces* indicates the number of available traces, *Doc BCL* the documented cycle length and *Comp BCL* the computed BCL.

synchronization and thus also selected as reference during the automatic BCL determination. Next, the preceding and the subsequent activity were detected. Correlation was used to align the activation complexes precisely and the respective time intervals between the central and the neighboring activations determined as cycle lengths.

R peaks were detected using the IBT biosig toolbox for ECG processing. One single lead of the surface ECG was processed automatically as outlined in Chapter 5.2.

The resulting measures for all eight datasets are outlined in Table 11.2. A total of 503 individual traces was processed. Considering the BCL, both the clinically documented value and the result of fully automatic processing were in good agreement. While a total of 808 R peaks was annotated manually, automatic processing detected 810 R peaks. Visual inspection of the two respective signals revealed, that in both cases the missing R peak was located on the boundary of the recorded time frame and thus not annotated. Automatic analysis, however, detected these peaks in both cases. Considering the 808 coinciding annotations, an offset of -18 to 11 ms was present between the manual annotation and the result of automatic processing. The standard deviation of these values, however, was below 3.5 ms, indicating a consistent behavior for each patient.

Concluding, the automatic processing worked very well for both the BCL determination and the detection of R peaks. The exact position of manual annotation, however, differed from the automatic one.

11.1.2 Algorithms for Activity Detection

The duration of activity in EGMs plays an important role during diagnosis, as prolonged fractionated activity indicates a pathological propagation of excitation. Active parts of EGMs have been assessed as feature for algorithms in research addressing AFib [208]. During diagnostics of AFlut, however, this topic has hardly been addressed.

Inspired by the characteristic properties of intracardiac EGMs and well-known processing signal techniques, several algorithms were implemented and benchmarked to assess their ability to identify activity in the bipolar EGMs of the database. The presented work was part of a student project [215] that was co-supervised by Gustavo Lenis and subsequently published [216].

General workflow In order to obtain comparable results for the performance of different activity detection algrorithms, a common processing workflow was set up. As the signals were already filtered, an additional pre-filtering was in general not included. The first step comprised a mathematical transformation which represented the central part of the processing scheme and was chosen from the following methods:

1. Energy-based (NLEO)
2. Hilbert-transformation
3. Wavelet-filtering
4. Matched-filter
5. Voltage-based

The transformed signal was subsequently squared to suppress noise and ensure positiveness of all values. Low-pass filtering with cut-off frequency f_c and thresholding with value T represented the third and forth step, respectively. Both f_c and T were expected to stongly influence the outcome of annotations. Thus each parameter was varied within a reasonable search range to find an optimal pair of values for each method. Hereby, T was defined as product between the standard deviation of the signal and a proportional factor k, with the latter being optimized. Details of this generalized workflow were adapted for each respective method.

Last, a post processing step is included. According to physiological considerations, truely separate activity has to be disconnected by an inactive segment which is of similiar length as the refractory period. Therefore, activities were merged when the separating inactivity was shorter than 42 ms. Additionally, active segments with physiological origin are expected to have a certain minimum duration. Thus active regions of sporadic duration of less than 10 ms were also removed [132]. For rapid processing, these steps were implemented using morphological operations opening and closing according to

$$S_{\mathrm{pp}}(n) = (S(n) \bullet W_{42}) \circ W_{10} \tag{11.1}$$

Cycle of interest for statistical analysis Goal of the presented algorithms was the correct annotation of atrial activity in the EGMs. Therefore, just the atrial components were marked during the manual annotation of the database. In order to avoid that ventricular activity compromised the results of benchmarking, only one atrial flutter cycle without synchronous QRS complex was considered for analysis.

The cycle for analysis was automatically selected based on a linear quality measure which penalized proximity to R-peaks. Based on this criterion, the cycle for analysis was chosen out of four different possibilities. The restriction to four discrete options was introduced to allow for the resampling of sequentially acquired clinical data in map-based analysis (see Chapter 18). If one R peak occurred early or late within the surface ECG, the cycle was chosen to begin or end with the central activation of the reference EGM, respectively. If no QRS complex was detected, or two on either sides of the central reference LAW, the cycle which was centered on the reference LAW was selected. If the ventricular depolarization

occurred simultaneously to the reference activity, the cycle had to be split apart for the statistics, and thus one early and one late portion of the signal was analyzed. As the AV node did not allow for every excitation to pass to the ventricles, it was always possible to detect a cycle without simultaneous ventricular activity.

This procedure is demonstrated in Figure 11.4. The R peaks can be clearly seen in the surface ECG. They were manually annotated and correctly identified by automatic signal processing. The cycle which was not synchronous to the ventricular depolarization was chosen for analysis. Its length was equal to the BCL.

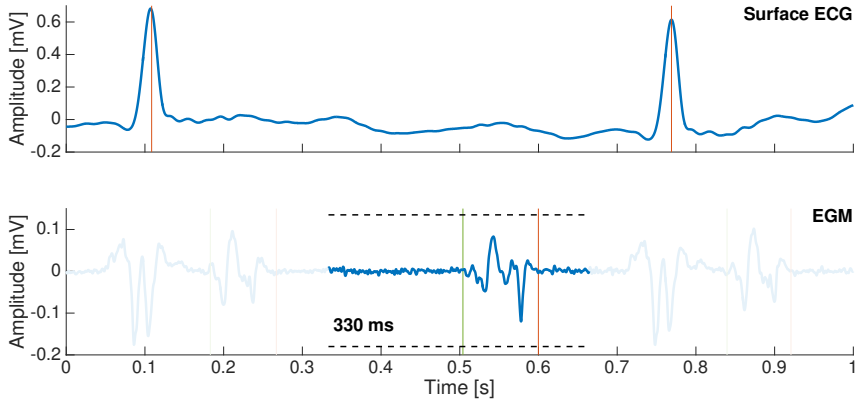

Figure 11.4: Example for the analyzed cycle during ventricular diastole. Two QRS complexes can be noted in the surface ECG, with simultaneous ventricular far fields in the EGM. The cycle chosen for benchmarking of activity detection algorithms was selected during the diastole of the ventricles, thus being not compromised by VFF. Vertical lines represent the manual annotations of R peaks and the beginning and end of atrial activity.

Measures for performance evaluation Several statistical features were computed in order to assess the accuracy of annotation. In this context, the correct detection of activity in a sample was defined as true positive (TP), with correct detection of inactivity termed true negative (TN). Manually annotated activity, which was not detected by the automatic algorithm, was referred to as false negative (FN), with false positive (FP) being detected activity which was not annotated by hand.

Based on these measures, the classification accuracy was measured for the samples within the cycle of length N in terms of

- Correct rate (CR), being the ratio of correctly detected (in-)activity to the total length of the cycle in samples:

$$\mathrm{CR} = \frac{\sum_N \mathrm{TP} + \sum_N \mathrm{TN}}{N} \tag{11.2}$$

- Sensitivity (SE), being the ratio of correctly detected activity to all annotated activity:

$$\mathrm{SE} = \frac{\sum_N \mathrm{TP}}{\sum_N \mathrm{TP} + \sum_N \mathrm{FN}} \tag{11.3}$$

- Specificity (SP), being the ratio of correctly detected inactivity to the entire amount of manually annotated inactivity:

$$\mathrm{SP} = \frac{\sum_N \mathrm{TN}}{\sum_N \mathrm{TN} + \sum_N \mathrm{FP}} \tag{11.4}$$

- Positive predictive value (PPV), given by the ratio of correctly detected activity to the total amount of samples marked manually as 'active':

$$\mathrm{PPV} = \frac{\sum_N \mathrm{TP}}{\sum_N \mathrm{TP} + \sum_N \mathrm{FP}} \tag{11.5}$$

- Negative predictive value (NPV), given by the ratio of correctly detected inactivity to the total amount of samples marked manually as 'inactive':

$$\mathrm{NPV} = \frac{\sum_N \mathrm{TN}}{\sum_N \mathrm{TN} + \sum_N \mathrm{FN}} \tag{11.6}$$

From a more abstract point of view, SE desribes the ability of an activity detection algorithm to correctly identify activity, while SP represents the ability to correctly identify inactivity. A measure for precision of activity identification is provided by the PPV, with NPV describing the accuracy of an activity detection algorithm for identification of inactivity.

Energy-Based The instantanteous energy has been shown to indicate activity in EGMs. While its maximum value has been applied to annotate the LAT (compare Chapter 8.1), its course over time has already been utilized to detect active segments and derived measures [208]. As these research focused on classification of AFib EGMs, a benchmarking had not yet been performed. The energy-based approach was thus included to get a quantitative evaluation and an optimal parameter setting for this method.

As additional preprocessing step, a Butterworth filter with a cut-off frequency of 100 Hz was applied to each EGM to assure that the frequency content was below one eighth of the sampling frequency of 2034.5 Hz. As transform, the energy E of each sample n of the signal x was computed as given by the NLEO to

$$E_n = x_n^2 - x_{n+1}x_{n-1}.$$

This operation accentuated both high amplitudes and high frequency components. Squaring was replaced by the absolute value since the NLEO already included squaring. Low-pass filtering, comparison with the threshold and post processing was done as outlined in the *General workflow* paragraph. The appliation of this process to an example signal is shown in Figure 11.5.

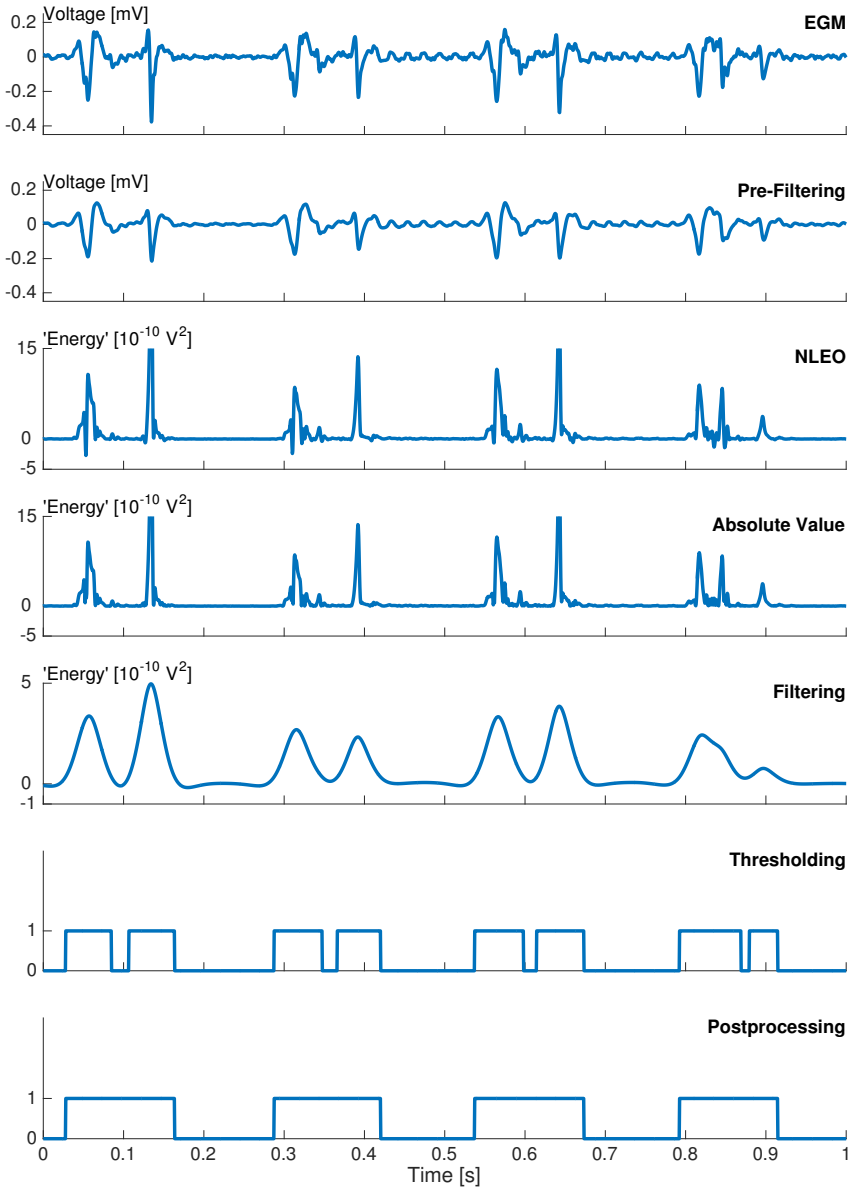

Figure 11.5: Processing steps of energy-based activity detection. The original signal was low-pass filtered at 100 Hz to comply with the frequency restrictions of the NLEO. Next the instantaneous energy was determined and its absolute value computed. The resulting signal was low-pass filtered at f_c and compared to the adaptive threshold. Adjacent segments were merged during post processing. Both f_c and the adaptive factor k were optimized during algorithm development as their value showed a huge impact on detection performance.

The low-pass frequency f_c was varied in steps of 2 Hz from 10 to 30 Hz. The second parameter, proportional scaling factor k, was varied between 0.1 and 1.0 in increments of 0.1. The classification performance for each combination of these parameters is visualized in Figure 11.6. It can be noted, that no parameter combination could simultaneously optimize all statistical measures. Therefore, the CR was chosen as optimization criterion. The

best performance was obtained with a cut-off frequency of 16 Hz and a k factor of 0.3, corresponding to a CR of 91%.

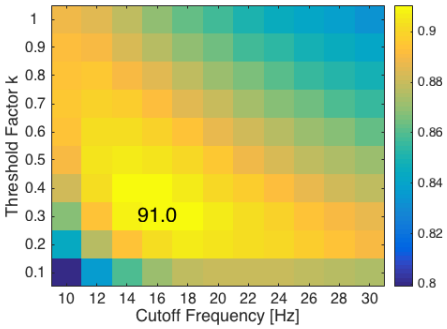

(a) Correct rate.

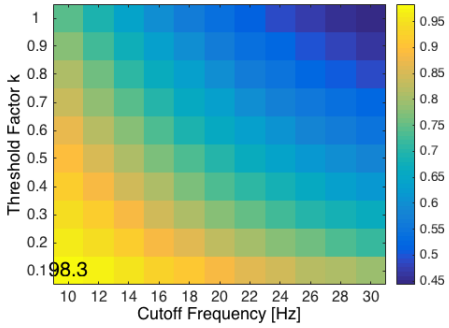

(b) Sensitivity.

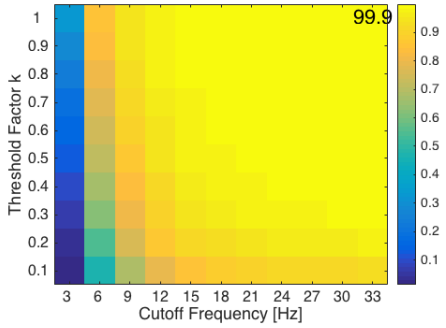

(c) Specificity.

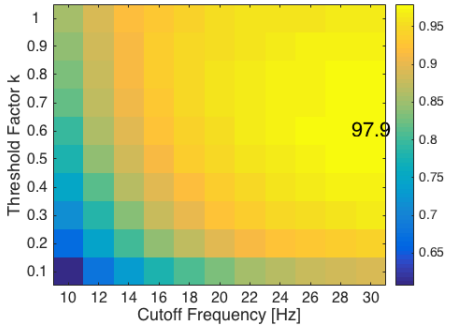

(d) Positive predictive value.

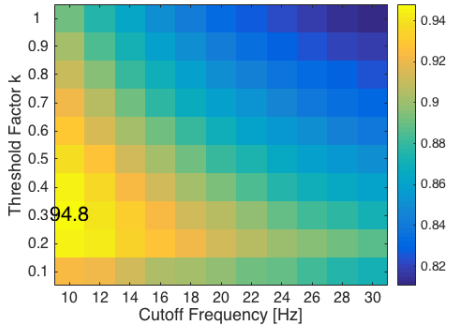

(e) Negative predictive value.

Figure 11.6: Statistical measures for energy-based activity detection. The parameters f_c and k were varied from 10 to 30 Hz and 0.1 to 1.0, respectively. The correct rate was chosen as optimization criterion as its maximum showed to balance all measures. Best performance of 91.0% accuracy was found for $f_c = 16Hz$ and $k = 0.3$.

Hilbert Based Central part of the Hilbert-based approach was the computation of the envelope of the EGM. Therefore the analytic signal $x_a(t)$ was determined as outlined in Chapter 3.2.2. The envelope was calculated as absolute value of the analytic signal and subsequently squared. All post processing steps were the same as presented above. The corresponding steps are visualized in Figure 11.7, which shows the processing of an EGM with f_c=18 Hz and k=0.3.

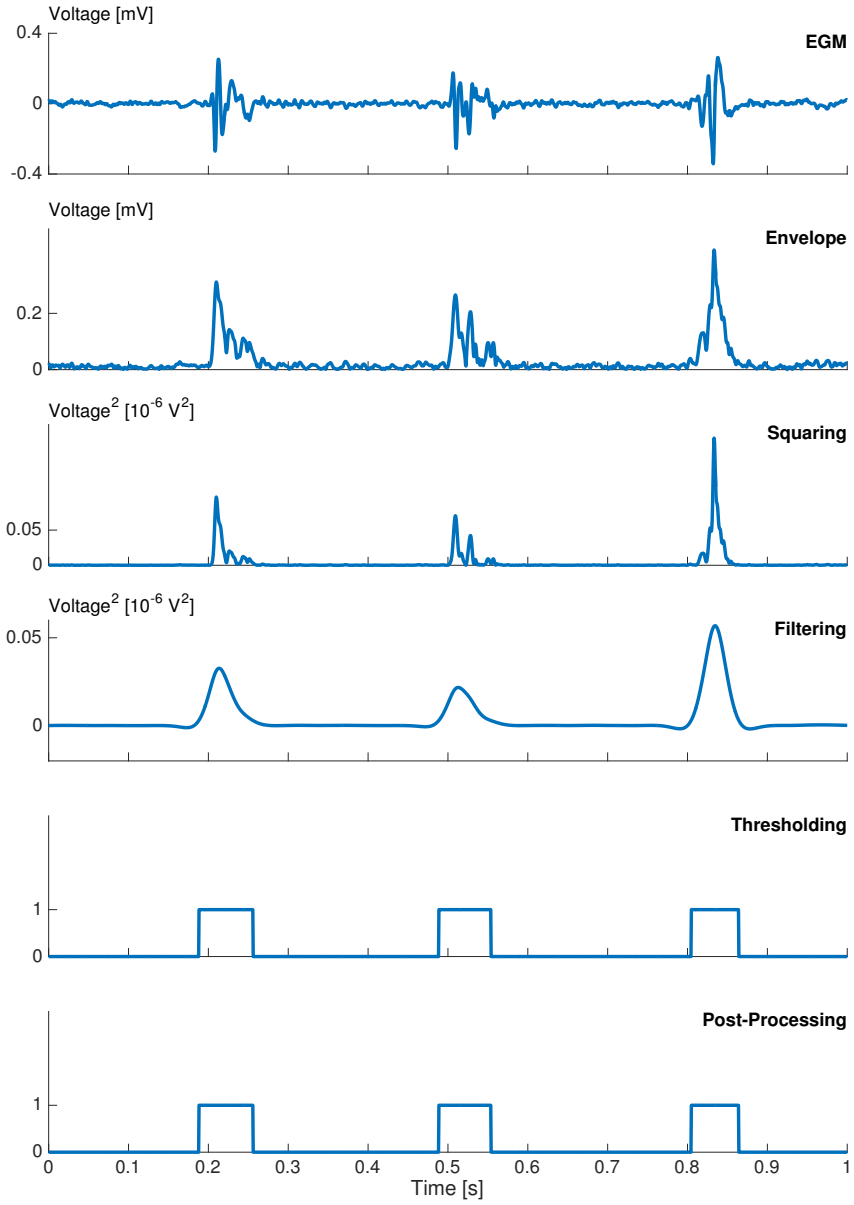

Figure 11.7: Processing steps of the Hilbert-based activity detection. The envelope of the signal was computed as absolute value of the analytic signal. Squaring, low-pass filtering and thresholding and post processing were applied as outlined in the general workflow.

To optimize the performance of this technique, f_c was varied in steps of 3 Hz ranging from 3 Hz to 33 Hz. The search span for k was evaluated between 0.1 and 1.0 in steps of 0.1. With all combinations evaluated, the highest CR of 91.9% was achieved for the cut-off frequency of 18 Hz and a k factor of 0.3.

Matched Filter Analysis of EGMs in the frequency domain lead to the observation that most power in the spectrum resulted from the active parts of the signal. Goal of the matched-filter approach was to design a filter which approximated the spectrum of the active segments, being able to preserve their information while diminishing other components.

First, the power spectral density (PSD) of the complete EGM was computed. A Gaussian was fitted into the spectrum by minimizing the least-squares-error. The EGM was convoluted with the inverse Fourier transform of this Gaussian. Squaring, low-pass filtering with f_c, thresholding and post-processing were performed as previously outlined. An example of the corresponding workflow is depicted in Figure 11.8.

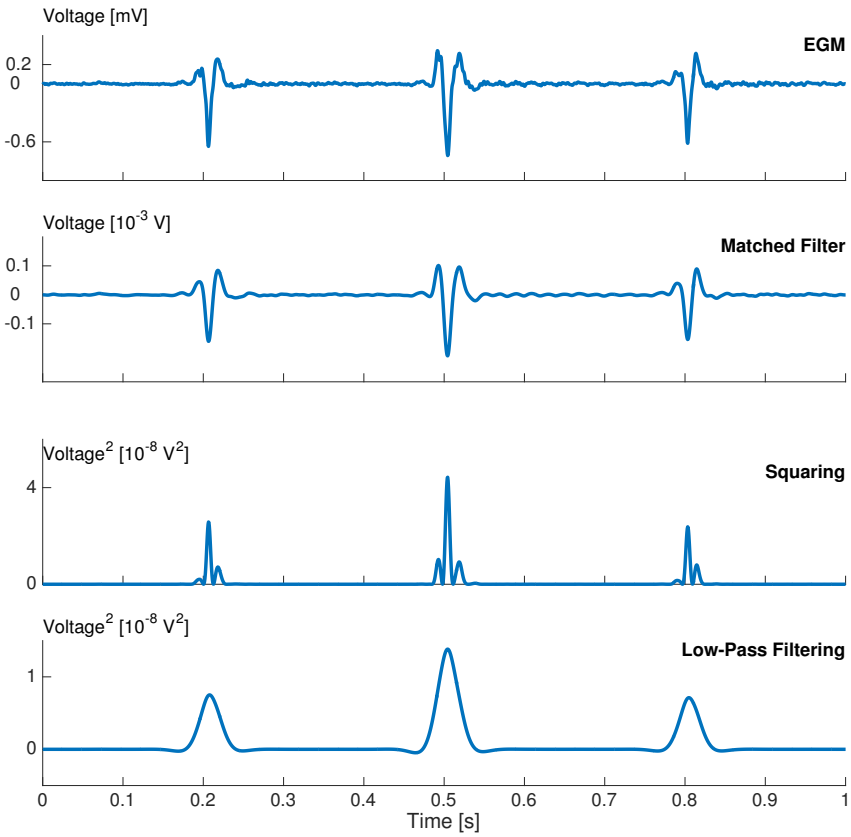

Figure 11.8: Processing steps of the matched filter-based activity detection. The output of the matched filter was squared and post processed as outlined in the general workflow. f_c=20 Hz and k=0.2 were used for computation.

The parameter search space ranged from 5 to 55 Hz and 0.1 to 1.0, with increments of 5 Hz and 0.1 for f_c and k, respectively. Within these combinations, a CR of 92.5% was achieved (f_c=20 Hz, k=0.2).

Wavelet Based Wavelet-based analysis techniques were already applied for electrogram analysis in previous work [217], in which an existing approach was extended [218]. Within the scope of this work, a second wavelet-based method was introduced and benchmarked.

Spectral analysis had indicated that the centroid of energy in the spectrum was located at 53 Hz (mean over all usable signals). Accordingly, the essential bandwith containing 95% of energy showed a mean of 121 Hz. Little power was observed in the low frequency domain since all signals were filtered with a high-pass of 30 Hz (common for bipolar EGMs). With the sampling rate being 2034.5 Hz for all signals in the database, the detail levels 4, 5 and 6 covered this frequency range of 16 to 128 Hz.

Wavelet decomposition was performed and subsequently the signal was reconstructed using only the three detail levels 4, 5 and 6. For each level, the reconstructed signal was squared and these subsequently added. This process is demonstrated in Figure 11.9 for the wavelet Biorthogonal 1.5 with f_c=30 Hz and k=0.4.

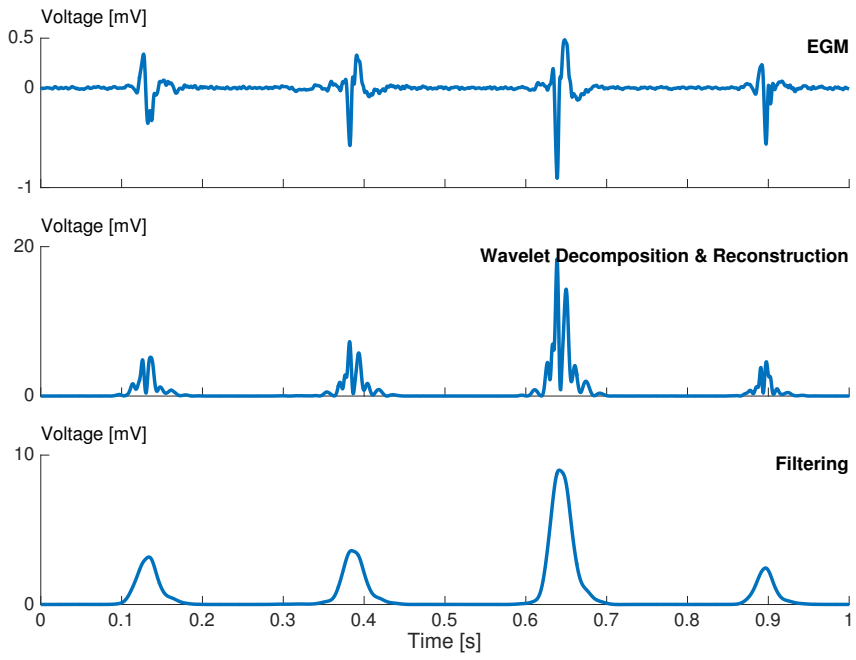

Figure 11.9: Processing steps of the wavelet-based activity detection. The Biorthogonal 1.5 wavelet was used with f_c=30 Hz and k=0.4. Selected detail coefficients were reconstructed, squared, added, and low-pass filtered.

The cut-off frequency of the low-pass which was used to smoothen the reconstructed signal was varied between 5 Hz and 55 Hz in steps of 5 Hz, with the factor k varied in increments of 0.1 between 0.1 and 1.0.

As the wavelet type was expected to have a major effect on the performance of the algorithm, five different wavelets were assessed. An overview of the tested wavelets is provided in Table 11.3, together with the achieved performance. Best results were achieved with the wavelet Biorthogonal 1.5 (92.3% with k=0.4 and f_c=35 Hz).

Wavelet	Correct rate	Sensitivity	Specificity	PPV	NPV
		in %			
Coiflet 4	91.6	87.4	94.0	86.2	93.8
Coiflet 5	91.6	87.7	93.7	85.8	93.9
Daubechies 4	91.7	84.5	95.6	88.5	92.7
Daubechies 5	90.3	85.2	93.5	82.6	92.9
Symlet 5	90.4	84.1	94.0	84.2	92.5
Biorthogonal 1.5	92.3	84.9	96.1	90.4	93.0

Table 11.3: Results for wavelet-transform-based activity detection with various wavelet types. Besides the cut-off frequency f_c and the factor k, also the type of wavelet was varied in this technique. Best results were achieved for Biorthogonal 1.5.

Voltage Based One very intuitive method for activity detection was directly based on the voltage amplitude of the EGM. Therefore, a sliding window was used to analyze the signal with 50% overlap. For each window, the difference between maximum and minimum signal values was determined and compared to a fixed threshold. The initial concept of this approach was published [219], and subsequently subject of further evaluation.

This approach significantly differed from the previous methods. Accordingly, different parameters were selected for optimization: Both the length of the sliding window w and the fixed threshold T were variable. Neither low-pass filtering nor squaring were applied, post-processing, however, was kept to merge adjecent segments and remove sporadic activity. The method of voltage-based activity detection is presented in Figure 11.10.

The search range for optimization spanned the values between 2 ms and 22 ms for w, with steps of 2 ms. The voltage threshold T was varied in steps of 0.02 mV from 0.01 to 0.19 mV. For one single fixed pair of parameters, the optimum performance was found to be 88.7%, obtained with w=14 ms and T=0.05 mV.

However, a dependency of the parameters on signal voltage was observed. The CR for different ranges of signal amplitudes is summarized in Table 11.4. The performance improved for increasing peak to peak amplitude, with optimal parameters for T increasing and for w decreasing.

For a more detailed analysis, classes containing 200 EGMs each were formed depending on the peak to peak amplitude. Optimal parameters were determined for each class independently, as shown in Figure 11.11. In order to find optimal value pairs for the analysis of new data, a functional relation was determined to relate amplitudes and analysis parameters.

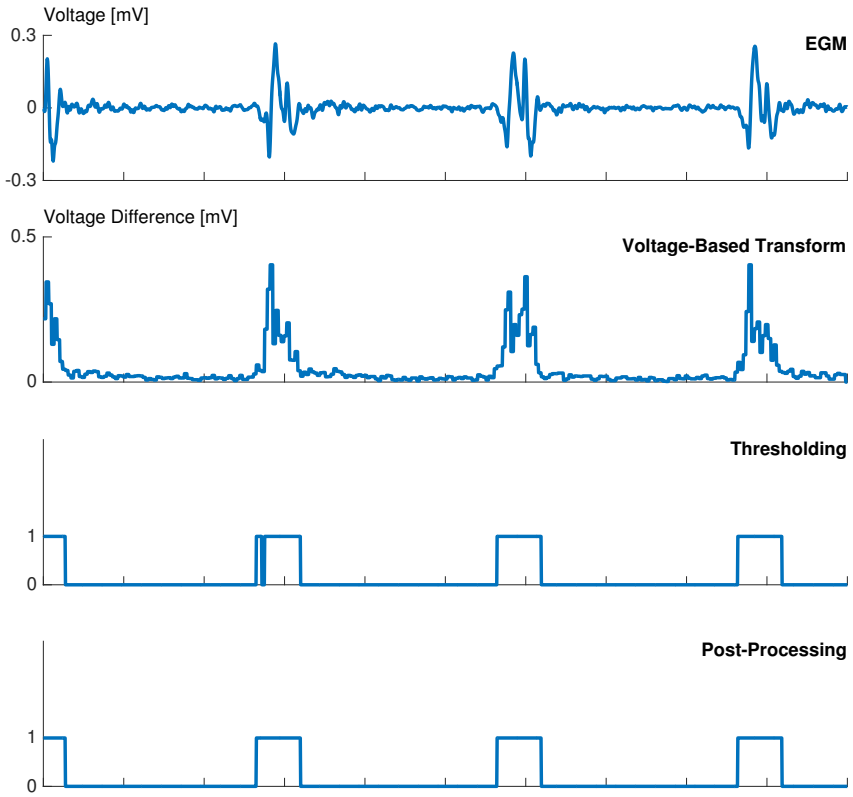

Figure 11.10: Processing steps of the voltage-based activity detection algorithm. The voltage difference of each sliding window was direclty subject to thresholding.

Class	P2P range [mV]	optimal parameter values Threshold [mV]	Window width [ms]	Correct rate [%]
1	0.035 – 0.23	0.03	18	89.9
2	0.23 – 0.55	0.05	18	92.3
3	0.55 – 1.40	0.07	14	94.0
4	1.40 – 17.74	0.11	10	95.7

Table 11.4: Dependency of voltage-based performance on signal amplitude.

Therefore, polynomials up to degree of 3 and exponentials up to 2 were fitted to the clustered measurement data.

All models and their combinations were subsequently used to dynamically compute the parameters for analysis. Comparison of the resulting CR indicated the best performance of 93.3% for exponential model functions. Based on the bipolar peak to peak amplitude A, the resulting non-linear functional relations were determined to:

$$w = 19.92 \exp\left\{-0.17 \frac{A}{\mathrm{mV}}\right\} \ [\mathrm{ms}] \tag{11.7}$$

$$T = 0.08 \exp\left\{0.14 \frac{A}{\mathrm{mV}}\right\} - 0.07 \exp\left\{-2.65 \frac{A}{\mathrm{mV}}\right\} \ [\mathrm{mV}] \tag{11.8}$$

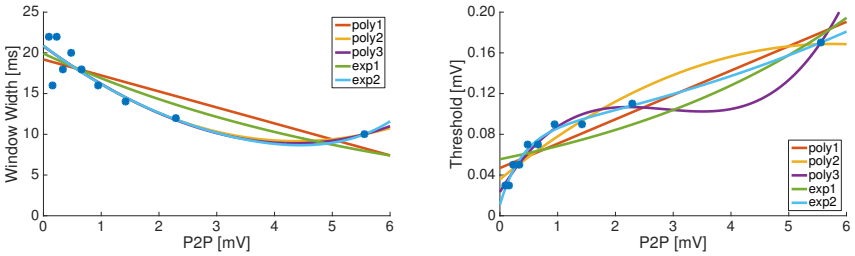

Figure 11.11: Class specific parameters and fit for the voltage dependent method.

Comparison of methods All provided good results. Details about the performance of each technique can be seen in Table 11.5.

	Correct rate	Sensitivity	Specificity	PPV	NPV
NLEO-based	91.0	84.6	94.2	87.6	92.3
Hilbert-transform-based	91.9	83.0	96.2	91.1	92.4
Matched-filter-based	92.5	85.9	95.6	90.3	93.5
Wavelet-transform-based (Biorthogonal 1.5)	92.3	84.9	96.1	90.4	93.0
Voltage-based activity detection (fixed parameter values)	88.7	81.0	93.7	85.5	91.2
Voltage-based activity detection (P2P-dependent parameters)	93.3	87.6	95.7	91.1	94.3

Table 11.5: Overall performance results of all activity detection methods. All values given in [%].

11.1.3 Double Potential Detection

Double potentials are of special interest during diagnosis, as the presence of two activity complexes typically indicates a conduction disturbance. As the time interval between both deflections often falls below the refractory period of atrial myocardium, they cannot be caused by depolarization of the same tissue [207]. Consequently, double potentials (DPs) indicate that spatially adjacent areas show a considerable delay in activation. High-density epicardial studies mapping a canine model demonstrated that this delay reflected the passing of activation on either side of a central obstacle, instead of being caused by a central slow conduction [220]. The obstacle is typically caused by functional or anatomical block, with either one being a potential obstacle for reentry.

Both persistent and functional DPs were studied during clinical mapping of RA flutter. Both were found stable over time while the tachycardia persisted. During SR and rapid pacing, however, the latter could not be observed [207]. The automatic detection of DPs would consequently aid the diagnosis of the flutter mechanism itself and additionally support the analysis of stimulated excitations aiming for detecting arrhythmogenic substrate. Also after the generation of linear lesions, monitoring the presence of DPs on the ablation line was suggested and demonstrated as valuable tool to localize gaps in the lesion [221].

Recent studies confirm the importance of DPs in diagnosis and treatment of atrial arrhythmias [221, 222]. But despite their value, no signal processing technique is known to the author which has been presented to reliably detect and annotate double potentials based on electrogram morphology.

Therefore, part of the presented research was the development of a classifier to distinguish between normal EGMs and DPs. Several features were considered, all in agreement with the definition of DPs and respective their peculiar morphological properties. These features were subsequently provided to a decision tree which assessed their usability during cross-validation. The development of corresponding features and the classification process was part of a student project [215] which was co-supervised by Gustavo Lenis and is currently under review for publication.

Features Since DPs are defined by the presence of two activity complexes within one atrial cycle, the first approach was to simply count the *Number of Activity Complexes*. As the cycle of interest was defined based on ECG criteria independently from the annotation of activation complexes, it was possible that an activity complex was cut off by the cycle boundary (compared Figure 11.12 (b)). Therefore, each activity was weighted by the relative amount of its duration inside the cycle. The sum of all relative values provided an estimation for the number of activation waves per BCL. As demonstrated in Figure 11.12, the total value was close to 1 for EGMs with single deflections, while the presence of DPs was indicated by a sum close to 2.

Although this measure was very intuitive, it strongly depended on the correct annotation and precise discrimination of all local activation waves. If activity was not detected, or spurious activity was wrongly annotated, the number of activities was too sensitive. Therefore, the cycle length coverage of single signals was added as feature. While the duration of single deflections usually was rather short, fractionated and double potentials tended to exhibit longer activities. Although this cannot discriminate between fractionation and real DPs, it was considered as feature *Activity per Cycle*.

A novel concept of identifying dominant deflections in the EGM was based on assessing the instantaneous energy within the active parts of the signal. As demonstrated in Figure 11.13 (a), local activation waves (LAWs) that contain just one single deflection also have one single maximum of energy. Additionally, the time of the maximum is very close to the centroid of the energy distribution of each activation complex. For double potentials, each deflection results in an individual peak which can be identified in the course of energy. These peaks are located further away from the centroid of the energy, as can be observed in Figure 11.13 (b). In order to evaluate the presence of multiple components within one LAW, the two features *Number of Peaks* (being the average number of peaks in the considered signal) and the *Peak-Centroid Distance* (being the average distance between peaks and the centroid of each individual LAW) were introduced.

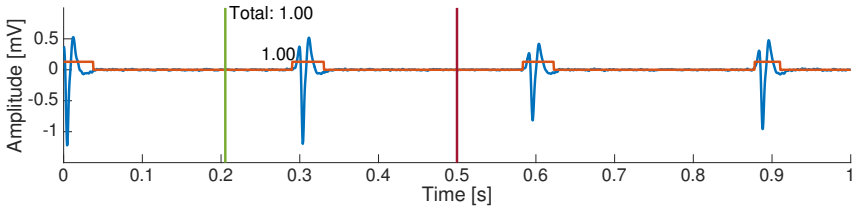

(a) EGM with single deflection within the considered cycle.

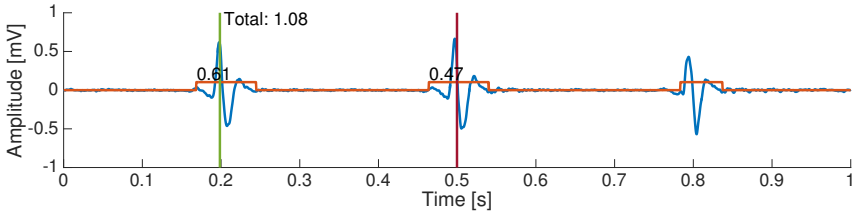

(b) EGM with one single deflection at the cycle boundary.

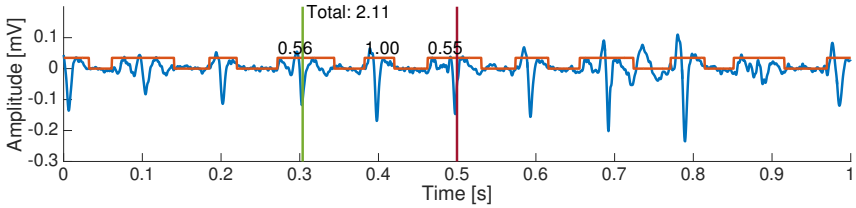

(c) Double potential with two activities per BCL.

Figure 11.12: Example demonstrating the feature *Number of Activity Complexes* for DP detection. Three EGMs are shown (blue) together with the manually annotated activity (red). If just one single deflection is present, it may be located completelly within the considered cycle (a). If the activity is located at the boundary of the considered cycle, the relative duration inside the cycle has to be considered (b). This allows to estimate the number of activations also in case of double potentials (c).

Double potentials are frequently defined by the existence of an isoelectric baseline separating LAWs. In the presence of noise, however, short segments of baseline may not be detected during initial annotation and subsequently cause the detection of a fractionated potential of long duration. Therefore two additional ways to analyze the baseline were incorporated as potential features for DP detection.

Short segments of baseline were often removed during the post processing of activity detection. Keeping this in mind, the annotated activity prior to post processing was analyzed. Only the baseline was assessed which was located between two subsequently joined activity complexes. Its longest duration was evaluated and included as feature *Baseline 1* (see Figure 11.14 (b)).

Since the low-pass filtering may already cause a smoothing of the signals before merging, a second measure was introduced. Feature *Baseline 2* was based on the voltage of the original EGM. The variance of voltage values was computed within the inactive parts of the signal and considered to be a measure for the noise level. Subsequently, a threshold of three times the standard deviation was defined and used to identify baseline segments within annotated

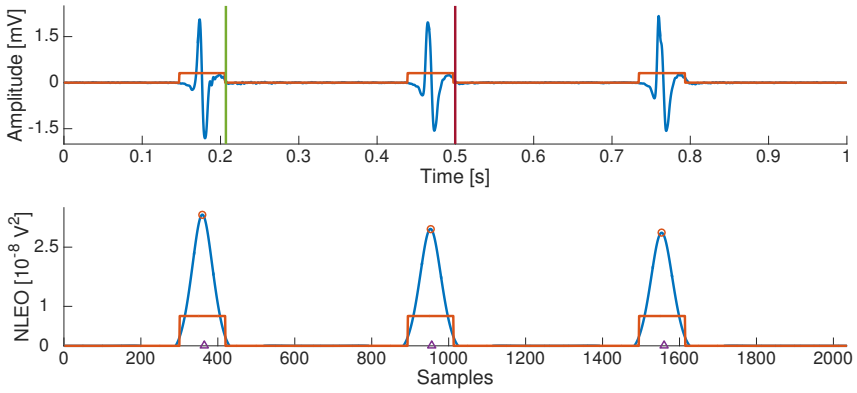

(a) EGM with one deflection per BCL.

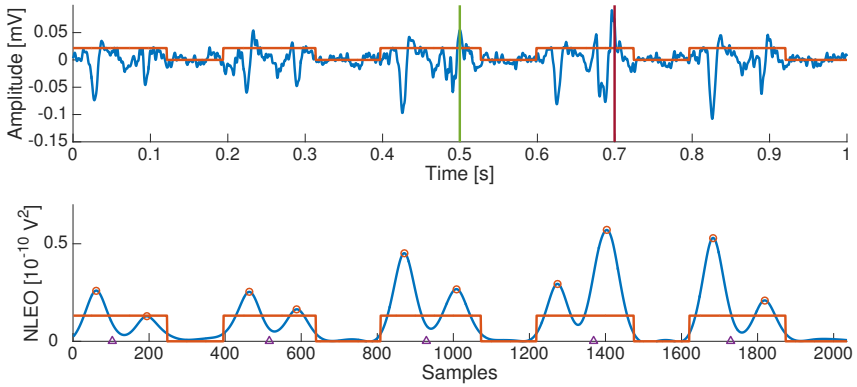

(b) Double potential within a prolonged EGM.

Figure 11.13: Example demonstrating the feature *Number of Peaks* for DP detection. The instantaneous energy was assessed within all detected LAWs. While the presence of a single peak indicated one deflection (a), multiple peaks could be related to DPs which were annotated as one larger LAW (b). The distance between each peak and the centroid of energy was evaluated for the feature *Peak-Centroid Distance*.

LAWs. The longest duration of these values was considered the length of the baseline and thus used as feature as shown in Figure 11.14 (c).

Two additional features were included to assess the similarity between detected LAWs. For all LAWs which were at least partially located inside the cycle of interest, mean and standard deviation of their durations was computed. While the length of all active segments could be considered similar if just one type of morphology was present per cycle, the individual components of DPs were also observed to have different lengths. This led to higher values of the standard deviation, making *LAW* μ and *LAW* σ potentially relevant features. Another measure, although not included, may be the correlation coefficient between LAWs (compare Chapter 13.2). This however, would require an annotation of the LAT and correlation in time domain, making it a more complex and due to the fractionation of DPs probably less robust feature.

Performance evaluation All features introduced in the previous paragraph strongly rely on the correct detection of activity. Within this project, several techniques for activity

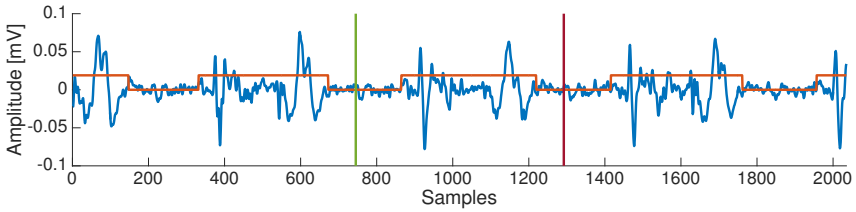

(a) Result of automatic annotation using the NLEO-based method.

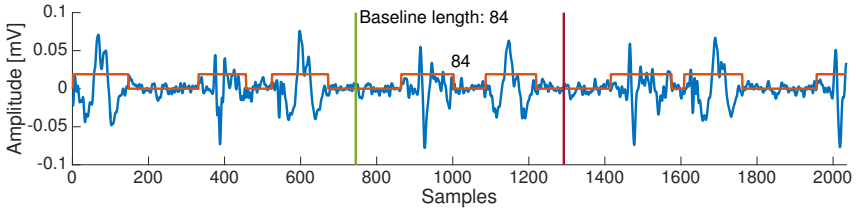

(b) Baseline determined from the intermediate processing result without merging of adjacent activities.

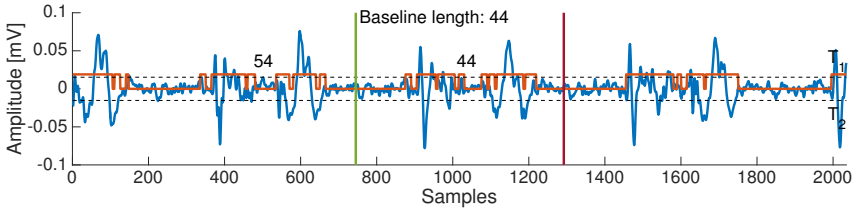

(c) Baseline determined from the low amplitude segments within the detected LAWs.

Figure 11.14: Example demonstrating the *Baseline* features for DP detection. Activity detection using the NLEO based method joint adjacent deflections (a). Evaluating the intermediate processing step prior to merging of active segments demonstrated the presence of a baseline. Its duration was determined as used as feature *Baseline 1* (b). The amplitude of the EGM within the annotated activity was directly assessed for feature *Baseline 2*. Isoelectric intervals of short duration could be detected this way (c).

detection were developed and benchmarked. All these algorithms demonstrated classification accuracy above 90% (see Section 11.1.2). Despite these values, the possibility could not be excluded that one technique was more suited for the detection of DPs than the others. Thus, the process of feature calculation, classifier training and cross-validation was executed for every of these preprocessing method.

As the voltage based annotation did not involve an energy-based measure that could be used to compute *Number of Peaks* or *Peak-Centroid Distance*, the NLEO was additionally computed and evaluated within those segments of the signal that were determined as active based on their amplitude.

Another issue was brought up by the difference in numbers: As the normal EGMs (1827 signals) heavily out numbered the DPs (154 signals), balancing of the training data was required. This was done by one cycle of random-oversampling, i.e. a random replication of signals from the minority class [223]. Despite an increased possibility of leading to over-fitting, comparison with other techniques for balancing demonstrated very good performance and little increase in tree complexity for random-oversampling [224].

For each preprocessing method, a tree was grown using the Gini Diversity Index as split criterion (see Chapter 3.3.1). The complexity of the resulting tree was restricted to 10 decisions, with branch node observations limited to minimum of 10 and leaf node observations set to 1. These measures were applied to prevent overfitting.

Performance of the induced trees was assessed using leave-one-out cross-validation. In order to test the suitability of the features and the classification procedure, an additional tree was generated based on the manual annotations instead of the automatic activity detection. The resulting performance of 99% correctly annotated signals indicated that the chosen features were very well applicable to distinguish between both classes.

The resulting correct rates when using the automatic algorithms for annotation are summarized in Table 11.6. Depending on the preprocessing algorithm, the correct rate varied between 77.2% and 90.5%. Best performance was observed for the voltage-based activity detection. The resulting tree grown with all available data is visualized in Figure 11.15. The *Activity per Cycle* was identified as most relevant feature, directly followed by the *Number of Activity Complexes* in the second level.

11.1.4 Conclusion

The morphology of individual EGMs is inspected by the physician during mapping, as it provides important information about both the excitation and the underlying substrate. While single clear LAWs are generally observed during uncompromised propagation, prolonged and fractionated components are assumed to indicate the presence of injured, fibrotic or remodelled tissue. Special clinical value is attributed to signals covering over 50% of the tachycardia cycle length, as the regions where they can be measured often represent the critical substrate for tachycardia perpetuation. Also the presence of DPs is of high diagnostic relevance, as they indicate functional or anatomical lines of block.

	Correct rate	Sensitivity	Specificity	PPV	NPV
Manual annotations	99.0	99.6	98.4	98.4	99.6
NLEO-based	79.7	69.2	90.2	87.6	74.5
Hilbert-transform-based	83.4	79.1	87.8	86.7	80.8
Wavelet-transform-based	78.7	65.5	91.7	88.8	72.7
Voltage-based (fixed parameters)	85.4	89.1	81.7	83.0	88.2
Voltage-based (P2P-dependent parameters)	90.5	91.3	89.6	89.8	91.2
Matched-filter-based activity detection	77.2	61.1	93.3	90.1	70.6

Table 11.6: Cross-validation results of decision trees for DP detection. All values given in [%]. For the wavelet-transform-based approach, the Biorthogonal 1.5 wavelet was used. For the voltage-based approach, *Number of Peaks* and *Peak-Centroid Distance* were calculated using the results of the NLEO-based activity detection algorithm. Best performance was observerd for the voltage-based approach with about 90% accuracy.

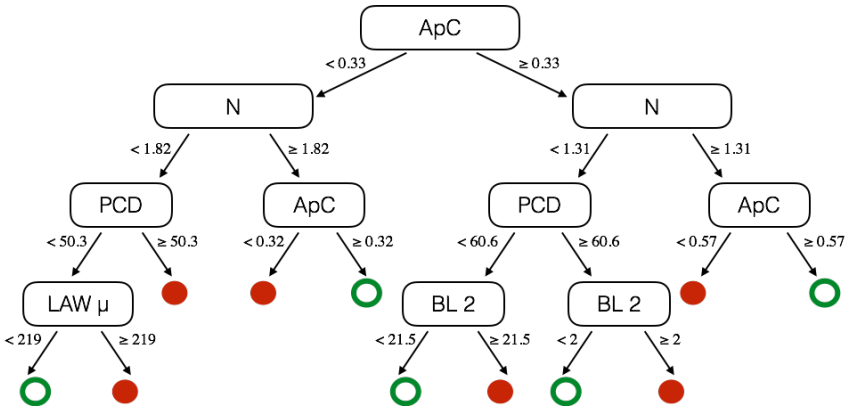

Figure 11.15: Decision tree for DP detection. Inspected EGMs were labeled as normal signal (green circle) or DP (filled red dot), depending on the values of the five following features: *Activity per Cycle (ApC), Number of Activity Complexes (N), Peak-Centroid Distance (PCD), LAW μ, and Baseline 2 (BL 2).*

Performance Within the scope of this research, different methods were developed to determine the activity of intracardiac electrograms. Therefore, a database with 2864 EGMs was set up and manually annotated. It provided the opportunity to benchmark the performance of automatic annotation algorithms. After parameter optimization, accuracies of over 90% were achieved. While the voltage-based activity detection performed best, all other methods also achieved values close to or above 90%.

For the automatic detection of DPs, a corresponding classifier was developed. First different features were generated, all related to the morphological peculiarities of DPs. A decision tree was induced as classifier with all eight features and subsequently grown using the Gini Diversity Index as split criterion. Comparison of different processing techniques showed that the voltage-based activity detection performed best, with a resulting accuracy of over 90%.

The resulting classifier comprised a variety of features which addressed different properties of DP morphology. The *Number of Activity Complexes* was included, as well as the total *Activity per Cycle*. Detection of dominant deflections within active segments was addressed by the *Peak-Centroid Distance* and the feature *Baseline 2*. Also the *LAW μ* was included.

Clinical application Both the activity annotation algorithms and the resulting DP classifier were included into the analysis workflow for clinical AFlut data. After processing, an atrial map was generated that indicated the regions in which DPs were detected. Figure 11.16 shows the processing result of an example dataset. The LAT map indicated a line of block on the anterior wall, delaying activation between the inferior and superior aspect. This coincides with the DP map, which indicated the presence of a conduction block at the very same location.

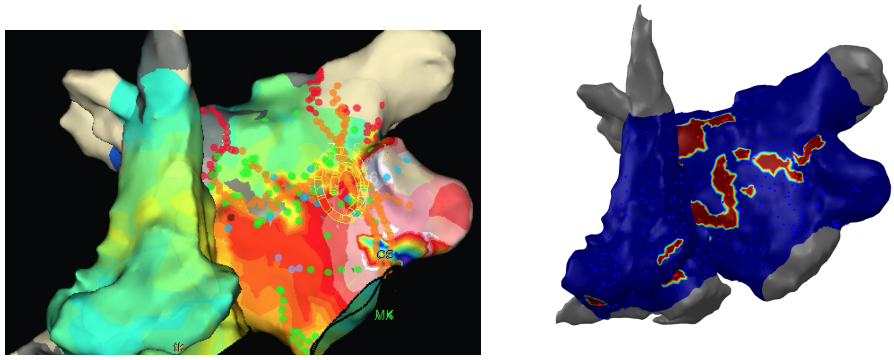

(a) LAT map. **(b)** Double potential map.

Figure 11.16: Demonstration of a DP map and its relation to the cardiac excitation pattern. The LAT map indicated a delay in activation between the inferior and the superior part of the anterior wall (a). This was in agreement with the DP map, which indicated the presence of a conduction block at this location (b).

11.2 Measures Based on Multichannel Information

While the analysis of individual EGMs provides information about the local excitation, the combined analysis of multiple channels allows to assess the spatio-temporal excitation pattern. Assuming a stable pattern of excitation, both simultaneously measured electrograms and synchronized data from sequential mapping can be taken into account for these techniques. All of the following techniques presume stable excitation patterns as observed during AFlut. For dynamically changing excitation processes like AFib, statistical analysis techniques may be preferable (compare Chapters 12 and 13).

11.2.1 Virtual Mapping of Atrial Activity during Sustained Flutter

In order to quantify the atrial activity and relate it to the depolarizing myocardium, simulated scenarios from the database outlined in Table 10.3 were virtually mapped. Therefore a total of 1000 and 1500 measurement points were acquired from the RA and LA, respectively. These were drawn randomly from all vertices in the respective atrium. As the fast-marching simulator (FaMaS) directly provided the LATs at each vertex, no electrogram preprocessing like detection or annotation of the activitiy was required. Instead, activity was centrally inserted on the LATs with a Normal distributed duration $N(20\,ms, 4\,ms)$.

The spatial information of virtual measurement points and their activity were rearranged into the format used for the processing of clinical atrial flutter data. Coverage maps and interpolation matrices were computed as outlined in Chapters 6.3 and 8.4, respectively.

LAT maps were computed in order to visualize the cardiac excitation pattern. Therefore one vertex located at the central posterior mitral valve annulus was chosen to represent the reference CS recording. The first activation in the CS lead after two seconds of simulated AFlut

was chosen as reference time, corresponding to the synchronization process in clinical data. The cycle length was automatically detected by inspecting the preceeding and subsequent LAT of the reference channel. The LAT map of the mapped tachycardia was then constructed based on the the LATs of all virtual electrodes within one BCL centered at the reference CS activation. It was interpolated to the endocardial shell using the Nearest-Neighbor-Technique.

Three demonstrative cases were chosen from the database depicted in Table 10.3 for exemplary analysis and will be discussed in the following. These covered all three major excitation patterns, being a macroreentry around the mitral valve (*sc12*), a focal source at the anterior RSPV ostium (*sc40*) and a scar-related microreentry at the postrior LIPV isolation (*sc21*).

11.2.2 Mapping of the Atrial Cycle

A first indicator for the nature of the underlying tachycardia mechanism is given by the amount of cycle length which can be annotated when all recorded signals are assessed in conjunction. Reentry is typically suspected as mechanism for atrial flutter if activation times for at least 85 % of the BCL can be successfully mapped [225]. For each moment of the covered time, accordingly, an EGM can be found somewhere in the atrium which exhibits activity and whose LAT can be annotated. Inversely, no activity can be detected for less than 15% of the cycle length. Given a sufficiently high-density of intracardiac measurements, the atrium is suspected to be in rest during this inactive time, excluding the presence of a reentrant source and endorsing a truly focal source. The coverage of macroreentry activation was shown to be about 95.9±4.3% (range 90 % to 100 %) in clinical mapping studies [188]. This is one important indicator that can be assessed when all recorded electrograms are analyzed jointly.

The buffer of 15% is frequently applied since some endocardial aspects of the flutter cycle may not be reachable during mapping, or the flutter may propagate on the epicardial aspect of the atrium. Thus the excitation wave cannot be observed at these locations and no LAT can be annoted. In addition, also highly fractionated potentials are assigned just one LAT value, despite the fact that they may cover significant parts of the cycle length. Studies have shown prolonged activation at the critical isthmus lasting mean durations of 200±80 ms, with individual potentials having duration of 360 ms (mean 200±80 msec) [195]. This demonstrated a situation in which the annotation of LAT will not lead to optimal results. Instead, an activity based approach is suggested in the following.

In order to quantify the mapped cycle length and relate it to the depolarizing myocardium, the activity of each virtual electrode was mapped onto the surrounding atrial surface as surrogate for the amount of depolarizing tissue. This was done for each sample, resulting in a time-continuous course of the amount of active tissue for each individual atrium. By dividing this value through the total amount of covered atrial surface, the relative amount of active tissue was determined. It was low-pass filtered with a cut-off frequency of 2 Hz to ensure a smooth course.

From a theoretical point of view, two important findings could be derived from these measures. First, they allow to comment on the mapped cycle length. The time in which the relative amount of active tissue is non-zero indicates observed and ongoing depolarization. This allows to separate between macro reentrant activites (> 85 % of the cycle mapped) and non-reentrant mechanisms or passively activated atria. Second, the presence of a critical isthmus can be assessed. If the amount of depolarizing tissue is very little at some point in time, this most likely indicates the passing through of a critical isthmus.

In the following, this is demonstrated using three simulated scenarios of tachycardias (see Figures 11.17 to 11.19). For each example, LAT maps are depicted at the top, indicating the excitation pattern seen from anterior (a) and posterior (b). The relative amount of active tissue is plotted underneath (c), for each atrium individually. Its time-continuous value is plotted for a duration of 1 s. During this time, a repetitive pattern can be observed in the amount of active tissue. The cycle used to generate the LAT map is indicated by green and red lines, respectively, and shown together with the colorbar. This allows to relate the relative amount of active tissue and the propagation pattern seen in the LAT map. For a statistical overview, please see Table 11.7.

The analysis of simulated scenario *sc12* is depicted in Figure 11.17. The LAT map indicated a counter-clockwise perimitral flutter in the LA. The relative amount of active tissue in the RA varied between 0 % and 30.2 %, with a total of 67.0 % of BCL showing activity. The time of RA activation coincided with the LATs colored in yellow, green and cyan, which matched the propagation pattern visualized in the LAT map. For the LA, 100 % of BCL could be mapped, with instantaneous values ranging from 2.8 % to 11.2 %. This corresponds to an active area of 3.3 cm^2. This was in agreement with the expected finding that activity would be present in the LA during the complete cycle length of the macro reentrant mechanism. The RA showed passive activation only.

Focal activity originating from the anterior RSPV is simulated in *sc40*. For none of the atria, the cycle could be covered to 100%. More precisely, for 15% of the BCL no active tissue was found, indicating complete depolarization of both atria and thus excluding a reentrant mechanism. This is in agreement with the absence of blue colored regions in the LAT map.

A scar related micro reentrant flutter form is shown in Figure 11.19. The LAT map indicated an excitation pattern originating from the postrior LIPV ostium. Qualitative inspection of right and left atrial relative activity indicated that most of the atrial tissue depolarized during the second half of the cycle length, being in agreement with the dominance of green and blue areas in the LAT map. Quantitatively, the relative activity in the RA ranged from 0 % to 26.1 %, with a covered cycle of 52.9 %. For the LA, the relative activity ranged from 0.3 % to 20.5 %, with 100 % coverage of the cycle length and a minimum surface area of active tissue of 0.4 cm^2. This clearly indicated the presence of a reentrant mechanism with a critical isthmus.

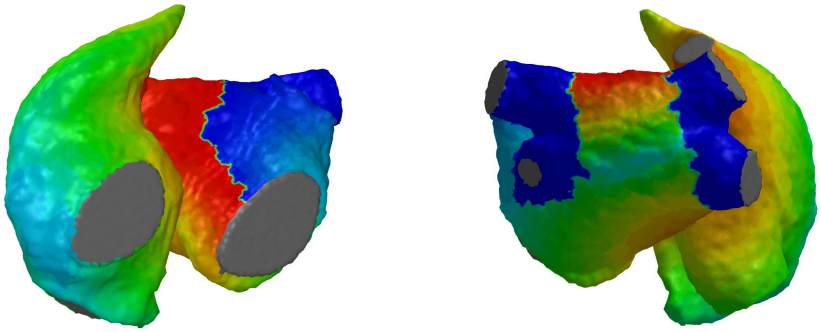

(a) LAT map in anterior view.

(b) LAT map in posterior view.

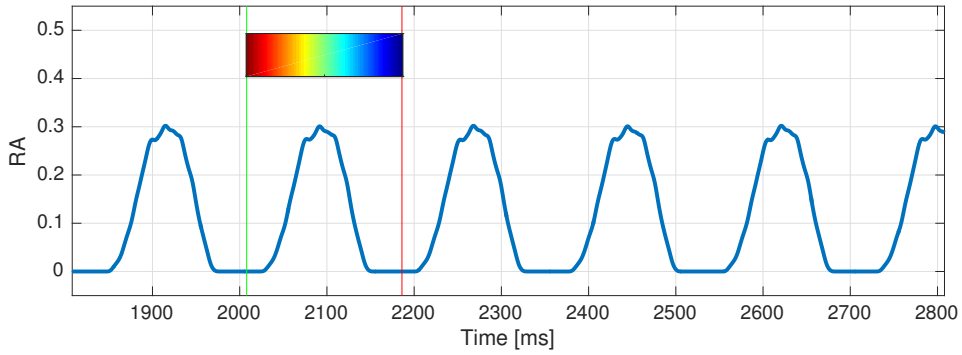

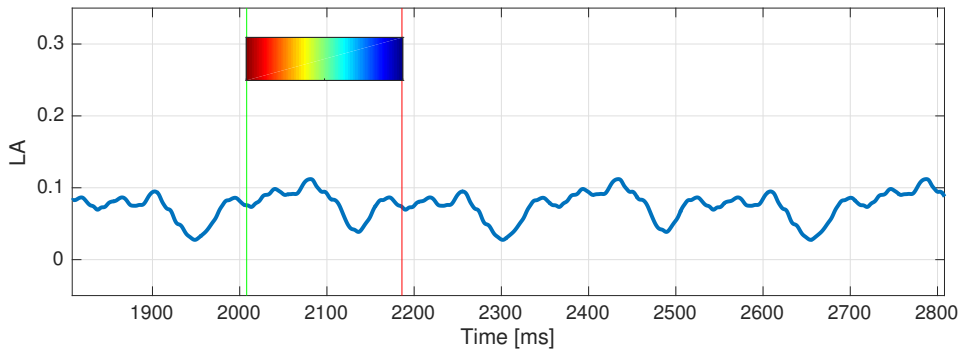

(c) Relative amount of active tissue for both atria.

Figure 11.17: Relationship between LAT and depolarizing tissue in *sc12* (perimitral atrial flutter, BCL 177 ms). Counter-clockwise activation can be observed in the RA covered to 67.0%, LA covered to 100%.

11.2.3 Cycle Length Coverage by Area

Although the joined analysis of all recorded signals allowed to differentiate between truly focal and reentrant based mechanisms, it did not allow to differentiate between micro and macroreentry, respectively. Therefore a more localized analysis of cycle length coverage is required. Clinical studies demonstrated that the complete BCL of localized micro reentries could be covered in areas with a diameter of less than 2 cm [65] (compare also Figure 11.1).

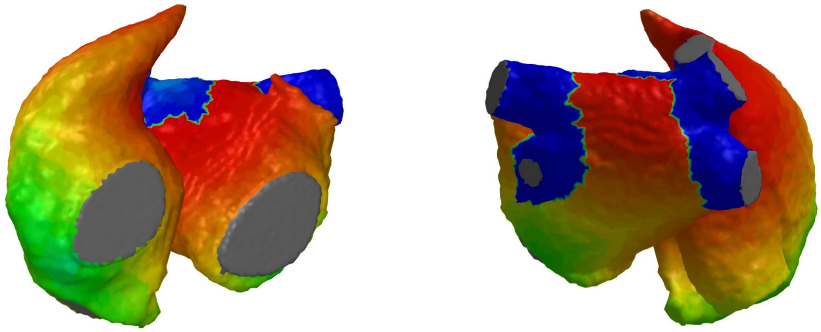

(a) LAT map in anterior view.

(b) LAT map in posterior view.

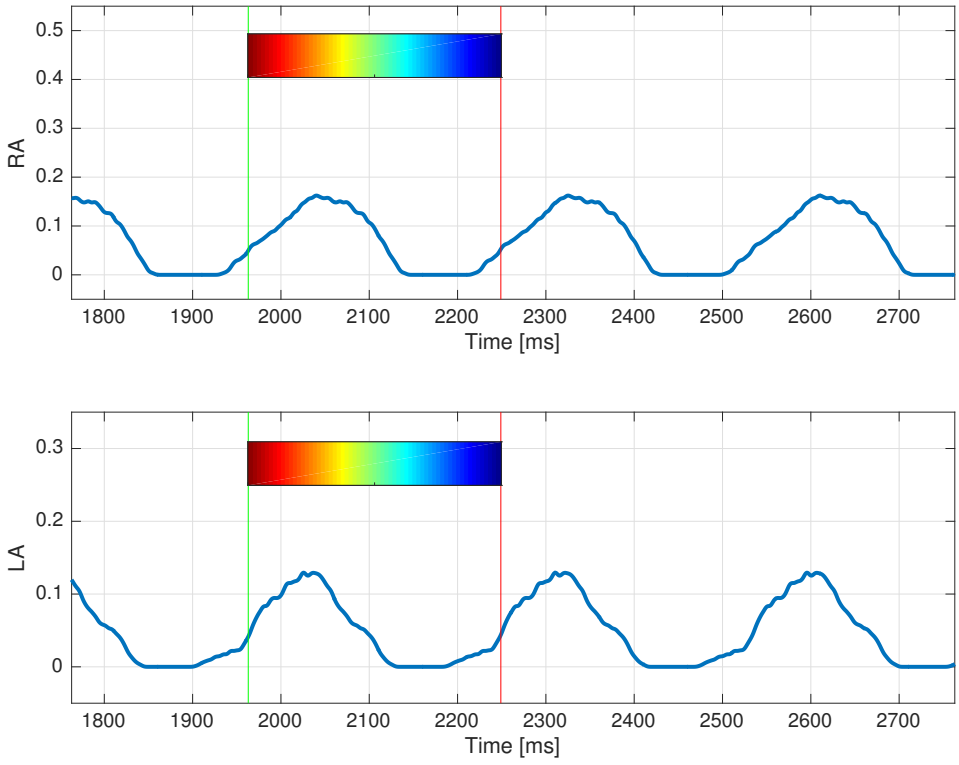

(c) Relative amount of active tissue for both atria.

Figure 11.18: Relationship between LAT and depolarizing tissue in *sc40* (focal source at anterior RSPV, BCL 285 ms). RA covered to 74.6%, LA covered to 80.1%.

Literature values suggest the coverage of least 75% of BCL within <3cm for micro reentrant sources [211], while macro reentrant mechanisms require a circuit diameter of >3 cm [8].

Therefore, an algorithm was developed to jointly analyze only data from neighboring measurement points within this distance. For each vertex of the anatomy, the surrounding region within an Euclidean distance of 1 cm was considered. The cycle length coverage was assessed for this area by a logical OR-conjunction of the activity information over time. As this was done with respect to all acquired data comprehensively, it allowed to detect

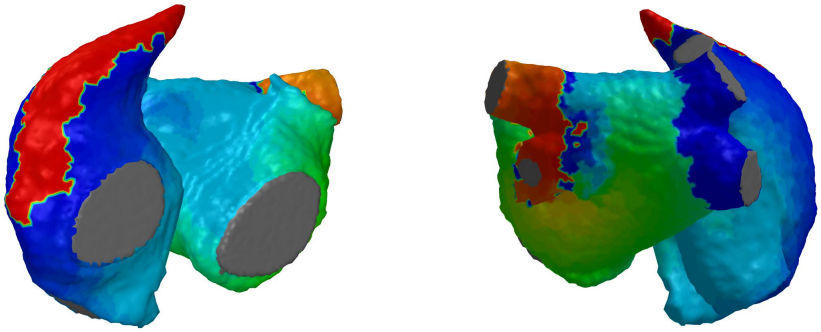

(a) LAT map in anterior view.

(b) LAT map in posterior view.

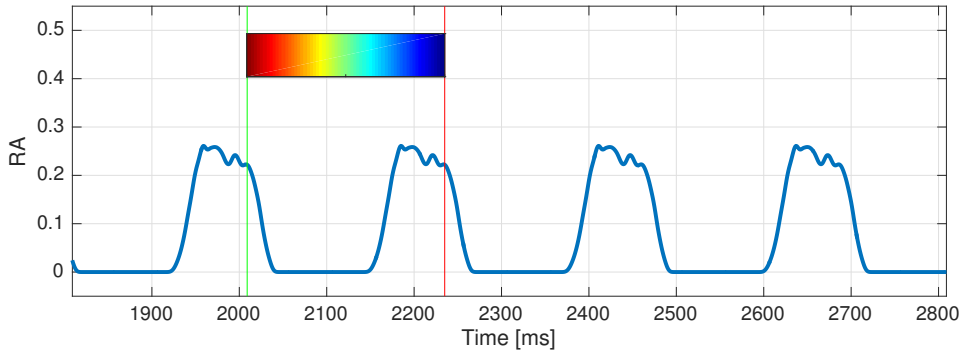

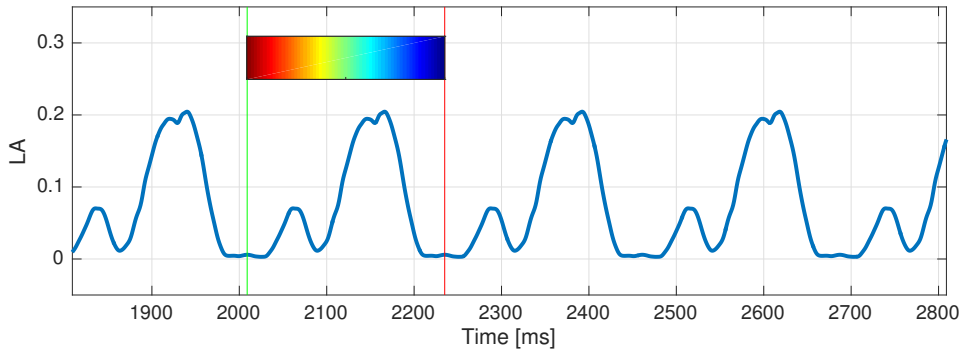

(c) Relative amount of active tissue for both atria.

Figure 11.19: Relationship between LAT and depolarizing tissue in *sc21* (scar related flutter at LIPV, BCL 226 ms). Most of the atrial tissue depolarized during the second half of the cycle length. The cycle was successfully mapped for 52.9% in the RA and covered to 100% in the LA. Strong variations and very small values for the relative activity in the LA indicated the presence of a critical isthmus.

micro reentries even if they were not covered by a catheter completely within one single measurement.

The result of this analysis technique applied to exemplary cases of AFlut is visualized in Figure 11.20. While no significant coverage was found in the both macro reentrant case *sc12* (maximum of 62% in LA) and for focal activity *sc40* (maximum of 36% in LA), a microreentry was detected and identified correctly in *sc21* with 100% of area-based CLC.

11.2.4 Locating Diastolic Activity

Since AFlut is a continuous process, the starting point can be set arbitrarily. For Figures 11.17, 11.18 and 11.19, the reference time was set to the CS activity. This is reflected by the green color surrounding the CS in the LAT maps. The rest of the cycle was colored accordingly.

In the clinical environment, however, a diagnostically more valuable setting of the color map is frequently applied. An adjustment of the window of interest is suggested, which brings the head-meets-tail color shift (blue to red) right to the critical isthmus [188]. Based on the concept of a mid-diastolic potential, the window of interest for LAT annotation is centered on the P wave of the surface ECG. From an engineering point of view, this corresponds to the time when the majority of atrial tissue depolarizes. Accordingly, the limits of the window of interest correspond to the times at which little activity is present in the atria, coinciding to the wave passing through the critical isthmus. In clinical practice, this can be used to easily identify the isthmus by the color shift. Within this thesis, corresponding methods were developed to automatically adjust the window of interest for consistent visualization and to highlight areas suspected to be the critical isthmus.

First, the amount of covered cycle length in each atrium was evaluated. Assuming a macro reentrant mechanism limited to one atrium, the passively activated atrium is expected to show less cycle length coverage than the driving one. Thus the atrium showing more BCL coverage was selected as the one harboring the perpetuating mechanism. For this atrium, the course of the amount of active tissue was assessed in the second step, and its minimum used to define the time of activation for the critical isthmus. All LATs were subsequently re-referenced so that the window of interest began at the point in time at which the cardiac activation exited the isthmus. This is equivalent to shifting the phase of the flutter circuit if the propagation would be described in terms of angle instead of time.

The effect of this shift can be observed in Figure 11.21. While the general pattern of excitation is in agreement with the previous visualizations in Figures 11.17, 11.18 and 11.19, it can be noted that the activation of the inferior posterior wall is no longer located in the middle of the cycle. Instead, the head-meets-tail transition (blue to red) is set to be as small as possible, being much more localized and providing a potential spot for ablation.

In order to make the identification of the location of the isthmus easier, an approach was developed which highlights areas that exhibit activity during the time in which most of the atrial mycardium is at rest. Therefore all electrodes of one atrium were inspected individually. For each electrode, the time of the cycle was analyzed in which the electrode showed activity. The relative amount of active tissue was extracted within this time and subsequently its 0.1-quantile determined, reducing the effect of erroneous annotation.

Considering an electrogram that showed activity while huge parts of the atrium depolarize, the corresponding values for the relative amount of active tissue were found to be in the order of 0.1 (compare Figure 11.19). For an electrode which measured activity while the remaining mycardium was already depolarized, the values ranged in the order of 0.03. This only changed slightly by application of the quantile operation.

The results are visualized in Figure 11.22. For each scenario, different locations can be identified as possible candidates for the isthmus. These always comprised the true locations, being the lateral left atrial appendage (LAA) area in *sc12*, the anterior RSPV in *sc40* and the posterior RSPV ostium in *sc21*. However, additional areas like the lateral right atrial appendage could be identified. This could be explained by the fact that these were the latest depolarizing areas of the RA. Since the presented algorithm did not consider causality, it could not distinguish between the active areas causing subsequent depolarization and those just being activated last.

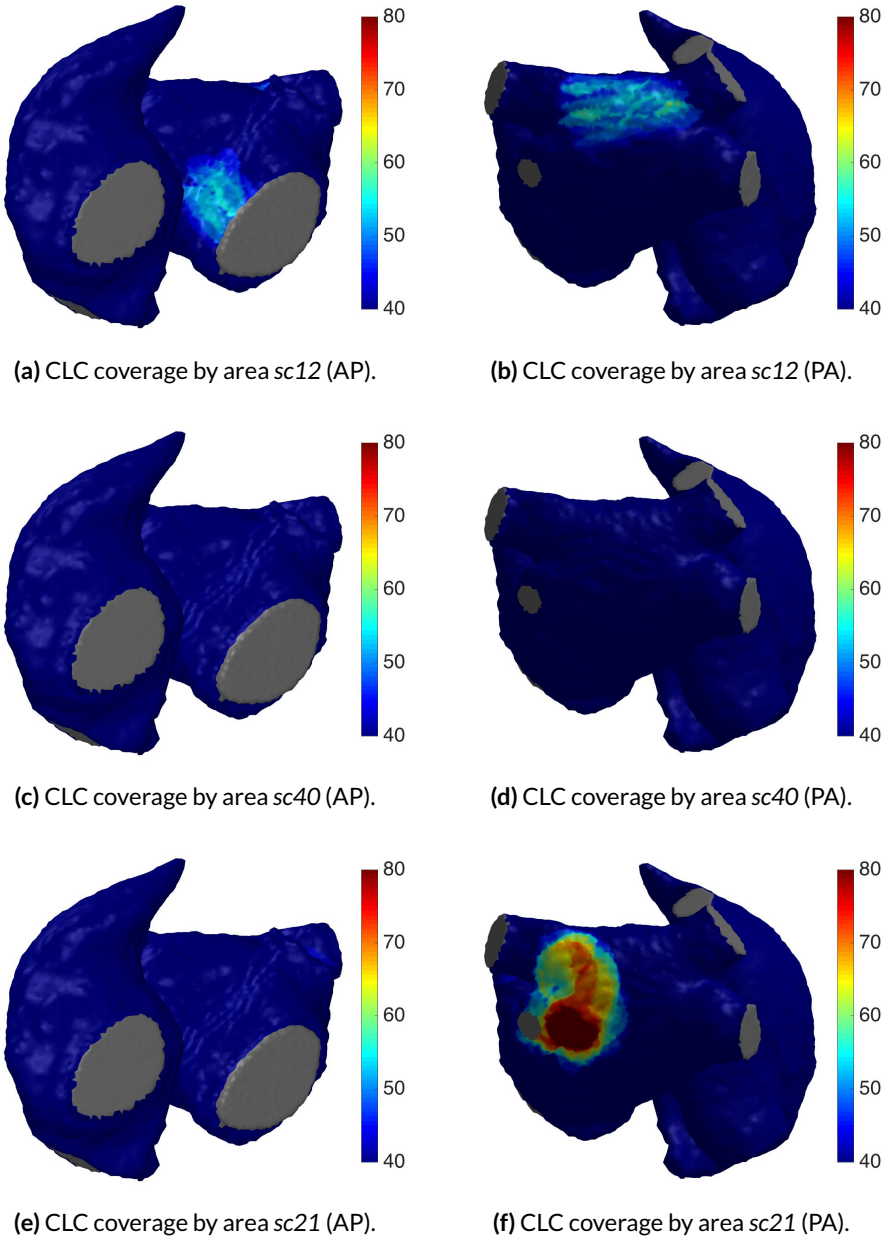

(a) CLC coverage by area *sc12* (AP).

(b) CLC coverage by area *sc12* (PA).

(c) CLC coverage by area *sc40* (AP).

(d) CLC coverage by area *sc40* (PA).

(e) CLC coverage by area *sc21* (AP).

(f) CLC coverage by area *sc21* (PA).

Figure 11.20: Area based cycle length coverage of sustained flutter. The local CLC was computed for an area with radius of 1 cm. For macro reentrant scenarios (*sc12*), the maximal values for cycle length coverage were about 62 % and could be found in regions of wavefront collision. For the focal source, CLC was below 40% (*sc40*). For the micro reentrant tachycardia, however, values of 100 % were observed. Their location was in agreement with the position of the driving circuit at the posterior LIPV ostium (*sc21*).

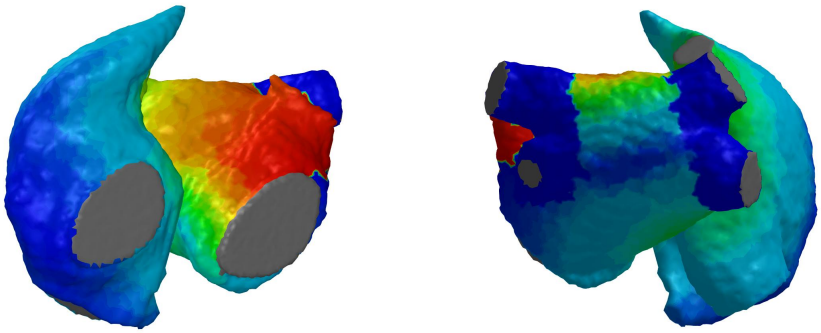

(a) LAT map *sc12* (AP).

(b) LAT map *sc12* (PA).

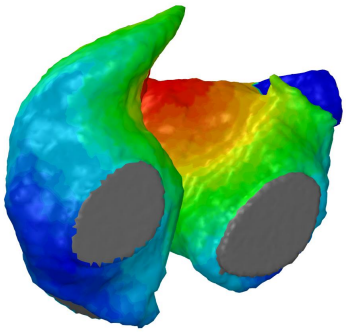

(c) LAT map *sc40* (AP).

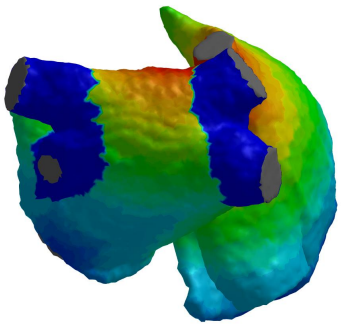

(d) LAT map *sc40* (PA).

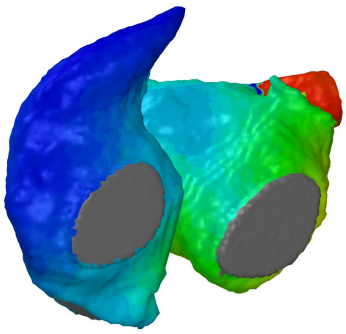

(e) LAT map *sc21* (AP).

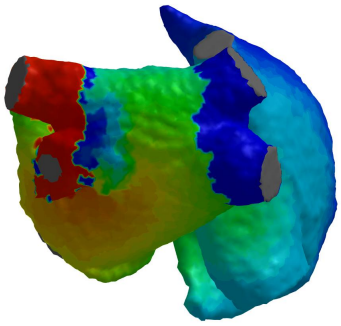

(f) LAT map *sc21* (PA).

Figure 11.21: Normalization of LAT maps to start at the diastolic isthmus. After the time of diastolic activity was detected, all LATs were re-referenced so that the beginning of the window of interested coincided with the time of exit of activation from the isthmus. By this, the spatial extension of the head-meets-tail phenomenon was strongly reduced (compare *sc12* in Figure 11.17).

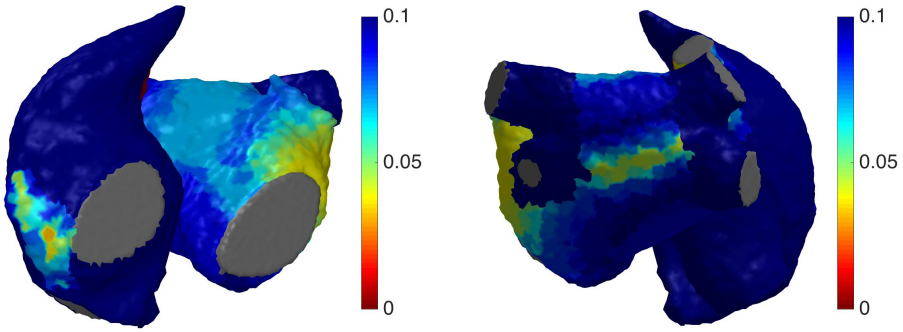

(a) Diastolic activity *sc12* (AP). **(b)** Diastolic activity *sc12* (PA).

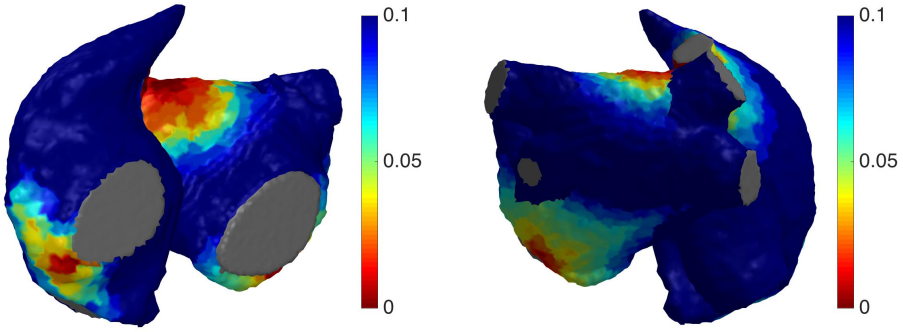

(c) Diastolic activity *sc40* (AP). **(d)** Diastolic activity *sc40* (PA).

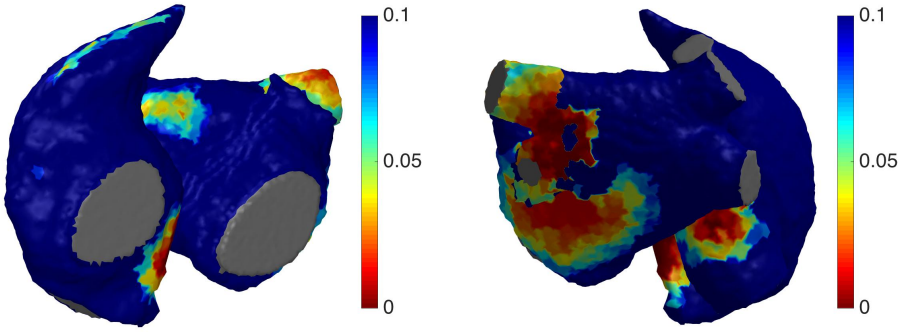

(e) Diastolic activity *sc21* (AP). **(f)** Diastolic activity *sc21* (PA).

Figure 11.22: Diastolic activity during atrial flutter. Red areas highlight potential ablation targets and always comprised the true driver. Additional areas were annotated as causality was not considered.

11.2.5 Conclusion

The mulitchannel analysis techniques demonstrated in the previous chapters were applied to the complete database of simulated AFlut cases from Table 10.3. The results of quantitative analysis are summarized in Table 11.7. For each scenario, the type of mechanism and the harboring atrium is given. Considering the global CLC as addressed in Chapter 11.2.2, both the total value as well as the values for each individual atrium are given. In the fourth column, the range of active tissue over time is given for each atrium as relative value. It is followed by the maximum CLC which was achieved in each atrium using the area-based approach depicted in Chapter 11.2.3. The minimal areas of active surface during one cycle for each atrium are listed in the last column.

Several aspects are of interest. First, the global CLC which was computed by considering all measurements from both atria reached 100% for all re-entrant mechanisms, while it reached only 85% for focal mechanisms (*sc40* to *sc43*). This was in agreement with clinical observations that reentry should be considered as driver if at least 85% of BCL can be mapped [225].

Second, the complete coverage was achieved only in the atrium which harbored the driver. The global CLC reached 100% for the RA measurement locations in *sc10* and *sc11*, both being right atrial tachycardias. In all other reentrant forms, the cycle was covered in the LA.

Third, the area-based CLC allowed to differentiate between macro- and micro-reentrant mechanisms. Although complete mapping of the cycle was achieved for all types of reentrant drivers, only the micro-reentrant types *sc20-sc23* and *sc50-sc54* exhibited complete local coverage within a field of diameter 2 cm. This was in agreement with literature values [211].

In agreement with all previous statements, the minimum of active surface area over time was found to be 0.0% for all atria in which no reentrant source was simulated. For all macro-reentrant mechanisms (*sc10-sc13*, *sc30-sc32*), the amount of active surface area exceeded 3cm^2 for any instance throughout the measurement, making the presence of an isthmus less likely. For most of the scar-related micro-reentrant scenarios *sc20-sc23*, however, the active surface area was found to be as small as 0.7 cm^2.

Concluding, it can be stated that all algorithms were able to extract diagnostically relevant parameters from the simulations which met the clinically expected values. Therefore the resulting workflow will be applied to clinical data in Chapter 18.

In addition to the above mentioned methods, further parameters of excitation could be considered to further support diagnosis. For example, conduction velocity could be assessed to identify zones of slow conduction. Various techniques were suggested for this task, like the Cosine Fit algorithm [161], and are well described in literature [226]. Parameters quantifying EGM complexity like approximate entropy [227] may also be of help to identify zones of dissociation or complex conduction.

ID	Mechanism	Global CLC value [%] RA / LA total	Active tissue range [%] RA LA	Area based max CLC [%] RA / LA	Active surface min area [cm^2] RA / LA
sc10	Macro	100 / 88	4.3 - 19	88 / 39	5.8 / 0.0
	in RA	100	0.0 - 13		
sc11	Macro	100 / 71	4.6 - 21	63 / 37	6.2 / 0.0
	in RA	100	0.0 - 18		
sc12	Macro	67 / 100	0.0 - 30	32 / 62	0.0 / 3.3
	in LA	100	2.8 - 11		
sc13	Macro	72 / 100	0.0 - 25	37 / 60	0.0 / 4.8
	in LA	100	4.0 - 12		
sc20	Micro	68 / 100	0.0 - 34	35 / 100	0.0 / 1.6
	in LA	100	1.3 - 26		
sc21	Micro	53 / 100	0.0 - 26	27 / 100	0.0 / 0.4
	in LA	100	0.3 - 21		
sc22	Micro	65 / 100	0.0 - 24	33 / 100	0.0 / 0.6
	in LA	100	0.5 - 15		
sc23	Micro	77 / 100	0.0 - 23	34 / 100	0.0 / 0.7
	in LA	100	0.6 - 16		
sc30	Macro	91 / 100	0.0 - 17	35 / 36	0.0 / 3.1
	in LA	100	2.5 - 9		
sc31	Macro	78 / 100	0.0 - 21	39 / 39	0.0 / 3.6
	in LA	100	3.0 - 11		
sc32	Macro	91 / 100	0.0 - 17	37 / 48	0.0 / 3.4
	in LA	100	2.8 - 10		
sc40	Focal	75 / 80	0.0 - 16	29 / 36	0.0 / 0.0
	in LA	85	0.0 - 13		
sc41	Focal	51 / 53	0.0 - 33	27 / 28	0.0 / 0.0
	in LA	70	0.0 - 22		
sc42	Focal	46 / 43	0.0 - 28	20 / 20	0.0 / 0.0
	in LA	59	0.0 - 19		
sc43	Focal	45 / 42	0.0 - 33	21 / 21	0.0 / 0.0
	in LA	63	0.0 - 24		
sc50	Micro	66 / 100	0.0 - 30	36 / 100	0.0 / 0.4
	in LA	100	0.4 - 16		
sc51	Micro	74 / 100	0.0 - 21	38 / 100	0.0 / 0.3
	in LA	100	0.2 - 16		
sc52	Micro	84 / 100	0.0 - 21	51 / 100	0.0 / 2.8
	in LA	100	2.3 - 15		
sc53	Micro	88 / 100	0.0 - 25	48 / 100	0.0 / 2.4
	in LA	100	2.0 - 15		
sc54	Micro	92 / 100	0.0 - 22	52 / 100	0.0 / 2.7
	in LA	100	2.2 - 13		

Table 11.7: Flutter scenarios with results of automated analysis. See text for detailed discussion. For details about each scenario, see Table 10.3.

CHAPTER 12

Analysis of Continuous Excitation during Fibrillation

Major challenges in the development of algorithms for the analysis of electrograms (EGMs) recorded during atrial fibrillation (AFib) are posed by the dynamic changes of the observed process over time. Although dominant mechanisms may perpetuate the arrhythmia, signals recorded by individual electrodes frequently exhibit a pseudo random behavior. To account for this, several statistics-based approaches were implemented and utilized during the presented research. As described in Chapter 12.1, a fuzzy-decision-tree was applied to classify complex fractionated atrial electrograms (CFAE) based on their morphology. Differentiation between different types of activation patterns was addressed with a support vector machine (SVM) as outlined in Chapter 12.2. Modeling the excitation dynamics directly was central aspect of the research presented in Chapter 12.3.

12.1 Classification of CFAE Signals

Ablation of CFAE has been suggested as additional treatment strategy with favorable success rates [56]. Therefore, this approach is frequently applied after isolation of the PVs in patients with persistent AFib. Only two algorithms for the automatic identification of CFAE are implemented in current electroanatomical mapping system (EAMS), and the need for manual and thus subjective parameter setting is one drawback of these algorithms. In addition, they only assess single EGM characteristics which may or may not relate to clinical experience from different centers. Consequently, interpretation of studies addressing the effect of CFAE based substrate ablation is difficult [6, 7]. Several groups have started work on the automatic and reliable identification of potential ablation targets [201, 228–234].

In previous research, a new algorithm for CFAE annotation was developed and published [208]. Morphology of the EGMs was assessed by 18 descriptors, which were jointly analyzed by a fuzzy-decision-tree. This classifier was trained by annotated EGMs, allowing to respect different levels of electrogram complexity. This approach was considered to more

realistically reflect clinical assessment of potential ablation targets. It will be outlined in the following and compared to clinical criteria in Chapter 19.

Classes of fractionated electrograms Studies have shown that the result of automatic annotation with the conventional algorithms do not always concur with clinical perspective [91]. To be of real help for physicians, however, resembling their judgment is required. Based on this clinical experience, four different classes of CFAE were defined. *Class 0* was defined as being non-fractionated with high activation frequency. Fractionated EGMs with periodic activity were labeled *class 1*. If a mixture of both fractionated and discrete activities was observed, the signal was annotated *class 2*. *Class 3* represented CFAE with continuous activity. Corresponding EGMs are plotted in Figure 12.1 and exhibit an increasing degree of complexity.

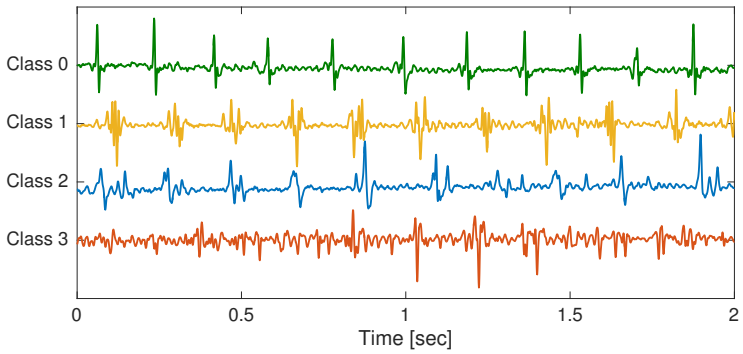

Figure 12.1: EGMs representing different classes of CFAE signals. Classes 0 to 3 indicate an increasing degree of complexity, ranging from period discrete activity to continuously fractionated EGMs.

Classification using the fuzzy-decision-tree A database of 605 EGMs from 11 different patients was compiled for learning and benchmarking. All underwent catheter ablation for AFib at Städtisches Klinikum Karlsruhe and provided written informed consent. Each signal was 5 s long and sampled at 1200 Hz. All EGMs were annotated independently by two experts from different centers according to the criteria outlined above. The annotation matched in 429 signals, providing the training data for the fuzzy decision tree (FDT). This data base has meanwhile also been used by other groups in research on CFAE complexity [227, 234].

Aiming for classification, a total of 18 features was subsequently computed to describe the morphology of each signal. Features were selected to describe the time domain behavior (e.g. length of activation complexes, mean number of local maxima per active segment, ...) as well as frequency information (e.g. wavelet decomposition). Also similarity-based measures and amplitude statistics were included (see [208] for details).

Subsequently, a FDT was implemented, validated and benchmarked to distinguish between these CFAE classes. This type of classifier was chosen as it provided a measure for certainty for each annotation and the fuzzy zones were expected to account for a potential

overlap between different CFAE types. Using 10x5 cross validation, an average correct rate of 81±3% was achieved. It has been applied during the presented research in region specific study of fractionation as described in Chapter 19.

12.2 Classification of Cardiac Excitation Patterns

The fuzzy decision tree outlined in Chapter 12.1 was designed to determine potential ablation targets for substrate modification. Therefore, the complete EGM of duration 5 s was assigned to one class. In a complementary approach, a classifier was developed to differentiate between the most common types of excitations that could be passing the catheter. A corresponding support vector machine was trained on simulated activation patterns and subsequently applied to clinical data. This work was central part of a student project [168] and is currently submitted for publication. The project was co-supervised by Markus Rottmann, who also provided the simulated depolarization patterns.

Training data and feature definition Simulated data were used to train the classifier and verify the suitability of the suggested features. Four common depolarization patterns were virtually mapped to obtain a variety of excitations for training. Snapshots of transmembrane voltage (TMV) are shown in Figure 12.2 for each pattern. Plane wave, block and ectopic focus were simulated on a square patch of 400 voxels edge length and 0.2 mm spatial resolution. The rotor was simulated on a more detailed geometry (1000 × 1000 voxels with 0.1 mm isotropic edge length). The electrophysiological cell models developed by Courtemanche and Nygren were used for simulation in *acCELLerate*, respectively. All scenarios were induced by suitable stimulation protocols.

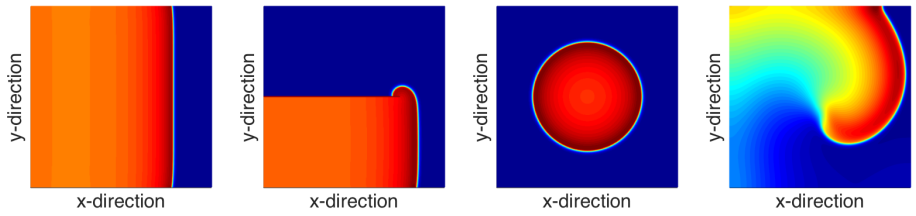

(a) Plane wave. **(b)** Block. **(c)** Focus. **(d)** Rotor.

Figure 12.2: Simulated excitation patterns. Four types of depolarizations were simulated and subsequently mapped with virtual catheters. These represented different dominant types of excitation patterns: Plane wave (a), line of block (b), ectopic focus (c) and rotational excitation (d).

Virtual models of three different catheter types were available for this research project, being a circular single-loop catheter, a double loop spiral and a star-shaped catheter resembling the PentaRay™ design. Diameter of the single-loop catheter was variable between 15 and 25 mm, and both 10 and 20 pole configurations could be defined. For the PentaRay™,

both the 4-4-4 mm equal spacing and the paired spacing of 2-6-2 mm was addressed. The presented data was generated using a single-loop 20 pole catheter with a diameter of 25 mm. The catheter was moved over the patches in equidistant steps and rotated between 0 and 180° at each position. Temporal scaling was included to evaluate the effect of conduction velocity (CV) between 500 and 1000 mm/s. In order to reduce computational time, forward calculation of extracellular potentials was waived. Instead, the local activation time (LAT) for each electrode was determined based on the maximum TMV upstroke velocity of the nearest tissue voxel. Corresponding LAT patterns over all measuring electrodes are depicted in Figure 12.3.

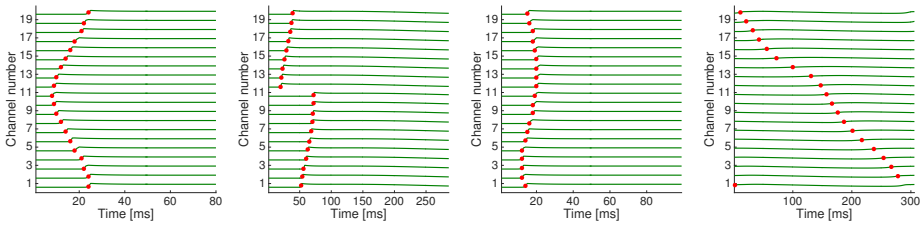

(a) Plane wave. **(b)** Block. **(c)** Focus. **(d)** Rotor.

Figure 12.3: Exemplary LAT patterns for the simulated scenarios. A computational 20 pole spiral catheter was used to virtually map the excitations shown in Figure 12.2. The maximum upstroke velocity of the TMV (green lines) from the closest tissue voxel was detected to assign the LAT for each electrode (red dots). Combined assessment of all electrodes exhibited specific LAT patterns for all scenarios, inspiring the research on this approach.

Striking similarities were observed in the LAT patterns of different phenomena, when the catheter was positioned away from the center of the mapping field. If the block scenario was mapped, for example, but the catheter did not overlap the block line, it just saw a plane wave passing by. This was found to cause incorrect classifications during initial evaluation. Therefore, new subclasses were defined which more precisely described each scenario by specifying if the catheter overlapped with the area of interest (*Near*) or not (*Far*). This lead to following seven classes of excitation patterns: *Plane*, *FocusFar*, *FocusNear*, *OffBlock*, *OnBlock*, *RotorFar* and *RotorNear*

A total of 500 realizations was generated for each class. After visual inspection of these LAT patterns, different features were developed which could be summarized in the following groups: Fitting features, spectral analysis of the LAT pattern, statistical values of pairs of LATs at defined locations, cycle length coverage and baseline duration within the cycle or LAT pattern.

An SVM with Gaussian kernel was chosen as classifier to distinguish between the different scenarios. It was first trained with all features and benchmarked using 10-fold cross validation. Kernel scaling parameter σ and penalty parameter C were initially set to standard values as described in literature [235], yielding a resulting classification accuracy of 85.1%.

Subsequently, feature selection was performed. Classification accuracy of each single feature was first assessed individually. Subsequently, canonical correlation analysis was

used to assess redundancy in linear combination of features. Features were discarded if they showed a predictive accuracy below 0.7 or similarity above 0.98 by the combination of more significant features. The resulting reduced feature set was used for cross-validation and showed increased performance of 91.9% for noise-free data.

In a last step, σ and C were optimized empirically by assessing classification performance for all parameter combinations. The search range was set to have the best accuracy inside the given value boundaries. The resulting classification performance resulted in 97.4%. This proved the validity of the chosen approach and the usability of the developed features. The chosen technique additionally allowed to obtain a posterior probability, indicating a trustability measure for the annotation.

Application to clinical data during flutter After the classifier was successfully trained on the simulated data, it was applied to clinical cases of different complexity. First data from atrial flutter (AFlut) was analyzed. Clinical mapping data was available from a patient who presented with a perimitral macro reentrant mechanism and was mapped using a 20 pole spiral catheter. During mapping, a line of block could be observed at the anterior wall.

In measured data, LATs could not be defined based on TMV, as this value was not acquired during mapping. Instead they were determined based on the energy of bipolar EGMs as outlined in Chapter 8.1. Two different catheter positions were chosen to test the classification approach. First a location at the posterior wall was analyzed, which exhibited a depolarization pattern like a plane wave. The catheter position and the respective LAT map are shown in Figure 12.4 (a). The normalized energy and the annotated LATs are plotted in part (b), followed by the classification result in (c). For the latter, the relative number of annotations is given for all seven possible subclasses. As the general shape of a plane wave would also match to the scenarios *FocusFar* and *OffBlock*, all these reasonable scenarios were marked in green. In contrast, the scenarios *OnBlock* and *RotorNear* were colored red, as these could be excluded by visual inspection of the corresponding clinical LAT map. The resulting annotation was *FocusFar* for about 70% of annotated waves.

Next a position directly over the block line was classified. Data and resulting annotation are shown in Figure 12.5. Indeed, the scenario *OnBlock* was correctly identified in all cases.

Application to clinical data during fibrillation Finally, the classifier was applied to a set of continuous data recorded during AFib. The EGMs were acquired with a 10 pole spiral catheter in a 65 year old female undergoing routine catheter ablation for persistent AFib. LATs were determined in the bipolar signals based on local energy maxima and respecting a refractory period of 150 ms. The EGM with least noise between atrial activities was chosen as reference channel. In this channel, the dominant frequency was computed as described in Chapter 8.2. A window of 66% of the local cycle length was then set around the activations in the reference channel and subsequently wavefronts were defined within this window in

(a) Clinical map.

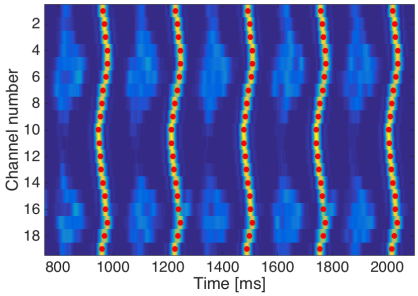

(b) Annotated LATs.

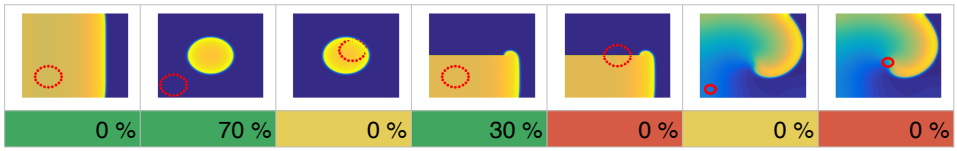

(c) Classification outcome.

Figure 12.4: Classification of a clinical depolarization pattern of type plane wave. The LAT map at the catheter position indicated an excitation by a planar wavefront (a). This was in agreement with the sinusoidal shape of the LAT pattern, which is plotted on top of the instantaneous energy of each channel (b). Pictograms indicate all possible subclasses for annotation, in which reasonable outcomes are marked in green. Excitations within this case were most often classified as slightly curved plane wave of type *FocusFar* (c).

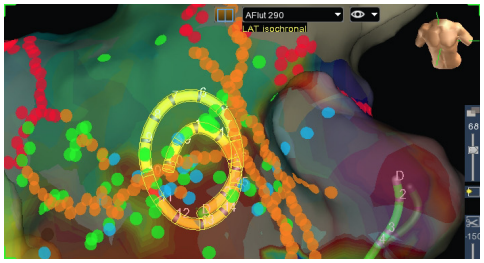

(a) Clinical map.

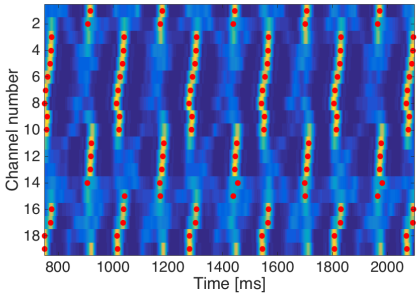

(b) Annotated LATs.

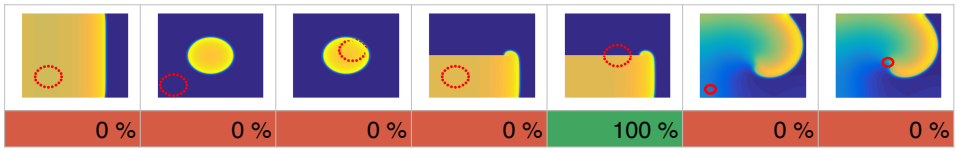

(c) Classification outcome.

Figure 12.5: Classification of a clinical depolarization pattern of type block. The catheter was placed directly on a line of block (a). Correspondingly, EGMs showed activity in two distinct parts of the atrial BCL (b). The *OnBlock* scenario was identified clearly (c). (See Figure 12.4 for details).

all other simultaneous EGM traces. Three representative activation patterns are shown in Figure 12.6.

As the true excitation pattern was not known for these clinical data, it was not possible to quantitatively assess the correctness of annotation. Qualitative assessment, however, indicated a high presence of strongly curved or discontinuous conduction patterns. Within 14 segments of total duration 159.7 s, 738 individual excitation waves were identified. From these, 78% were annotated as *RotorNear* and 21.7% labeled as *OnBlock*. No pattern was classified as being plane wave.

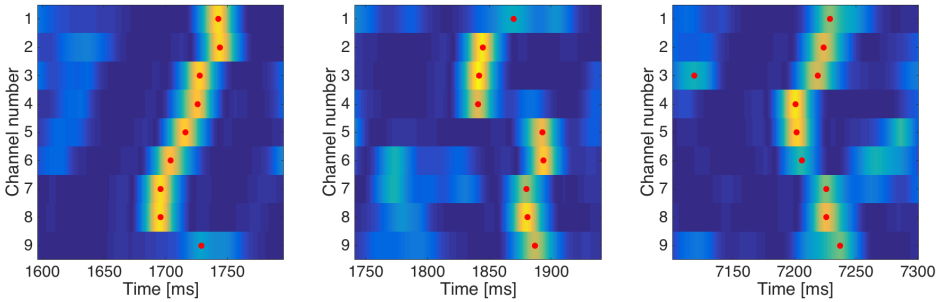

(a) Rotor near. **(b)** On block. **(c)** Focus near.

Figure 12.6: Classification of clinical depolarization patterns during AFib. Three scenarios were selected for demonstration, which were classified as *RotorNear* (a), *OnBlock* (b) and *FocusNear* (c).

Discussion and conclusion The identification of depolarization patterns during AFib would help to better understand the underlying mechanisms and represent a major progress in the design of patient-specific treatment strategies. Classification could very well help to distinguish between the dominant types of excitation, allowing physicians to gain a first impression of the observed processes.

Within this chapter, the concept of a corresponding classifier was presented. Simulated data was used to define suitable features for discrimination between different activation patterns and to benchmark the resulting classifier. A classification accuracy of 97.4% confirmed the suitability of the chosen approach of using a kernel SVM.

The concept was subsequently applied to clinical cases, in which promising results were achieved for AFlut data. Analysis of AFib EGMs, however, did not show any plane wave but indicated a strong bias towards classes of strongly curved or discontinuous conduction. Although the occurrence of at least some plane waves could have been expected, there was no proof to assume that these assignments were incorrect. A more detailed differentiation between pattern, however, would be desirable also during mapping of AFib.

Two ideas may help to explain this outcome. First, rather idealized simulations of all scenarios were used during the learning phase. Although they did include realistic CV and setup dimensions, and temporal jitter was added to the LATs, they did not account for anisotropic conduction or catheter deformation / imprecise localization. This variety of depolarization patterns could be included into future simulation setups, potentially providing more realistic data. Second, the implemented features may have been not able to cope with

the increased complexity of clinical scenarios. When a broader set of simulation setups is available, a second look on the feature definition may be appropriate.

Concluding, the developed classifier very well indicated the increased complexity observed during AFib. Individual wavefronts were successfully detected subsequently classified also during AFib, providing a good proof-of-concept for this approach.

12.3 Statistical Modeling of Propagation Dynamics

Excitation dynamics during AFib can be quite complex. For treatment, however, knowledge about the dominant excitation pattern would be of interest. Multivariate autoregressive modeling was suggested in literature as one way to identify the underlying mechanism during cardiac excitation. It was successfully applied to simulated and measured data from AFlut and AFib during initial work [236]. Subsequently, this approach was extended to sparse modeling, which allowed to incorporate the distance between measuring points into model estimation [237]. Due to the large diameter of basket-type catheters, this was considered a very favorable property for correct estimation of excitation patterns. The corresponding approach for partial directed coherence (PDC) analysis was implemented at Institute of Biomedical Engineering (IBT) within the scope of a student project [192]. Central mathematical aspects, its potentials and limitations will be outlined in the following.

Estimation of sparse multivariate models for excitation dynamics Considering EGM data with N channels, the corresponding N-dimensional multivariate signal $\mathbf{x}$ can be represented for each time step n as weighted sum of the m past values according to

$$\mathbf{x}(n) = \sum_{k=1}^{m} \mathbf{A}_k \mathbf{x}(n-k) + \mathbf{w}(n). \tag{12.1}$$

The parameter matrices $\mathbf{A}_k$ (with $k = 1,\ldots,m$) describe the model behavior and are defined by $N \times N$ weighting coefficients $a_{ij,k}$. A white noise process is incorporated by $\mathbf{w}(n)$.

Equation 12.1 can be extended to T observations and expressed in matrix form to be [237]

$$\mathbf{X} = \mathbf{Y}\mathbf{B} + \mathbf{W}, \tag{12.2}$$

with

$$\begin{aligned}
\mathbf{X} &= [\mathbf{x}(m+1)\cdots\mathbf{x}(T)]^T = [\mathbf{x}_1\cdots\mathbf{x}_N] \\
\mathbf{W} &= [\mathbf{w}(m+1)\cdots\mathbf{w}(T)]^T \\
\mathbf{B} &= [\mathbf{A}_1\cdots\mathbf{A}_m]^T = [\beta_1 \ldots \beta_N] \\
\mathbf{y}_n &= [\mathbf{x}(m-n+1)\cdots\mathbf{x}(T-n)]^T \\
\mathbf{Y} &= [\mathbf{y}_1\cdots\mathbf{y}_m] = \begin{bmatrix} \mathbf{x}^T(m) & \cdots & \mathbf{x}^T(1) \\ \vdots & \ddots & \vdots \\ \mathbf{x}^T(T-1) & \cdots & \mathbf{x}^T(T-m) \end{bmatrix}.
\end{aligned} \tag{12.3}$$

Different methods can be used to estimate the parameters $a_{ij,k}$, like the ordinary least-squares solution as given by

$$\tilde{\mathbf{B}} = (\mathbf{Y}^T\mathbf{Y})^{-1}\mathbf{Y}^T\mathbf{X}. \tag{12.4}$$

The Bayesian information criterion was used to determine the optimal model order m. To introduce the sparsity in model estimation, an approach using the least absolute selection and shrinkage operator (LASSO) was suggested, as it allowed for both parameter selection and estimation [237]. To introduce a-priori knowledge about the distance information, an extended weight factor was defined being

$$\alpha_{i,j}(d_{i,j}) = \exp\left(\frac{1}{2}\frac{d_{i,j}^2}{\gamma_2^2}\right), \quad \gamma_2 > 0. \tag{12.5}$$

This factor increased with larger distances $d_{i,j}$ between electrodes i and j, fostering that the corresponding parameters will be estimated to be zero during model estimation. Parameter γ_2 could be adjusted to the specific mapping catheter.

To assess the presence of causal coupling in frequency domain, the PDC was introduced [238]. It is evaluated at a specific frequency, which is suspected to be the dominant frequency of the observed process. The significance of detected couplings was assessed by surrogate data testing [239]. Therefore a set of artificial surrogate time series were generated, which lacked the coupling to be assessed. Statistical testing of the resulting data indicated the significance of the coupling. All significant couplings were subsequently plotted into coupling graphs for visual interpretation. This process is summarized in Figure 12.7.

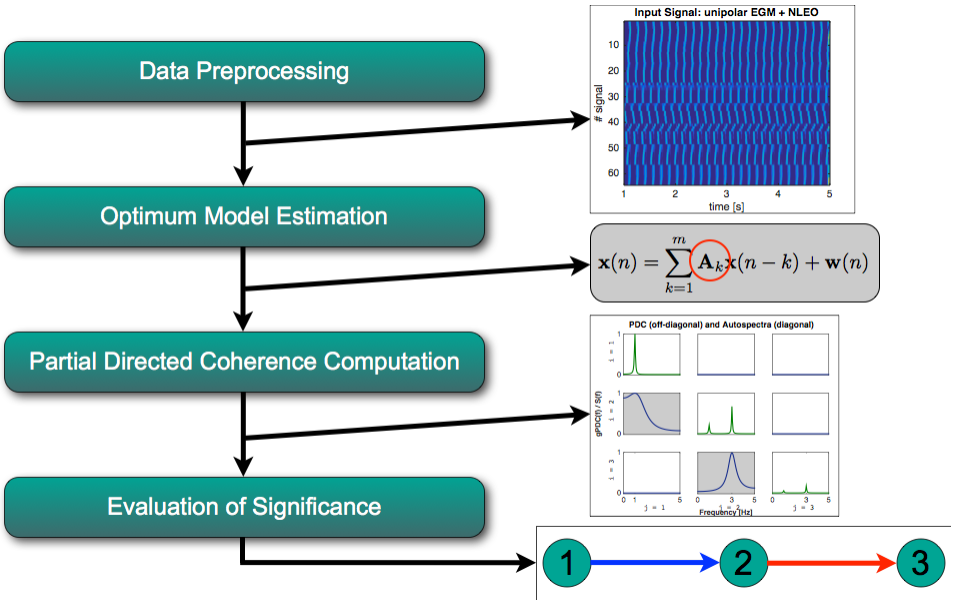

Figure 12.7: Concept of coupling analysis. See text for details.

Signal processing EGMs were preprocessed before model estimation to gain a low frequency signal with pronounced fundamental frequency. Therefore the non-linear energy operator (NLEO) was computed and subsequently low-pass filtered with a cut-off frequency of 24 Hz. Notably, the morphology of the signal was not retained. The resulting signal was down sampled to 100 Hz [236].

Performance assessment As the underlying excitation pattern was known in case of simulated data, it was possible to statistically assess the performance of coupling detection. Therefore ideal coupling graphs were generated based on the LATs measured at each electrode. Coupling was introduced between neighboring electrodes in the direction of excitation propagation.

Both the ideal coupling graph and the outcome of model were compared by computing the sensitivity (defined as probability to detect truly existing couplings) and the specificity (being the probability of rejecting a coupling which did not exist).

12.3.1 Model-based Analysis of Stable Excitation Patterns

Simulated atrial flutter To verify correct implementation in a well defined scenario, computational AFlut was processed. A focal mechanism was chosen for analysis, originating from the anterior right superior pulmonary vein (RSPV) (scenario *sc40* from Table 10.3). The tachycardia was simulated as described in Chapter 10.1.

Subsequently, a computational basket catheter was inserted (compare Chapter 4.2) and simplified EGMs computed at all electrode positions (see Chapter 2.4). The tachycardia mechanism and the resulting coupling graphs are shown in Figure 12.8. Surrogate data testing was used to identify significant couplings. Using the simple LS algorithm achieved a sensitivity of 0.25 and a specificity of 0.73. Using the dagLASSO yielded values of 0.21 and 0.87, respectively. Thus the approach did not detect all the couplings present the ideal coupling graph, but successfully rejected not existing connections.

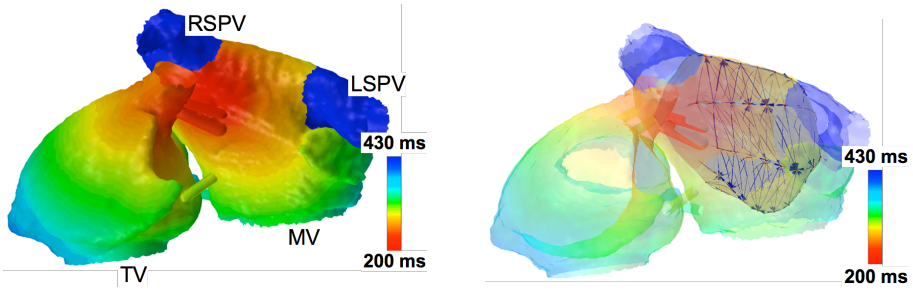

(a) LAT map. **(b)** Coupling graph.

Figure 12.8: Coupling during simulated AFlut. Focal activity originated from the anterior RSPV ostium (a, scenario *sc40* from the flutter database). A computational basket catheter was introduced and utilized to acquire virtual EGMs. The resulting coupling graph was in agreement with the LAT pattern, indicating propagation from septal to lateral along the splines (arrows in b).

Measured atrial flutter Data from a stable tachycardia was evaluated to obtain a first impression about clinical applicability. EGMs were recorded at the anterior wall during perimitral flutter (see Chapter 18.4.1 for a detailed case report). The catheter was positioned directly over an anatomical conduction block, causing a delay in activation of the inferior and superior anterior wall. A segment with 19 bipolar traces of duration 18 s was preprocessed and analyzed. Coupling was determined using the agLASSO and significance determined using surrogate data testing.

Catheter position, LAT map and the resulting coupling graph are plotted in Figure 12.9. Visual assessment of the activation pattern indicated a lateral to septal activation in the inferior part of the anterior wall, while the superior aspect was activated in opposite direction. This was very well represented by the couplings determined by PDC analysis. Notably, no couplings were determined crossing the anatomical block.

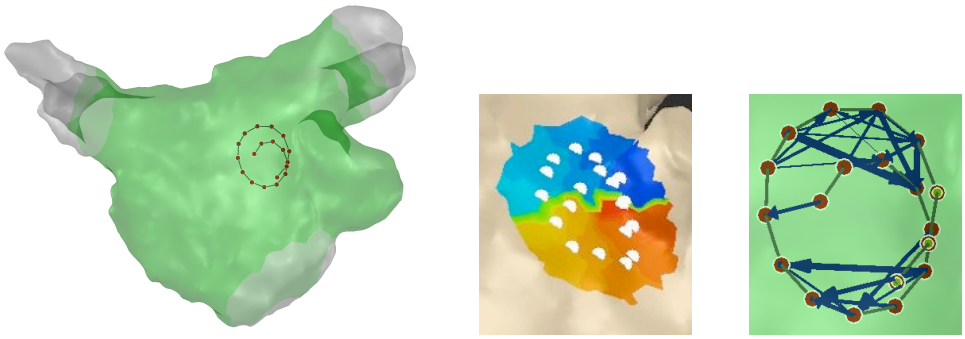

(a) Position of the catheter. **(b)** LAT map. **(c)** Coupling graph.

Figure 12.9: Coupling during clinical AFlut. A 20 pole spiral catheter was positioned on a line of block which was located at the anterior wall (a). An LAT map was generated for one BCL, confirming that both parts of the cycle were mapped (b). Coupling was in agreement with this observation and demonstrated propagation of two depolarization waves in antidromic direction (c).

12.3.2 Analysis of Unstable Excitation Patterns

Analysis of simulated fibrillation The excitation patterns during AFib change dynamically, complicating the identification of dominant mechanisms. To assess the effect of unstable depolarization on coupling, a sequence of simulated AFib was analyzed. Please refer to Chapter 17.1 for details about this scenario. It was virtually mapped using a 20 pole spiral catheter positioned at the inferior anterior MV annulus.

First the complete sequence between 0.6 s and 5.6 s was analyzed. Resulting coupling graphs, however, did not show a consistent pattern of activation (see Figure 12.10). Visual inspection of the TMV during fibrillation indicated a collision of two wavefronts in the interval from 0.6 s to 2.6 s, and a rather consistent depolarization caused by one broad wavefront in the following interval. Therefore, the analysis time frame was split in two parts

with each one being analyzed individually. Indeed, both coupling graphs demonstrated a more consistent activation pattern.

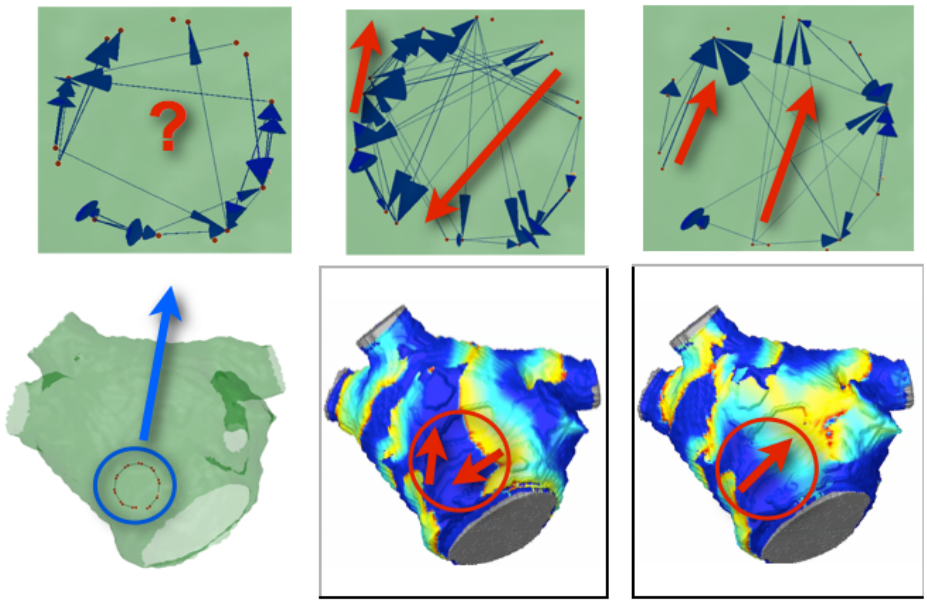

(a) Interval 0.6 s - 5.6 s. **(b)** Interval 0.6 s - 2.6 s. **(c)** Interval 2.6 s - 5.6 s.

Figure 12.10: Coupling in simulated AFib. A sequence of simulated AFib was virtually mapped using a single-loop spiral catheter with paired bipolar spacing (a). As analysis of a 5 s window produced contradicting outcomes, it was split into two time frames with each showing a rather consistent activation pattern. While two excitation waves entered the mapping field in the first interval (b), one dominant depolarization was observed after 2.6 s (c). Red arrows were manually added to ease interpretation.

Clinical recording of varying rhythms In order to evaluate the effect of an unstable and thus changing rhythm in clinical electrograms, a dataset with paced excitations was analyzed. Data was available from a previous research project [11, 161]. It was recorded using a 10 pole circular catheter which was positioned at the central posterior wall achieving full contact. Recorded electrograms contained 13 s of normal sinus rhythm (NSR) at about 66 beats per minuted, followed by paced excitations from CS 7/8 with 500 ms BCL.

EGM data were analyzed in a window of duration 8 s, which was shifted from the beginning of the dataset until it just covered paced excitations. The resulting coupling graphs are depicted in Figure 12.11. The initial segment from 5 s to 13 s only contained NSR and indicated a propagation originating from the upper right part of the plot. Anatomically, this was the direction of the RSPV and thus well matched with the depolarization pattern as expected during NSR. The coupling graph for the time span 13 s to 21 s just comprised paced episodes and well indicated the position of CS 7/8 as origin. The two intermediate segments (8 s to 16 s and 11 s to 19 s, respectively) were chosen to contain both types of excitations.

This was reflected by an increased diversity of directions in the coupling graphs, being well in agreement with the tendency to transition between both rhythms.

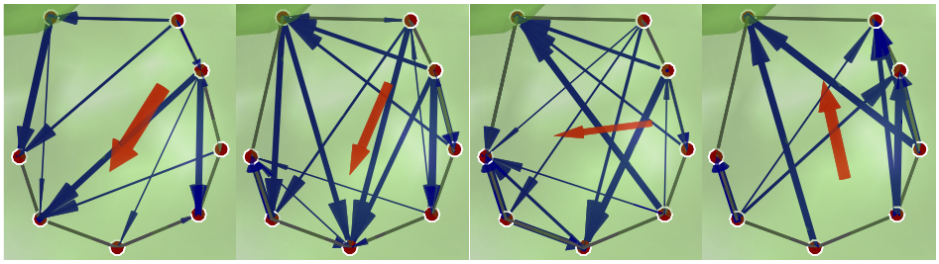

(a) Interval 5 s - 13 s. **(b)** Interval 8 s - 16 s. **(c)** Interval 11 s - 19 s. **(d)** Interval 13 s - 21 s.

Figure 12.11: Coupling during the transition from NSR to pacing. During NSR, the source of excitation was located towards the RSPV (a). As an increasing number of paced excitations was comprised in the analysis window, coupling was found more diffuse and the dominant direction shifted towards the CS ostium (b, c). Analysis of a segment containing only paced beats clearly pointed towards the stimulation bipole CS 7/8.

Discussion and conclusion The challenges in identifying mechanisms for perpetuation of AFib can largely be attributed to the dynamic alternations between different excitation patterns. Within this chapter, a sparse modeling approach was presented to identify the dominant depolarization type. It was already described in literature [237] but not yet available in our institution. After implementation, the concept was applied to simulated and clinical data of different complexity. For stable tachycardias like AFlut, the resulting coupling graphs very well reflected the excitation pattern. This held true not only for a simple planar activation sequence, but also for a block scenario in which bi-directional depolarization was present.

Subsequently, the sparse modeling approach was applied to inconsistent activation patterns, as these were expected to more realistically depict the clinical situation. Assessment with simulated AFib indicated ambiguous results when the evaluated signals were governed by more than one excitation pattern. This phenomenon was also observed during the analysis of clinical data, in which two different excitation patterns were induced by pacing. Restricting the analysis sequence to a time frame containing only one dominant pattern, the latter was well reflected by the coupling graphs.

During mapping of clinical AFib, however, no information about the consistency of the excitation pattern is available. Consequently it may be possible, that resulting coupling graphs represent a combination of different patterns. Although this information could be utilized to assess the local variety / complexity of the depolarization process, it may compromise the possibility to uniquely identify a dominant pattern.

CHAPTER 13

Assessment of Individual Excitation Waves

Continuous intracardiac electrogram data allows to evaluate the stability of the cardiac rhythm over several minutes. During sinus rhythm, e.g., the occurrence of extrasystoles can be assessed. And although the depolarization during atrial fibrillation (AFib) shows rather chaotic behavior, evidence has been found that certain phenomena can be observed regularily in an individual patient. This comprises the mechanisms during both the initiation of AFib [240] and its perpetuation [241].

Within this thesis, two approaches were developed to compare and cluster individual excitations passing a catheter. First, the morphology of all electrograms was evaluated to assess the stability of the underlying depolarization process. Second, the sequence of activation was assessed, being the pattern of local activation times.

13.1 Simulated Excitation Patterns

In order to benchmark the following classification techniques, the procedure *Pattern Composition* was implemented to model sequences of cardiac excitation and their respective electrograms (EGMs) on a planar patch. In addition, the fast-marching simulator (FaMaS) was applied to simulate different excitation patterns on a realistic biatrial surface model. This resulted in local activation times (LATs) for each vertex of the geometry, but without the corresponding EGM. Both will be presented in the following paragraphs.

13.1.1 Pattern Composition

Plane waves and ectopic foci were simulated using the bidomain model on a patch of cardiac tissue by Axel Loewe (10 cm x 10 cm, resolution 0.1 mm per voxel, thickness 1 voxel, remodeled model as in [101], compare Chapter 2.4). Plane waves originated parallel to each

side and the foci were located in each of the four corners. This resulted in a total number of 8 different excitation patterns. Single-loop spiral catheters with 20 electrodes and an equal interelectrode spacing of 4 mm and a paired spacing of 1-4.5-1 mm were modeled to gain realistic positions of the virtual electrodes. The unipolar electrograms (UEGMs) of each electrode were computed as 150 ms long snippets of EGM recordings for each excitation pattern and direction of incidence. Artifacts from the stimulation and boundary effects were removed by blanking, assuring that the signal morphology was not affected. Two examples for simulated excitation patterns and their respective EGM sequences are depicted in Figure 13.1.

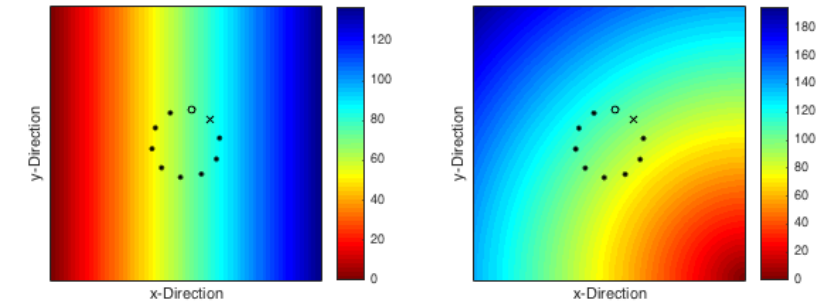

(a) Plane wave from left. **(b)** Ectopic focus from lower right.

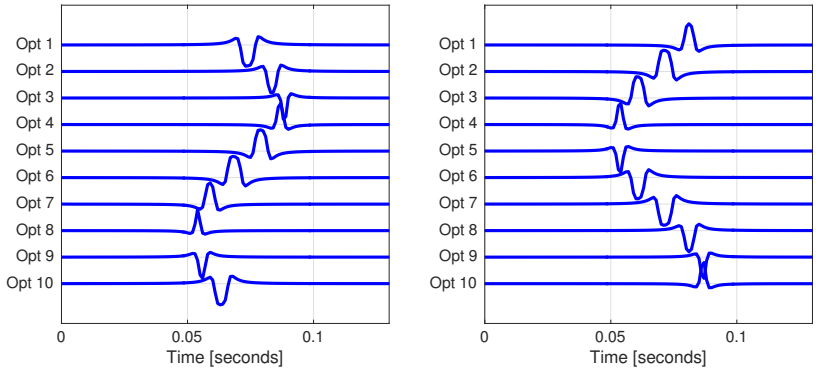

(c) EGM Plane wave from left. **(d)** EGM Ectopic focus from lower right.

Figure 13.1: Simulated excitation patterns with corresponding EGMs. A planar wave from the left was simulated (a) and the resulting BEGMs computed (c). Ectopic activity originating from the lower right corner is depicted as second example (b, d). Electrodes 1 and 2 are plotted as circle and star, respectively. Earliest EGM activity can be observed in the bipolar channels which point towards the source. Note that both the time of incidence and the morphology of each LAW vary for different excitation patterns.

The individual snippets were concatenated to simulate virtual measurements with well-defined properties. For each artificial measurement, both catheter type (equal vs. paired spacing) and total duration (in seconds) could be specified. Individual excitation patterns were added one after the other until the desired duration was reached. Therefore, first the

type of excitation (plane / focal, direction) was drawn from a uniform distribution of all eight initial patterns and added once to the EGM. Second, additional repetitions of each pattern were included to reproduce transient linking of excitation waves [241]. The number of additional repetitions was given by a realization drawn from a Poisson distribution according to the probability function

$$P(k) = \frac{\lambda e^{-\lambda}}{k!}, \tag{13.1}$$

with λ being the expected value. The time between individual excitations was chosen from a uniform distribution ranging from 50 to 150 ms. This approach allowed to test the complete processing workflow including the detection of LAWs in the EGMs.

13.1.2 Biatrial simulation of SVES

A second method was implemented to generate artificial mapping data representing the occurrence of supraventricular extra-systoles (SVESs). Simulations were conducted using the FaMaS and a heterogeneous anisotropic surface model [172]. They included excitations originating in the sinus node area, as well as SVES from the left and right superior pulmonary veins (PVs)). Paced excitations were simulated from the proximal coronary sinus (CS) region. After the desired origin for each pattern was defined on the anatomy, individual excitations were triggered from the 30 closest vertices. After simulation of all 120 individual cardiac excitations was completed, LATs for each of the 13,748 vertices of the anatomy were available.

Two catheters were simulated to gain realistic measurement positions, resembling the shape of a PentaRay™ catheter located at the posterior wall of the left atrium (LA), and a 4 pole ablation / mapping catheter in high right atrium (HRA) position. The LATs corresponding to the ten left and one right atrial positions were extracted from the simulations. Representative LAT maps of the four dominant patterns are depicted in Figure 13.2, together with the electrode locations. For subsequent analysis, synthetic LAT sequences were generated by randomly drawing the LATs from the 120 patterns according to an equal distribution. This data was used for benchmarking the developed algorithms within a student project [183, 242].

13.2 Evaluation of Electrogram Morphology

The morphology of activation complexes in a bipolar EGM highly depends on both tissue properties (e.g. fibrosis, scar) and the relative orientation between measuring dipole and progress of depolarization [90, 140]. When the physician holds the catheter at a stable position during mapping, both catheter orientation and tissue characteristics can be assumed steady during the measurement. Consequently, changes in the morphology of activation complexes can be related to changes in the excitation pattern itself. The recurrence of similar

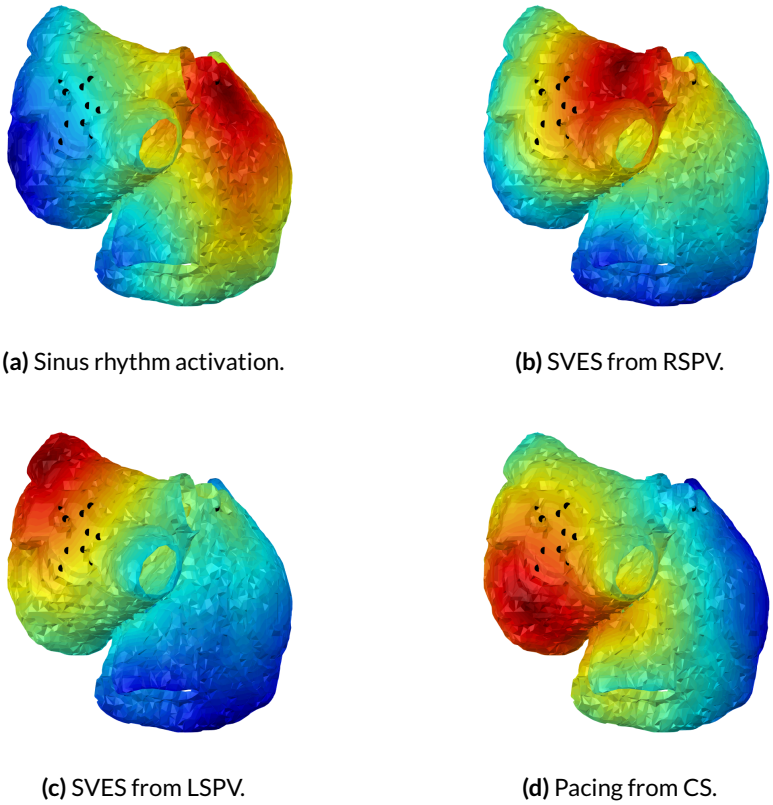

(a) Sinus rhythm activation.

(b) SVES from RSPV.

(c) SVES from LSPV.

(d) Pacing from CS.

Figure 13.2: Biatrial excitation patterns used to benchmark the algorithms for assessing spatio-temporal dynamics. The FaMaS was used to generate representations of four different excitation patterns, being NSR (a), SVES from the RSPV (b), SVES from the LSPV (c) and paced excitations from the CS (d). The LAT was extracted at 10 LA locations, resembling the shape of a PentaRay catheter. In addition, one RA electrode at HRA was recorded. These positions are visualized as black circles in the images. Time of activation is indicated in color from red to blue.

patterns allows to assess the stability of the excitation pattern [243]. Mathematical methods to quantitatively evaluate these aspects are presented in the following sections.

13.2.1 Detection and Comparison of Local Activation Waves

As a first step in the presented analysis, atrial activation complexes were detected in the continuous mapping data. For each of these LAWs, the LAT was assigned using the maximum of the non-linear energy operator (NLEO) as described in Chapter 8.1. A window of duration 90 ms was subsequently centered around each LAT and used to extract the local activity. This resulted in a total of N LAWs in the considered bipolar channel, each having a duration of p samples.

A measure to assess the morphological similarity between LAWs, was suggested in literature [244]. These were compared pairwise, resulting in a regularity index that represented the organization in an EGM. In order to reduce the influence of wall contact and thus signal

amplitude on the analysis results, it was suggested to normalize each LAW x_i using its norm to s_i as given by

$$s_i = \frac{x_i}{\sqrt{\sum_{j=1}^{p} x_{ij}^2}}. \tag{13.2}$$

In order to quantify the similarity between two normalized LAWs s_i and s_j, the distance metric $d(s_i, s_j)$ of the unitary sphere was determined according to

$$d(s_i, s_j) = \arccos(s_i \cdot s_j), \tag{13.3}$$

in which the arcus cosine of the scalar product of both waves was computed.

The similarity index S was defined by comparing the distance metric between two waves to a threshold ε. The relative number of similar pairs was subsequently assessed using the Heaviside function Φ

$$S(\varepsilon) = \frac{2}{N(N-1)} \sum_{i=1}^{N} \sum_{j=i+1}^{N} \Phi(\varepsilon - d(s_i, s_j)). \tag{13.4}$$

Based on study data, the parameter ε was suggested as $\varepsilon = \pi/3$ [244]. This technique was subsequently applied to determine the regularity of intracardiac recordings, in which $S \simeq 1$ indicated high regularity within the signal and $S \simeq 0$ chaotic patterns without repetition. This value was combined with information about the cycle length to identify signals with high rate and high similarity (suspected to be drivers for AFib) and signals with high rate and low similarity (suspected to indicate critical substrates) in recent work [166, 245].

Related research utilized the cross correlation coefficient between LAWs to assess their morphological similarity, suggesting a threshold of 0.8 to distinguish between similar and dissimilar pairs of LAWs [243]. The boolean value was plotted in a morphology recurrence plot for each signal, which in turn was quantitatively analyzed. The utilized features included statistics about the relative number of recurrences and information about the number of subsequent similar excitation patterns or those showing a comparable sequence over time.

13.2.2 Classification of Local Activation Waves

Both similarity index and recurrence plots judge similarity based on thresholding as a boolean value and operate on individual EGMs only. However, simultaneous multichannel mapping data is frequently available in clinical practice, and current research has indicated the presence of transient linking of excitation waves [241]. This has inspired the idea of a class-based analysis of intracardiac propagation patterns, which was part of the presented research and will be detailed in the following. In order to demonstrate and benchmark the performance of the proposed method, a database of simulated excitation patterns was generated using the *Pattern Composition* technique. Previous work in the field included the clustering of activity in the principal component analysis (PCA) space using the first 5 principal components (PCs) and a hierarchical cluster tree [132].

Within the scope of the presented work, the measures for similarity were first applied to cluster LAWs that exhibit comparable morphologies within one single channel. This allowed for easy visualization of similar activation patterns in the EGM and for assessment of the stability of each class quantitatively. Furthermore it facilitated to draw attention on patterns that occurred often.

First, the distance metric d was computed between each pair of LAWs based on the correlation coefficient. Then an iterative strategy was applied to generate clusters. In each iteration, the pair exhibiting closest similarity was processed. It was added to an existing cluster, if either a) one of the two LAWs was already part of the cluster and the similarity between the other LAW and all members of the cluster was below a manually set threshold thr_{intra}, or b) both LAWs were not yet assigned and below the threshold for an existing cluster. Otherwise a new class was generated. This process was repeated until the best similarity exceeded a given stop threshold thr_{stop}.

Two exemplary results of this process are visualized in Figure 13.3. An artificial EGM including 10 simultaneous bipolar channels of duration 40 s was generated based on the *Pattern Composition* method. LATs were detected in each individual channel using the NLEO-based approach (see Section 8.1). The correlation-based clustering was applied to the complete signal with thresholds of $thr_{intra} = thr_{stop} = 0.8$. The resulting class-membership of each LAW is indicated color-coded in the EGM as shown in Figure 13.3. Considering the 2.5 s of BEGM data from channel 1, 11 LAWs were classified into two different classes. Data from channel 2, however, were classified into three different classes, being in agreement with visual inspection of the respective EGMs.

A comparison between the class assignments in both channels indicated, that different excitation patterns may lead to similar activation complexes in some channels, while they show different morphologies of LAW in other channels: While the first 6 of the depicted excitations showed matching class labels in both channels, the LAWs 7 to 9 exhibited deviating combinations of annotations. This information can be exploited in multichannel analysis as will be outlined in the following chapters.

13.2.3 Quantification of the Stability of Excitation Patterns

Different measures were introduced to allow a quantitative analysis of the excitation patterns. These were inspired by work on morphology recurrence plots [243, 246] and adapted to the multi-class problem statement. While recurrence plots indicate the similarity of LAWs in general, respective measures for pattern specific evaluation need to consider each class of morphologies individually. Therefore the quantities were computed for each individual class as follows.

First, the number of singular classes was assessed. During classification, it is possible that only one single LAW is assigned to a class. In most cases, these single events are not important for further analysis. To measure the occurrence of these outliers, the amount of singular classes Cs was computed as percentage of all classes C. In addition, the relative

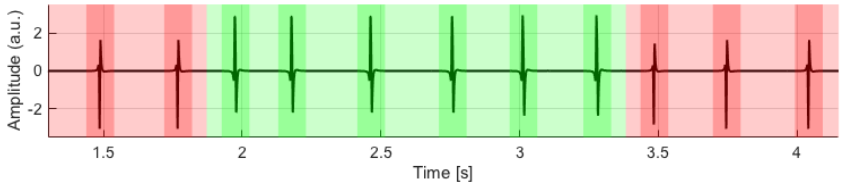

(a) Channel 1.

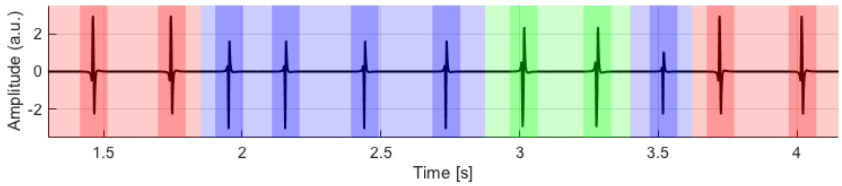

(b) Channel 2.

Figure 13.3: Clustering of LAWs in simulated bipolar EGMs. Two channels of simultaneous EGMs were processed individually, resulting in annotated LAWs for each EGM. The 11 consecutive activations shown in the figure were clustered in two and three classes for channels 1 and 2, respectively. Note that the classes were assigned for each channel individually, thus the annotation using a red background does not imply any relation between the LAWs of channels 1 and 2.

number of LAWs which were annotated using singular classes Ns was computed. It was based on the total number of identified LAWs N. These values provided general information about the measured site and could be compared to the embedding dimension of recurrence plots.

For each individual class c, the number of respective LAWs N_c was counted to indicate its frequency of occurrence within the mapped sequence. This value can be considered as recurrence rate RR_c for each individual class. It can be expressed as

$$RR_c = \frac{N_c}{N} \tag{13.5}$$

Vertical lines in the recurrence plot are known to indicated stationarity. In the class-based approach, this is reflected by consecutive LAWs being assigned to the same class. Laminarity LAM_c can be computed to assess the frequency in which LAWs of a specific class appear at least v_{min} times subsequently. v_{min} was set to 2 within this work. With $P(v)$ indicating the probability of a series of activations within the class having length v, LAM_c can be computed as

$$LAM_c = \frac{\sum_{v=v_{min}}^{N} vP(v)}{N_c}. \tag{13.6}$$

Trains of similar activations can also be quantified by computing the sequence mean length SM_c and sequence standard deviation SS_c of all sequences longer than v_{min}. The analog to SM_c is known as trapping time in recurrence plots.

Also the analysis of diagonal lines (besides the main diagonal) is of great interest in recurrence plots, as this indicates the presence of repetitive sequences. In the class-based approach, this would be reflected by alterations of specific class labels. Consequently, it was of no use when computed for each individual class. Instead, alternative measures could be used to quantify the information contained within the sequence of LAW classes. One

example is the Shannon's entropy H, which is computed for the sequence of LAWs according to

$$H = -\sum_{c=1}^{C} RR_c \cdot log_2(RR_c). \tag{13.7}$$

Additionally, it is possible to compute more complex parameters for the class patterns by considering word length or information gain as in text processing. Also time dependent analysis could be considered to assess the alterations in rhythm over segments exceeding 30 s. All of the above mentioned parameters can also be computed to assess the properties of a multichannel pattern as presented in the following section.

13.3 Multichannel Analysis

While the analysis of single channels only indicates the stability of the spatio-temporal excitation pattern over time, the evaluation of multiple simultaneous channels yields the possibility to assess the spatio-temporal pattern itself. Therefore, the LAWs detected in each individual channel have to be combined to wavefronts passing the catheter as will be outlined in the following section. Subsequently, activation patterns can be evaluated based on either the preceding classification of LAW morphology or the LAT pattern in the EGMs.

13.3.1 Combination of Excitation Wavefronts

After the LATs were identified in each channel individually, they were combined in order to construct complete wavefronts passing the catheter. An approach for the generation of the corresponding wavefront matrix (i.e. matrix with one row for each electrode and one column for each wavefront) was implemented as inspired by Richter [247]. It was extended by adapting its iterative clustering strategy as outlined in the following.

The wavefront matrix was initialized with all LAT values from a first channel. Then one channel after the other was inserted in the matrix, until all channels were processed. The order of this iterative processing could be specified by a user-defined quality criterion. This allowed to proceed according to the assumed quality of data (e.g. clear activations tend to have higher amplitude), spatial considerations (neighboring channels are expected to be more correlated than distant measurements), or other user-defined metrics.

The LATs of each processed channel were compared to the LATs of the first channel. Starting with the smallest time difference between LATs, the new values were inserted into an existing wavefront if their distances in time were below a given threshold $thr_{LATtime}$. Otherwise, the LATs were compared with the second already inserted channel and so on. Consequently, LATs within one channel were processed first if they showed a good fit to already existing values in the wavefront matrix. If the number of LATs in one channel was

lower (e.g. block or scar) or higher (double potentials), these were inserted to appropriate positions in the LAT matrix **W**:

$$\mathbf{W} = \begin{bmatrix} t_{1,1} & ud & ud & t_{1,4} & \cdots & t_{1,N_1} \\ t_{2,1} & t_{2,2} & t_{2,3} & t_{2,4} & & t_{2,N_2} \\ 0 & 0 & 0 & 0 & & 0 \\ \cdots & & & & & \\ 0 & 0 & 0 & 0 & \cdots & 0 \end{bmatrix} \tag{13.8}$$

After processing, each column of W represented one activation wavefront. If no LAT information was available for a specific channel within one wavefront, the respective entry was denoted as undefined (*ud*). Individual wavefronts could be rejected from analysis if these wave trains were only detected in few channels, potentially being far field. If the number of LATs within single channels was much lower than in others (e.g. due to bad electrogram quality, high amount of noise, ...), these channels could now be excluded from subsequent processing. Comparisons of the LAT patterns of subsequent activations is an alternative approach to evaluate the excitation pattern [247] and could potentially be combined with the morphological analysis as outlined above.

13.3.2 Classification of Propagation Patterns based on LAT

As outlined above, both catheter position and atrial anatomy can be considered stable, and thus changes of the LAT pattern of the wavefront matrix reflect alterations in the depolarization dynamics.

The degree of clustering of similar waves is strongly related to the diagnostic intention. Having the clinical applicability in mind, this process was designed as an operator dependent workflow. First those wavefronts were processed, for which LAT information in all channels was available. After this data was clustered and potentially annotated, the remaining wavefronts with one or more missing LAT data were classified.

For the initial process, the LATs of all channels were centered to have zero median. Median was used in this context to reduce the potential effects of erroneously annotated LATs (outliers). Then the PCA was computed on all centered LAWs. The number of utilized PCs N_{PC} was set to explain at least 90% variance (this threshold could be changed by the user if required). The corresponding N_{PC} scores were used for subsequent classification.

Since the number of classes for the clustering depends on the diagnostic aims as defined by the operator, the classification was performed in an interactive way. First, classification was computed for a series of classes, with the initial range of cluster numbers defined by the user (e.g. 2 to 5 classes). While a little number of classes would limit the possibility to distinguish different excitation patterns in this context, a large number of classes does also not seem appropriate since the dominant mechanisms should be in the focus of analysis. If a high number of classes is really required to appropriately represent the data, the suitability of this approach can be in doubt. The outcome was processed to generate a median LAT map for all classes and clusters. These were shown to the user in the form of 3D LAT maps,

projected onto the atrial anatomy. The user could inspect the properties of the individual LAT maps and decide up to which level the usage of individual classes was reasonable. The corresponding result was taken over as final annotation.

To demonstrate this approach, the simulated dataset described in Chapter 13.1.2 was used. A randomized sequence of the 120 different wavefronts was compiled and subject of analysis. The resulting dendogram plot is shown in Figure 13.4. It indicated that classification into increasing numbers of classes strongly reduced the dissimilarity within the clusters. For up to 4 clusters, increased performance by adding individual classes could be observed. Using more clusters led to a further improvement, however this was rather asymptotic. Although it would be highly desirable to automatically specify a threshold for the number of classes based solely on the dendrogram, this would be independent from any diagnostic use and was therefore not followed further.

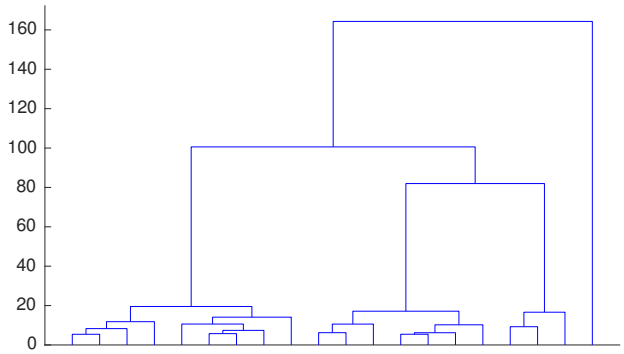

Figure 13.4: Dendrogram plot representing the hierarchical clustering. Horizontal lines represent the split into two new classes. The length of the vertical lines indicates the distance between both clusters. While the dissimilarity is large for a little number of classes, classes become progressively similar for an increasing number of clusters.

An example for clustering into varying number of classes is shown in Figure 13.5. Note that the division into 2 classes separated NSR originating in the RA from excitations starting in the LA. By averaging all LA excitations, a rather uniform excitation in the field of view of the PentaRay catheter could be observed for 2 clusters. Using 4 clusters resulted in LAT maps that closely resembled the demonstration examples of input data as depicted in Figure 13.2. Adding a fifth cluster did not generate a new cluster with significant differences in the field of view of the PentaRay catheter.

Different approaches can be applied to classify the PC scores, like Gaussian Mixture Models or a hierarchical cluster tree [233]. The latter was chosen for this clustering task and based on the furthest city block distance between the scores, since it is not a starting value depending algorithm.

Subsequently, wavefronts with missing LAT information could be classified. The class of each wavefront was determined by comparing its LAT pattern to the ones initially annotated.

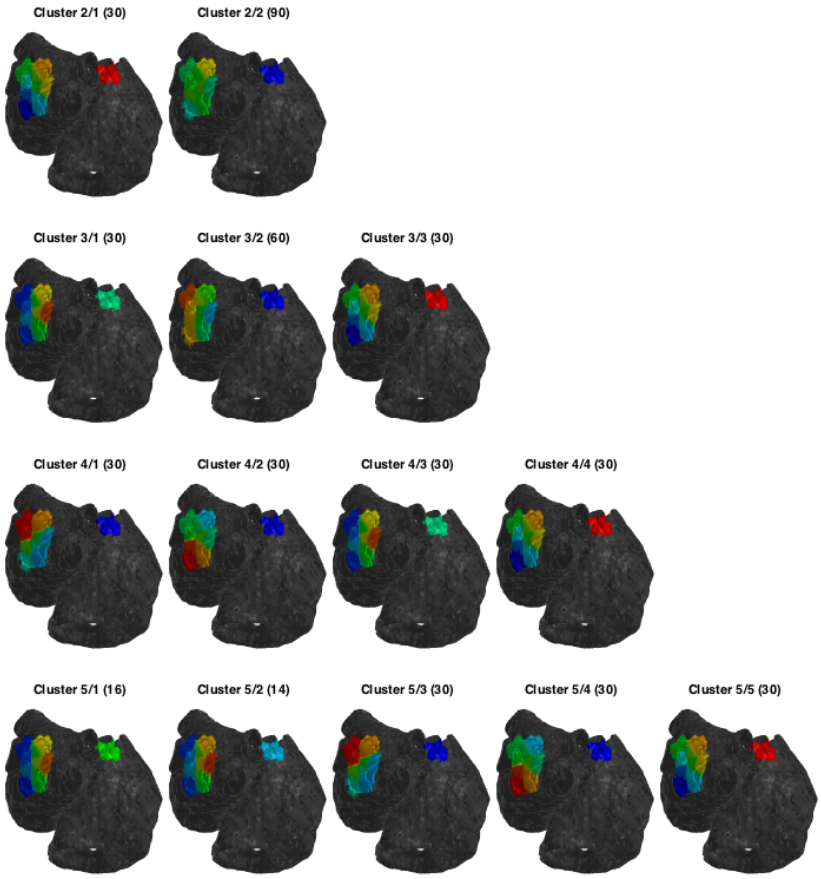

Figure 13.5: Representative LAT maps for different number of classes of excitation patterns. The complete dataset with 120 excitations was subject to analysis and classified in 2 to 5 classes. Numbers in parenthesis indicate the number of wavefronts within each class.

The root-mean-square-error between the known LATs was used as criterion for the quality of fit, allowing to discard wavefronts which did not show a consistent activation profile. Since the centering to zero median may have influenced the results, the optimum was searched within a time range of -50 to +50 ms.

13.3.3 Clustering of Propagation Patterns based on LAW Morphology

As described in Chapter 13.2, the morphology of LAWs in individual channels of EGM data could be assessed to identify prevailing types. Although this could provide information about the local stability of excitation patterns over time, it does not allow to draw conclusions about the direction of depolarization itself. Therefore, multichannel information was required.

After classification was performed in the individual EGM channels, data was combined again using the wavefront matrix. Although the exact LAT in the individual channel may not be unambiguous during fibrillation or fractionated activity, it was considered accurately

enough annotated to generate wavefronts. Each wavefront thus consisted of a sequence of class labels, one present for each annotated channel. As these represented categorical variables, the *k-medoids* function was applied with the Hamming distance for subsequent clustering, addressing the number of coordinates which differ.

This method was applied to the simulated EGM already presented in Chapter 13.2.2. After LAWs were annotated in all channels based on their morphology, the wavefront matrix was generated. Clustering was performed for a specified value of 8 classes. The result is depicted in Figure 13.6, in which the very same time span is shown as in Figure 13.3. However, all 10 channels are shown this time, while only leads 5 and 9 were plotted previously. The pattern which was detected exactly matched the initially simulated sequence of foci and planar waves.

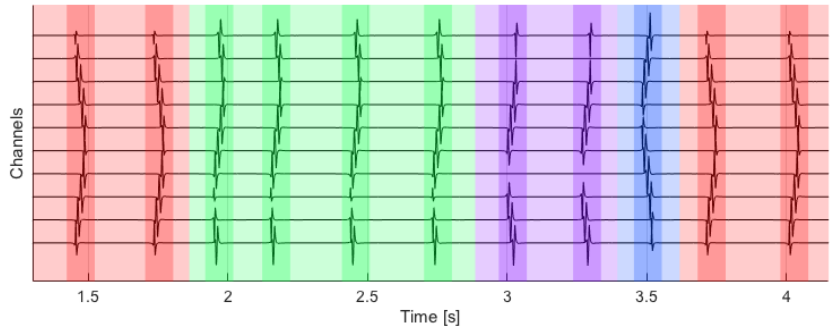

Figure 13.6: Multichannel clustering of LAWs based on morphology. Considering the individual LAW morphologies detected in all channels, the complete activation sequence was detected as initially simulated.

13.4 Discussion and Conclusions

Statistical approaches are frequently applied in the analysis of cardiac activity. Especially during AFib, classification of EGM morphology has been used to annotate potential ablation targets [201, 228–233, 248]. However, all these techniques assess a continuous trace of single channel EGM data with a typical duration of about 5 s.

Rationale and advantages To understand the underlying mechanisms and depolarization pattern during AFib, an analysis of each passing wavefront is required. Subsequently, statistics can be generated to identify the most prominent patterns and their dynamics. Using high-density epicardial mapping data, transient linking was observed between wavefronts during ongoing AFib. Given this rationale, trains of activations with similar direction could be expected during mapping. Their frequency may in turn provide information about the perpetuating mechanism.

The delineation of individual depolarizations is generally easier using electrodes of small size. These represent also very sensitive recording dipoles and are typically mounted on

high-density mapping catheters. As they only acquire information from a limited field of view, however, their ability to determine the macroscopic direction of depolarization may be more inaccurate as if panoramic mapping catheters were applied. To address both scales of analysis, two methods were presented within the previous paragraph, one utilizing the LAT pattern to distinguish between different types of activations (macroscopic), and one based on the morphology of individual LAWs (microscopic).

Both methods were successfully applied on respective sets of simulated data. Measures for quantification have been proposed in this chapter and can be used to assess the outcome of annotation statistically. The methods will be applied to detect SVES (Chapter 16) and in the analysis of AFib data (Chapter 20).

Limitations Despite the possible advantages and options to gain new insights into the perpetuation of AFib, fully automatic usage of the methods is currently limited. One major challenge is the definition of the number of clusters which should be used for classification. Especially for the classification of SVES, variable positions of measuring electrodes do not allow for a general fixed threshold. With respect to diagnosis, however, setting the required level of differentiation between varying excitations was considered an advantage which allows physicians to more precisely delineate between rhythms.

For the analysis of AFib data, however, additional research will be required to define an optimal set of parameters for analysis. As the underlying truth is not known, physicians do not have a point of orientation.

Especially in the presence of complex depolarization pattern, the unambiguous annotation and generation of the wavefront matrix may be complicated. This is one aspect to consider during the mapping of AFib.

CHAPTER 14

Systems and Programs for Clinical Application

It cannot be questioned that physicians with year-long experience in electrophysiological examinations are experts in the diagnosis of cardiac arrhythmias. However, the amount of electrogram data which is acquired using state-of-the-art EAM systems, poses a huge challenge for any human expert. New algorithms were shown to be able to extract diagnostically relevant information from this mapping data. These algorithms were inspired by and designed according to expert experience, and demonstrative examples have indicated their general usability. However, any analysis cannot help in the treatment of a current patient if it is performed weeks after the procedure.

One important technical limitation hampers the application of algorithms in the clinical environment, which is that EAM systems prohibit the testing of new algorithms on the system itself. Analysis on a second system is generally possible, it requires, however, access to the clinical data.

Therefore it was one goal of this research project to setup a system which comprised the complete workflow from data acquisition up to visualization of the final analysis result. Therefore an iMac was setup up with all required software and installed in the Städtisches Klinikum Karlsruhe. The software comprised MATLAB for data analysis, as well as Paraview and the custom made visualization platform KaPAVIE for the visualization [146].

14.1 Requirements

Several requirements can be formulated considering both the clinicians' and engineers' perspectives.

Clinical requirements Some aspects have to be met by any system in the clinic. First, these address safety issues, so that the success of the procedure is not compromised in any

way. Second, the system has to be accepted by the physicians, which leads to additional design considerations. Following issues were identified as important aspects:

- Compliant with safety regulations
- No disruption of the clinical procedure
- Correct and rapid processing
- Suitable visualization of results

As only already existing equipment and standard laptops were used for processing, the first point could easily be fulfilled. Most analysis was done retrospectively after the procedure was finished. If technical personnel was present during the procedure, it stayed in the background so that neither the physician nor the workflow was impacted.

With respect to processing speed, discussions with physicians revealed that a time of about 5 min for signal analysis was considered short enough to be potentially included in a clinical routine. In terms of visualization, it should be in agreement with common data presentation styles as much as possible. This comprises typically used values for ECG sweep speed or familiar color scales.

Requirements from engineering perspective Also from the engineering perspective, several requirement can be formulated which simplify subsequent data analysis:

- Standardized workflow
- Clear naming conventions
- Usage of predefined equipment and settings
- Availability of all data
- Comprehensive documentation of all procedural details and relevant events

As the initial treatment approach may be adapted during the procedure due to unexpected events, it is generally difficult to perform exactly according to a predefined and standardized acquisition protocol. Therefore, flexibility is required on the engineering side. Since the time for study specific documentation during the procedure is rather limited, a debriefing with the physician has proven reasonable. As access to the clinical data acquisition systems is limited due to safety reasons, the availability of clinical data has been one major limitation to the direct application of analysis routines in the clinical environment and will be discussed in the following chapters.

14.2 Accessibility of Clinical Data

In previous work, import functions were implemented in order to read EP data from the recording device LabSystem PRO (Boston Scientific, former BARD, USA). Furthermore, functions were available to read data exported from the electroanatomical mapping system (EAMS) EnSite NavX 8 (St. Jude Medical, USA). Within the scope of this research, these existing algorithms were updated to handle data from the successor EAMS EnSite Velocity

and optimized with respect to processing speed. In addition, algorithms were implemented to import data from the EAM systems CARTO 3 (Biosense Webster) and Rhythmia (Boston Scientific). The types of exported and thus available data for each system and the corresponding format will be outlined in the following.

Recorder LabSystem PRO The LabSystem PRO is an EP recorder which acquires electrograms from all ECG leads and intracardiac channels during the complete procedure for documentary purposes. Events like isolation of the PVs, conduction block or termination of the arrhythmia can be annotated in a log file, so that the corresponding traces can be easily addressed and exported during review. Information about the atrial geometry or the position of the electrodes, however, is neither acquired nor stored. Data of up to 1 s duration can be exported in ASCII format on USB drive, including detailed information about name and filter settings of each channel. This allows for an easy import of the continuous electrogram data.

EnSite Velocity The mapping system Velocity provides the option to explicitly specify different kinds of clinical data for export. Individual components can be selected in a dialog and are subsequently saved into an uncompressed folder on DVD. All data is exported in individual *.xml and *.csv files in ASCII, making them easy to read. Right and left atrial geometries can be tagged and exported as separate models, jointly with labels and lesions as annotated during the procedure.

Focusing on map-based data, a typical export bundle analyzed in the presented research additionally contained information about all acquired points, like the position in space, their projection on the anatomy, electrogram information as well as simultaneous traces of intracardiac reference and surface ECG. For LAT maps, data for 1 s was exported as fixed setting, while for CFE maps data of 5 s could be exported. In addition, the result of automatic map analysis was available, given as coloring of the virtual geometry.

With respect to continuous mapping data, a time interval could be chosen for which the following quantities were typically exported for analysis: Filtered and raw surface ECG, unfiltered unipolar electrogram data, bipolar electrograms as filtered in the clinic, as well as locations of all electrodes over time and the respiration curve. These data allowed to rapidly review the interval when looking at their filtered data, and provided options for research when different filtering or processing techniques were applied. For all data, sampling rate was given as 2034.5 Hz.

CARTO 3 The CARTO 3 EAMS allowed to export data in the form of a complete study file. This compressed *.zip file contained individual files in ASCII format with information about all maps acquired during the procedure. For each, the captured geometry was included, together with catheter positions and electrogram traces for every recorded point and the simultaneous surface ECG. The duration of recorded EGMs was 2.5 s for LAT maps and could be adjusted for CFE maps, both recorded at 1000 Hz. Continuous mapping data, however, could not be exported due to technical limitations.

Within the scope of this thesis, an algorithm was developed which could read the geometry of acquired maps and concatenate all information from the individual point files without uncompressing the respective study file. As the uncompressed folder was frequently about 20 GB in size, this approach proved very memory efficient. Duration of the resulting import scaled proportional to the number of acquired points but was reduced by parallelization. It typically lasted for about 2 min.

Rhythmia The Rhythmia mapping system also allowed to export the complete study including screenshots and animations. As opposed to the CARTO study file, it did not include the specific electrogram information from every point of the acquired map. However, the sole geometry and both the continuous electrogram data and the catheter position for the complete study were available. All data are saved in binary format, embedded in an *.xml file.

Despite of the compression, typical sizes of study files range between 2 and 4 GB, complicating direct import into MATLAB. Thus a three step approach was developed for the import: First, the binary content was completely removed and replaced by an information about the corresponding byte indices within the original file. The resulting file contained pure xml content with less than 10 MB. Second, the xml information was evaluated, allowing the user to explicitly choose the data to import. Third, the actual binary content was read and converted into values according to the format specifications contained in the xml file.

Electrogram information was acquired at a sampling rate of 953.7 Hz, with positions recorded at 20 Hz. The complete process of importing clinical patient data was in the order of minutes.

14.3 Handling of Clinical Data

Although varying types of data were available when recording was done using different systems, the reusability of algorithms independently from the mapping system was an important design consideration. Therefore, the clinical data were converted into standardized and specified formats after import. The most important data structures are outlined in this chapter.

Atrial Geometry As outlined in Chapter 6.1, atrial anatomies were exported as closed triangulated surface meshes from all EAMS. For processing, these were separated and saved in two independent entries of a structure array representing the geometrical model. Using one representing each atrium allowed to loop over both surfaces during data analysis and processing each one individually.

In a second step, the endocard was extracted using clinical annotations or manual interaction (compare Figure 6.1 and Chapter 6.1). The valve geometry was saved equivalently. A table of corresponding point indices allowed to map data between both geometries.

Mapping points which were acquired in vessels or valves were discarded at this point. Information of the remaining positions was then used to compute the atrial coverage as outlined in Chapter 6.3 and shown in Figure 6.3. The coverage was also used during visualization as spatial filter to reject unreliable data.

Map-based data Data acquired during sequential mapping could be directly exported from EnSite Velocity and CARTO 3. The resulting files contained information about the location of each acquired point, the measuring electrode pair, the result of analysis within the EAMS and the original electrogram information of all channels. In the original format, surface ECG and intracardiac reference EGMs were saved for every acquired point. But also during sequentiall mapping, multipolar catheters allow to record information from each electrode in one simultaneous measurement. Electrogram information of these simultaneous recordings is therefore redundant.

Thus the map-based data were rearranged aiming at two major goals. First the measurements acquired from right and left atrial positions were separated so that processing could be performed in matrix form directly in combination with the respective atrium. Second the simultaneously measured surface ECG and intracardiac electrogram data were extracted from the list of sequentially mapped points and added into a listing of simultaneously recorded traces. This was memory efficient and the detection atrial rate or QRS complexes had only to be done once.

Continuous segments of EGMs Continuous traces of electrogram data and the respective measurement positions could be extracted from the EAMS EnSite Velocity and Rhythmia. These data were subject of analysis using various algorithms, and therefore the utilized format was kept application specific.

Remapping from continuous segments The export of map-based data was not possible from the Rhythmia EAMS. In clinical practice, however, this system is currently most frequently used for the sequential analysis of stable tachycardias. While maps with over 10,000 point ease the understanding of flutter mechanisms during the EP study, the lack of export options for this mapping data inhibits the development of new algorithms. Therefore a technique was developed to remap the atria based on the continuous electrogram and position information of the Orion catheter. This project was part of a supervised bachelor thesis [141] and is outlined briefly.

For remapping, the user first had to select the map of the desired tachycardia. The geometry of this map was used as atrial anatomy. This information also allowed to address the electrogram data which were recorded during the ongoing arrhythmia. For each segment of continuous data, stable positions of the Orion catheter were detected as described in Chapter 6.2. Both QRS complexes and CS activity were annotated as outlined in Chapters 5.2 and 8.1, respectively.

For each vertex of the endocardial geometry, the distance to each electrode in each stable position was determined. Selection of the minimal distance led to potential electrode

positions for remap data acquisition. A maximum distance of typically about 5 mm could be defined to ensure sufficient proximity to the endocard. After position and electrode number of the mapping point were identified, one snippet of roving EGM data had to be chosen for synchronization. Therefore the amplitudes of all activities in the measured EGM were assessed. The strongest signal which did not coincide with a ventricular contraction was chosen and synchronized according to its CS activity. This process was performed for each atrium if a biatrial map was generated. The analysis of the resulting mapping data will be demonstrated in Chapter 18.

14.4 Interactive Visualization Software KaPAVIE

As described in Chapter 14.1, the appealing representation of analysis results is an important requirement for novel algorithms to be accepted and utilized in the clinical environment. Although MATLAB provides intensive signal processing capabilities, its possibilities for interactive visualization are rather limited. Aiming for the final goal of applying new analysis techniques during EP studies, a computer program was developed that allowed an appropriate visualization of analysis results in the clinic. This system and the fundamental design considerations were subsequently published [146].

Design Considerations When novel algorithms are designed, initially neither correct functionality nor usefulness are verified. To allow physicians assessing these aspects, it was found important to provide the chance to relate the analysis result and quantities they were familiar with. Therefore, the visualization system was required to allow the simultaneous display of surface ECG, intracardiac reference EGM and the EGM which was currently subject to analysis. As the amplitude of electrograms could vary over orders of magnitude, automatic normalization of amplitudes was included and could be engaged if required. The sweep-speed of electrogram display was adjusted to values common in clinical practice.

The positions of all measurement points were indicated by small spheres on the atrial shell. The corresponding electrogram was displayed by selecting a site by mouse-click. Both EGM trace and the matching sphere were plotted in the same color to clarify togetherness if multiple points were selected.

In agreement with the well-known clinical maps, the atrial surface could be colored according to the result of automatic analysis. For time dependent processes, the respective map could be varied over time. In combination with the selected electrogram traces, this allowed to comprehend spatio-temporal processes.

Implementation The graphical user interface (GUI) was implemented using the Qt C++ framework (Qt version 5.3.0), which is open-source and allows cross-platform development. The VTK C++ framework (VTK version 6.1.0) was utilized for rapid and interactive visualization, including existing components for the display of data. The 3D representation of the atrial anatomy was visualized by an existing Qt-plugin that was distributed with VTK.

Electrograms were plotted by QCustomPlot which is an open source project licensed under GPL. Usage of Qt and VTK assured compatibility to all common operating systems (Window, Mac, Linux). For Macintosh OS X, KaPAVIE was bundled into an application package which allowed easy distribution to other machines.

14.5 Clinical Application

To allow an immediate retrospective analysis, a Macintosh system (21.5 inch iMac, 2.8GHz quad-core Intel Core i5 , Retina display, 1TB fusion drive SSD, 16GB RAM) was set up and installed at Städtisches Klinikum Karlsruhe. Its technical specification ensured rapid and parallelized processing.

The installed software included MATLAB for data processing and KaPAVIE for the visualization of analysis results. Paraview was added to generate publication quality images. Software for file compression and unarchiving was installed, as well as various developer tools like the VTK library, MacPorts and Xcode.

Processing of clinical data was structured in a two step process, consisting of import and analysis. For the import of new clinical data, corresponding MATLAB scripts were available for each type of EAMS and exported electrogram data. These scripts were used to both read the data and convert them to a standardized format as outlined in Chapter 14.3.

Data analysis itself was performed in the second step. As the format was standardized after import, data from all EAMS could be analyzed using the same algorithms. Analysis of atrial flutter data will be presented in the following paragraph and Chapter 18.

An application of KaPAVIE to visualize the result of a novel diagnostic algorithm is shown in Figure 14.1. Acquired electrograms were assessed with respect to the amount of fractionation present in the signal and classified accordingly using a fuzzy decision tree developed during previous work [208]. The atrial regions surrounding each measured EGM were colored accordingly. While signals located in blue and green regions could be expected to show little fractionation, coloring in yellow or red indicated increased fractionation. Examplary EGMs were selected from the different regions and are plotted in the EGM display on the left hand side. This potentially diagnostically relevant information is directly related to the atrial anatomy.

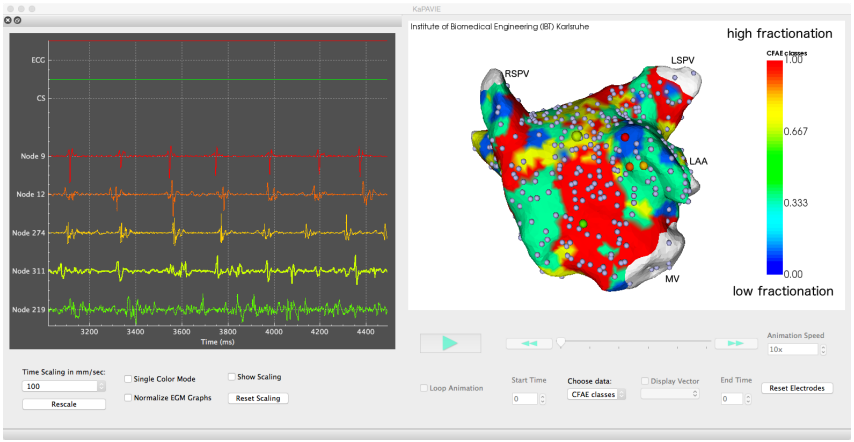

Figure 14.1: Screenshot of KaPAVIE. Reprinted from [146] with permission of the publisher.

PART III

CLINICAL APPLICATIONS AND TRIALS

CHAPTER 15

Analysis of Catheter Contact

15.1 Orion Mini-Basket

The Orion™ mini-basket is a new high-density mapping catheter which is primarily used with the Rhythmia™ mapping system for sequential mapping of stable tachycardias (compare Chapters 2.3.1 and 2.3.2). For this purpose, it has proven to be a useful tool in rapid acquisition of mapping data during sequential data collection [9, 75, 76].

In some situations, however, also the ability of simultaneous mapping is of great interest. This can for example be required for the precise localization of critical sites in a reentrant mechanism, or during the mapping of unstable rhythms like atrial fibrillation (AFib). In this case, knowledge about the field of view is important to develop methods which can correctly assess the excitation pattern.

Clinical data Although the shape of the Orion catheter already allows to deduct some hypotheses concerning the potential field of view, atrial geometry and catheter maneuverability may strongly affect the achievable wall contact. Therefore a database of 25 anonymized patient files was set up. Data from two centers were included in the study, with 15 from Karlsruhe and 10 from Munich, respectively. Patients underwent routine ablation for atrial tachycardias like atrial flutter (AFlut) or AFib, and inclusion in the study was independent of age, gender, indication or procedural outcome. Electrogram data, positions of all electrodes over time and atrial geometries were exported retrospectively from the Rhythmia system for analysis and imported at Institute of Biomedical Engineering (IBT). If more than one atrial map was acquired for a patient, the one with the longest available position data was selected for analysis.

Study design The presence of wall contact for each individual electrode was defined as an Euclidean distance from the electrode to the atrial geometry of less than 5 mm. Stable positions of the catheter were automatically determined using the algorithm described in Chapter 6.2. They were utilized for statistical evaluation if more than 6 electrodes were in

contact to the atrial wall. The frequency of contact for each electrode was determined based on the total number of catheter positions of all patients.

Due to the catheter shape, a rotational symmetry of the results was expected. In order to get a more representative view of the actual contact pattern, the splines were circularly shifted so that the dominant contact point was centered at the spline pair D/E. This was achieved by determining a shift which led to a compact coverage centered between splines D and E. An example of this procedure is visualized in Figure 15.1, next to a photograph of the Orion catheter.

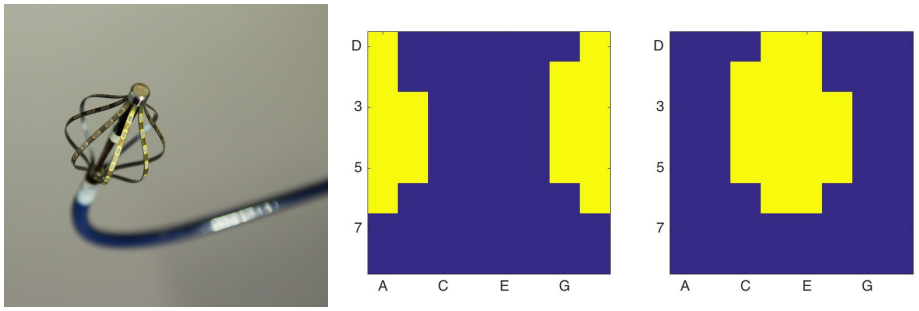

(a) Orion catheter. **(b)** Measured contact. **(c)** Contact after centering.

Figure 15.1: Effect of centering the Orion contact data. Due to the rotational symmetry of the Orion catheter (a), the analysis of wall contact was performed before and after centering the point of contact to the spline pair D/E. In this demonstrative example, wall contact was found for several central electrodes on splines A, B, G and H (b, marked in yellow). Centering the contact information allowed to deduct more detailed contact statistics as data from all stable catheter positions became comparable (c).

Results of analysis For most of the 25 subjects, data from the LA was chosen for analysis as it was more intensively mapped than the RA. This was probably due to the increased anatomical complexity of the LA. The duration of available position data in each patient ranged from 9.7 min to 42.6 min (mean 23.5±10.3 min). The mean number of stable catheter positions was 162±67.4, with a mean duration of 4.6±6.2 s.

Good contact was found for the distal electrodes D to 5 with values exceeding 49%. The contact was nearly equally distributed over all splines, see left hand side of Figure 15.2. Average contact frequency of the distal electrodes D of all splines was 56% and decreased to a value of 19% for the proximal electrodes. Considering the number of electrodes simultaneously in contact, 15, 20 and 30 electrodes were at the endocard in 80%, 67% and 40% of cases.

After mapping data was centered around the dominant contact point, it became apparent that contact was most frequent for the two central splines D/E and electrodes 2-5, with a resulting mean relative contact of 86.6±6.0%.

Depending on the degree of opening of the catheter, this resulted in a field of view of about 1 cm^2 with 8 simultaneous channels in a trapezoidal area.

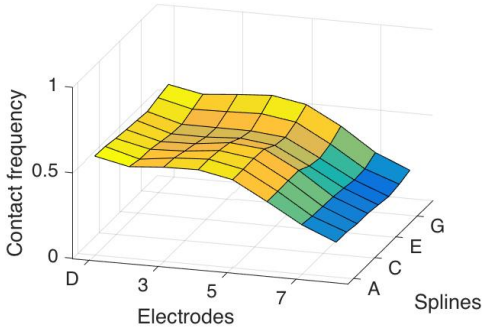

(a) Contact distribution as measured.

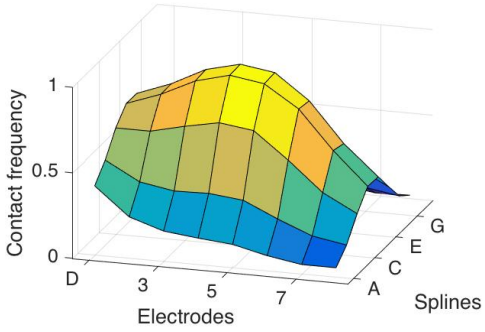

(b) Contact distribution after centering.

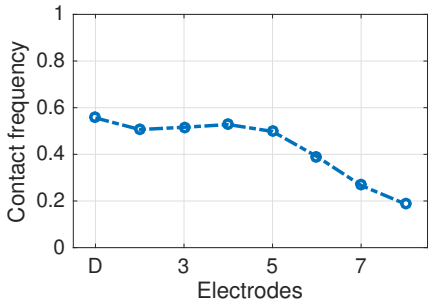

(c) Average contact for electrodes.

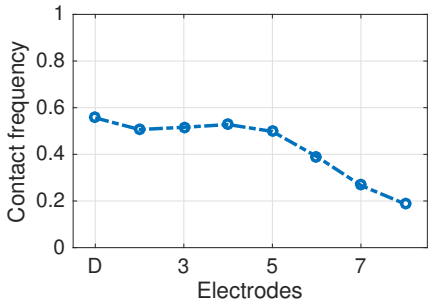

(d) Average contact (centered).

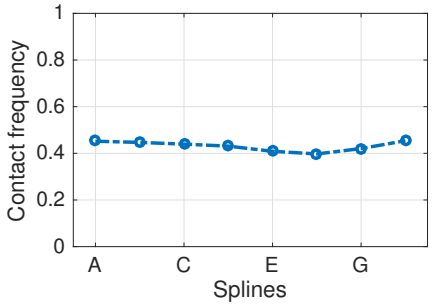

(e) Average contact for splines (measured).

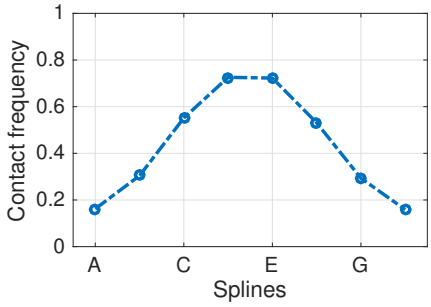

(f) Average contact (centered).

Figure 15.2: Orion contact statistics. Analysis of the measured Orion catheter positions (a) showed good coverage for the distal electrodes (c) and nearly rotational symmetry over all splines (e). After rotating the measured contact with respect to the central spline pair, the statistical contact pattern became more apparent indicating that two central splines had most contact (b, f). Average contact along the splines remained unaltered (d).

15.2 Panoramic Baskets

Panoramic baskets provide several unique options for acquisition of simultaneous mapping data (compare Chapter 17). Clinical experience, however, has indicated potential constraints by spline bunching [125] and limited coverage in septal regions [80]. To quantitatively assess these issues, clinical and simulated data were evaluated as outlined in the following chapters.

15.2.1 Clinical Experience

Clinical data Electroanatomical mapping data were available from 9 patients in whom data acquisition was performed using the Constellation™ basket (5 male, mean age 61±11 years) at Städtisches Klinikum Karlsruhe. All provided informed consent. Electrogram and position information were recorded by the Velocity mapping system. A detailed atrial anatomy was acquired using either the basket catheter or an additional circular mapping catheter.

Four catheter positions were chosen for analysis. These were selected based on the clinical experience that they allowed to keep the catheter stable and provided good wall contact:

1. RA antero-lateral
2. RA central
3. LA postero-superior
4. LA lateral

Study Design 22 mapping positions were retrospectively selected from the 9 patients and considered for statistical analysis. To reduce the influence of respiration and cardiac movement, average locations were computed for each electrode based on their positions 100 ms prior to the ventricular contraction as indicated by the QRS complexes in the surface ECG.

Following atrial regions were manually annotated in all subjects:
RA: lateral, posterior, septal, roof and CTI
LA: anterior, septal, posterior, roof, right PV ostium, left PV ostium

The Euclidean distance between two adjacent splines was determined for quantitative assessment of the interspline distance. The atrial coverage was computed as outlined in Chapter 6.3, considering electrodes closer than 10 mm to the endocardial shell. A very conservative distance threshold of d_m=10 mm was chosen for coverage analysis. The relative coverage was determined for both the complete atrium and all individual atrial regions. A set of example data is shown in Figure 15.3.

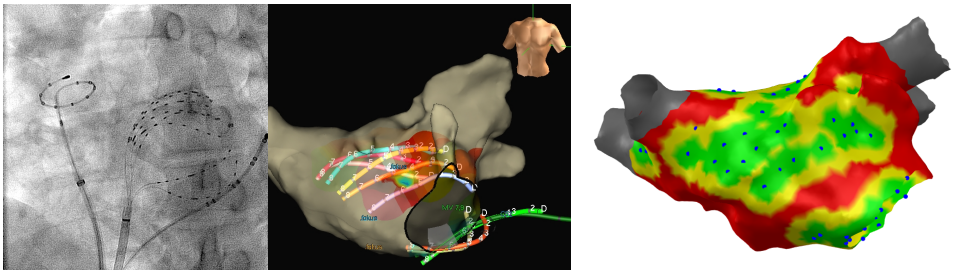

(a) X-ray image. **(b)** EAMS screenshot. **(c)** Coverage map.

Figure 15.3: Clinical example of spline bunching in a panoramic basket. Spiral, CS and basket catheter can be seen on an X-ray image acquired during the procedure (a). Position of the basket catheter was also visualized in the EAMS during the intervention. Due to adaption to the cardiac anatomy, two splines were shifted towards the MV, leaving a huge part of the posterior wall uncovered (b). The resulting coverage map reflected a good coverage of the anterior wall with four splines, while the remaining splines were located at the roof (2 splines) or at the MV (2 splines). Uncovered regions are marked in red (c).

Results In order to acquire baseline characteristics, a Constellation basket of size 60 mm was measured ex-vivo. Mean interspline distance was determined to be 11.9±0.6 mm (distal electrodes), 20.3±0.9 mm (equatorial plane) and 18.1±0.6 mm (proximal electrodes).

The interspline distances as measured in clinical data are summarized in Figure 15.4. RA positions showed similar distances between all splines, indicating a rather undeformed state. Especially the LA postero-superior position, however, exhibited large variations caused by spline bunching.

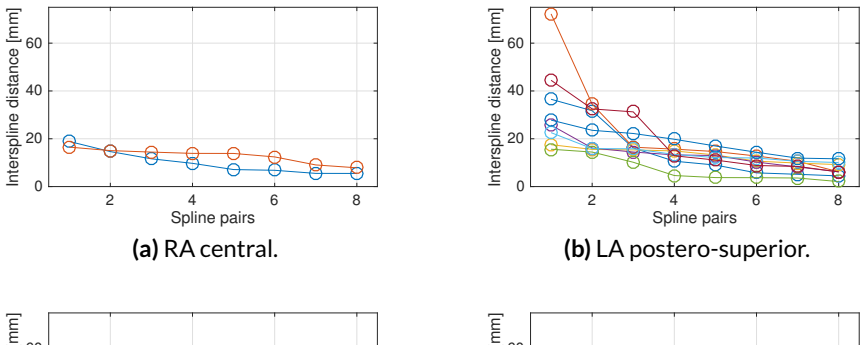

(a) RA central. **(b)** LA postero-superior.

(c) RA antero-lateral. **(d)** LA lateral.

Figure 15.4: Interspline distances observed during clinical mapping. Especially the postero-superior position in the LA was found prone to severe spline bunching. Interspline distances of about 20 mm were observed in nearly all positions. Spline pairs were sorted in descending order, colors indicated different datasets.

The result of coverage analysis is shown in Figure 15.5. Boxplots were generated from all available mapping positions, indicating the value ranges in different patients. The length of the green bar indicates the median coverage for each region. For RA positions, higher coverage was determined for the antero-lateral position when compared to the central location (53% vs. 35%). Little coverage was observed for the cavo-tricuspid isthmus (CTI) region (<21%) and septal aspects (<37%). Considering the LA, a coverage of 47% was achieved in the postero-superior position, which was higher as in the lateral position (40%). While posterior and anterior areas were covered comparably well, coverage of the roof was reduced in the more lateral position (89% vs. 50%). Both septal areas and PV antra were only sparsely covered.

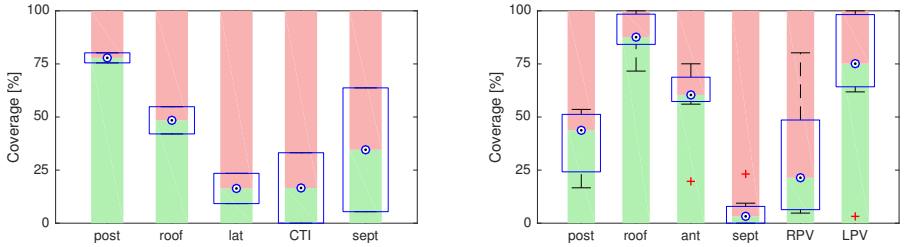

(a) RA central (35.1%). **(b)** LA postero-superior (46.9%).

(c) RA antero-lateral (53.2%). **(d)** LA lateral (40.1%).

Figure 15.5: Coverage achieved during clinical basket catheter mapping. Both CTI in the RA and LA septal regions were hardly covered, being in agreement with earlier clinical observations [80]. Despite an optimistic coverage inclusion range of 10 mm around each electrode, hardly 50% of the atrium were covered. Values in parenthesis indicate the average total surface coverage.

15.2.2 Simulated Data

Study design Computational catheter models were implemented as outlined in Chapter 4. Two types of electrode arrangement were chosen, resembling two commercially available catheter designs (*Constellation EA* and *FIRMap EA*, see Chapter 4.2).

To study the relationship between catheter size, deformation and coverage, the diameter of the computational basket was modified. In agreement with the LA size of 51 mm, catheter diameter was increased from 40 mm to 51 mm in steps of about 1 mm. The smallest and

largest resulting catheter shapes for each electrode arrangement are visualized in Figure 15.7, together with the corresponding coverage.

For statistical analysis, both the interspline distance and the atrial coverage were computed as outlined for the clinical data. Additionally, the Euclidean distance between electrodes and the endocard was computed as surrogate measure for wall contact.

Results The resulting interspline distances, electrode-endocard distances and coverage values are summarized in Figure 15.6 for both catheter types. A nearly equal spacing between all splines could be observed for the smallest diameter of 40 mm. For an increasing diameter, however, spline bunching could be observed which was reflected by huge deviations in the interspline distance. In addition, a tendency in reduction of electrode to endocard distance could be observed. Total coverage increased for both catheter types (*Constellation EA*: 40% to 49%; *FIRMap EA*: 50% to 65%).

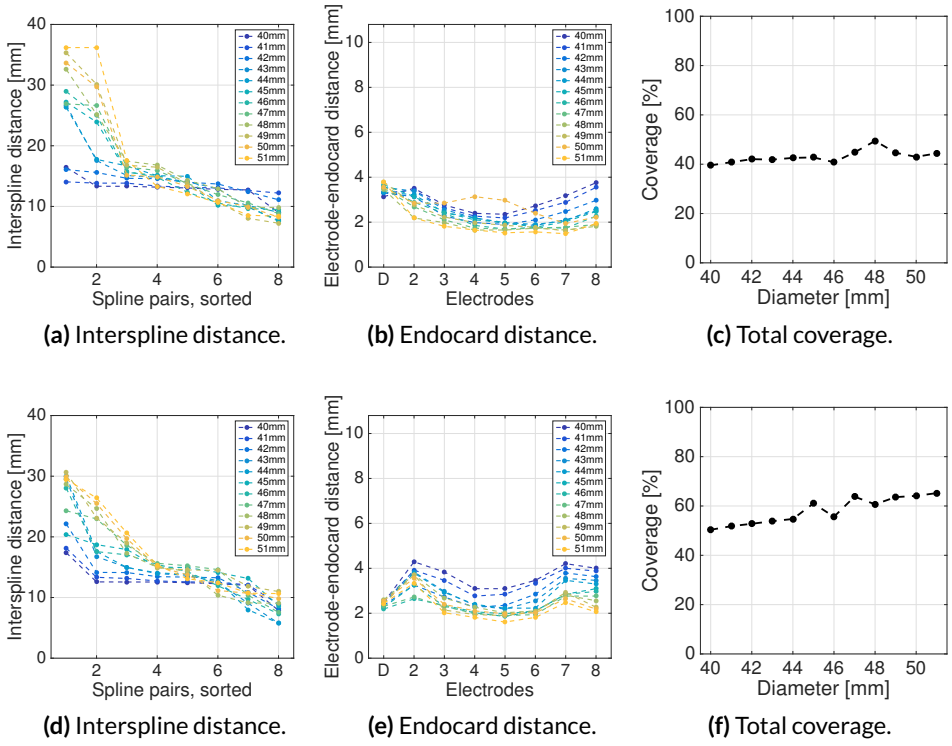

(a) Interspline distance. **(b)** Endocard distance. **(c)** Total coverage.

(d) Interspline distance. **(e)** Endocard distance. **(f)** Total coverage.

Figure 15.6: Effect of catheter diameter on performance measures. The diameter of the computational baskets was varied to study the effect on interspline distance (a,d), distance to the endocard (b,e) and total coverage (c,f). Data for *Constellation EA* is plotted in the upper row, values for the *FIRMap EA* in the lower row. Data indicates a tendency to pronounced spline bunching for increasing diameter. Coverage, however, also increased when bigger baskets were chosen.

The undersized and oversized catheters of each type are plotted in Figure 15.7. Uncovered regions on both the anterior and the posterior wall could be observerd for the 61 mm diameter

basket. As expected due to the modified electrode arrangement, an increased septal coverage was achieved with the *FIRMap EA*.

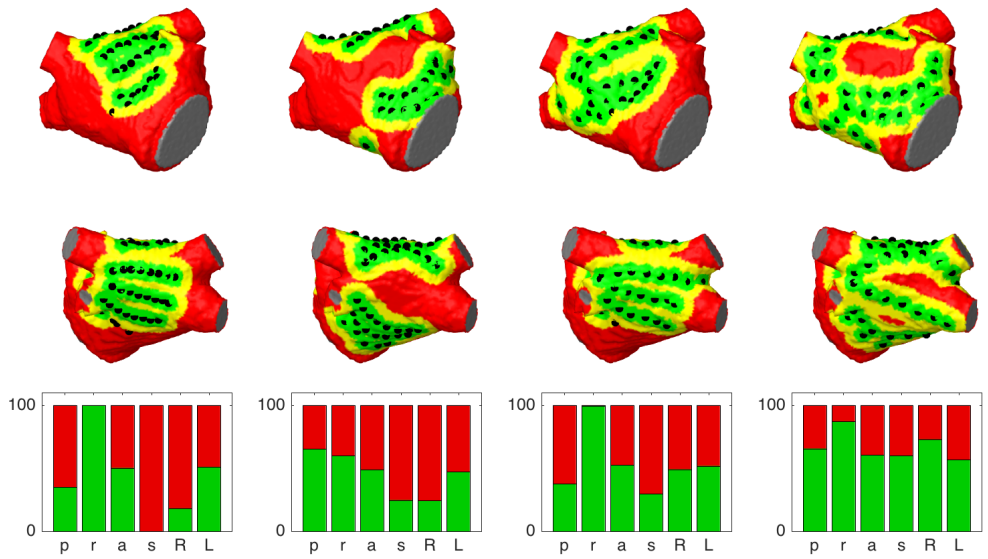

Figure 15.7: Coverage for over- and undersized computational baskets. Coverage maps were plotted for both electrode arrangements (*Constellation EA* left, *FIRMap EA* right) in anterior (top row) and posterior view (middle row). The pair representing minimum and maximum simulated size is shown. Coverage is also assessed specifically for each region (lower row). Uncovered regions are indicated in red. *p: posterior; r: roof; a: anterior; s: septal; R: right PV ostium; L: left PV ostium*

15.3 Discussion and Conclusions

Local high-density mapping with the Orion catheter Averaged contact analysis over all 25 patients indicated, that the wall contact during mapping was rotationally symmetric. Thus there is no obvious preferred mapping position during clinical data acquisition.

Although the Orion is generally accepted as mini-basket, certain peculiarities can be noted concerning its shape. First, its design is rather rigid compared to the fully flexible arrangement of panoramic basket catheters. Second, the first 5 electrodes are arranged on a nearly linear spline segment, after which a strong bend can be recognized (see Figure 15.1 (a)). As the atrial anatomy has only little curvature in most areas, simultaneous contact of all electrodes along one spline is difficult to achieve. This hypothesis was in agreement with the result of wall contact analysis, showing that contact frequency strongly decreased past electrode 5 on all splines.

With respect to the field of view, also the number of splines which can be in contact simultaneously is of interest. Statistics after centering to spline pair D/E indicated, that two splines were in contact for 70% of cases, with four splines being in contact for still 50% of cases. As data were acquired during routine procedures focusing on sequential mapping or

generation of the anatomy, it cannot be excluded that more simultaneous coverage could be achieved. Nearly complete coverage was also observed in some positions within the presented coverage study. Corresponding locations, however, were primarily located inside the pulmonary veins (PVs) or the left atrial appendage (LAA).

Considering an interelectrode spacing of 2.5 mm, five consecutive electrodes span over 1 cm. Depending on the level of opening, the interspline distance is about 2 mm at the distal electrodes and about 5 - 8 mm measured at the equatorial plane. Assuming the contact of four splines and their five distal electrodes, this leads to a contact area of trapezoidal shape with bases of 6 mm and 24 mm, and a height of 10 mm. The resulting field of view amounts to 1.5 cm^2. If additional 2 mm were considered as good measure for each boundary electrode, the mapping field increased to 2.7 cm^2, covered by 20 electrodes and thus resulting in an average density of 7.5 electrodes per cm^2.

These findings were not incorporated into algorithm development during this research. However, they were considered as relevant finding which have to be kept in mind for the development of future substrate mapping techniques.

Deformation of panoramic baskets Significant spline bunching could be observed in both simulated and clinical data. The resulting increased interspline distance was frequently determined to exceed 20 mm. This is an important finding, as studies suggest that a maximum interspline distance of 10 mm is required for the detection of rotational sources [249].

With respect to the atrial coverage, maximum values of 53% (RA antero-lateral) and 47% (LA postero-superior) were achieved. This was in line with studies by other groups. Considering a population of 19 patients, coverage of 43$\pm$16% was observed in the LA and 60$\pm$23% in the RA [250]. In a study focusing on electrogram characteristics near rotor sites, merely 54$\pm$15% of LA surface were found closer than 10 mm to any basket electrode [251].

Due to the limited number of commercially available diameters, mapping with a perfectly sized basket is rather seldom in clinical practice. Consequently, the issues of spline bunching and limited coverage have to be considered during the development of algorithms for panoramic basket signal analysis. As will be shown in Chapter 17, panoramic baskets offer unique mapping possibilities. But correct interpretation of acquired data is only possible when information about the geometrical position of electrodes and anatomy is available.

CHAPTER 16

Analysis of Ectopic Activity

The concept that triggers in the pulmonary veins initiate atrial fibrillation (AFib) has led to the consensus that pulmonary vein (PV) isolation is a cornerstone in treatment of AFib. In this step, the PVs as such are generally electrically decoupled from the atria, so that ectopic activity cannot propagate through the ablation line. Consequently, there is no need to exactly localize the source of the ectopic activity.

Multiple evidence suggests, however, that also non-PV triggers can initiate atrial flutter (AFlut) or AFib [27]. Since these triggers are located outside the isolated area, their excitation is not confined and requires specific localization and ablation. Considering the presented research, this has motivated the development of a patient-specific approach to evaluate the existence and location of ectopic triggers. After testing on simulated data as demonstrated in Chapter 13.3, the approach was applied to measured data from a well defined scenario, and subsequently to clinical patient data.

16.1 Classification of Paced Excitations

The idea to distinguish different kinds of atrial excitations based on their LAT pattern was first applied to clinical data recorded during pacing. In each dataset, normal sinus rhythm (NSR) was present when pacing was turned off. Considering the paced beats as surrogates for monomorphic supraventricular extra-systoles (SVESs), goal was subsequently to correctly identify the paced beats during SR. This allowed to test the classification process based on a two-class problem, in which the goal was to correctly distinguish SR activity from intermittent SVES.

Clinical data and preprocessing steps Data were available from a previous study [11, 193]. During mapping, a spiral catheter was placed on either the anterior or the supero-posterior wall. Best possible contact of all electrodes and stable position were assured by the physician. Pacing from the coronary sinus was performed during NSR from either CS 3/4 or

CS 7/8. Three datasets were chosen for analysis, in which NSR and pacing could be clearly defined by manual annotation.

In order to generate a ground-truth for the evaluation of the classification result, manual annotation of all data was performed. Therefore, all available channels (surface ECG, four bipolar CS leads, nine bipolar leads from the mapping catheter) were visualized. A consistent morphology of QRS complexes was ensured to exclude the presence of ventricular extrasystoles. The presence of an isoelectric line on all intracardiac channels was used to identify individual atrial complexes. The presence of a stimulation artifact in the CS leads and subsequent capture was used to identify paced beats. The consistency of the excitation pattern on both coronary sinus (CS) and mapping catheter was visually inspected to exclude the presence of real SVES during NSR. Detailed patient characteristics are depicted in table 16.1.

The clinical data were recorded using the EnSite™ NavX™ electroanatomical mapping system (EAMS) at a sampling rate of 1200 Hz. Filtered bipolar data were available for four leads of the CS catheter and nine channels of the mapping catheter, together with the position in space of all measurement points and the atrial geometry.

Since visual inspection excluded the presence of high voltage artifacts (>10 mV) in the mapping data, no channels were excluded during preprocessing. The time of individual pacing events was automatically determined from the pacing artifact within the stimulation channel. In order to avoid the analysis being compromised by the stimulation artifact in the mapping channels, a time period of about 10 ms before and after the stimulus was blanked in all mapping channels by interpolation using cubic splines.

The LAT was detected as outlined in Chapter 13.3 with a refractory period of 100 ms. Subsequently, the wavefront matrix was generated using an inclusion time of 90 ms and a minimum length of 2 for wave trains.

Data were recorded during a pacing protocol which included the step-wise reduction of coupling intervals from about 500 ms to 300 ms in steps of 50 ms, with 10 stimulations per basic cycle length (BCL). Therefore, dynamic changes were expected during the course of pacing, representing the cycle length dependent restitution properties of the atrial tissue. These indeed could be observed in the wavefront patterns. To focus on the differentiation between NSR and paced excitations, only the first principal component (PC) was used for classification. Of note, application of the common threshold of 90% explained variance was shown to additionally distinguish between paced episodes of different BCL.

The clustering of wavefront types was performed for a fixed value of 2 clusters in each dataset. All wavefronts were classified, including those in which LATs could not be assigned in all channels. The resulting classes were compared to the manual annotations. For statistical evaluation, true positives were defined as correctly identified paced beats. Accordingly, sensitivity indicated the correct automatic annotation of manually labeled paced beats.

Result of analysis A short segment of EGM data from patient *PtW1* is shown in Figure 16.1. NSR was present for the first 13 s, after which pacing from CS 7/8 was applied with

a BCL of 500 ms. Differences in the activation pattern can be seen between both rhythms, with the EGM labeled *OPT 5* being activated last during NSR and first during pacing.

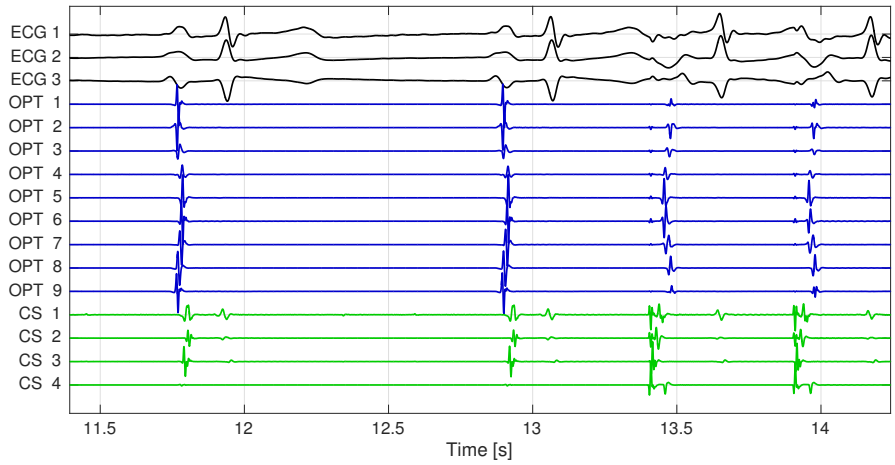

Figure 16.1: Electrograms recorded at the onset of pacing. The sequence of activation was different for NSR and stimulated excitations. Stimulation artifacts were observed in all intracardiac leads. P wave morphology differed between NSR and paced excitations.

The result of analysis for all patients is summarized in table 16.1. The number of automatically detected wavefronts was in agreement with the automatic data analysis. Values of all statistical parameters close to 1.00 indicated a good overall performance of the new method.

Patient ID	Catheter position	Stimulation (BCL range [ms])	LAWs annotated / detected	SE	SP	PPV	NPV
PtW1	post	CS 3/4 (500-300)	101/101	1.00	0.93	0.99	1.00
PtW1	post	CS 7/8 (500-300)	111/111	1.00	1.00	1.00	1.00
PtW2	ant	CS 3/4 (600-300)	161/161	0.99	1.00	1.00	0.97

Table 16.1: Data used for clinical benchmarking. Three datasets were analyzed, each containing NSR and paced beats. The number of manually annotated LAWs is provided together with the number of LAWs which were automatically detected. Sensitivity (SE), specificity (SP), positive predictive value (PPV) and negative predictive value (NPV) were computed as performance indicators. *post: supero-posterior wall; ant: anterior wall*

16.2 Detection and Analysis of SVES

After the successful demonstration of the proof-of-concept, the processing scheme was applied to clinical data from a patient in whom SVES were observed during mapping. Related research was part of a student project [242] and subsequently published [183].

Clinical data and preprocessing Data was available from a patient in whom biatrial basket catheter mapping was performed for ablation of paroxysmal atrial fibrillation using the EnSite™ Velocity™ EAMS at Städtisches Klinikum Karlsruhe. During mapping, the patient presented in SR with intermittent SVES. A continuous segment of duration 190 s was exported and retrospectively analyzed. It comprised unfiltered unipolar data of 126 channels from the two basket catheters (electrodes H 3/4 of the LA basket were not connected) and one pair of the reference channel CS 7/8. Since the ablation procedure did comprise PVI but did not include the localization and ablation of non-PV triggers, no detailed knowledge about the origin of the SVES was available for statistical assessment based on a clinical ground truth.

First, bipolar electrograms were computed for the reference channel and all pairs of basket catheter electrodes along the splines. Due to the unconnected electrodes, three channels of the theoretical maximum of 112 were not available and thus data from 109 bipolar mapping channels were processed. The EGMs were filtered using high-pass and low-pass of 30 Hz and 300 Hz, respectively.

QRS complexes were automatically detected as outlined in Chapter 5.2. In order to identify channels which only contained noise or VFF and no atrial activity, data recorded simultaneously to the QRS were blanked using cubic splines. Channels which subsequently exhibited a bipolar amplitude < 1 mV were rejected (36 channels). In addition, high voltage artifacts from electrodes touching each other were removed by rejecting channels with amplitude peaks >10 mV (5 channels). Consequently, 68 channels were used for subsequent processing.

The signal without blanking was processed for the detection of LAWs. In order to reduce the presence of VFF prior to wavefront analysis, the PCA-based VFF removal technique was applied (compare Chapter 7.1). Since the excitation patterns of SVES (which do not originate from the sinus node) were expected to be different from NSR activity, the morphology of the atrial activity was expected to be decoupled from the VFF.

The LATs in each channel were detected with a refractory period of 100 ms, resulting in a minimum of 187 and a maximum of 595 LATs per channel. This high number was inspected visually and revealed spurious VFF activity which was still present after filtering and detected as LAT in channels close to the MV.

The wavefront matrix was generated including LATs up to a time difference of 150 ms to the reference channel, allowing to comprehend the complete biatrial activation. The minimum number of electrodes required to detect a wavefront was accordingly set to 20, excluding spurious VFF. A total of 214 waves were automatically detected using this approach.

Classification of activation waves All wavefronts were centered to have median 0 ms. All wavefronts in which the LAT could be determined in all electrodes were used for the initial classification (148 LAWs). The classification was performed as described in Chapter 13.3, with PCs explaining over 90% of variance and 2 to 6 classes shown to the user with the dendrogram (compare Figures 16.2 and 16.3). The first two branchings in the dendrogram can be found at metrics of about 1800 and 1400, leading to four classes.

Additional branchings start from 1000 and are located more close, indicating an increased consistency of the classes to be split.

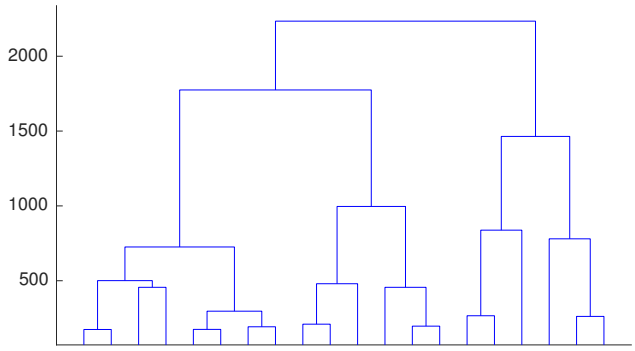

Figure 16.2: Dendrogram plot representing the hierarchical clustering. Horizontal lines represent the split into two new classes. The length of the vertical lines indicates the distance between both clusters. While the dissimilarity is large for a little number of classes, classes become progressively similar for an increasing number of clusters.

Resulting LAT maps are depicted in Figure 16.3. In case of 2 clusters, the LAT maps primarily represented an excitation starting at the SN (class 2 with 136 elements), while the second cluster contained extrasystoles (class 1 with 12 waves). For 3 clusters, 15 additional extrasystoles were separated leaving 121 NSR activations. Of note, the branch containing NSR depolarizations was not split further for up to 6 clusters. SVES were further distinguished when 4 clusters were used, splitting septal from lateral origin (classes 1 and 2, respectively). Only minor changes in the LA activation sequence were observed when the class number was increased to 6 clusters. After visual inspection, a number of 4 classes was manually chosen for analysis.

Now the 68 remaining activation patterns were compared to all classified wavefronts based on their RMSE and subsequently annotated. Representative LAT maps of the 4 classes are plotted in Figure 16.4, in which all types are marked by an individual color. A short segment of the completely annotated EGM signal is shown in Figure 16.5. The background color is in agreement with the annotation of the representative LAT maps in Figure 16.4. Differences between the classes can be observed in the activation sequence of the electrograms, which are in agreement with the LAT plots: For NSR beats (class 1), earliest activity could be observed in the RA with subsequent activation of the LA. Both shown NSR beats presented a consistent activation pattern. The excitation at time 27.8 s showed earliest activation in the LA and subsequent RA activation, being in agreement with the LAT map of class 4. For the forth beat at 29.4 s of class 2, activation of RA and LA began nearly simultaneously. This demonstrated both the congruence of electrogram pattern and LAT map, and the facilitation of interpretation of electrogram data in the form of representative LAT maps.

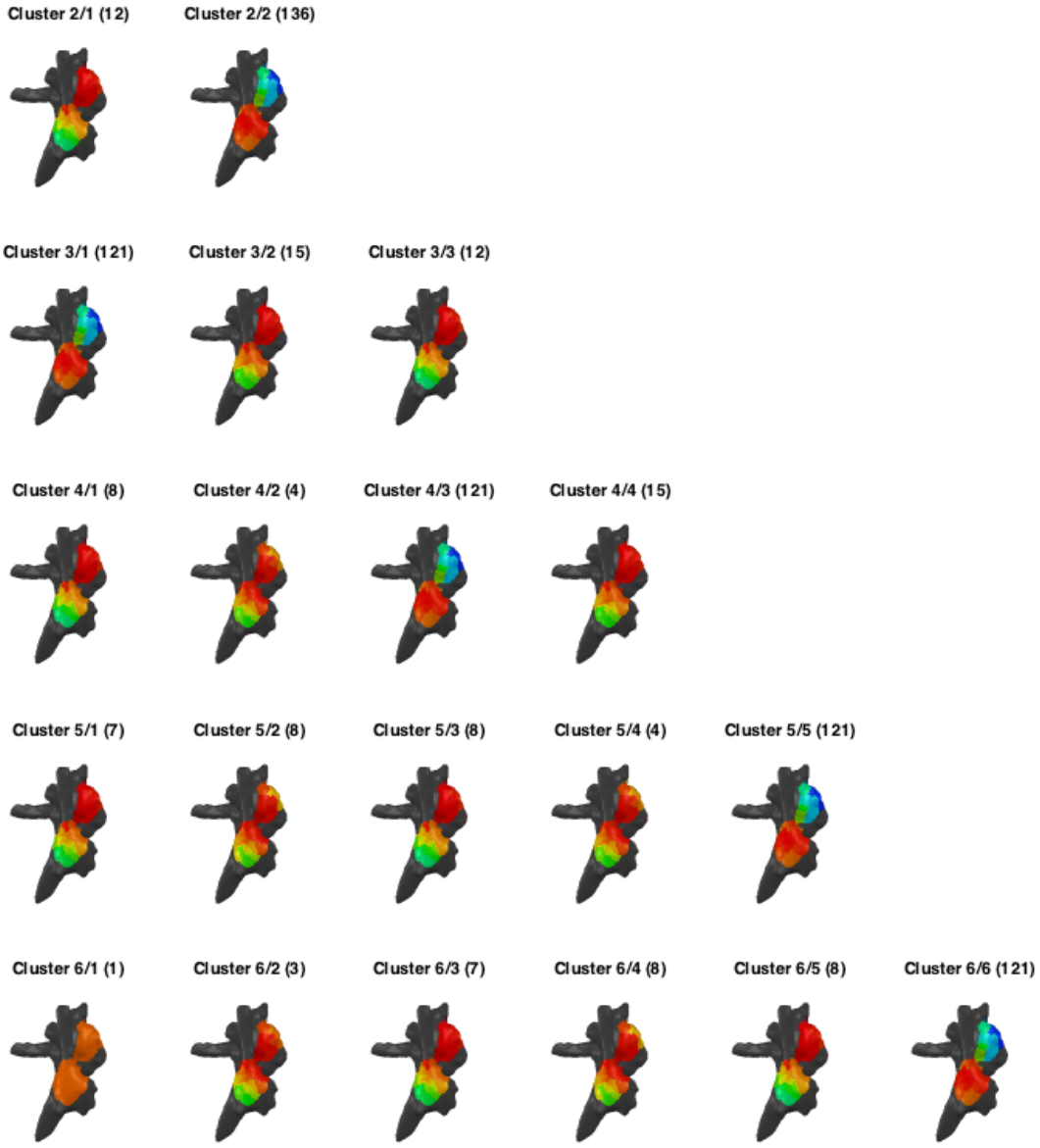

Figure 16.3: LAT maps representing the activity pattern for different amounts of clusters. Each row represents the result of classification using two (top) to six clusters. The resulting LAT patterns for each class are plotted in the columns, with number of waves shown in parenthesis. Manual inspection of the clusters allowed to determine an appropriate number of individual patterns, depending on the desired type of analysis.

In order to provide quantitative information about the frequency of SVES, the activation sequence was evaluated with respect to the relative appearance of each pattern and its recurrence within the analysis window. The most prominent pattern was class 3 (representing SR activity, 61.2%), followed by class 4 (LA SVES, 26.6%), class 1 (LA SVES, 8.4%) and class 2 (septal SVES, 3.7%). When similar patterns were considered to be one type, SVES originating from the LA roof were observed in 35% of excitations.

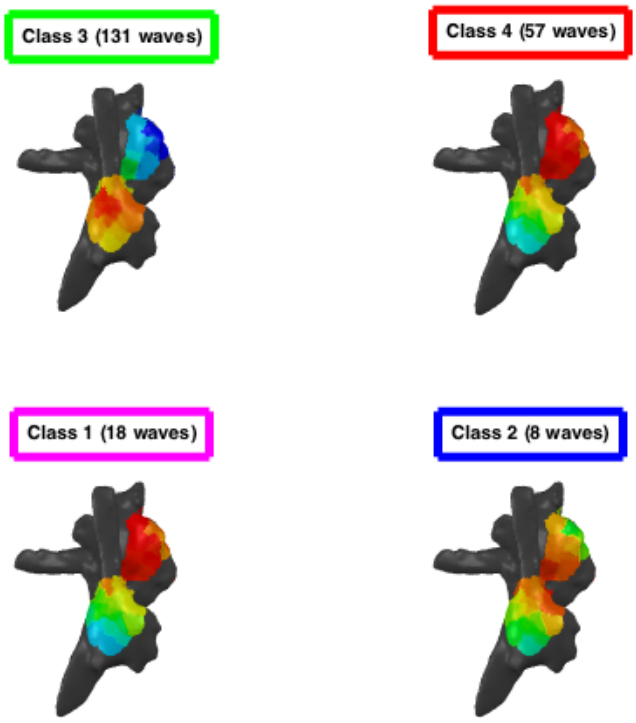

Figure 16.4: LAT maps of the resulting clusters after all 214 LAWs were annotated. The representative LAT map for each cluster is plotted, starting with the most frequent cluster at the top left corner. Visual interpretation allowed to distinguish between three dominant patterns: Excitations starting in the area of the sinus node (class 3), SVES originating in the LA (classes 4 and 1), and SVES starting at the septum (class 2). Classes 4 and 1 were separated due to differences in activation on the LA posterior wall.

Excitation type	Class	Occurrence	Consecutive activations
SR	Class 3	131 (61.2%)	6.2 ± 7.8
SVES LA	Class 4	57 (26.6%)	3.2 ± 5.9
SVES LA	Class 1	18 (8.4%)	1.8 ± 1.1
SVES septal	Class 2	8 (3.7%)	1.0 ± 0.0

Table 16.2: Statistics of SVES during biatrial basket catheter recording. A total number of 214 individual excitations was detected during 3:10 min of data acquisition. Analysis indicated four different clusters, which represented three kinds of dominant patterns: SR (61%), SVES LA (35%) and SVES septal (4%).

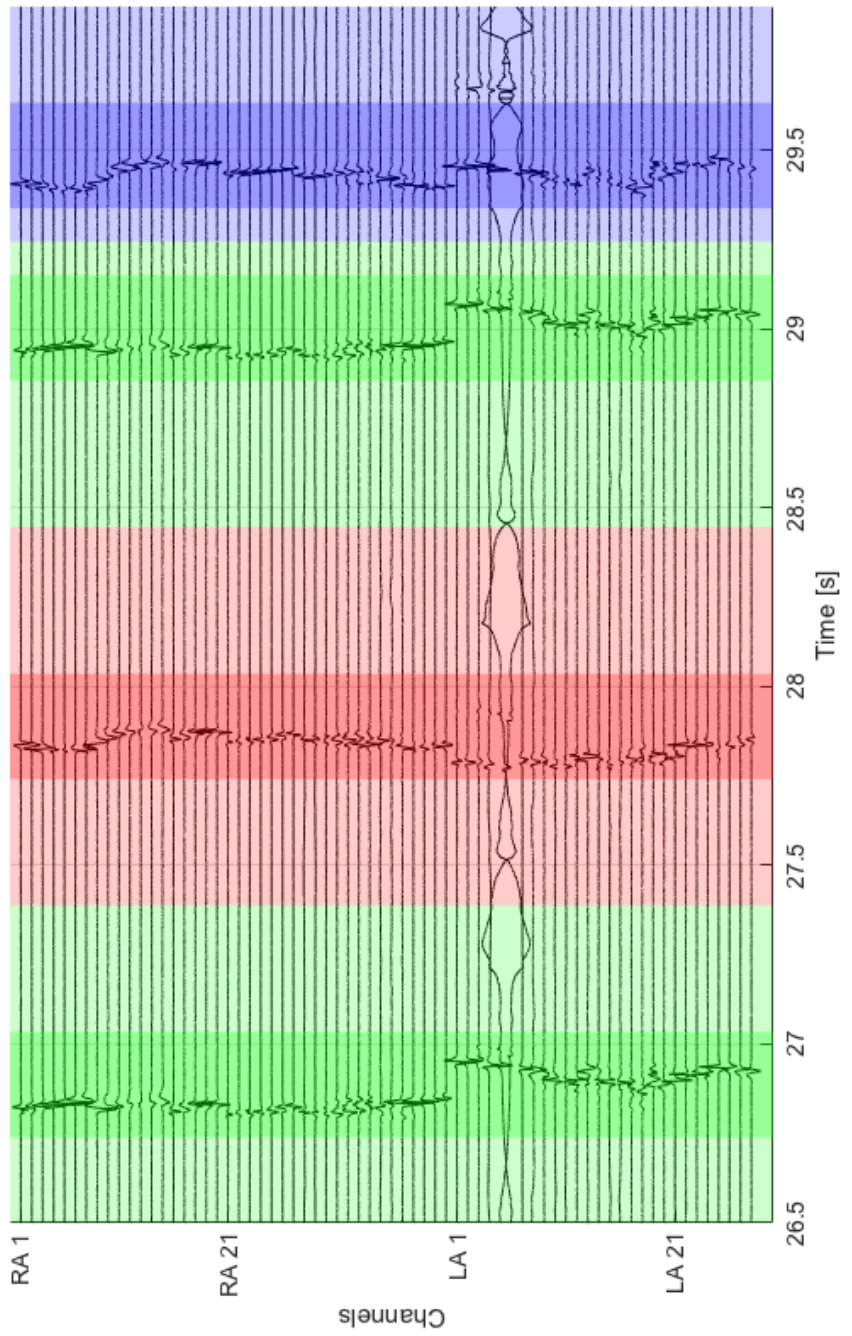

Figure 16.5: Clinical multichannel EGM with annotation of dominant excitation patterns. Biatrial panoramic mapping data were analyzed, including 68 channels of good quality. Four prevailing types of excitation complexes were distinguished and annotated by individual background color as defined in Figure 16.4. Earliest activation in the EGM could be observed in the RA channels for class 3 (green), and in the LA channels in class 4 (red). A nearly simultaneous onset of activation could be observed in both RA and LA channels of the excitation assigned to class 2 (blue), which was in agreement with a septal origin of the SVES.

16.3 Discussion and Conclusions

The analysis of ectopic activity from outside the pulmonary veins is an important step in the treatment of focal supraventricular tachycardias and paroxysmal AFib. However, the locations of all ectopic foci have to be determined prior to ablation. Multichannel mapping allows to acquire simultaneous data from several atrial positions. This information can be evaluated in order to quantify the number of different excitation patterns, differentiate between monomorphic and polymorphic extrasystoles, and statistically assess their occurrence. This can subsequently aid the remapping to precisely locate the focal source.

Corresponding data analysis required the automatic detection of each excitation wave and the subsequent clustering of similar waves. Identification of individual depolarizations was successfully achieved in all clinical data. The term 'similar', however, always reflects a trade-off between the number of waves and their applicability to statistical evaluation: Although the best possible fit could be achieved by using an individual class for each excitation, the huge amount of clusters with only one single element would not allow statistical evaluation.

In general, quantities like the difference between the measured LATs of each wave and the representative cluster LATs could be considered as threshold. The selection of the appropriate cut-off, however, reflects the level of sensitivity used to distinguish different types of excitation patterns. Since the wavefront propagation is a complex spatio-temporal process, the appropriate sensitivity is related to the sampling of the process as defined by the electrode positions. Consequently, there is no optimal parameter value which can be generally applied for clustering. Instead, the presented semi-automatic approach contains a step which requires the user to set a reasonable patient-specific value for the number of classes. This assessment is done by considering both the resulting LAT pattern and dendrogram of the hierarchical cluster tree.

After the demonstration on artificial data, the method was successfully applied to clinical data as presented in this chapter. In the first example, stimulated excitations were used as surrogate for SVES and detected using a two class approach. Assessment of sensitivity and specificity indicated the correct differentiation between NSR and paced beats. In the second dataset, analysis was performed retrospectively on basket catheter data, and thus no remapping was performed. Since some positions were not sufficiently covered during basket mapping (compare Chapter 15.2), exact localization could not be performed and the ground truth is not known.

The presented approach is independent from the number and type of utilized catheters and can thus be applied in any combination. The possibility of using only CS electrograms for the detection of different rhythms could not be assessed since no panoramic activity was available during the local mapping described in the first section, and just one CS channel was available during the second trial. However, multiple rhythms could show a similar CS activation sequence, because of which the combination with a second spatially remote reference should be considered.

One application for this type of analysis includes rhythm monitoring, indicating the amount, type and potential source region of extrasystoles. After clustering and annotation of some representative excitations, new data can be acquired and automatically classified. In addition, the capability of differentiating the type of excitation allows to reconstruct activation maps for each individual type during complex rhythms using a mapping catheter.

CHAPTER 17

Interpretation of Panoramic Mapping Data

Usage of panoramic basket catheters has gained significant attention in the last years. This can primarily be attributed to their ability to simultaneously acquire electrical information from 64 distributed atrial sites and related diagnostic advances [27].

Algorithmic support to analyze this kind of data, however, is strongly limited. Two clinical observations motivated the research which will be presented in the following. First, the deployed basket catheter is designed highly flexible and thus adapts to the atrial wall. This causes a shifting of the splines, leading to non-uniform spacing of the electrodes. Although the location of the atrial shell and the catheter electrodes can be recorded using an electroanatomical mapping system (EAMS), this information is not considered in the analysis technique mentioned before. The author is convinced that knowledge about the recording positions is fundamental for correct assessment of the spatio-temporal depolarization process.

Second, the amount of data recorded during basket catheter mapping is too extensive for visual inspection. Actually, it cannot even be visualized in the clinic as the electrogram display screens do not provide enough space. Therefore, novel analysis techniques are a prerequisite to evaluate basket catheter mapping data. One potential topic, being the detection of a supraventricular extra-systole (SVES), has been addressed in Chapter 16.2. In the upcoming chapters, additional tools and considerations for the analysis of basket catheter data will be presented.

17.1 Diagnostic Pitfalls of Spline Separation

Spline bunching was frequently observed during clinical mapping of the LA. Quantitative analysis indicated interspline distances of more than 20 mm, making basket deformation a potentially relevant parameter in diagnosis (see also Chapter 15.2). An in silico approach was chosen to evaluate the effect of spline separation on the outcome of mapping. The data and the corresponding conclusions will be presented in the following.

Parameters of the simulation Atrial fibrillation was simulated using the anatomical model already described in Chapter 8.4. Chronic atrial fibrillation (AFib) remodeling was represented by an adapted variant of the Courtemanche et al. cell model [101]. Depolarization was computed using the *acCELLerate* solver (see Chapter 2.4). In order to induce AFib, a premature stimulus of diameter 5 mm was applied near the right superior pulmonary vein (RSPV) during the vulnerable phase.

Virtual basket position The simulated AFib was mapped using a computational model of a Constellation basket of size 60 mm in lateral position. This diameter was clearly oversized for the atrium of size 51 mm. However, it proved very useful to demonstrate the effect of spline separation. After the catheter shape was adapted to the cardiac anatomy, spline A was located at the anterior MV annulus. Spline B had moved to the high anterior wall, leaving a huge part of the anterior wall uncovered. The catheter position is visualized in Figure 17.1.

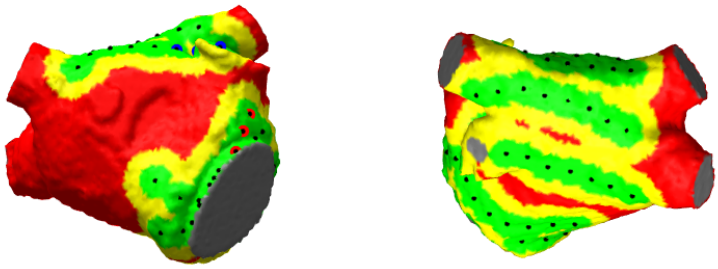

(a) Anterior view. **(b)** Posterior view.

Figure 17.1: Coverage of the oversized basket. While the posterior wall was covered well, spline bunching led to a lack of coverage at anterior wall between splines A (anterior MV annulus) and B (anterior roof).

Signal analysis Extra cellular potentials were extracted from the simulation at all electrode positions. The EGMs of the first 3 electrodes from splines A and B are plotted in Figure 17.2. For each signal, the phase was determined using sinusoidal recomposition and Hilbert transformation as described in Chapter 8.3. The phase values of the selected 6 electrodes indicate a gradient that persisted for all shown cycles.

The phase was computed for all 64 basket catheter electrodes and will be considered at four distinct time steps in the following. These time instances correspond to the vertical lines plotted in Figure 17.2. A conventional 2D representation of the phase values is shown in the left row of Figure 17.3, in which each line corresponds to one time step. As no distance information was incorporated in this type of visualization, a rotational pattern around electrode 2 of spline pair A/B could be seen very clearly.

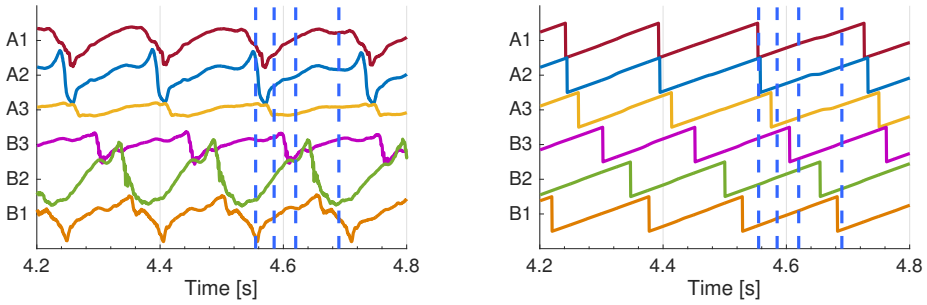

(a) Electrograms. **(b)** Phase values.

Figure 17.2: Exemplary EGMs and phase values. A gradient in activation could be observed along the circular path A1 A2 A3 B3 B2 and B1.

In order to reflect the spatial relationships, the phase was also interpolated on the atrial surface and plotted in 3D as outlined in Chapter 9.2. As the huge distance between electrodes A3 and B3 becomes apparent, the gradient is not directly interpreted as rotational source.

The true propagation pattern is visualized in the two central 3D plots of Figure 17.3. They represent the TMV extracted directly from the simulation. While the posterior wall is excited by broad wavefronts which travel from septal to lateral, the anterior wall is excited by three different wavefronts which collide at the central anterior wall. As this area is not covered by any spline, the collision remains undetected and may falsely be interpreted as rotational source.

Discussion and conclusion Analysis of panoramic mapping data using common electrogram visualization is very demanding, as the simultaneous visual assessment of 56 bipolar leads is overwhelming. Grasping the spatio-temporal relationships is even more complex. Therefore different techniques have been particularly designed for this kind of mapping data. Already in 1999, a sphere-like 3D representation of the catheter was introduced to visualize basket catheter data [252]. The most widely spread illustration used today, however, is a grid-like 2D plane [27]. For this display, splines and electrodes are arranged in an equally spaced matrix, enticing the observer to assume an isotropic distribution of measurement points inside the cardiac chamber. As demonstrated above, visualization of non-uniformly sampled data on this equidistant grid represents a potential pitfall during diagnosis.

Visualization on the anatomical shell retains the spatio-temporal relationships and allows to assess the excitation process more objectively. This is especially advantageous when the assumption of equal spacing between measurement points is not fulfilled.

The example outlined above should be regarded as a concrete case in which the spline separation was demonstrated to be diagnostically relevant in case of an oversized basket. In order to quantitatively assess this effect, multiple mapping positions, catheter size, atrial anatomies and fibrillation processes should be evaluated. This has not been done within the presented research. However, this example strongly emphasizes two aspects. First, the real position of measuring points should be incorporated in the analysis of spatio-temporal

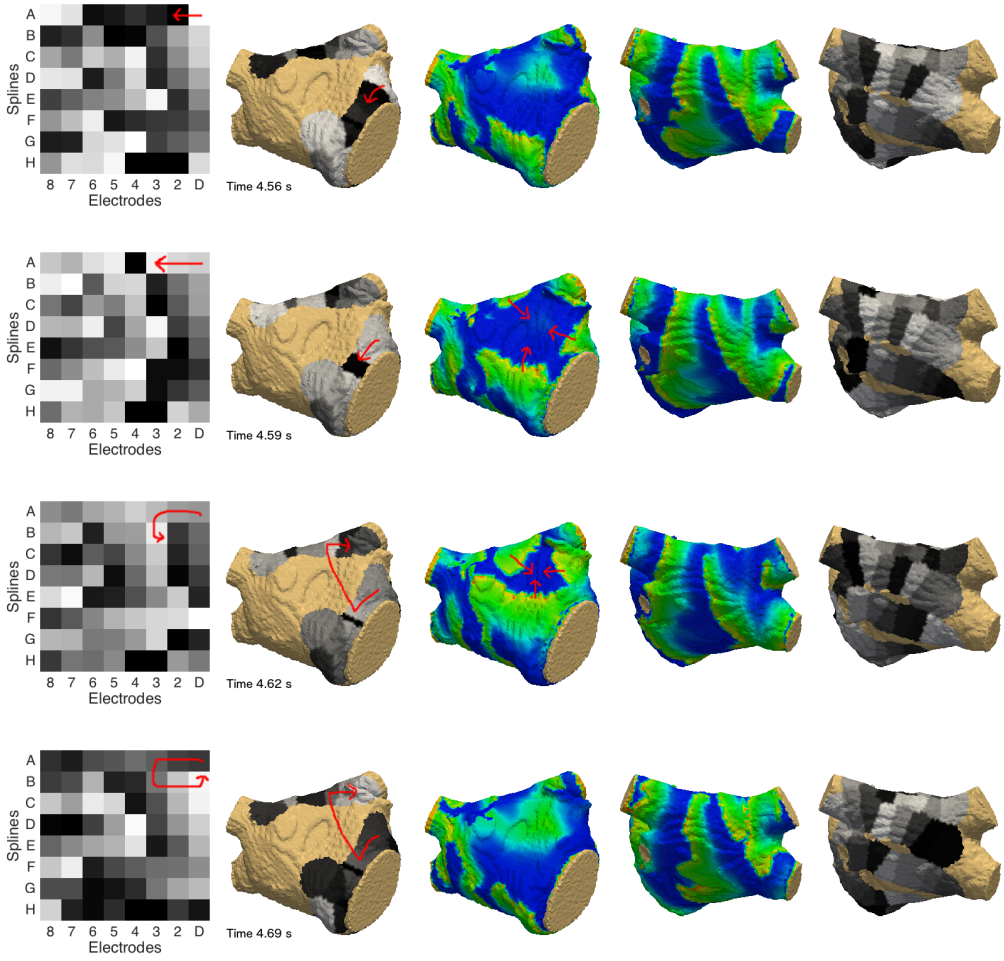

Figure 17.3: Cardiac excitation represented by TMV and phase maps in 2D and 3D. After the phase values were determined for each of the 64 electrodes, data for four distinct time steps (rows, indicated by vertical lines in Figure 17.2) were plotted in the common 2D representation (left column). Phase values were also visualized on the 3D atrial geometry (2nd and 5th column). In this representation, the spatial relationships are maintained, and the large distance between splines A and B becomes apparent. The TMV as given in the simulation shows that a collision of three wavefronts took place at the anterior wall, and no rotational activity was present (columns 3 and 4).

processes. Second, assumptions about the required mapping density for the observed process should be formulated for signal processing algorithms. Compliance with the resulting sampling density should be assured during data acquisition.

17.2 P wave Analysis

Long-term Holter ECG recordings are a valuable tool for monitoring cardiac activity. Besides the detection of arrhythmia episodes, they can also be used to assess the effects of pharmacological treatment. As annotation of the individual components in the ECG is

both tedious and operator dependent, algorithms for the automatic delineation of different waves are important instruments. Benchmarking of novel methods is complicated, however, as the cardiac activation sequence is not known and thus the algorithms are developed to approximate best previous manual annotations.

With respect to this issue, panoramic mapping offers the unique possibility to acquire comprehensive information about each single atrial depolarization. Considering simple processes like sinus rhythm or typical atrial flutter (AFlut), basket catheters are very well suited to understand the endocardial excitation pattern [80, 82, 126]. Within the presented research, data was prepared which in turn was used to develop and benchmark a novel algorithm for the delineation of the P wave. The resulting ECG analysis technique was subsequently published with Gustavo Lenis [135].

Clinical data Simultaneous ECG and EGM recordings were available from a 54 year old female patient who was subject of routine catheter ablation for paroxysmal AFib at Städtisches Klinikum Karlsruhe and provided informed consent. Simultaneous biatrial mapping was performed using the Constellation basket in combination with the Velocity EAMS. Data were exported from an intermittent episode of normal sinus rhythm (NSR). This segment was 33 s long and contained 32 P waves. Available data comprised a 12 lead ECG and the positions and EGMs of 128 electrodes (126 leads from the baskets, 2 leads of coronary sinus (CS) reference). The right atrial basket was positioned to achieve high coverage of the posterior SVC ostium, being the area in which the sinus node was located.

The position of both baskets is depicted in Figure 17.4, together with a short segment of synchronous EGM and ECG recordings. All recordings from the right and left atrium were colored in green and blue, respectively. This allowed to easily relate EGMs and recording positions. Bipolar EGMs were analyzed in this study to reduce the effect of far fields.

Outcome and conclusion Within this research project, a new wavelet based approach was developed to delineate the P wave in the surface ECG. The performance of 10 different wavelets was assessed, also considering different levels of wavelet decomposition. First, the validity of the proposed method was confirmed using synthetic data. Amplitude, shape and the amount of noise was hereby varied to obtain representative results. Then the delineation performance was assessed by comparing the atrial activity as seen in the intracardiac mapping and the result of automatic annotation. The ground truth for the beginning of the P wave was defined as the earliest point in time at which activity was detected in the EGMs of at least three electrodes. Best results were obtained for the reverse biorthogonal wavelet 3.3 (mean accuracy of 1.95 ± 5.61 ms), which was subsequently applied to the QT database from PhysioNet. Overall performance showed an accuracy of -0.27 ± 12.2 ms for annotation of the P wave onset in 3194 ECGs.

This work is a neat demonstration of the joint analysis of intracardiac mapping data and surface ECG during algorithm development. As the basket catheters were positioned directly at the source, averaging effects as on the torso were strongly reduced. The panoramic baskets

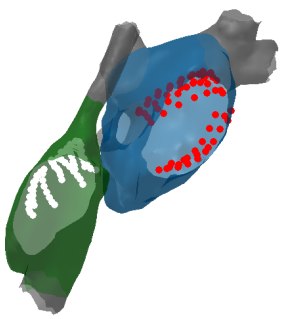

(a) Catheter position (LAO).

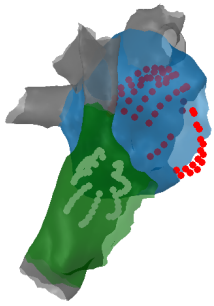

(b) Catheter position (RAO).

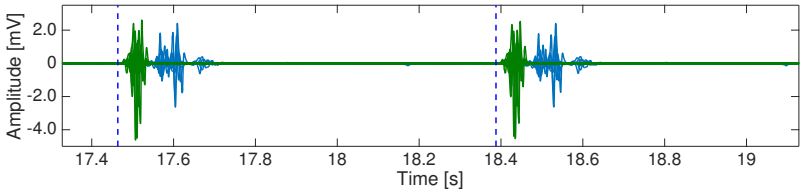

(c) Intracardiac EGMs of both basket catheters.

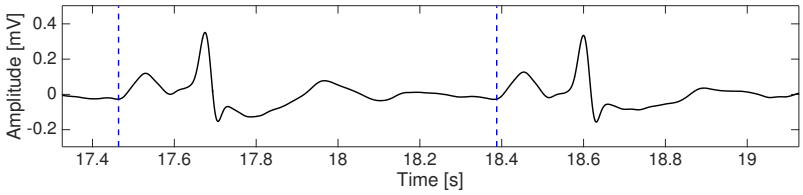

(d) Surface ECG (lead II).

Figure 17.4: P wave analysis using basket catheters. Intracardiac EGMs were recorded during simultaneous biatrial mapping of sinus rhythm. Data from the RA is shown in green, while LA information is plotted in blue. The BEGM traces clearly demonstrate that the RA was depolarized before the LA. Vertical lines indicate the beginning of the P wave. Analysis of both BEGM and surface ECG data allowed to assess the performance of new algorithms for P wave delineation [135].

provided simultaneous view on the endocardial wall, helping to directly relate intracardiac EGMs and P wave.

17.3 Mapping of Atrial Flutter

Although the interspline distance of panoramic basket catheters may be too large to adequately sample complex depolarization patterns like during AFib, it may be sufficient to comprehend more simple rhythms like AFlut.

Clinical data After multiple catheter ablations for AFib, a 54 year old male patient presented with persistent atypical AFlut at Städtisches Klinikum Karlsruhe. A stable BCL of 253 ms was measured with distal to proximal CS activation and considered indicative

for a reentrant mechanism. The EP study was performed with the Velocity EAMS. After acquisition of the atrial anatomy using a 10 pole circular catheter, a 60 mm Constellation basket catheter was introduced to acquire an LAT map as single shot technique. Although the basket position allowed good coverage of roof and anterior wall, it was not possible to acquire activity for the complete cycle. Therefore detailed data from the sequential mapping with the spiral catheter was evaluated in addition.

Level of detail in panoramic and sequential mapping Data from both the single shot panoramic approach and the sequential mapping was analyzed retrospectively. EGMs which only contained noise (bipolar voltage <0.1 mV) and those recorded inside the vessels were rejected. Thus a total of 40 and 158 points was evaluated from basket and sequential mapping, respectively (compare Chapter 6.3). As depicted in the comparative arrangement in Figure 17.5, limited septal coverage could be observed when mapping was performed with the panoramic basket. The septal to lateral arrangement of electrodes along the splines could be seen clearly. Data from all atrial structures were acquired during sequential mapping. For both datasets, interpolation threshold d_m was set to 10 mm.

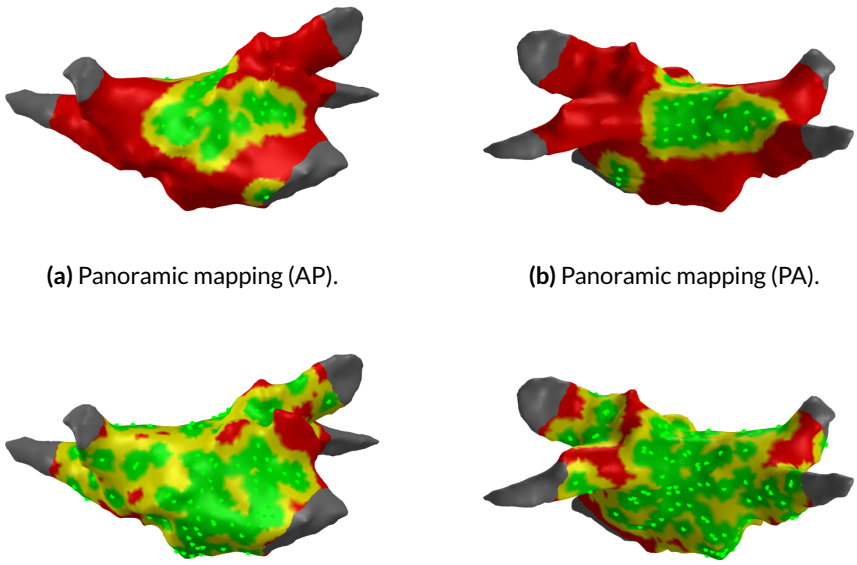

(a) Panoramic mapping (AP).

(b) Panoramic mapping (PA).

(c) Sequential mapping (AP).

(d) Sequential mapping (PA).

Figure 17.5: Coverage in simultaneous and sequential mapping. Positions of the acquired points matched well with the electrode arrangement of a Constellation basket introduced via transseptal puncture. As splines accumulated at the roof and MV, the interior-septal part of the posterior wall remained uncovered (a, b). More homogeneous distribution of measurements was achieved with sequential mapping (c, d).

Clinical data was retrospectively analyzed with the workflow outlined in Chapter 18.1 to determine the excitation pattern visible for both mapping approaches. The resulting LAT

maps are shown in Figure 17.6. The LAT map which was generated using basket catheter data very well indicated both the septal to lateral activation of the superior anterior wall and the activation gradient along the roof. Information about the depolarization pattern of septal regions and the inferior anterior wall was not available.

The excitation pattern in these regions was elucidated by detailed sequential mapping. The inferior anterior wall was depolarized from lateral to septal by a pivoting wavefront, covering more than 50% of the BCL but just being passively activated. The septal region, as opposed, exhibited activity which completed the mapping of the reentrant path. This confirmed the diagnosis of a roof-dependent macro reentrant mechanism.

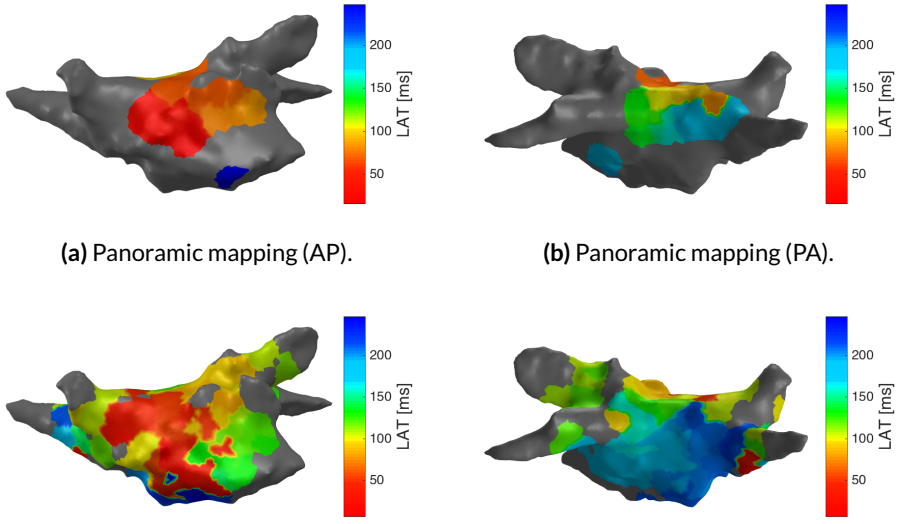

(a) Panoramic mapping (AP). **(b)** Panoramic mapping (PA).

(c) Sequential mapping (AP). **(d)** Sequential mapping (PA).

Figure 17.6: LAT maps acquired during sequential and simultaneous mapping. Septal to lateral activation could be observed on the anterior wall, passing the roof through an isthmus and depolarizing the posterior wall from lateral to septal. Septal and antero-inferior parts of the cycle remain uncovered during the panoramic mapping.

Dynamic visualization of the excitation pattern Data from simultaneous and sequential mapping were additionally processed for dynamic visualization. For each EGM, the instantaneous energy was computed and normalized as presented in Chapter 9. It was interpolated on the covered areas of the atrial anatomy and visualized as time-continuous movie. Snapshots of seven selected time instances are plotted in Figure 17.7. Note that the time scale chosen here is different from the isthmus-based reference time in Figure 17.6.

The pattern of excitation could clearly be traced in the sequentially acquired map, shown in both central columns. The inferior anterior wall was depolarized at around 50 ms. The excitation passed the roof through the lateral isthmus at about 70 ms and subsequently propagated along the posterior wall in septal direction, returning to the anterior wall at about 170 ms.

Also in panoramic mapping, the process of depolarization could be well tracked along the roof (50 ms to 130 ms). Excitation of the inferior anterior wall and the septal aspect of the macro reeentry could not be observed.

Discussion and conclusion Sequential mapping of stable tachycardias like AFlut is the common approach to acquired data for the identification of the underlying mechanism. Despite the option of automatic point collection in state-of-the-art mapping systems, the sequential collection of electrogram data is time consuming. In addition, the tachycardia may convert into other forms during mapping or stop due to mechanic stress induced by the catheter. This makes single shot techniques a desirable alternative to conventional sequential mapping.

The extended field of view offered by panoramic basket catheters in theory allows to acquire comprehensive information from different atrial structures simultaneously. The central question, however, is whether or not the decisive parts of the flutter cycle are covered during mapping. If this is the case, time for data acquisition in AFlut could be reduced to seconds.

In the example outlined above, the critical isthmus was covered by four splines of the basket catheter, allowing to deduce a target for ablation. Several atrial regions, however, were not covered by the basket electrodes. Thus only an incomplete part of the depolarization pattern was acquired. Nevertheless, repositioning the catheter to a complementary location would probably allow to amend the picture and clarify the mechanism. This does not represent a single shot technique any more, but still could be expected to reduce the time required for mapping. Due to the high costs of a basket catheter, this method seems especially reasonable if the presenting tachycardia is demonstrated to easily alternate between several mechanisms.

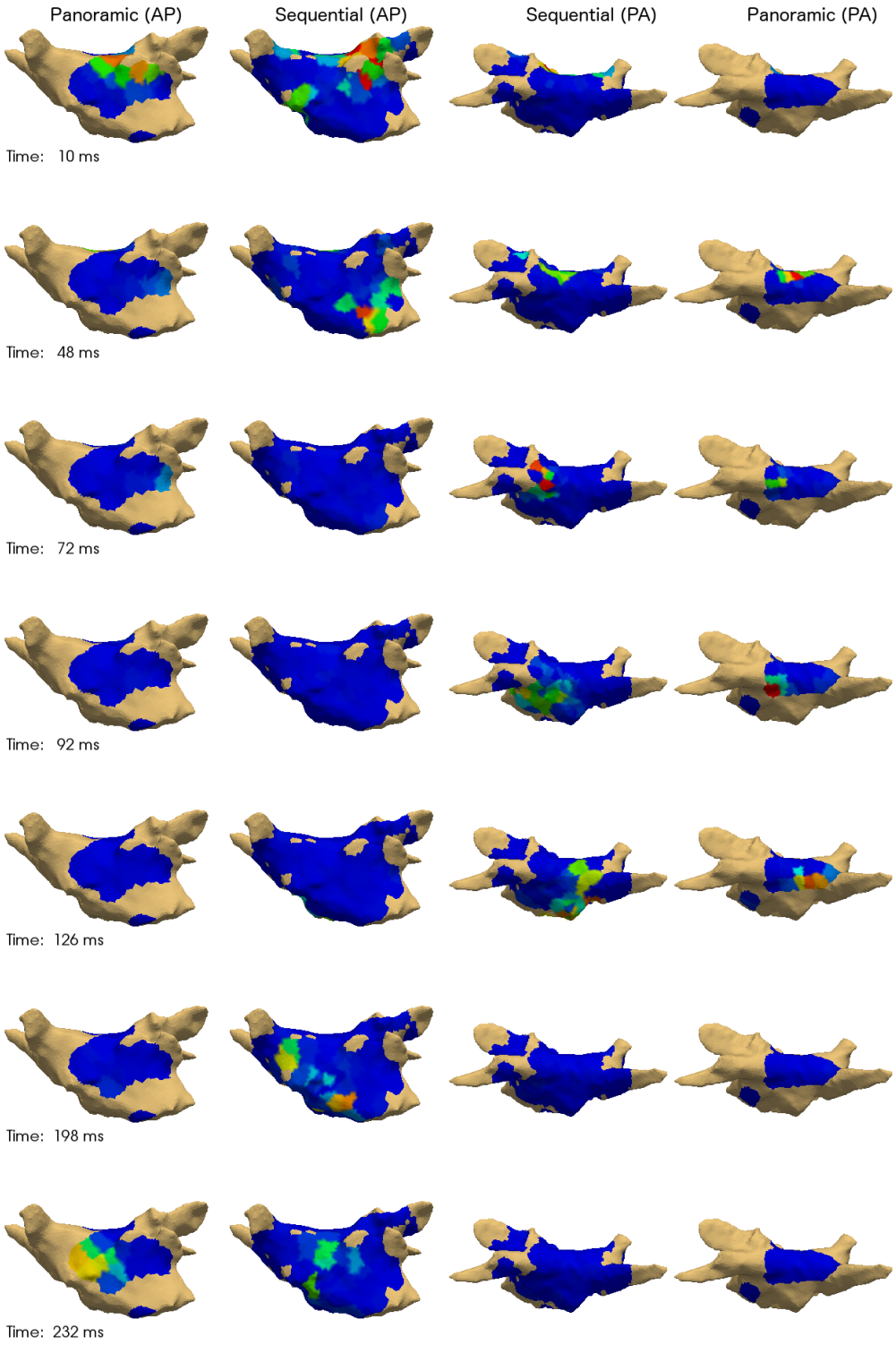

Figure 17.7: Dynamic visualization of cardiac excitation based on panoramic and sequential mapping data. Energy of the EGMs was computed and plotted color-coded on the atrial shell (for details see Chapter 9). The entire propagation pattern could be observed in the sequential mapping data (two central columns), while at time 198 ms no depolarization was found within the basket catheter's field of view (left and right columns).

17.4 Excitation Dynamics during Atrial Fibrillation

The most important field for application of panoramic mapping is the acquisition of non-stationary processes which do not allow for sequential mapping. AFib is the most prominent and wide spread example for such an arrhythmia. Hereby, the atrial depolarization pattern changes dynamically and seems pseudo chaotic. Although the exact mechanisms maintaining AFib are not clear, established theories consider meandering rotational sources or multiple wavelets that annihilate or proliferate by interaction.

Clinical data To demonstrate the possibilities and challenges of basket catheter mapping during AFib, a biatrial panoramic recording was available. Data was acquired during routine index ablation of paroxysmal AFib in a 54 year old female at Städtisches Klinikum Karlsruhe. Both atria were mapped simultaneously using Constellation catheters of diameter 48 mm and 60 mm. Electrograms and anatomical information was acquired using the Velocity EAMS. As only 128 channels could be recorded by this system, the CS catheter electrodes 7 and 8 had to be attached instead of H3 and H4 of the LA basket. Both basket catheters were positioned to achieve optimal wall contact and signal quality. Data were recorded for several minutes, of which a segment of length 30 s will be discussed in the following.

Signal processing Data were exported from the clinical system and analyzed retrospectively. Atrial anatomies were processed as outlined in Chapter 6.1. Stability of both catheters was confirmed already before data export. The mean position of all electrodes over the 30 s recording was computed and used to generate coverage maps as shown in Figure 17.8 (compare Chapter 6.3). While the anterior walls were covered well, especially coverage of the LA posterior wall was limited. Subsequently, data from 61 right and 62 left atrial electrodes could be analyzed with respect to the spatio-temporal depolarization process.

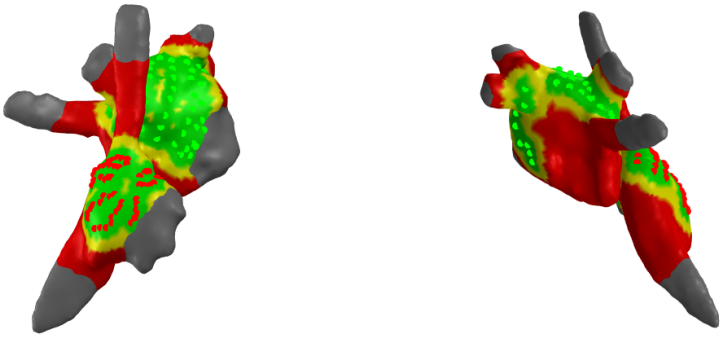

(a) Coverage (RAO). **(b)** Coverage (PA).

Figure 17.8: Coverage in biatrial mapping of AFib. One basket catheter was positioned in each atrium. Good coverage was achieved for the LA anterior wall and RA lateral wall. The posterior LA was hardly covered.

Unipolar signals were first filtered using a second order high-pass and low-pass of 1 Hz and 300 Hz, respectively. Based on visual inspection of the spectrum, additional artificial frequency components were filtered at distinct values of 50 Hz, 144 Hz, 145 Hz, 196.6 Hz and 203.5 Hz, together with their harmonics (see Chapter 5.1). Ventricular depolarizations were detected as presented in Chapter 5.2. Subsequently, the principal component analysis (PCA) was applied to reduce ventricular far fields (compare Chapter 7.1). The resulting unipolar EGMs from both basket catheters are shown in Figure 17.9.

Considering activation of the RA, nearly synchronous depolarization patterns were observed from the beginning of the shown segment up to about 22 s. Activity became less organized between 22 s and 25 s, as indicated by a lack of distinct gradients in the EGMs of splines D, E and F. At about 25 s, however, the nearly synchronous depolarization could be seen again.

Three splines in the LA primarily recorded ventricular far fields. Visual inspection revealed that these were located towards the MV, with splines H and A projected onto the inferior posterior wall and spline B onto the inferior anterior wall. No signal was recorded for H3 and H4, as the CS catheter was connected as positional reference. Splines C to G showed the complex activation pattern of the LA endocard.

The phase of all unipolar electrograms (UEGMs) was computed using sinusoidal recomposition and Hilbert transform (see Chapter 8.3). To determine the cycle length for recomposition, LATs were annotated based on the steepest negative derivative of the unipolar signals (compare Chapter 8.1). To avoid erroneous detections of EGMs low voltage, a refractory period of 120 ms was applied and a voltage difference of at least 0.1 mV was required within a window of ± 5 ms around the potential LAT.

Although the PCA-based VFF removal method was observed to strongly reduce the influence of far fields, these ventricular components were not completely diminished and could potentially be annotated as LAT. Thus the signal segments not synchronous to the

ventricular depolarization were evaluated with respect to the amplitude of their LATs. All signals were excluded from further processing which did not exceed a minimum of 0.5 mV amplitude in any of the respective detected LATs.

Excitation dynamics The instantaneous phase was subsequently interpolated on the atrium. Snapshots of selected time frames are visualized in Figures 17.10 to 17.12. All of them visualize the cardiac excitation corresponding to the electrograms shown in Figure 17.9.

A sequence reflecting the organized excitation of the RA between 20 s and 22 s is depicted in Figure 17.10. Two wavefronts entered the RA lateral wall at 20.24 s and depolarized it completely before colliding at the mid-lateral wall at 20.32 s. This collision could no longer be observed in both subsequent RA activations (starting at 20.42 and 20.56 s, respectively). Instead, a first wavefront depolarized the superior TV annulus and was stopped by a functional block (20.44 s and 20.60 s, respectively), while a second wavefront arriving clockwise from inferior excited the remaining tissue (20.50 s and 20.66 s). No propagating wavefronts could be observed between these depolarization processes.

LA excitation was less clear to interpret. Phase movies indicated a passive activation by wavefronts traversing the roof (20.26 s, 20.44 s) or coming from the lateral wall (20.24 s, 20.52 s, 20.70 s). Excitation from the septal side was also observed (20.36 s, 20.50 s, 20.70 s).

Starting at about 22 s RA activation became more complex with nearly continuous depolarization. However, still a dominant excitation pattern could be observed which propagated from the lower posterior lateral wall in anterior direction. For the LA, the phase maps presented no broad activation pattern but were more indicative for excitation by multiple wavelets.

As already indicated by the EGMs, activation became more regularized after 25 s. The sequence of images shown in Figure 17.12 covers a duration of about 400 ms in which the RA was depolarized three times by broad wavefronts coming from the roof in counter-clockwise direction (25.56 s, 25.76 s and 25.98 s). Wavefront collision on the lateral wall was just observed in the last depolarization (26.00 s).

Similarly, activation of the LA appeared more organized within this time frame. Broad wavefronts were found to come from the lateral wall (25.54 s, 25.68 s and 25.86 s) and the septum (25.74 s and 25.96 s). For both the RA and the LA, time instances were found in which no depolarization was observed (e.g. from 25.64 s to 25.74 s in the RA; 25.64 s or 25.84 s in the LA).

Discussion and conclusion Understanding the excitation dynamics during AFib is the most challenging task in the field of contemporary cardiac rhythmology. Due to their ability of simultaneous panoramic electrogram acquisition, basket catheters are promising tools to tackle this issue. Analysis and interpretation of the measured data, however, confront physicians with tremendous challenges. Most importantly, the spatio-temporal process of

depolarization has to be perceived within the measured data, and subsequently the dominant mechanisms need to be identified.

As outlined previously, dedicated software has been designed for the visualization of basket catheter data for research purposes already in 1999 [252]. Result of signal processing was projected on a 3D sphere, reflecting the shape of the catheter. It was demonstrated on data from AFlut patients, in whom it generated LAT maps for every recorded cycle. Mapping of unstable tachycardias, however, had not been performed.

Analysis of AFib data is the focus of a recently launched commercial software for the diagnostic assessment of basket catheter data. Although details about the utilized processing are not known up to now, promising success rates in the treatment of AFib have fostered usage of this approach [27]. As discussed in Chapter 17.1, geometrical information from the specific patient is not incorporated in that approach.

Within the scope of the presented research, a method for visualizing the cardiac excitation dynamics in 3D was developed. It was applied to AFib data within the presented chapter. Considering the truly measured electrode positions allowed to precisely relate atrial anatomy and electrogram information for spatio-temporal analysis. Unipolar EGMs were transferred to phase-space in order to allow for visual interpretation by human experts.

Certain parameters were semi-automatically determined during this process, like the fibrillatory cycle length, interpolation distances, voltage thresholds for LAT annotation and refractory times. Although all values were chosen within physiological reasonable range, the influence of parameter selection was not assessed.

The depolarization pattern derived from phase-mapping was compared to a version that was directly determined based on the annotated LAT values. Although this was done for several dozens of representative time steps, no quantitative comparison between both techniques was performed.

Although issue of spline bunching was successfully addressed by considering the true electrode positions within the analysis, the problem of limited coverage was also encountered in the presented case. Due to deformation of the basket catheter, the LA posterior wall was hardly covered. Excitation dynamics presented in Figures 17.10 to 17.12 demonstrated a LA depolarization caused by wavefronts emerging from the LA posterior wall. A more detailed analysis was not possible, however, due to the lack of data acquired there. If this information would have been available directly during clinical mapping, a specific mapping of the posterior wall may have been considered.

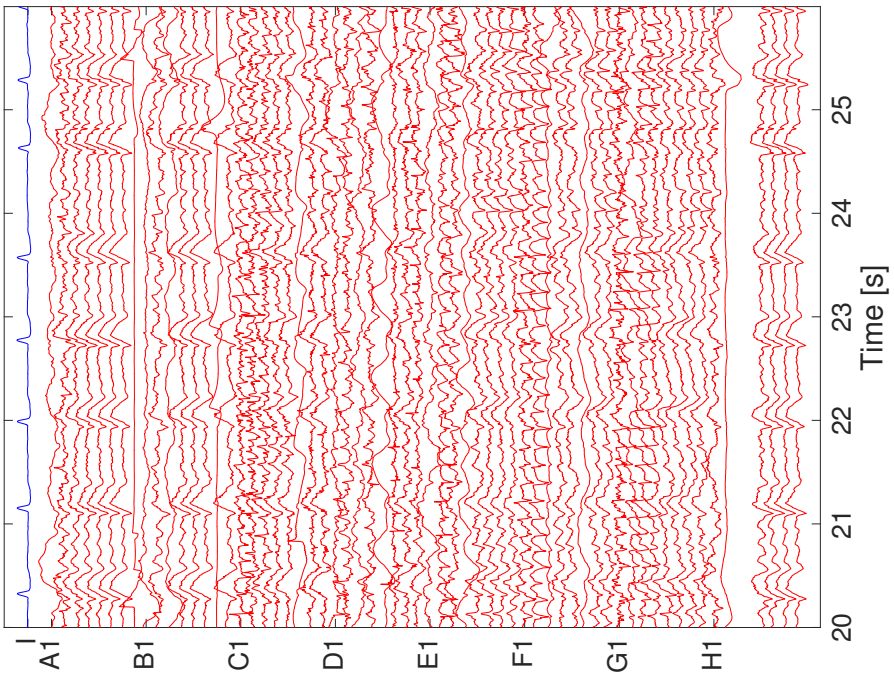

(a) Unipolar signals recorded in the LA.

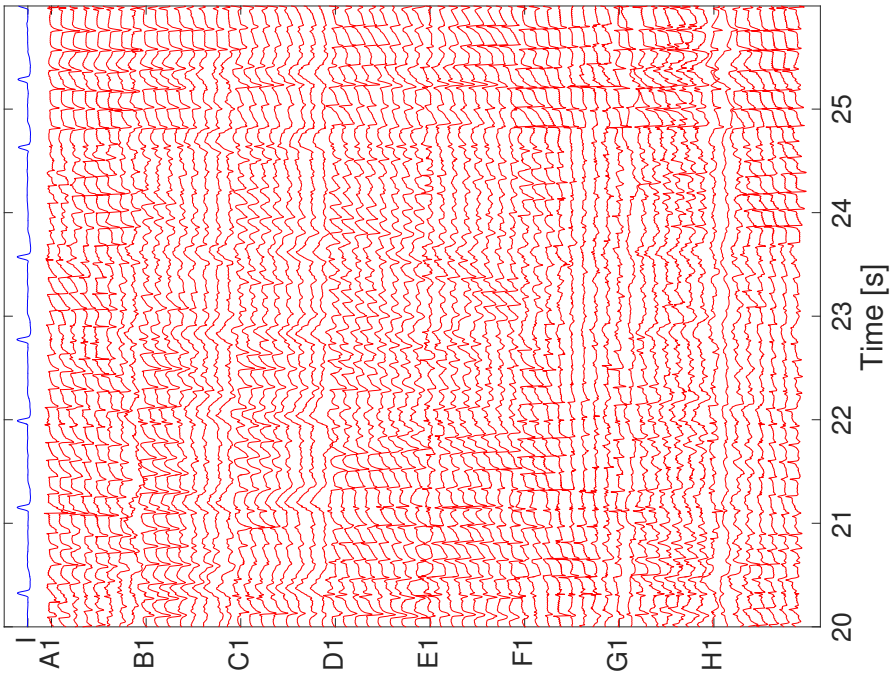

(b) Unipolar signals recorded in the RA.

Figure 17.9: Unipolar EGMs during AFib. Data were recorded by simultaneous biatrial basket catheter mapping in the RA (a) and LA (b), respectively. Surface ECG lead I is shown at the top of each plot. Preprocessing included band-pass filtering and the removal of artificial discrete frequencies. Ventricular far fields were reduced by a PCA-based technique. Note the decrease of right atrial organization between 22 s and 25 s.

Figure 17.10: Phase plots indicating organized activity in the RA. Instantaneous phase was determined from the EGMs and visualized on the atrial geometry. The right lateral wall was depolarized by distinct broad wavefronts, whose site of collision changed dynamically. Activation of the LA was more complex but seemed to be driven by waves originating from the posterior wall.

Figure 17.11: Phase plots of unorganized activity in both atria. Continuous depolarization was observed on the RA lateral and LA anterior wall.

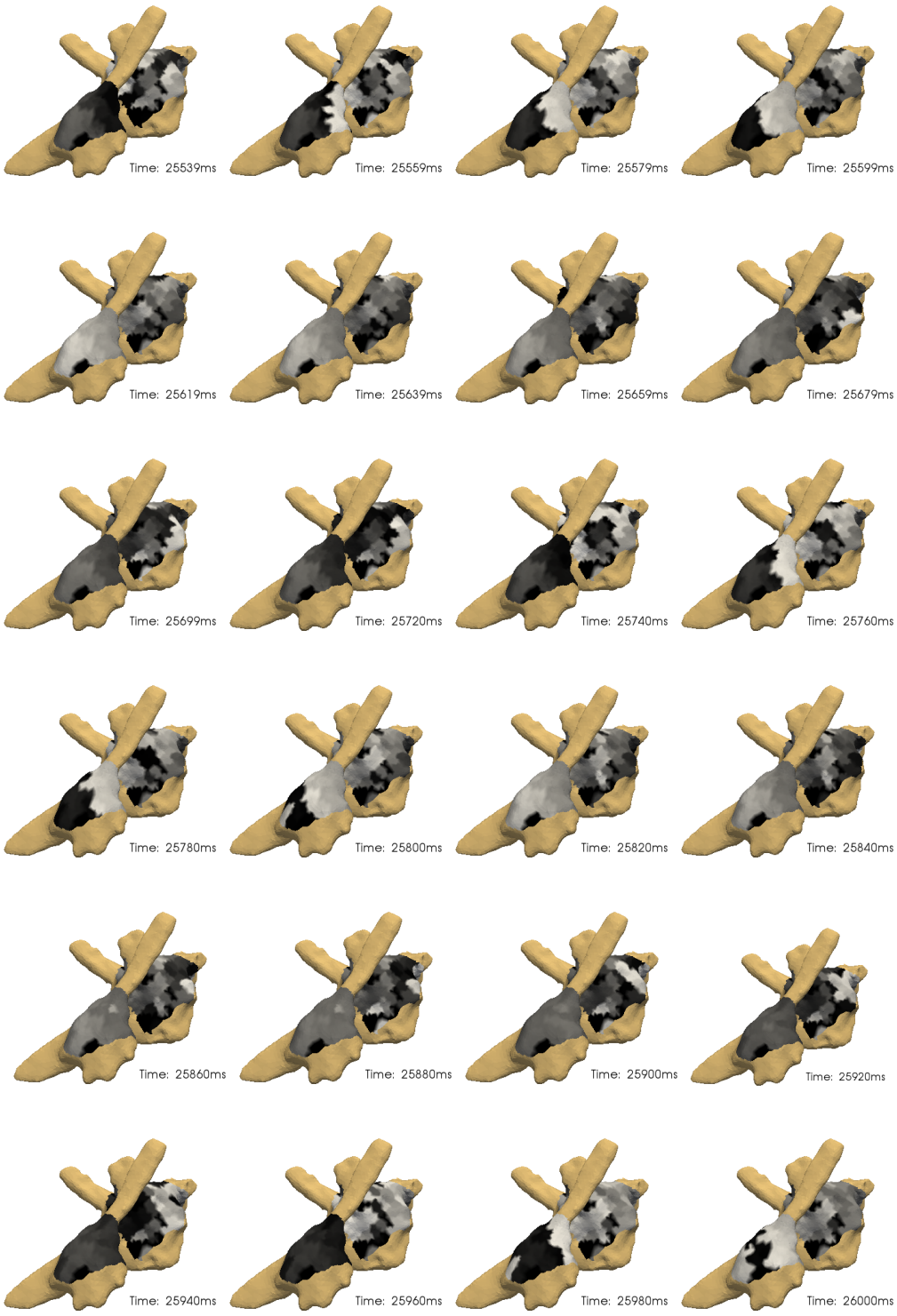

Figure 17.12: Phase plots during organized activity in both atria. The anterior walls of both RA and LA were activated by broad wavefronts, also showing times without electrical activity.

17.5 Discussion and Conclusions

Panoramic mapping with a 64 electrode basket catheter provides huge amounts of data, complicating analysis with conventional techniques. Both the deformation of splines and the large number of simultaneously recorded electrograms make visual assessment of the underlying excitation pattern highly challenging. This inspired research for novel methods of data processing and visualization.

Coverage and spline bunching Several issues limit the ability of basket catheters to record complete panoramic mapping data. First, the number of electrodes is restricted to 64. Although this is a threefold increase when compared to other conventional catheter types, this averages less than about 0.5 electrodes per cm^2 in an atrium of 150 cm^2. Second, the recording positions are strongly determined by the bending of splines along the atrial wall. Selection of a strongly oversized catheter may cause a lack of coverage due to spline bunching. Third, commercial availability of catheter sizes is limited by the product palette, making choice for the individual patient a trade-off.

Although these issues cannot be avoided, knowledge about their effects allows to design appropriate analysis techniques. Incorporation of recording positions and the patient specific anatomy is a major advantage of the presented algorithms, excelling state-of-the-art signal analysis. As demonstrated in Chapter 17.1, neglecting spline bunching may pose a pitfall for diagnosis. When the true electrode positions are incorporated into analysis, however, comprehension of depolarization dynamics is more reliably possible.

The applicability of this approach has also been shown on clinical mapping data in Chapters 17.3 and 17.4. In case of AFlut, the critical isthmus was well covered by the basket catheter. Due to limited septal coverage, however, it was not possible to acquire data from the complete cycle. The latter could be sampled by sequential mapping. Sequences of biatrial panoramic mapping data of AFib were processed and illustrated in Chapter 17.4. Patterns of different complexity were found by visual inspection and matched very well with the level of organization in recorded EGMs. Due to a lack of coverage on the posterior wall, however, exact evaluation of the driving source was not possible.

Sampling and identification of cardiac processes Cardiac depolarization is a dynamic process, whose understanding requires a certain level of measurement information. In signal processing theory, correct reconstruction of a signal is possible if the sampling theorem is fulfilled: The signal must not have frequency components above the Nyquist frequency. Formulation of a corresponding spatio-temporal theorem for cardiac excitation patterns could be based on the electrode positions as spatial measurement points and the cardiac wave length given by conduction velocity and refractory period.

Cardiac tissue, however, is strongly heterogeneous. Especially the presence of scar from previous ablation of fibrosis caused by structural remodeling make assumptions for homogeneous tissue patches invalid. Due to the variety of possible tissue characteristics in

clinical patients, a general recommendation with regard to spatial sampling density does not seem reasonable. During epicardial mapping studies with a spoon-shaped electrode array (244 electrodes, interelectrode spacing 2.25 mm), individual excitation waves were reconstructed during AFib [34]. Statistical analysis showed a mean number of 4.5 waves per cm^2 within the mapped field per AFib cycle. Processes of this complexity cannot be accurately evaluated during panoramic mapping. Analysis of excitation patterns on a more global scale, however, are not prohibited by the given interelectrode spacing of a basket catheter. For more detailed mapping of regions of interest, a combined approach utilizing catheters with smaller interelectrode spacing is recommended (e.g. Orion catheter, interelectrode spacing of 2.25 mm).

Special attention needs to be paid to the varying interelectrode spacing along and between splines. While the spacing along splines is defined by manufacturing and thus the basket catheter type, the interspline distance varies with spline bunching. For the detection of rotational sources, an inter electrode spacing of 10 mm is generally considered sufficient [249]. Especially for panoramic basket catheters, distances between splines frequenty exceed 20 mm, however, violating a frequently posed prerequisite for accurate analysis.

Applicability of panoramic mapping Concludingly, panoramic mapping can be considered a valuable tool for the acquisition of comprehensive mapping data on a macroscopic scale. Effects like spline bunching and limitations in coverage can be incorporated into analysis techniques, allowing an appropriate handling of these issues.

During the presented research, several techniques have been developed to analyze basket catheter recordings. Projection of the dynamic processes onto the atrial shell allows to correctly interpret the depolarization pattern and represents a significant improvement compared to the state-of-the-art. It provides the basis for subsequent visual assessment of the excitation pattern. With respect to future research, automatic detection of dominant patterns is considered a valuable addition to the existing processing. It has been implemented for the detection of SVES as describend in Chapter 16.2, but analysis of unstable rhythms like AFib pose additional challenges. If such an analysis would be performed within the procedure, remapping of interesting areas may have been performed. A combined approach of simultaneous large-scale and relevance-based sequential mapping may offer an alternative way to cope with the limited coverage in panoramic mapping.

CHAPTER 18

Diagnosis of Atrial Flutter Forms

The interpretation of EP data for the clinical diagnosis of atrial flutter (AFlut) mechanisms is currently based primarily on the experience of the cardiologist. During data acquisition, the physician has to closely observe the EGM and manually annotate extraordinary morphologies like double potentials, prolonged activity or diastolic potentials. While simultaneous inspection of EGM data is possible when acquired with 20 pole spiral catheters, the analysis and interpretation of data recorded by a 64 pole mini-basket cannot be carried out by any treating physician. State of the art automatic signal analysis is limited to voltage and activation time mapping, strongly simplifying morphological properties. Interpretation of these maps can be time consuming as no computational means are available.

Advanced methods for the automatic analysis of intracardiac mapping data have been presented in the previous Chapters in **Part 2** of this thesis. Up to now, the rationale behind these methods was outlined, and they were individually benchmarked using simulated or annotated clinical data. In the following, their ability to support diagnosis will be demonstrated on clinical cases which were recorded at the Städtisches Klinikum Karlsruhe. It will be shown that they are capable of extracting more comprehensive information from the mapping data and highlight specific atrial regions for closer inspection by the cardiologist.

18.1 Analysis Procedure

An automatic signal analysis workflow was developed within the scope of this thesis, incorporating the different techniques outlined in the previous chapters. To allow processing of mapping data from all clinically utilized electroanatomical mapping systems (EAMSs), a common data structure was defined as described in Chapter 14.3. Both geometrical and electrical data were prepared before the common processing was executed.

Preprocessing steps First the stability of the arrhythmia was assessed. Therefore the CS activation was evaluated for each single acquired point. The instantaneous basic cycle length (BCL) was computed for each mapped cycle as described in Chapter 8.2. The progress

of BCL over time was shown to the cardiologist, and the median BCL was suggested as reference measure.

After this reference BCL was confirmed by the physician, all recordings whose BCL deviated more than 10% were rejected from further analysis. This allowed to exclude extrasystoles from analysis in case they did not represent the desired rhythm. In addition, the correlation of LAWs within the reference trace was assessed and the recording discarded if its value was below 0.6. This procedure was also used to exclude all acquisitions which synchronized on an LAW that was not similar to the mean morphology of all recordings.

Next all QRS complexes were annotated in the surface ECG as described in Chapter 5.2. This information was used to determine one cycle of the tachycardia which was free of ventricular depolarization artifacts. As described in Chapter 11.1.2, this time span had to be defined for the computation of measures like the cycle length coverage (CLC).

Subsequently, the coverage was determined and visualized (compare Chapter 6.3). The interpolation functions were prepared as described in Chapter 8.4.

Analysis of individual EGMs Single signals were analyzed first. The amplitude of each signal was computed to assess the presence of atrial activity and exclude signals which only contained noise. The NLEO was computed and normalized to permit the time-continuous visualization of the depolarization process. As shown in Chapter 9.1, this avoided the potentially erroneous annotation of LAT in prolonged EGMs or DPs.

The activity of each EGM was determined by using the methods introduced in Chapter 11.1.2. For each channel, the CLC of the single signal was computed. Classification of each EGM was performed to detect DPs (compare Chapter 11.1.3).

As the instantaneous BCL was allowed to vary within $\pm 10\%$ of the reference BCL, time dependent measures may not be comparable when determined once for a short and once for a long instantaneous BCL. Considering a tachycardia with a reference BCL of 300 ms, tissue which is depolarized at the end of the cycle may be annotated active at 270 ms or 330 ms, respectively. To minimize this effect, all data were resampled to 2 kHz and normalized to exactly match the reference BCL. The instantaneous BCL of each acquired point was used to compute the factor for normalization. The LAT of each signal was determined within this normalized single cycle (compared Chapter 8.1). In addition, the data allowed to compute statistics about the jitter of BCL.

Multichannel analysis After the activity was assessed in each single signal, the multichannel measures were determined (compare Chapter 11.2). Based on the active surface regions around each measurement point over time, the progress of depolarization and the relative amount of active area were computed (see Chapter 11.2.2).

Next the area-based CLC was determined as described in Chapter 11.2.3. The amount of activite tissue as a function of time was also evaluated to identify diastolic activity and define the reference time of LAT maps accordingly (see Chapter 11.2.4).

Visualization All resulting measures were interpolated on the atrial anatomy and plotted in MATLAB. This allowed to gain a first impression of the analysis results and determine if an adaption of parameters was required.

Data were additionally exported for the visualization in KaPAVIE after processing was finished. This enabled the combined visualization of electrograms and analysis results as will be demonstrated in Figure 18.12.

18.2 Focal Source

The general concept of regenerating an LAT map retrospectively using clinical data is demonstrated using data from AFlut with a focal mechanism.

18.2.1 Focus from posterior RSPV

A 52 year old female was referred to catheter ablation due to a suspected left atrial focal tachycardia with cycle length of 190 to 270 ms. Intracardiac mapping was performed using the Rhythmia system and the Orion catheter. An LAT map of the RA showed earliest activity close to the SVC, and subsequent left atrial activation mapping revealed focal activity originating from the posterior RSPV. The LAT map as generated by the mapping system during the procedure is visualized in Figure 18.1, and will be referred to as *Clinical LAT map* for the course of this chapter. Encircling the right PVs converted the tachycardia to sinus rhythm. Ongoing focal activity could be observed during mapping inside the RSPV.

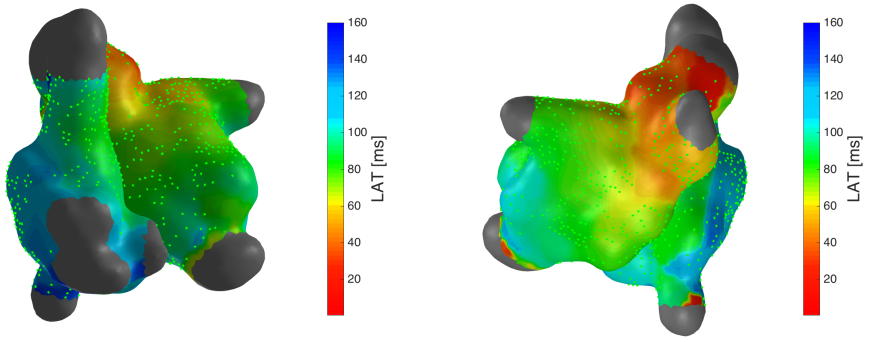

(a) LAT map in anterior view. **(b)** LAT map in posterior view.

Figure 18.1: Clinical LAT map. Earliest activation indicated a focal source located at the posterior RSPV. Data were acquired using the Rhythmia mapping system. Electrode positions as found during remapping are shown in green.

The study data were exported and transferred to Institute of Biomedical Engineering (IBT). Both atria were remapped based on the continuous position and electrogram data as outlined in Chapter 14.3. After stability analysis of the CS activation sequence, 416 and 701

EGMs were available from the RA and LA, respectively. Their positions are indicated by green dots in Figure 18.1. BCL was determined to 190 ms. The automatically generated LAT map is plotted in Figure 18.2. This type of retrospectively created map will be indicated by *remapping at IBT*. The LAT reference time was correctly adjusted to represent the focal origin as earliest point of activation. Good general agreement between the clinical map and the reconstructed map could be observed.

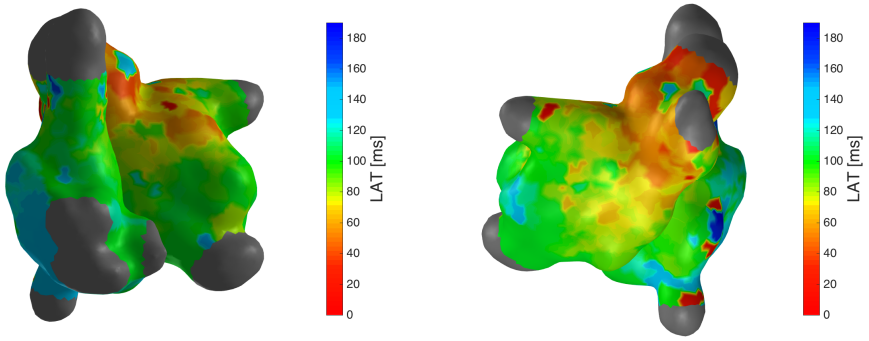

(a) LAT map in anterior view. **(b)** LAT map in posterior view.

Figure 18.2: LAT map as generated by remapping at IBT. Qualitatively, good agreement to the clinical map as shown in Figure 18.1 was observed.

18.3 Microreentry

Algorithms for the identification and localization of micro reentrant sources of AFlut were outlined in Chapter 11.2.2. These will be demonstrated on two sets of clinical data in the following chapters.

18.3.1 Microreentry RIPV

A male patient aged 64 was treated for persistent atrial tachycardia. Previous procedures included PVI, isthmus ablation, and bypass surgery. Biatrial LAT mapping was performed using the EnSite Velocity system and a 10 pole spiral catheter. The corresponding LAT map is shown in Figure 18.3 and indicated an early activation close to the RIPV, with passive activation of the RA. Visual inspection of EGMs in this region revealed a microreentry which was documented in the clinical procedure report. Ablation at the area of the mid-diastolic potential terminated the arrhythmia and restored normal sinus rhythm (NSR).

Data could be exported and imported directly, without the need to remap the tachycardia. 116 EGMs were acquired in the RA and 223 EGMs in the LA. Analysis of the area based cycle length coverage clearly highlighted the region at the posterior RIPV, in which the

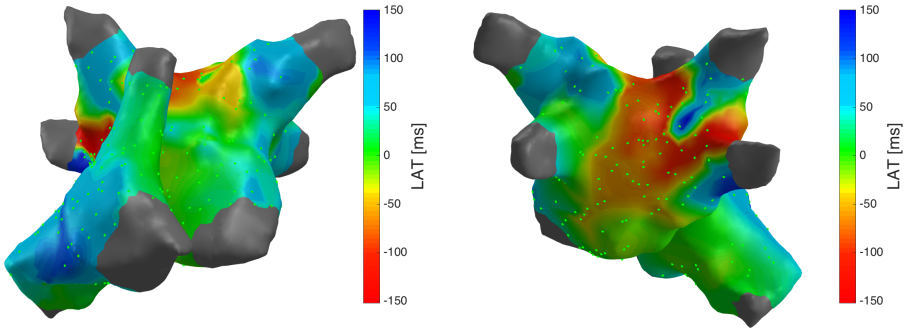

(a) LAT map in anterior view. **(b)** LAT map in posterior view.

Figure 18.3: Clinical LAT map. Earliest activation was found close to the RPVs with passive activation of the RA.

microreentry had been observed by visual EGM assessment during clinical mapping (see Figure 18.4). Notably, this area was identified automatically, without the need of EGM annotation.

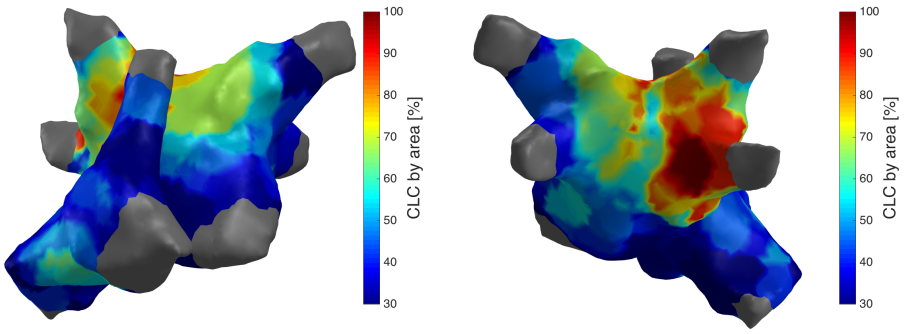

(a) CLC in anterior view. **(b)** CLC in posterior view.

Figure 18.4: Cycle length coverage by area. The increase of CLC at the RIPV clearly highlights the location at which a microreentry was observed during clinical mapping.

18.3.2 Figure 8 Reentry at Anterior Wall

A Figure 8 reentry was observed during activation time mapping of an atypical AFlut in a 68 year old female patient. The EP study was performed using the Rhythmia EAMS. The corresponding LAT map is shown in Figure 18.5. A crowding of isochrones could be observed at the anterior wall, representing a huge gradient of activation between adjacent areas. The posterior wall, as opposed, was activated from septal to lateral by one broad wavefront.

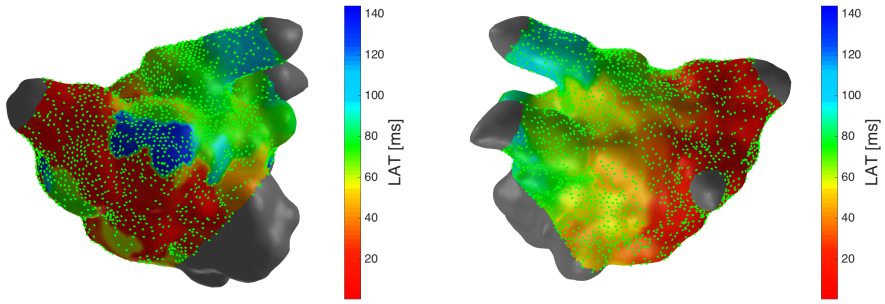

(a) LAT map in anterior view. **(b)** LAT map in posterior view.

Figure 18.5: Clinical LAT map. A figure 8 reentry could be observed on the anterior wall, while the posterior wall was only activated passively.

Remapping of the study data allowed to analyze 2898 EGMs in the LA. The result of area-based cycle length coverage analysis indicated several notable regions (see Figure 18.6). These comprised the anterior wall and left PV antra. Additional evaluation of the diastolic activity is presented in Figure 18.7. Analysis indicated that diastolic activity was present at the anterior wall, coinciding with the both the LAT gradient and the high cycle length coverage.

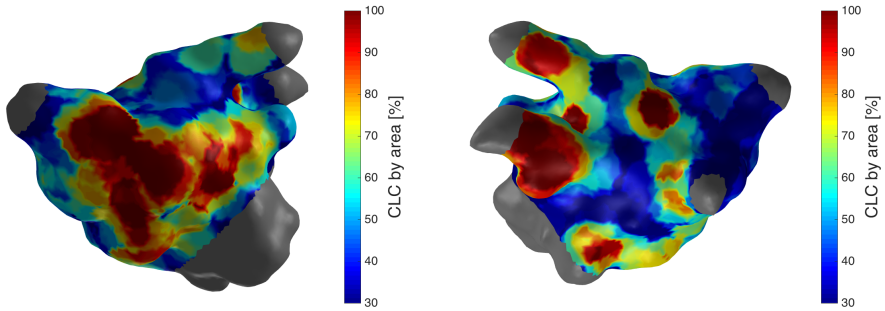

(a) CLC map in anterior view. **(b)** CLC in posterior view.

Figure 18.6: Cycle length coverage by area. Multiple regions are highlighted for closer inspection, including the anterior wall and reflecting the sensitivity of the approach.

Comparison between the clinically measured LAT map and the remapped data indicated good agreement. The reference time for the remapped LAT map was automatically set to match the exit point of the micro reentrant mechanism (compare Figure 18.8). Also the septal to lateral activation pattern of the posterior wall was present, which originated from the septal exit point of the figure 8 reentry.

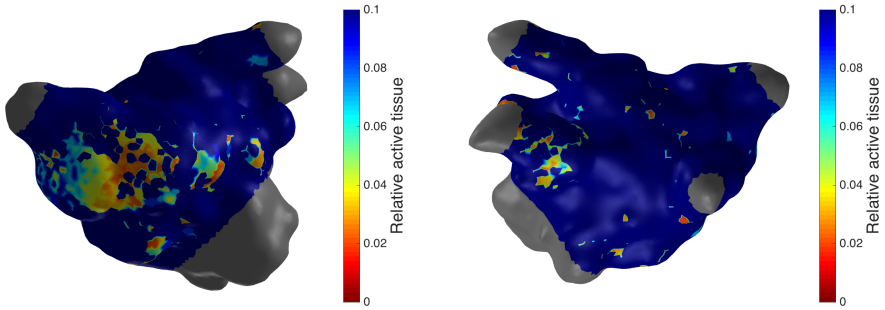

(a) Diastolic activity in anterior view. **(b)** Diastolic activity in posterior view.

Figure 18.7: Diastolic activity. Evaluation of the activity over time indicated a region on the anterior wall, which showed activity while the rest of the LA was already depolarized. This location coincided to the critical isthmus.

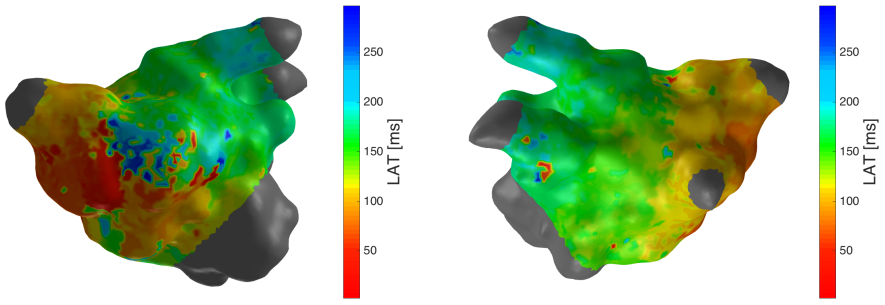

(a) LAT map in anterior view. **(b)** LAT map in posterior view.

Figure 18.8: LAT map generated based on remapping at IBT. The general excitation pattern matched with the clinical observation.

18.4 Macroreentrant Mechanisms

18.4.1 Counter-Clockwise Perimitral Flutter

Counter-clockwise perimitral flutter was observed in a 56 year old male patient after ablation for atrial fibrillation (AFib) (including PVI and substrate modification). Mapping was performed using a 20 pole spiral catheter connected to the EnSite Velocity EAMS. The resulting map contained a total of 280 right and 366 left atrial usable measurement points after CS evaluation. The LAT map which resulted from retrospective analysis was in good agreement with the clinical one and is shown in Figure 18.9.

Activation progressed from lateral to septal at the anterior wall and from septal to lateral at the posterior wall. This movement around the MV annulus was in line with a macro reentrant mechanism. Analysis of the area-based cycle length coverage did not indicate a region with more than 80% of coverage (compare Figure 18.10).

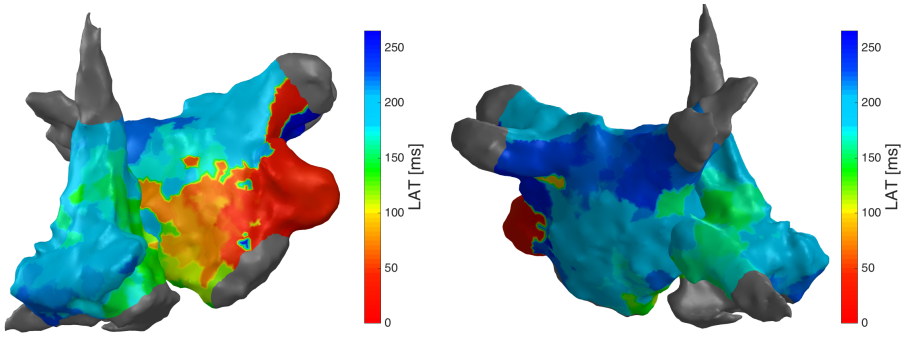

(a) LAT map in anterior view. **(b)** LAT map in posterior view.

Figure 18.9: LAT map as generated by the proposed analysis procedure. The resulting pattern was in good agreement with the clinical map.

A huge gradient in activation times and an increased cycle length coverage could be observed at the central anterior wall. Classification of signals indicated the presence of double potentials (DPs) in this region, confirming the presence of a conduction block (compare Figure 18.11).

The occurrence of DPs could also be verified by direct visual inspection in KaPAVIE. Two screenshots of the software during analysis of this dataset are shown in Figure 18.12. Panel A shows the clinical LAT map on the right with selected EGMs on the left. The progress of depolarization can be seen clearly in the gradient of activation times. A zoomed view on the region of conduction block is depicted in panel B, showing a reduced signal amplitude along the line of block. While signals which were acquired superior or inferior

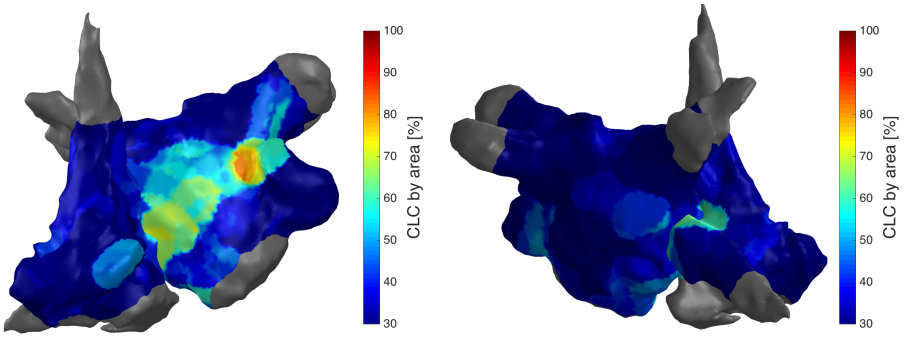

(a) CLC map in anterior view. **(b)** CLC in posterior view.

Figure 18.10: Cycle length coverage by area. No region was highlighted to represent a high CLC. Also during clinical mapping, no microreentry was observed. This was in agreement with the underlying perimitral macro reentrant mechanism.

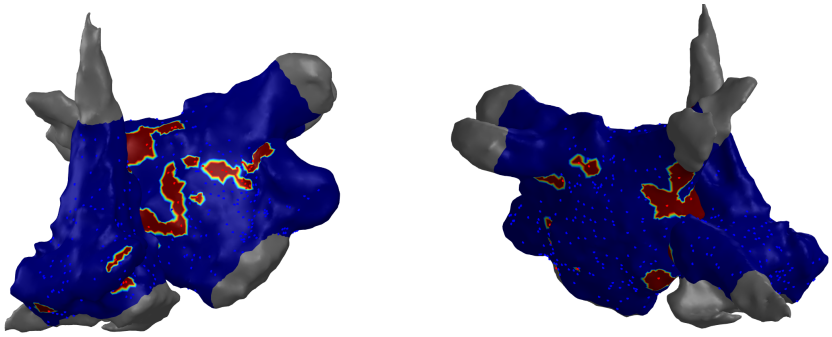

(a) Double potential map in anterior view. **(b)** Double potential map in posterior view.

Figure 18.11: DP map. The activation gradient on the anterior wall was found in agreement with the presence of DPs along this line of block.

to the block exhibited clear deflections in their respective part of the cycle, DPs could be observed directly on the line of block.

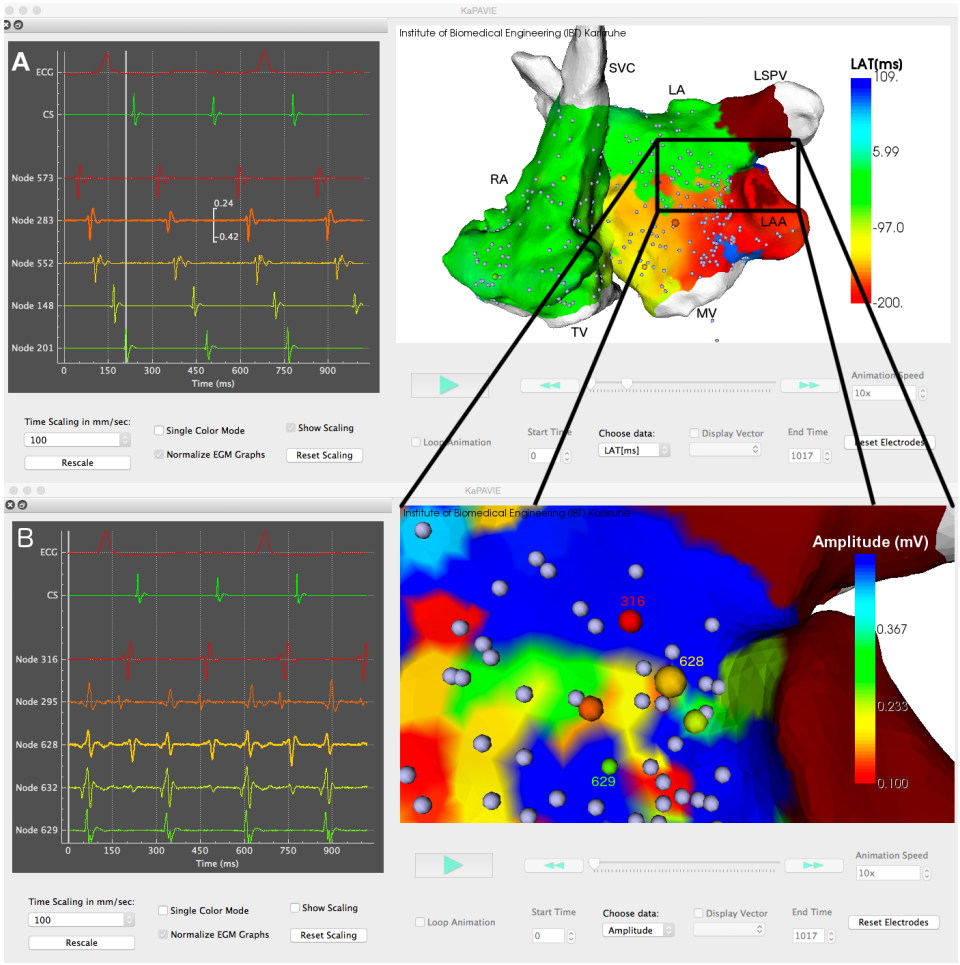

Figure 18.12: Screenshot of KaPAVIE. Panel A: Clinical LAT map indicating a block between the inferior and superior aspect of the anterior wall. Panel B: Signals recorded on the line of block indeed show reduced amplitudes and DP morphologies. Reprinted from [146] with permission of the publisher.

18.4.2 Roof Dependent Flutter Around LPVs

A roof dependent macroreentry was observed during mapping for atypical AFlut in a 70 year old female patient after previous ablation of AFib. During the EP study, several tachycardias occurred and transitioned between each other. All exhibited a slow conducting region at the central anterior wall (compare the virtualizaton described in Chapter 10.2). The corresponding LAT map as acquired by the Rhythmia EAMS is shown in Figure 18.13.

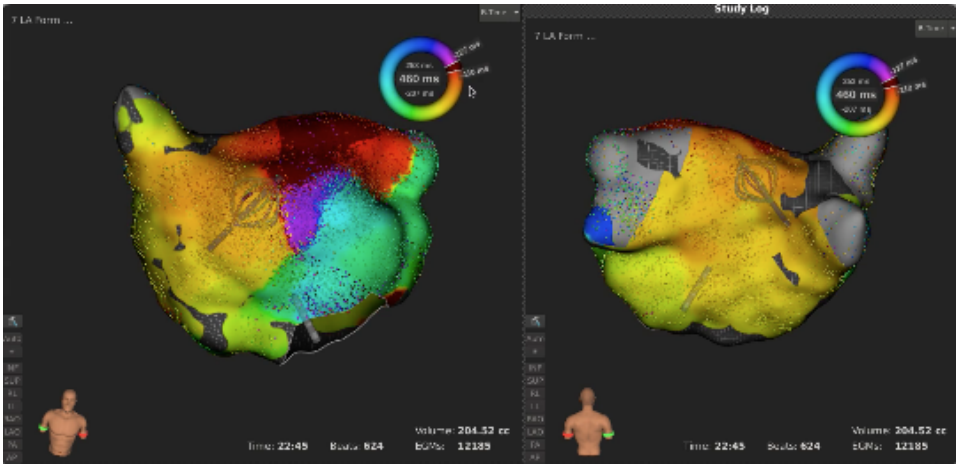

Figure 18.13: Clinical LAT map of roof dependent flutter. A zone of slow conduction was observed at the central anterior wall, showing huge gradients in activation towards surrounding regions.

After remapping, 539 EGMs were available for analysis. The resulting LAT map is visualized in Figure 18.14 and shows good agreement to the clinical map.

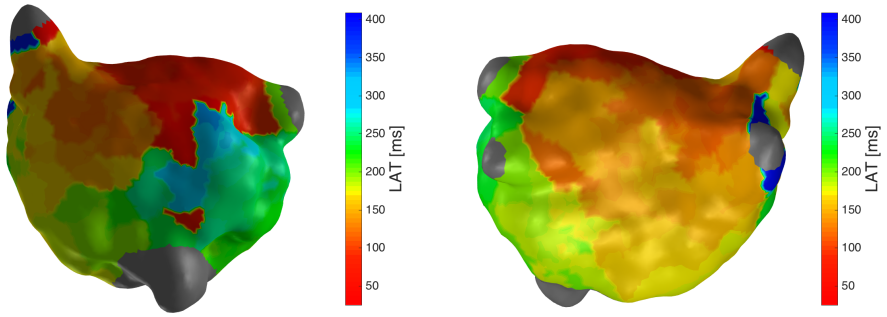

(a) LAT map in anterior view. **(b)** LAT map in posterior view.

Figure 18.14: LAT map generated after remapping at IBT. Activation of both anterior and posterior wall very well matched to the clinical mapping outcome.

The amount of active left atrial tissue over time is plotted in Figure 18.15 (a), above the reference CS traces of the analyzed atrial cycle. It can be seen that most myocardium

depolarizes slightly prior to the reference activation, which is consistent with the dominance of orange and green areas in the LAT map. Continuous electrogram traces including two cycles of the tachycardia are depicted in part (b). Two QRS complexes can be identified in the surface ECG at about 20 and 450 ms, respectively, compromising the ability to clearly annotated the respective P waves. For the CS activation at about 950 ms, a simultaneous P wave can be seen in the ECG. As both the maximum of active tissue and the P wave concur with the CS activation, this reinforces the idea, that the active tissue may be used as surrogate for the P wave in diagnosis.

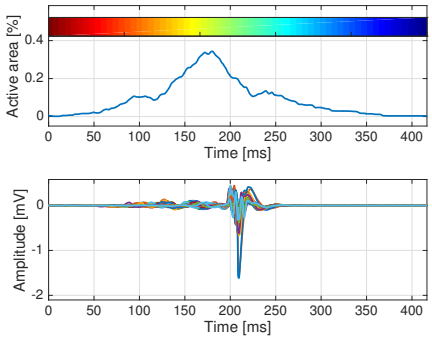

(a) Active myocardium related to the CS reference activation.

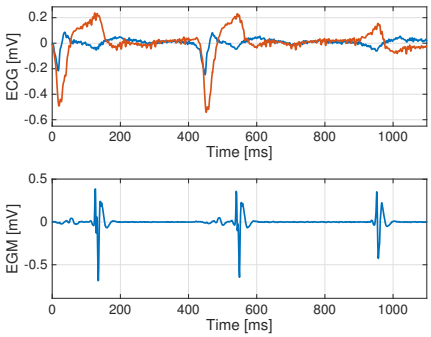

(b) Relationship between CS activation and P waves in the ECG.

Figure 18.15: Relationship between CS activation, active tissue and P wave. (a) The amount of active tissue over time (top) is plotted synchronously to the reference CS activation (bottom). The colorbar of the LAT map is included, indicating a good agreement between the coloring of the LAT map and the amount of active tissue. (b) About 1 s of surface ECG (top, two leads) and CS trace (bottom) are depicted to demonstrate the relationship of P waves in the ECG and CS activation.

The assessment of diastolic activity indicates the presence of an isthmus at the central anterior wall, which was in very good agreement to the clinical mapping (compare Figure 18.16).

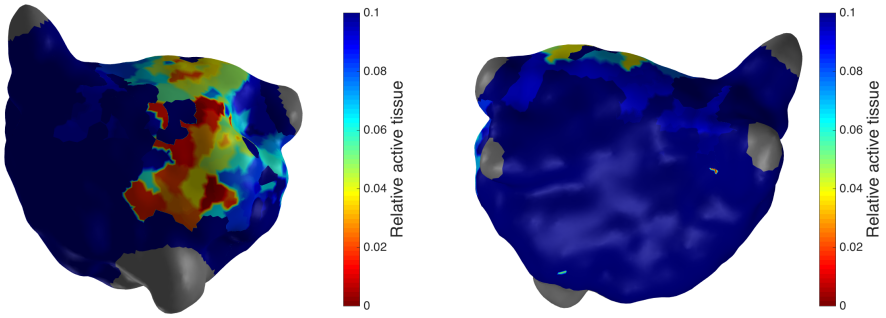

(a) Diastolic activity in anterior view. **(b)** Diastolic activity in posterior view.

Figure 18.16: Diastolic activity. A region in the central anterior wall was highlighted for closer inspection. It correctly reflected the critical isthmus as detected during clinical mapping.

18.5 Discussion and Conclusions

Concept and achievement Even in state-of-the-art mapping systems, conventional voltage and amplitude mapping are the only automatic signal processing tools available to support physicians during diagnosis of AFlut. During this research, several new diagnostic algorithms were invented, implemented and benchmarked. Primary goals were to ease comprehension of the tachycardia mechanism and highlight regions for detailed inspection for the physician.

The assessment of active surface regions was a central part of the algorithms. Activity within the EGMs hereby indicates the depolarization of tissue adjacent to the measuring electrode. Given a sufficient density of mapping points, this allows to evaluate the amount of depolarizing tissue within the flutter cycle. Three major implications were derived from this information.

First, the amount of depolarizing atrial tissue can be used as surrogate for the P wave. As the P wave results from a projection of the potential vector on the surface leads, its morphology is different in each lead. On the one hand, this can be used for diagnostic purposes prior to intracardiac mapping. In the presence of ablation scar, on the other hand, typical conclusions cannot be drawn from the presenting morphology. As intracardiac mapping data is available during the EP study, information about the depolarization may provide an alternative to the P wave.

Second, the progress of active tissue over time can help to identify the mid-diastolic isthmus. P waves are typically annotated to identify mid-diastolic potentials. As P waves indicate the depolarization of major parts of the atrial tissue, activity between P waves is typically confined to the critical isthmus. Within this thesis, a functional relationship was introduced which automatically highlights these areas without the need of LAT annotation.

It additionally allowed to set the reference time for LAT annotation on the exit point of the isthmus. Both these concepts were successfully demonstrated in the clinical examples.

Third, evaluation of cycle length coverage in small regions allowed to assess the presence of a micro reentrant source. Only if continuous activity could be found in a small area, this was considered a potential target for remapping and ablation. Analysis of clinical data also reflected the potential of this method.

Developed algorithms also allowed to automatically determine the BCL and assess the stability of CS activation. Manual interaction was only required to confirm the proposed reference BCL. Although it would have been possible to modify this value, the need to do so was never observed.

Dynamic visualization of the AFlut cycle was also successfully achieved for each subject. This way of displaying the spatio-temporal relationships of cardiac depolarization was the second major novel concept included in the signal analysis.

Limitations Although the successful application of the processing was demonstrated, it has to be noted that the number of patients was still limited. The analysis should be applied to data from additional subjects to gain more experience and identify the need for improvement.

As different clinical systems vary in signal quality, a manual setting of the noise level was required. While signals with peak to peak amplitudes of less than 0.1 mV were considered as scar when data from the Velocity system was analyzed, this could be reduced to 0.04 mV for Rhythmia electrograms. Furthermore, parameters such as the diameter for area-based cycle length coverage had to be adjusted in the range of 14 to 30 mm for different datasets. It seems reasonable to include an option to parameterize these measures within the clinical analysis.

The functional relation which highlights diastolic activity currently does not consider causality. Consequently, it does not clearly differentiate between true diastolic activity and regions which are activated last. Analysis of the propagation pattern may provide the possibility to identify the dominant path, which sustains the tachycardia. Along this path, in turn, the isthmus could be subsequently determined as recently presented [202]. Combined with automatic delineation of scars, this would be a major step towards fully automatic analysis of flutter data. Nevertheless, the presented techniques are expected to already represent a major step towards this goal.

Outlook Supporting the treatment of AFlut by automatic analysis of intracardiac mapping data was a major goal of the presented research. A corresponding analysis workflow was successfully implemented and led to promising results. Several novel algorithms were included and demonstrated to correctly identify interesting phenomena like micro reentrant sources or DPs. This is expected to reduce the stress during mapping and the risk of overlooking important aspects, as automatic signal analysis will help to identify extraordinary signal patterns without the need of continuous visual assessment of all EGM traces.

New presentation techniques, such as a combined plot of LAT and DPs, may help to ease comprehension of the presenting tachycardia. Additionally, the dynamic visualization is expected to help comprising the spatio-temporal depolarization pattern.

To evaluate its clinical value, however, processing the recorded data according to this workflow immediately after the procedure is an important next step. The direct retrospective analysis will allow to assess both the usability in the clinical environment and the ability of the workflow to correctly identify the tachycardia mechanism. These are critical milestones towards a blinded study.

CHAPTER 19

Analysis of CFAE maps

Following very promising success rates in catheter ablation of atrial fibrillation (AFib), targeting complex fractionated atrial electrograms (CFAE) became an important corner-stone of substrate based ablation strategies [56]. Reproducing these outcomes in other centers, however, has proven difficult [6, 7]. One limitation of corresponding treatment approaches is the lack of objective definition and therefore identification of complex fractionated atrial electrograms (CFAE).

Although state-of-the-art electroanatomical mapping systems (EAMSs) provide algorithms to automatically detect CFAEs, these possess two major limitations. First, their behavior can be adjusted by user specific parameters. As different clinical centers use different parameter settings, the results can hardly be compared [91]. Second, and although these algorithms are inspired by the original definition of CFAE, the resulting annotation does not always reflect the assessment as potential ablation target given by an experienced physician.

In an attempt to put the identification of CFAE on a quantitative footing, a classification algorithm was developed and published in previous work [208]. It was based on a fuzzy-decision-tree that assigned one of four distinct labels to each EGM. The classes ranged from C0 (regular) to C4 (continuously fractionated). Up to 18 features were considered to describe the EGMs and their complex morphology (for details see Chapter 12.1 or [208]). The database used for training and cross-validation of the classifier was congruently annotated by physicians from two international clinical institutions. Therefore, it was considered to represent the variety of clinically relevant CFAE morphologies.

Following scientific objectives will be addressed with this novel diagnostic algorithm:

- Compare the assigned CFAE classes with the commonly used CFE index
- Evaluate the regional distribution of CFAE classes within the LA
- Assess the impact of pulmonary vein isolation (PVI) on these measures

19.1 Study Design

Clinical data Data from a small cohort of 5 subjects (54.6±14.4 years, all male and treated for persistent AFib) was analyze within the scope of an initial study. All data were acquired during routine catheter ablation of AFib using the EnSite Velocity EAMS at Städtisches Klinikum Karlsruhe. CFE mapping was performed before PVI (bPVI) and after PVI (aPVI) using either a 10 or 20 pole spiral catheter. The number of available patients was limited as the complete left atrial mapping of bPVI and aPVI was required for inclusion in the study.

Annotation of LA anatomies The endocardial surface was extracted after import of clinical geometries as outlined in Chapter 6.1. In order to evaluated the anatomical relationships of CFAE, each atrium was annotated manually under supervision of an experienced cardiologist. Therefore a MATLAB GUI was implemented in which the following regions were annotated due to their clinical relevance:

- left pulmonary veins (PVs) (*LPV*)
- right PVs (*RPV*)
- left atrial appendage (LAA) (*LAA*)
- anterior wall (*ant*)
- posterior wall (*post*)
- roof (*roof*)
- septum (*sept*)

Preprocessing of EGMs All clinical data were imported first. During this process, all mapping points were removed that were either already rejected from analysis by the physician or not acquired using the spiral catheter. All EGMs were recorded at 2034.5 Hz with a duration of 5 s. To ensure consistency with the previously published approach, they were down sampled to 1200 Hz and filtered using a wavelet-based method [208]. Thus data from a total of 412±192 and 376±177 acquired points bPVI and aPVI were available for analysis, respectively.

Parameters computed First the *amplitude* was of interest, being a very common parameter. As several depolarizations were expected to be in the recorded signal, the difference between the total maximum and the total minimum of the signal may not reliably provide information about the underlying substrate. Thus the parameter amplitude was computed as maximum peak to peak amplitude of any single deflection within the signal in the scope of this study. This is similar to considering a sliding window of interest around each passing depolarization wavefront.

Instead of recomputing the *CFE index* using the exported EGM, the value determined by EnSite Velocity was directly assessed within the study. Standard settings for the CFE

algorithms were applied as common in the clinical practice: P-P sensitivity 0.04 mV, detection mode -dV/dt, refractory length 40 ms, and segment length 5 s.

Besides this clinical descriptor, also the *class* of CFAE morphology was of interest. Therefore 18 features were computed for all electrograms and subsequently they were classified by the fuzzy-decision-tree developed in previous work (compare Chapter 12.1 and [208]).

Assessment of regional distribution For further analysis of regional distribution, EGMs were excluded if their measurement locations were inside the pulmonary veins or the MV. They were also rejected if the distance between the atrial shell and the recording position exceeded 5 mm. To avoid that artifacts would compromise the statistics, EGMs were not considered if their amplitude exceeded a physiologically reasonable value of 20 mV. After this step, 341±141 and 320±159 acquired points bPVI and aPVI were available for regional assessment, respectively.

For each of the remaining measurement points, a coverage map was generated using 3 mm and 5 mm as thresholds d_i and d_m for the radius, respectively (see Chapter 6.3 for details about the assessment of coverage). The resulting coverage map is depicted in Figure 19.1 (a) for one demonstrative patient. An interpolation scheme according to the *Nearest Neighbor* was subsequently set up and used to interpolate the *amplitude* and the *CFE index* of all electrodes onto the anatomical shell. The distribution of the *CFE index* on the atrium is visualized in Figure 19.1 (b).

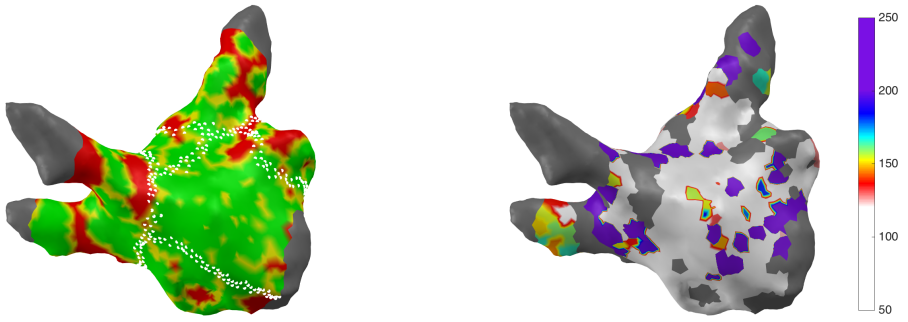

(a) Coverage. **(b)** CFE index.

Figure 19.1: Coverage and *CFE index* for one example patient bPVI. The atrial coverage was determined based on the position of all acquired measurement positions, leading to 96.6% in this example. Uncovered regions are colored red. White dots indicate the boundaries of atrial regions (a). The *CFE index* was directly provided by the mapping system and interpolated on the atrial shell. Its value was given in [ms] (b).

The regional distribution of *amplitude* values was assessed by computing the mean value for each anatomical region after interpolation on the surface. Complying with this approach, also the mean *CFE index* for each region was determined.

Three value ranges were defined for analysis of *CFE index* values, being R1 (CFE>200 ms), R2 (CFE 120-200 ms) and R3 (CFE<120 ms). These boundaries were specified in close collaboration with a physician, as regions with CFE index smaller than 120 ms are typically selected as ablation targets during substrate modification, while regions exhibiting values higher than 200 ms are considered healthy, making those in between secondary ablation targets. The color map in Figure 19.1 was chosen accordingly. The broad distribution of CFE values <120 ms emphasizes the need for algorithms which can specify potential ablation targets more precisely. The categorical values R1, R2 and R3 were interpolated on the surface mesh. Similarly, the CFAE *class* was interpolated on the anatomy.

For regional statistical assessment, the total surface area of each atrial region was computed, together with the amount of surface area covered by each CFAE *class* and *CFE index* range. This analysis was restricted only on the covered regions. As the increasing amount of scar compromises the analysis of CFAE areas, low voltage regions (<0.2 mV) were considered scar and treated as separate class during statistical analysis. The distribution of CFAE classes and scar tissue is plotted for one example patient in Figure 19.2 bPVI and aPVI, respectively.

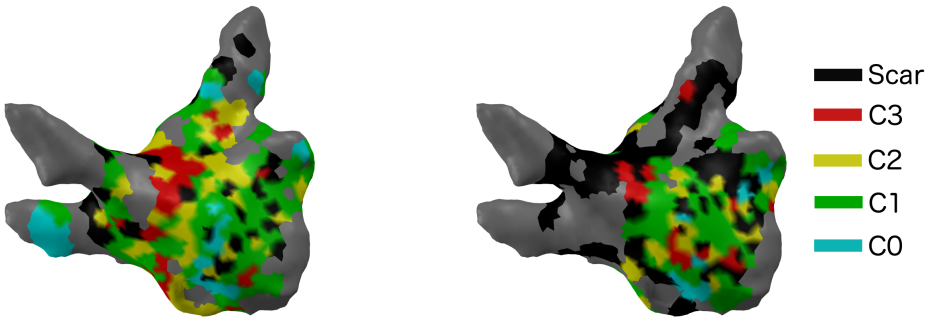

(a) CFAE classes (bPVI). **(b)** CAFE classes (aPVI).

Figure 19.2: CFAE classes before (a) and after PVI (b). An increase of low-voltage areas could be observed aPVI. See Figure 19.6 for definition of colors.

As final part of region specific assessment, analysis was focused on areas which exhibited the most fractionated activity class (C3) before PVI and were covered both bPVI and aPVI. For these, the *class* after successful PVI was evaluated.

To conclusively compare both algorithms for CFAE analysis, the occurrence of different CFAE *classes* was observed within the *CFE index* regions bPVI and aPVI. This analysis was only performed in regions which did not exhibit low voltage.

19.2 Results of Analysis

Coverage of atrial surface First the coverage of the atrial surface by the acquired measurements was assessed. Mean coverage values for the 5 subjects are visualized in Figure 19.3 and indicate a comparable coverage both bPVI and aPVI. Complete coverage of the endocard, however, was not achieved. This may be explained by the fact that all points had to be acquired manually and the resulting measurement density was judged during the procedure as being sufficient. Considering their values bPVI vs. aPVI, *ant* areas were covered to 75% vs. 73%, and *post* to 64% vs. 61%.

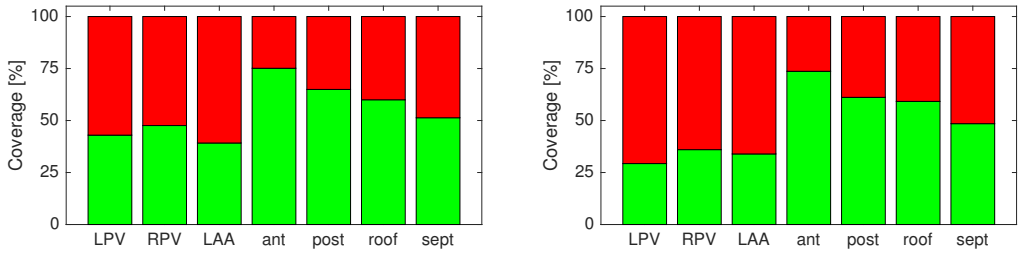

(a) Coverage (bPVI). **(b)** Coverage (aPVI).

Figure 19.3: Coverage of the atrial surface for the included datasets. Region specific values were determined bPVI (a) and aPVI (b).

Amplitude distribution For each patient, the mean *amplitude* per atrial region was computed. The statistics over all patients are visualized as boxplots in Figure 19.4. Three aspects are of interest in these values.

First, analysis of signal amplitudes indicated median values for the *LAA* of 3.7 and 3.6 mV bPVI and aPVI, respectively. These values were much higher than in all other atrial regions and were in agreement with clinical observations that EGM recordings at the LAA typically exhibit large amplitudes. It was also not affected by PVI. Second, the median amplitudes in the LPV and RPV regions were reduced by PVI from 1.1 and 0.9 mV to 0.3 and 0.3 mV, respectively. This was in agreement with presence of ablation scar in these regions. Last, the amplitudes in the remaining atrial regions (ant, post, roof and sept) were hardly affected by PVI, indicating that the ablation at the PV ostia did not modify the vitality of the surrounding tissue.

Distribution of fractionation For first assessment of fractionation, the mean *CFE index* was computed analog to the *amplitude* values and visualized in Figures 19.5. Most importantly, the *CFE index* in LPV and RPV regions was strongly prolonged by PVI. This reflects that the determined *CFE index* in scar regions results in a high value. However, it does not indicate a more regular excitation pattern but increased scarring without conduction. Off

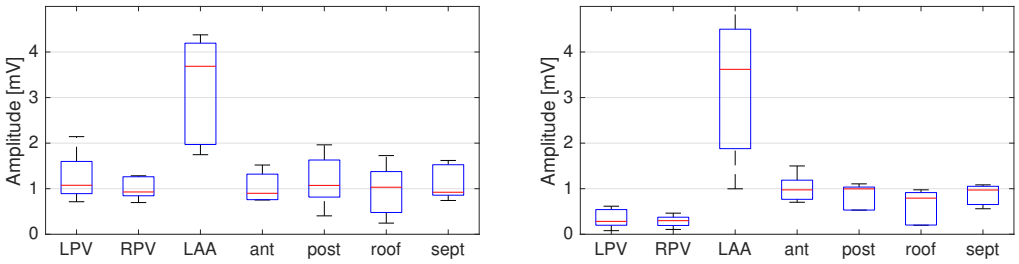

(a) Region specific amplitudes (bPVI). **(b)** Region specific amplitudes (aPVI).

Figure 19.4: Amplitude of EGMs. Amplitude were determined bPVI (a) and aPVI (b).

note, the median *CFE index* did not show strong deviation between regions bPVI on this level of aggregation.

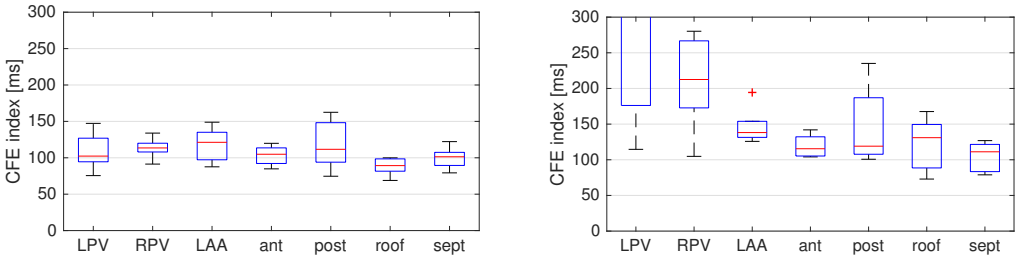

(a) Mean CFE index per region (bPVI). **(b)** Mean CFE index per region (aPVI).

Figure 19.5: Impact of PVI on *CFE index* distribution. The *CFE index* was determined bPVI (a) and aPVI (b).

Next, the *CFE index* was discretized in the regions R1 to R3, as outlined in the previous paragraph. The relative amount of *CFE index* regions was determined for each atrial region and averaged over all subjects. For this analysis, low voltage values were considered as scar. The increase of scar by PVI can easily be seen by comparison of the plots bPVI and aPVI in Figure 19.6. Of note, the amount of scar did increase in the remap after PVI, confirming a representative mapping.

In addition to the CFE index region plots (a) and (b), also the determined CFAE classes are depicted in parts (c) and (d). While only 2.1% and 7.8% of LAA surface showed the hardly fractionated value range R1 bPVI and aPVI, respectively, 90.3% and 94.6% were found to have rather regular morphologies of either class C0 or C1. This indicates that both algorithms differentiate the varying aspects of CFAE complexity.

CFAEs of *class* C3 exhibit continuous fractionated activity and are therefore typically assessed as potential ablation targets. Thus, it was of interest whether or not the regions found as C3 during mapping bPVI did remain class C3 signals after PVI. This also indicates if the excitation properties in regions distant to the PVI scarring were affected by ablation.

Therefore, regions were specifically analyzed which showed class C3 bPVI and were also covered during mapping aPVI. Corresponding EGMs were assessed by atrial region

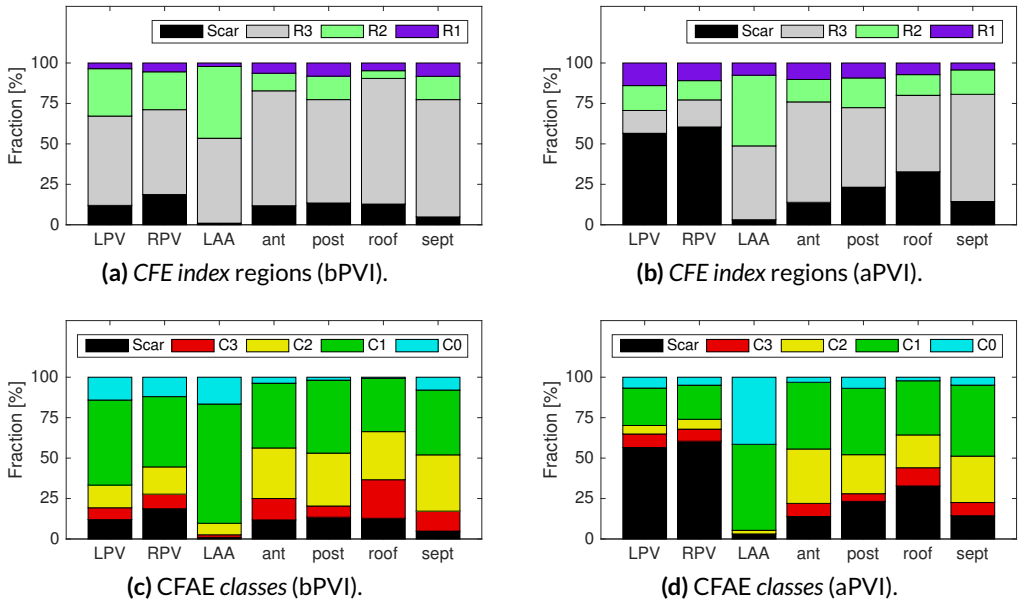

(a) *CFE index* regions (bPVI). **(b)** *CFE index* regions (aPVI).

(c) CFAE *classes* (bPVI). **(d)** CFAE *classes* (aPVI).

Figure 19.6: Anatomical distribution of fractionation. Fractionation was measured using the *CFE index* bPVI (a) and aPVI (b). The result of classification using the FDT was also evaluated bPVI (c) and aPVI (d).

and shown in Figure 19.7. Most C3 in LPV and RPV regions were transformed to scar. For the LAA, C3 region bPVI only was 1.0% and completely converted to C0 and C1. For the remaining regions, an increase in scar could be observed which was strongest in the roof and probably due to ablation in these regions. No dominant class was observed after PVI for C3 substrate.

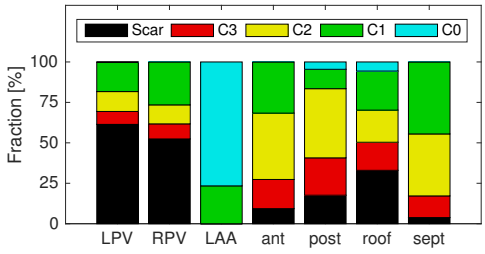

Figure 19.7: Signal classes aPVI assigned to signals which were annotated as C3 CFAE prior to PVI.

Differences between algorithms The comparative view of CFAE *class* and *CFE index* regions already indicated that both did not result in unanimous vote. As the *CFE index* is a widely spread criterion for the identification of ablation targets in CFAE mapping, it was assessed to what degree this measure reflected the morphology based classification of CFAE.

For bPVI and aPVI, the occurrence of CFAE *classes* within each *CFE index* region was assessed in each single patient and subsequently averaged in the statistics. The result

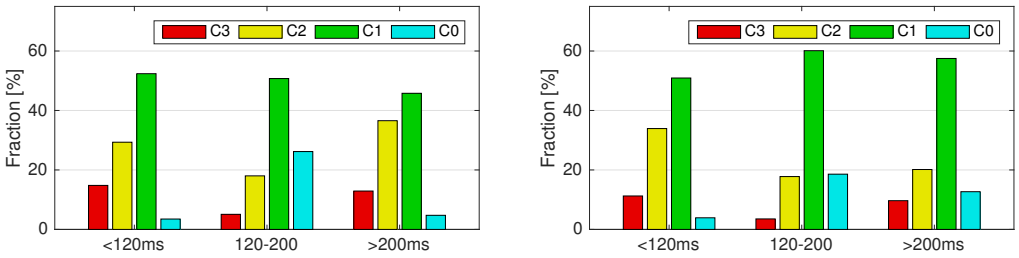

(a) Distribution of CFAE *classes* (bPVI). **(b)** Distribution of CFAE *classes* (aPVI).

Figure 19.8: Variability between *CFE index* and CFAE *classes*. The occurrence of different CFAE *classes* within each *CFE index* region was determined bPVI (a) and aPVI (b).

is visualized in Figure 19.8. Results indicated that signals with continuously fractionated morphology were also observed in regions with *CFE index* exceeding 200 ms.

19.3 Discussion and Conclusions

An automatic and reliable annotation of CFAE is important to identify specific targets for substrate ablation and preserve vital tissue. Within this small clinical study, the analysis result of two algorithms for the detection of CFAE was compared. The *CFE index* was addressed as widely used measure for fractionation, which is implemented in the EnSite EAMSs. The clinical annotation of this algorithm was contrasted with a morphology-based classification, which was based on a fuzzy decision tree and developed during previous work. The annotations provided by both algorithms were compared by considering the different atrial regions.

Both algorithms did not provide concordant annotations. This can most clearly be seen in Figure 19.8, which shows that signals of all fractionation *classes* were present in each *CFE index* region. Most notably, EGMS labeled with the continuously fractionated *class* C3 were also present in the *CFE index* region R1 with values >200ms. As the effect of ablation was not related to the annotation of the algorithms, however, it could be stated that these algorithms detect different aspects of the signals. The usefulness of corresponding ablation approaches cannot be judged. This is considered the most important aspect of future research. Its implementation and the corresponding study design, however, is not trivial, as ablation continuously modifies the substrate and thus monitoring of the arrhythmia and the ablation success is hardly possible.

Little fractionation and high amplitudes were observed in the LAA. This was in agreement with clinical observations, that this part of the myocardium is hardly considered an ablation target.

As the parameter settings for *CFE index* computation within the EAMS can be adjusted, this is an additional degree of freedom for evaluation. This issue has not been adressed within the study, as the parameter settings for one clinical center are typically fixed and based

on best practice. The resulting outcome, however, may or may not reflect the assessment as done by the physician.

CHAPTER 20

High-Density Mapping during Atrial Fibrillation

Mapping of atrial fibrillation is one of the biggest challenges in electro-physiological (EP) studies. Due to the unstable depolarization process, simultaneous mapping is required to comprehend the excitation pattern. But consequently the available data is limited by the field of view of the utilized catheter. Although panoramic baskets provide the option to record atrial activity from widely spread areas, this comes at the cost of significant sparsity of measurement points (compare Chapters 15.2 and 17).

An alternative option for signal acquisition is provided by small catheters for local high-density mapping, like different circular mapping catheters, PentaRay™ or Orion™. Although their field of view is limited to an area of about 20 to 30 mm diameter, it is covered by 20 to 64 electrodes, offering the possibility to more precisely comprehend the local excitation process.

High-density epicardial mapping of depolarization during AFib has brought evidence for so-called transient linking [241], being the tendency of excitation to exhibit distinct modes of propagation. Trains of waves propagating in similar direction were observed in 51% of cases of distinct depolarization events during ongoing AFib. In addition, predominant types of transition between the propagation patterns were observed.

Comparable analysis in clinical data may offer the possibility to gain information about both the excitation dynamics and the underlying substrate. Within the scope of the presented research, methods have been developed to identify depolarization events and cluster them based on the activation pattern or the morphology of local activation waves (LAWs) (see Chapter 13). In the following, this technique will be demonstrated using data recorded with the Orion catheter during AFib.

Clinical data and preprocessing A 62 year old female underwent catheter ablation for paroxysmal atrial fibrillation at Städtisches Klinikum Karlsruhe after multiple previous procedures for PVI. Continuous mapping data were recorded during routine data acquisition during ongoing AFib, exported from the Rhythmia™ system and processed retrospectively.

Stable catheter positions were identified within the mapping data based on information of the log file and subsequent visual inspection.

Two datasets were chosen for analysis. The first dataset was recorded at the antero-septal wall and 41.5 s long. The second segment of EGM data was recorded at the roof for a duration of about 66.5 s. Electrogram and position information was available for all 64 electrodes of the Orion catheter. Bipolar leads were computed along all splines, leading to 56 bipolar electrograms (BEGMs). Signals were filtered from 30 to 300 Hz. In addition, artificial specific frequencies were removed (compare Chapter 5.1).

The atrial geometry was preprocessed as outlined in Chapter 6.1. Electrodes were rejected from analysis if they were located further away from the surface mesh than 5 mm. Thus 13 and 38 electrodes were available for processing in datasets 1 and 2, respectively. Subsequently, coverage maps were computed (see Chapter 6.3). Both catheter position and coverage maps of both datasets are visualized in Figure 20.1.

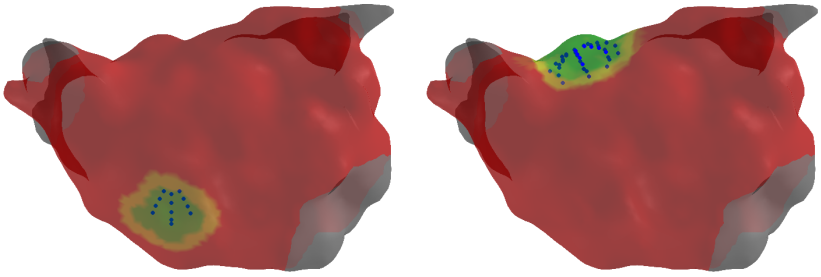

(a) Antero-septal position in dataset 1. **(b)** Roof location in dataset 2.

Figure 20.1: Catheter positions and coverage for both exemplary datasets. The LA is shown in antero-posterior view. The Orion catheter was positioned at the antero-septal wall in dataset 1 (a), with 13 electrodes on three splines having contact to the endocard. In dataset 2, the catheter was placed in frontal position at the roof, bringing 38 electrodes close to the atrial shell.

20.1 Classification of Morphology in Individual Leads

For the analysis of LAW morphology, first the LATs were annotated in each individual channel. Therefore local maxima of the instantaneous energy were detected using a refractory period of 150 ms. For each potential LAT, peak-to-peak amplitude of the bipolar EGM was evaluated within a window of ± 10 ms. LATs were only accepted if this value exceeded 0.05 mV. For each channel of dataset 1, 170 to 181 LATs were annotated. In dataset 2, 0 to 310 LATs were found, as some channels only contained noise.

For each LAT, the morphology of the corresponding LAW was extracted and clustered by a correlation-based approach (see Chapter 13.2.2). Thresholds thr_{intra} and thr_{stop} were set to 0.6 for automatic annotation. The resulting classification for three channels of dataset 1 is shown in Figure 20.2. Two types of morphologies could be recognized in channel 6, and automatic annotation matched to this visual inspection. Also for lead 5, LAWs after 1.8 s showed similar morphologies. A more complex pattern of LAW morphologies could be observed in channel 1.

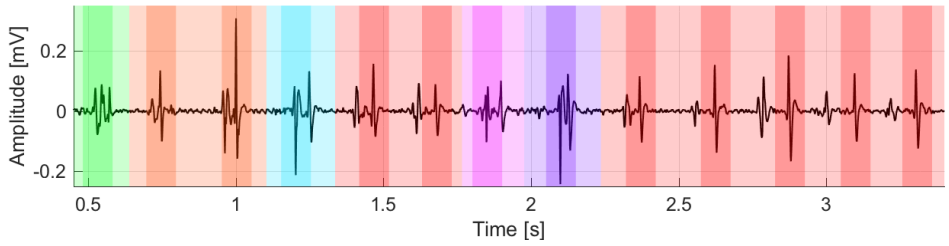

(a) Channel 1.

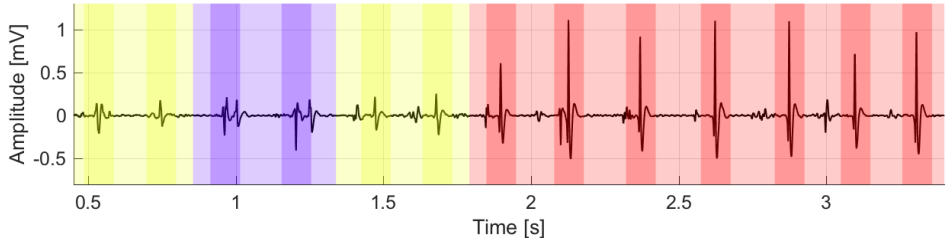

(b) Channel 5.

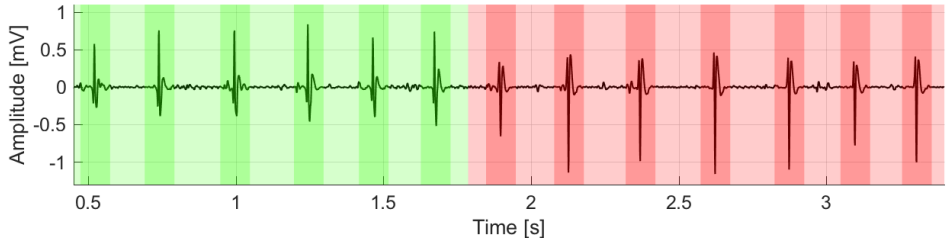

(c) Channel 6.

Figure 20.2: AFib EGMs with morphology-based annotation. Two major types of morphologies were identified in channel 6 (c). Channels 5 (b) and 1 (a) exhibited LAWs with increasing complexity. Consequently, more classes were used for labeling.

20.2 Multichannel Evaluation

After assignment of LAW classes in all individual channels, multichannel evaluation was performed. Wavefronts were generated as outlined in Chapter 13.3.1. A minimum length of 3 LATs was required for each wavefront, with a maximum search range of 90 ms. Subse-

quently, a number of 40 clusters was manually defined to detect similar activation patterns over all channels as outlined in Chapter 13.3.3.

For dataset 1, 183 wavefronts were generated. The EGMs of all 13 channels are plotted in Figure 20.3 (a), together with the detected wavefronts. While distinct activations could be observed in channels 5 to 7, fractionated activity was present in channels 1 to 4. Of note, this contrast reflected the change between two measuring splines. Particularly in the presence of double potentials as in lead 1, annotation of the LAT was found to alter between the first and the second component. The result of multichannel annotation of the excitation waves is shown in Figure 20.3 (b). Statistical analysis showed that 16 of the 40 clusters were singular. Therefore all classes which were found less than 6 times during annotation were rejected in further visualization and grayed out. The resulting labeling is depicted in part (c), indicating that the patterns including waves 3 and 8 were rarely observed.

For dataset 2, the wavefront matrix contained 351 entries. 12 channels were subsequently rejected as they did not contain LAT information for more than 20% of detected wavefronts. The EGMs of all initial 38 leads are plotted in Figure 20.4, together with the annotated wavefronts. After multichannel annotation of 40 different clusters, 8 classes were found to be singular. The 6 most often assigned classes were labeled during visualization, accounting for 55.8% of annotations, although they only accounted for 15% of annotated classes. The resulting annotation is depicted in Figure 20.4 (b), in which the 34 rare classes were grayed out and EGMs omitted.

20.3 Discussion and Conclusions

The high-density mapping catheter Orion has proven to be a valuable tool during sequential mapping of stable tachycardias. Mapping of several thousand points was achieved in combination with automatic data acquisition, providing the opportunity to precisely comprehend the underlying rhythm disorder [86, 253].

Its utility for mapping of an unorganized tachycardia like AFib, however, remains unclear. Research presented within this thesis has assessed the field of view of the Orion catheter as outlined in Chapter 15.1. In typical mapping situations, wall contact was achieved with 2 to 4 splines and approximately 20 electrodes, leading to a covered area of about 1 to 2 cm^2. Simultaneous mapping data from this field could be assessed to evaluate the local depolarization pattern during AFib.

Following the observation of transient linking between wave trains [241], directed coherent coupling [237] and recurrence of certain LAW morphologies [166, 243], statistical analysis of the dominant pattern was addressed within the scope of this research. Different clustering-based methods were presented in Chapter 13 and applied to Orion mapping data of AFib.

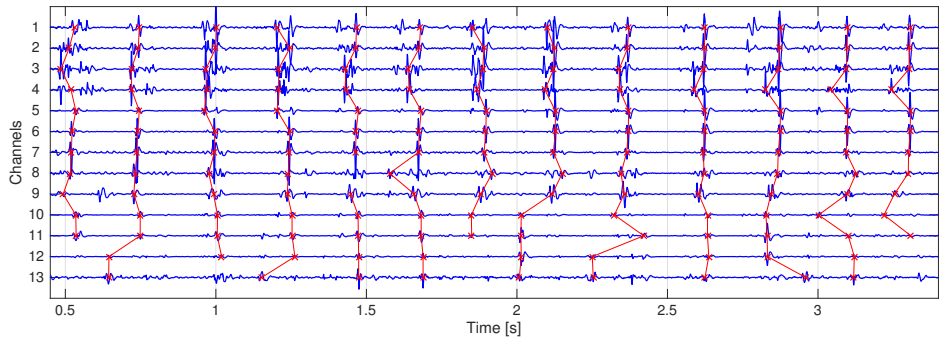

(a) Wavefronts.

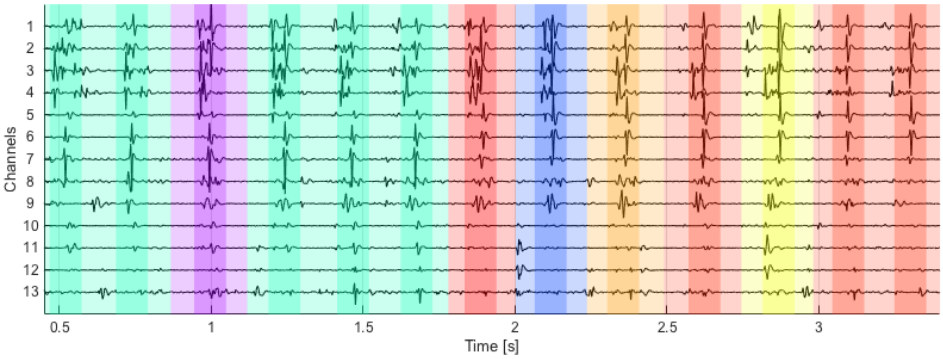

(b) Morphology based classification (all classes).

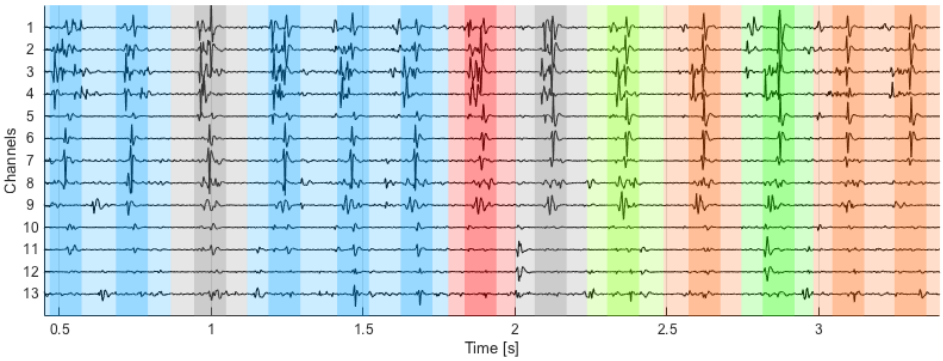

(c) Morphology based classification (classes occurring more than 5 times).

Figure 20.3: Morphology based multichannel classification. LATs (red crosses) and the generated wavefronts (red lines) are annotated in the multichannel EGM (a). Resulting annotations after multichannel labeling are shown for all classes (b) and when discarding singular clusters (gray, c).

Results indicate, that these methods are capable of identifying and separating dominant morphologies of LAWs in single channel EGMs. This option allows to quantitatively assess the stability of propagation. In addition, the number and sequence of dominant LAWs could be evaluated to identify dynamic alterations of the depolarization pattern.

Combined analysis of multiple simultaneous channels allows to additionally determine the propagation pattern within the field of view. This approach was applied to data from two mapping positions, and indicated that dominant types of excitation patterns were responsible

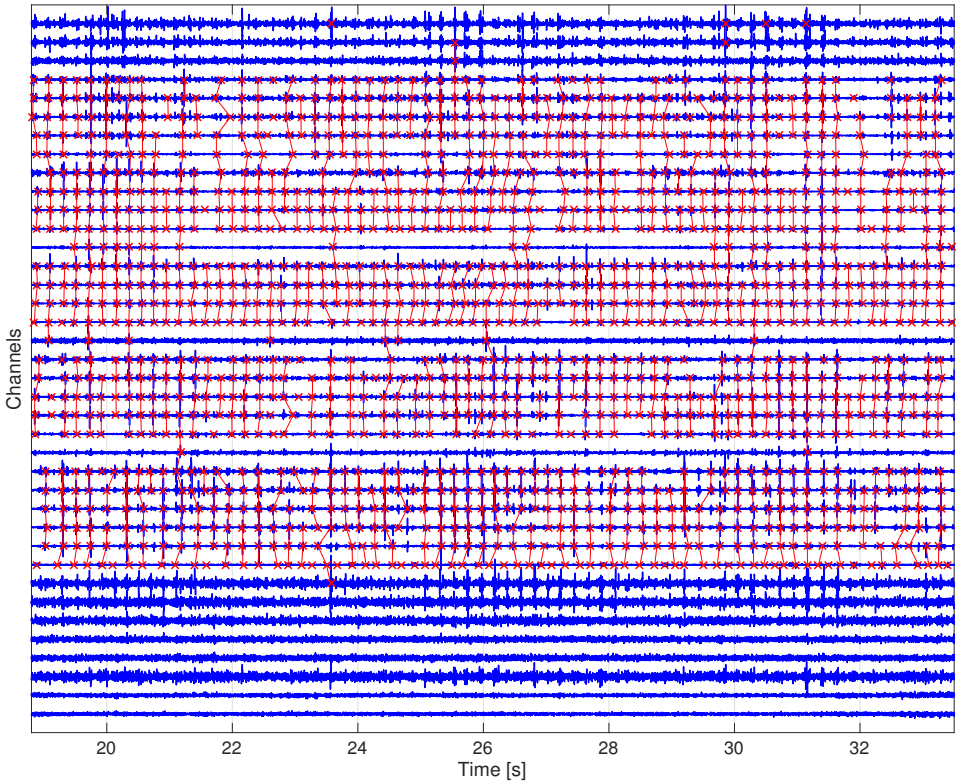

(a) Wavefronts.

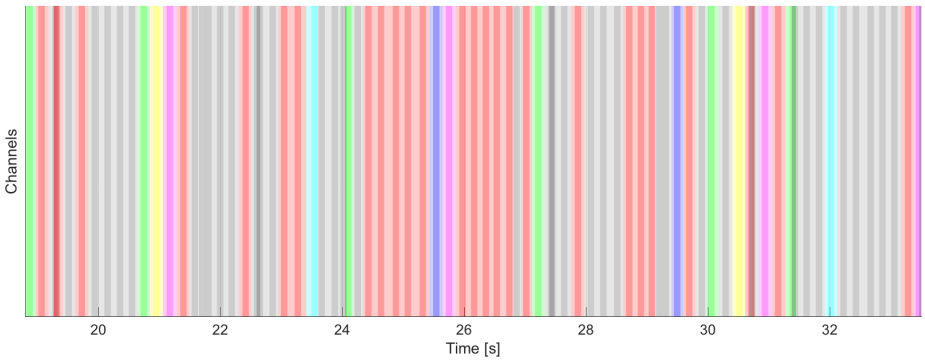

(b) Morphology based classification (all classes).

Figure 20.4: Repetitions in annotation of multichannel data. The dominant 6 classes accounted for >55% of wavefronts, although they represented only 15% of classes used for annotation. Both minority and majority classes formed trains of successive activations.

for the majority of distinct depolarization events. This is fostering the hypothesis that a certain degree of dynamic organization can be observed during ongoing AFib.

The analysis of dominant patterns in simultaneous endocardial high-density mapping data is a promising but challenging field of research. The evaluation presented in this chapter was based only on the morphology of LAWs but did not incorporate the LAT-based activation sequence. The latter was already demonstrated in Chapter 16 and could very well be applied

also in this context. Annotation of LAT may be compromised in the presence of fractionated activity, however.

Several distance criteria were proposed for clustering. Besides the correlation coefficient used in this chapter, also the similarity-index or principal component analysis (PCA)-based clustering could be applied to classify LAW morphologies (compare Chapter 13.2.2). Subsequent multichannel analysis is even more complex as only categorical variables are available when single EGM leads were annotated previously. A direct multichannel approach with suitable basis function could be considered at this point. The optimal way for single and multichannel data clustering is one central point for future research.

Within the presented methods, information about local excitation dynamics and the underlying substrate are jointly analyzed. It would be of great interest to separate these two aspects, allowing to identify the critical substrate maintaining the tachycardia. This should be another core aspect of future work. After statistical evaluation, the projection on the atrial anatomy will be a valuable step for final visual inspection.

CHAPTER 21

Conclusion

Four major goals were pursued within the presented research, aiming for novel ways to assist physicians in correctly interpreting intracardiac multichannel mapping data. First, algorithms for the diagnosis of atrial flutter were developed. Although this is a very well understood tachycardia, the design of a patient specific treatment approach is often quite challenging. At this point, automatic signal processing could aid the physician during the intervention. Second, techniques for the statistical analysis of complex arrhythmias like atrial fibrillation were developed. As the mechanisms perpetuating this tachycardia are hardly understood, its investigation is still a matter of basic science and could be fostered by novel signal processing techniques. Third, the diagnostic potential of novel catheter types was assessed. Lastly, the possible application of all algorithms within the clinical workflow was addressed as basic intention during all research.

Considering the treatment of atrial flutter, electroanatomical mapping systems have become useful tools during electrophysiological studies. They allow for a precise acquisition of the atrial anatomy, orientation in the virtual space, labeling sites of interest and additionally a reduction of radiation exposure. Automatic point acquisition can be applied to record electrical information from thousands of points on the endocard during stable tachycardias like atrial flutter. Despite this huge amount of information, automatic analysis in state-of-the-art systems is restricted to voltage and activation time mapping. Within the presented research, several additional methods were developed to extract diagnostically relevant information from the recorded data during atrial flutter:

- The periodic component analysis was developed as novel filtering technique, and shown to outperform the commonly used principal component analysis during stable atrio-ventricular coupling.
- Considering single lead recordings, methods for the detection of active segments within electrograms and the identification of double potentials were developed. They were benchmarked using a database of over 2,800 annotated electrograms, achieving over 90% accuracy.
- Addressing multichannel analysis, the activity of the atrial myocardium was suggested as surrogate for the P wave. Following this concept, an approach to automatically

determining diastolic activity was implemented, being capable of localizing the critical isthmus. Focusing on microreentrant tachycardias, the concept of cycle length coverage by area was introduced, which identifies regions of continuous excitation. These methods were successfully verified on a database of 20 simulated cases including all common maintenance mechanisms of atrial flutter.

- The resulting semi-automatic workflow was demonstrated on clinical data, and correctly highlighted the critical substrate.
- Aiming for the vision of virtual ablation planing, a semi-automatic method was developed and demonstrated to virtualize clinically presenting cases of atrial flutter.

All algorithms were inspired by the clinical approach to diagnosis, and subsequently reformulated as seen from an engineer's perspective. The potential benefit for diagnosis will be assessed in future studies by the author. The adaption of a patient specific model and subsequent arrhythmia induction is a fundamental step for computational assessment of ablation patterns and studies about subsequent reinducibility of follow-up tachycardias. It hopefully will lead to shortened procedure times and improved long-term success rates in the ablation of atrial flutter.

One central aspect of this thesis was the collaboration with both clinical partners and colleagues with a strong background in computer modeling. Exchanging ideas with cardiologists proved highly important to assess clinical relevance and assure correct understanding of the physiological fundamentals. In addition, it allowed to identify limitations in potential clinical application at an early stage. Although measured electrogram data did provide an impression of signal quality, however, it did not originate from a controlled environment. Simulations were of great help in this regard, as they allowed to precisely define environment conditions. Selection of parameters for the simulations, in turn, was based on clinical observations. This loop revealed to be an important aspect during the development of algorithms, as they could be verified using simulated data and subsequently be applied on clinical data.

Addressing the visualization of cardiac activity, conventional representation of the excitation pattern is based on activation time mapping. This method relies on the exact annotation of the passing depolarization wave, which is not unambiguous in case of double potentials of prolonged activity. Within the presented research, approaches for the time-dynamic visualization of cardiac excitation were addressed:

- Transformations for electrograms were developed based on phase, signal energy and activity, capable of retaining information about fractionation and double potentials.
- A realistic 3D representation was achieved using the patient specific atrial anatomy and acquired electrode positions.
- Dynamic excitation during atrial fibrillation was successfully visualized, incorporating simultaneous biatrial basket catheter mapping data from 126 intracardiac channels.

These methods allow to more intuitively comprehend spatio-temporal relation ships, as wavefronts can easily be tracked over time and the reentrant patterns or collisions be explained. Additionally, the new techniques allow to visualize continuous processes and are not limited

to a time span like the basic cycle length. They are particularly useful during mapping of unstable tachycardias like atrial fibrillation, as the cardiac activity is acquired continuously.

Focusing on statistical analysis, mapping the mechanisms that perpetuate atrial fibrillation is one of the most challenging tasks in contemporary electrophysiological research. Evidence has been found that the depolarization during fibrillation is not completely random but exhibits a certain level of organization. Within the presented thesis, different approaches were presented to identify the dominant excitation patterns:

- Classification and sparse modeling were assessed to understand excitation dynamics.
- Automatic detection of dominant patterns based on their activation time was implemented and successfully demonstrated to detect the frequency and origin of ectopic activity.
- Morphology-based analysis of local activation waves was introduced as a technique to determine the dominant patterns during atrial fibrillation.
- Measures for the quantitative analysis of detected excitation classes were introduced and combined with the annotation in time domain as method to structure the electrogram data for visual assessment.

Concluding, the analysis of individual wavefronts was suggested as promising approach due to the high variability of depolarization patterns. Both the spatio-temporal activation sequence and the morphology-based analysis were introduced as techniques to determine the dominant patterns during atrial fibrillation. Statistical evaluation allows to differentiate between singular events and more frequently occurring depolarization patterns. These two methods are considered valuable tools in the statistical analysis of fibrillatory activity and will be subject of further research. Implementation of additional signal processing and feature extraction is considered a very promising approach to delineate information about the atrial substrate and the process of depolarization.

With respect to novel devices, two major catheter types are of significant interest to the current cardiological community. While panoramic baskets provide the opportunity to record simultaneous electrogram information from a wide range of atrial sites, the Orion™ mapping catheter is designed for local high-density mapping. Within the presented thesis, the electrode to endocard contact was assessed for both catheter types:

- Computational catheter models were implemented, which allowed to simulate shape adaption and coverage of different electrode designs within the atrial geometry.
- The effect of spline bunching in panoramic mapping catheters was quantitatively assessed for both clinical and simulated scenarios.
- The field of view for the Orion catheter was quantified based on clinical mapping data from multiple centers.

Based on these examinations, knowledge about the position of electrodes in space was identified as fundamental prerequisite for correct data analysis with diagnostic purpose. Methods for the corresponding processing and visualization were demonstrated on multiple clinical datasets. The field of view of the Orion catheter is of special interest for mapping during atrial fibrillation, in which its utility was neither analyzed nor clinically evaluated up

to now. This knowledge will be helpful in the design of analysis algorithms to specifically analyze respective mapping data.

Considering the clinical application, three major achievements were accomplished within the presented research:

- Algorithms were developed to import mapping data from all three commercially available mapping systems.
- Data structure was standardized to allow processing of information recorded with all systems.
- Software was developed for the presentation of analysis results in the clinical environment, respecting the peculiar needs of physicians and engineers.

All algorithms were designed to highlight areas of interest to the treating physician for a more detailed inspection. Processing is done within minutes, allowing to include the analysis without prolonging the procedure. The processing techniques can cope with the enormous amount of mapping data acquired by state-of-the-art mapping systems, and help to identify substrate which is critical for the tachycardia.

Overall, many advances in the field of processing intracardiac electrograms have been described in this thesis. The multichannel analysis of mapping data allowed to automatically identify critical sites in several clinical cases of atrial flutter. Addressing the basic research on atrial fibrillation, different approaches were described to statistically evaluate dominant excitation patterns. These will hopefully aid in understanding the underlying mechanisms and allow to design patient specific treatment therapies. During the course of his PhD studies, the author co-organized the congress *Atrial Signals 2015*, which was attended by many renown international physicians and engineers. Although a lively debate about the underlying mechanisms of atrial fibrillation took place, all participants acknowledged the importance of intracardiac electrogram signal processing, as it can allow to understand both excitation dynamics and the atrial substrate. The presented techniques will hopefully aid in a more complete understanding of atrial arrhythmias, optimization of treatment strategies, reduction of costs to the health care system and ultimately reduce the burden on the individual patient.

Appendix A

Annotated Atrial Anatomy

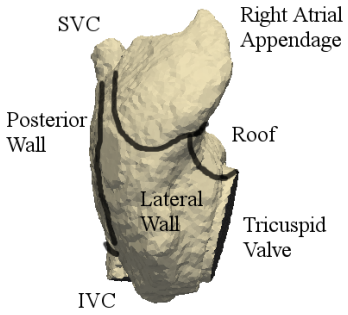

(a) Right atrium in lateral view.

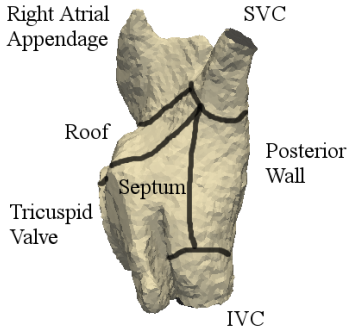

(b) Right atrium in postero-septal view.

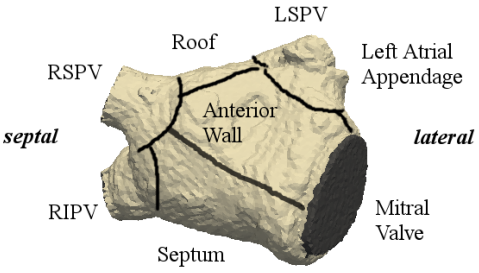

(c) Left atrium in AP view.

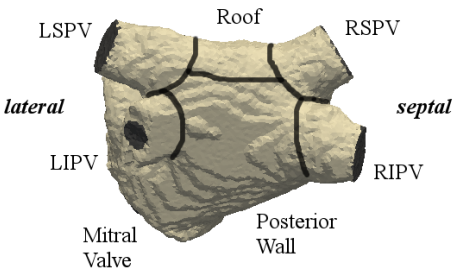

(d) Left atrium in PA view.

Figure A.1: Annotated atrial anatomy. Most simulations shown in the thesis were performed on this bi-atrial anatomical model, which was previously generated from segmented MRI data (see [172] for details). The right atrium (RA) is shown from lateral (a) and postero-septal view (b). For the left atrium (LA), the antero-posterior (*AP*, c) and postero-anterior (*PA*, d) view were chosen.

References

[1] S. N. Singh, "Costs and clinical consequences of suboptimal atrial fibrillation management," *ClinicoEconomics and Outcomes Research : CEOR*, vol. 4, pp. 79–90, 2012.

[2] B. P. Krijthe, A. Kunst, E. J. Benjamin, et al., "Projections on the number of individuals with atrial fibrillation in the European Union, from 2000 to 2060," *European Heart Journal*, vol. 34, no. 35, pp. 2746–2751, 2013.

[3] D. M. Lloyd-Jones, T. J. Wang, E. P. Leip, et al., "Lifetime risk for development of atrial fibrillation: the Framingham heart study," *Circulation*, vol. 110, no. 9, pp. 1042–1046, 2004.

[4] M. H. Kim, S. S. Johnston, B.-C. Chu, et al., "Estimation of total incremental health care costs in patients with atrial fibrillation in the united states," *Circulation. Cardiovascular Quality and Outcomes*, vol. 4, no. 3, pp. 313–320, 2011.

[5] P. A. Wolf, R. D. Abbott, and W. B. Kannel, "Atrial fibrillation as an independent risk factor for stroke: the Framingham study," *Stroke; a Journal of Cerebral Circulation*, vol. 22, no. 8, pp. 983–988, 1991.

[6] A. Verma, C.-y. Jiang, T. R. Betts, et al., "Approaches to catheter ablation for persistent atrial fibrillation," *The New England Journal of Medicine*, vol. 372, no. 19, pp. 1812–1822, 2015.

[7] J. Vogler, S. Willems, A. Sultan, et al., "Pulmonary vein isolation versus defragmentation: The chase-af clinical trial," *J Am Coll Cardiol*, vol. 66, no. 24, pp. 2743–2752, 2015.

[8] S. Castrejon-Castrejon, M. Ortega, A. Perez-Silva, et al., "Organized atrial tachycardias after atrial fibrillation ablation," *Cardiology Research and Practice*, vol. 2011, p. 957538, 2011.

[9] A. Bollmann, S. Hilbert, S. John, et al., "Initial experience with ultra high-density mapping of human right atria," *J Cardiovasc Electrophysiol*, vol. 27, no. 2, pp. 154–160, 2016.

[10] S. Silbernagl, *Taschenatlas physiologie*. Stuttgart [u.a.] : Thieme, 2012.

[11] F. M. Weber, *Personalizing simulations of the human atria: Intracardiac measurements, tissue conductivities, and cellular electrophysiology*, Karlsruhe Transactions on Biomedical Engineering, vol. 12. Karlsruhe: KIT Scientific Publishing, 2011.

[12] R. F. Schmidt and F. Lang, *Physiologie des Menschen*. Heidelberg: Springer Medizin Verlag, 2007.

[13] M. W. Krueger, *Personalized multi-scale modeling of the atria: Heterogeneities, fiber architecture, hemodialysis and ablation therapy*, Karlsruhe Transactions on Biomedical Engineering, vol. 19. Karlsruhe: KIT Scientific Publishing, 2012.

[14] A. J. Camm, G. Y. H. Lip, R. De Caterina, et al., "2012 focused update of the ESC guidelines for the management of atrial fibrillation: an update of the 2010 ESC guidelines for the management of atrial fibrillation–developed with the special contribution of the european heart rhythm association," *Europace*, vol. 14, no. 10, pp. 1385–1413, 2012.

[15] A. S. Go, E. M. Hylek, K. A. Phillips, et al., "Prevalence of diagnosed atrial fibrillation in adults: national implications for rhythm management and stroke prevention: the anticoagulation and risk factors in atrial fibrillation (atria) study," *JAMA*, vol. 285, no. 18, pp. 2370–2375, 2001.

[16] H. Calkins, K. H. Kuck, R. Cappato, et al., "2012 hrs/ehra/ecas expert consensus statement on catheter and surgical ablation of atrial fibrillation: recommendations for patient selection, procedural techniques, patient management and follow-up, definitions, endpoints, and research trial design," *J Interv Card Electrophysiol*, vol. 33, no. 2, pp. 171–257, 2012.

[17] C. T. January, L. S. Wann, J. S. Alpert, et al., "2014 aha/acc/hrs guideline for the management of patients with atrial fibrillation: Executive summary: A report of the american college of cardiology/american heart association task force on practice guidelines and the heart rhythm society," *Circulation*, 2014.

[18] G. K. Moe, "On the multiple wavelet hypothesis of atrial fibrillation," *Arch. Int. Pharmacodyn. Ther.*, vol. 140, no. 1-2, pp. 183–188, 1962.

[19] J. L. Cox, J. P. Boineau, R. B. Schuessler, et al., "Successful surgical treatment of atrial fibrillation. review and clinical update," *JAMA : the Journal of the American Medical Association*, vol. 266, no. 14, pp. 1976–1980, 1991.

[20] M. Haïssaguerre, P. Jaïs, D. C. Shah, et al., "Spontaneous initiation of atrial fibrillation by ectopic beats originating in the pulmonary veins," *New England Journal of Medicine*, vol. 339, no. 10, pp. 659–666, 1998.

[21] P. Jaïs, D. C. Shah, M. Haïssaguerre, et al., "Atrial fibrillation: role of arrhythmogenic foci," *Journal of Interventional Cardiac Electrophysiology*, vol. 4, no. 1, pp. 29–37, 2000.

[22] S. Ernst, F. Ouyang, F. Lober, et al., "Catheter-induced linear lesions in the left atrium in patients with atrial fibrillation: an electroanatomic study," *J Am Coll Cardiol*, vol. 42, no. 7, pp. 1271–1282, 2003.

[23] H. L. Estner, I. Deisenhofer, A. Luik, et al., "Electrical isolation of pulmonary veins in patients with atrial fibrillation: reduction of fluoroscopy exposure and procedure duration by the use of a non-fluoroscopic navigation system (navx)," *Europace*, vol. 8, no. 8, pp. 583–587, 2006.

[24] C. Pappone, S. Rosanio, G. Oreto, et al., "Circumferential radiofrequency ablation of pulmonary vein ostia: A new anatomic approach for curing atrial fibrillation," *Circulation*, vol. 102, no. 21, pp. 2619–2628, 2000.

[25] R. R. Tilz, F. Ouyang, J. Chung, et al., "Ablation von paroxysmalem und persistierendem vorhofflimmern mit der doppel-lasso-technik," *Journal für Kardiologie*, vol. 14, no. (Suppl B, Forum Rhythmologie), pp. 3–8, 2007.

[26] I. Deisenhofer, M. A. E. Schneider, M. Bohlen-Knauf, et al., "Circumferential mapping and electric isolation of pulmonary veins in patients with atrial fibrillation," *The American Journal of Cardiology*, vol. 91, no. 2, pp. 159–163, 2003.

[27] S. M. Narayan, D. E. Krummen, K. Shivkumar, et al., "Treatment of atrial fibrillation by the ablation of localized sources: CONFIRM (conventional ablation for atrial fibrillation with or without focal impulse and rotor modulation) trial," *J Am Coll Cardiol*, vol. 60, no. 7, pp. 628–636, 2012.

[28] V. I. Krinskii, "Spread of excitation in an inhomogeneous medium (state similar to cardiac fibrillation)," *Biofizika*, vol. 11, pp. 676–683, 1966.

[29] A. T. Winfree, *When time breaks down*. Princeton: Princeton University Press, 1987.

[30] J. M. Davidenko, P. F. Kent, D. R. Chialvo, et al., "Sustained vortex-like waves in normal isolated ventricular muscle," *Proceedings of the National Academy of Sciences of the United States of America*, vol. 87, no. 22, pp. 8785–8789, 1990.

[31] S. V. Pandit and J. Jalife, "Rotors and the dynamics of cardiac fibrillation," *Circulation Research*, vol. 112, no. 5, pp. 849–862, 2013.

[32] S. M. Narayan, K. Shivkumar, D. E. Krummen, et al., "Panoramic electrophysiological mapping but not electrogram morphology identifies stable sources for human atrial fibrillation: stable atrial fibrillation rotors and focal sources relate poorly to fractionated electrograms," *Circulation. Arrhythmia and Electrophysiology*, vol. 6, no. 1, pp. 58–67, 2013.

[33] M. Haïssaguerre, M. Hocini, A. J. Shah, et al., "Noninvasive panoramic mapping of human atrial fibrillation mechanisms: a feasibility report," *J Cardiovasc Electrophysiol*, vol. 24, no. 6, pp. 711–717, 2013.

[34] M. A. Allessie, N. M. S. de Groot, R. P. M. Houben, et al., "Electropathological substrate of long-standing persistent atrial fibrillation in patients with structural heart disease: longitudinal dissociation," *Circulation. Arrhythmia and Electrophysiology*, vol. 3, no. 6, pp. 606–615, 2010.

[35] N. M. S. de Groot, R. P. M. Houben, J. L. Smeets, et al., "Electropathological substrate of longstanding persistent atrial fibrillation in patients with structural heart disease: epicardial breakthrough," *Circulation*, vol. 122, no. 17, pp. 1674–1682, 2010.

[36] B. J. Hansen, J. Zhao, T. A. Csepe, et al., "Atrial fibrillation driven by micro-anatomic intramural re-entry revealed by simultaneous sub-epicardial and sub-endocardial optical mapping in explanted human hearts," *European Heart Journal*, *epub ahead of print*, 2015.

[37] M. C. Wijffels, C. J. Kirchhof, R. Dorland, et al., "Atrial fibrillation begets atrial fibrillation. A study in awake chronically instrumented goats," *Circulation*, vol. 92, no. 7, pp. 1954–1968, 1995.

[38] M. S. Spach, J. F. Heidlage, P. C. Dolber, et al., "Mechanism of origin of conduction disturbances in aging human atrial bundles: experimental and model study," *Heart Rhythm*, vol. 4, no. 2, pp. 175–185, 2007.

[39] J. Eckstein, S. Verheule, N. M. de Groot, et al., "Mechanisms of perpetuation of atrial fibrillation in chronically dilated atria," *Progress in Biophysics and Molecular Biology*, vol. 97, no. 2-3, pp. 435–451, 2008.

[40] D. Li, K. Shinagawa, L. Pang, et al., "Effects of angiotensin-converting enzyme inhibition on the development of the atrial fibrillation substrate in dogs with ventricular tachypacing-induced congestive heart failure," *Circulation*, vol. 104, no. 21, pp. 2608–2614, 2001.

[41] L. Yue, J. Feng, and R. Gaspo, "Ionic remodeling underlying action potential changes in a canine model of atrial fibrillation," *Circ. Res.*, vol. 81, no. 4, pp. 512–525, 1997.

[42] M. Allessie, J. Ausma, and U. Schotten, "Electrical, contractile and structural remodeling during atrial fibrillation," *Cardiovascular Research*, vol. 54, no. 2, pp. 230–246, 2002.

[43] H. R. Neuberger, U. Schotten, Y. Blaauw, et al., "Chronic atrial dilation, electrical remodeling, and atrial fibrillation in the goat," *J Am Coll Cardiol*, vol. 47, no. 3, pp. 644–653, 2006.

[44] K. T. S. Konings, C. J. H. J. Kirchhof, J. R. L. M. Smeets, et al., "High-density mapping of electrically induced atrial fibrillation in humans," *Circulation*, vol. 89, no. 4, pp. 1665–1680, 1994.

[45] H.-R. Neuberger, U. Schotten, S. Verheule, et al., "Development of a substrate of atrial fibrillation during chronic atrioventricular block in the goat," *Circulation*, vol. 111, no. 1, pp. 30–37, 2005.

[46] V. Jacquemet and C. S. Henriquez, "Genesis of complex fractionated atrial electrograms in zones of slow conduction: a computer model of microfibrosis," *Heart Rhythm*, vol. 6, no. 6, pp. 803–810, 2009.

[47] K. Tanaka, S. Zlochiver, K. L. Vikstrom, et al., "Spatial distribution of fibrosis governs fibrillation wave dynamics in the posterior left atrium during heart failure," *Circulation Research*, vol. 101, no. 8, pp. 839–847, 2007.

[48] C. Mahnkopf, T. J. Badger, N. S. Burgon, et al., "Evaluation of the left atrial substrate in patients with lone atrial fibrillation using delayed-enhanced MRI: implications for disease progression and response to catheter ablation," *Heart Rhythm*, vol. 7, no. 10, pp. 1475–1481, 2010.

[49] A. S. Jadidi, E. Duncan, S. Miyazaki, et al., "Functional nature of electrogram fractionation demonstrated by left atrial high-density mapping," *Circulation. Arrhythmia and Electrophysiology*, vol. 5, no. 1, pp. 32–42, 2012.

[50] A. S. Jadidi, H. Cochet, A. J. Shah, et al., "Inverse relationship between fractionated electrograms and atrial fibrosis in persistent atrial fibrillation: combined magnetic resonance imaging and high-density mapping," *J Am Coll Cardiol*, vol. 62, no. 9, pp. 802–812, 2013.

[51] M. Bettoni and M. Zimmermann, "Autonomic tone variations before the onset of paroxysmal atrial fibrillation," *Circulation*, vol. 105, no. 23, pp. 2753–2759, 2002.

[52] O. F. Sharifov, V. V. Fedorov, G. G. Beloshapko, et al., "Roles of adrenergic and cholinergic stimulation in spontaneous atrial fibrillation in dogs," *J Am Coll Cardiol*, vol. 43, no. 3, pp. 483–490, 2004.

[53] E. Patterson, S. S. Po, B. J. Scherlag, et al., "Triggered firing in pulmonary veins initiated by in vitro autonomic nerve stimulation," *Heart Rhythm*, vol. 2, no. 6, pp. 624–631, 2005.

[54] J. Zhou, B. J. Scherlag, J. Edwards, et al., "Gradients of atrial refractoriness and inducibility of atrial fibrillation due to stimulation of ganglionated plexi," *J Cardiovasc Electrophysiol*, vol. 18, no. 1, pp. 83–90, 2007.

[55] A. Luik, A. Radzewitz, M. Kieser, et al., "Cryoballoon versus open irrigated radiofrequency ablation in patients with paroxysmal atrial fibrillation: The prospective, randomized, controlled, noninferiority FreezeAF study," *Circulation*, vol. 132, no. 14, pp. 1311–1319, 2015.

[56] K. Nademanee, J. McKenzie, E. Kosar, et al., "A new approach for catheter ablation of atrial fibrillation: mapping of the electrophysiologic substrate," *J Am Coll Cardiol*, vol. 43, no. 11, pp. 2044–2053, 2004.

[57] E. Buch, M. Share, R. Tung, et al., "Long-term clinical outcomes of focal impulse and rotor modulation for treatment of atrial fibrillation: A multi-center experience," *Heart Rhythm*, vol. 13, no. 3, pp. 636–641, 2016.

[58] H. Kottkamp, J. Berg, R. Bender, et al., "Box Isolation of Fibrotic Areas (BIFA): A Patient-Tailored Substrate Modification Approach for Ablation of Atrial Fibrillation," *J Cardiovasc Electrophysiol*, vol. 27, no. 1, pp. 22–30, 2016.

[59] A. S. Jadidi, H. Lehrmann, C. Keyl, et al., "Ablation of Persistent Atrial Fibrillation Targeting Low-Voltage Areas With Selective Activation Characteristics," *Circulation. Arrhythmia and Electrophysiology*, vol. 9, no. 3, pii:e002962, 2016.

[60] N. Akoum, M. Daccarett, C. McGann, et al., "Atrial fibrosis helps select the appropriate patient and strategy in catheter ablation of atrial fibrillation: a DE-MRI guided approach," *J Cardiovasc Electrophysiol*, vol. 22, no. 1, pp. 16–22, 2011.

[61] R. J. Schilling, N. S. Peters, J. Goldberger, et al., "Characterization of the anatomy and conduction velocities of the human right atrial flutter circuit determined by noncontact mapping," *J Am Coll Cardiol*, vol. 38, no. 2, pp. 385–393, 2001.

[62] T. Itoh, M. Kimura, S. Sasaki, et al., "High correlation of estimated local conduction velocity with natural logarithm of bipolar electrogram amplitude in the reentry circuit of atrial flutter," *J Cardiovasc Electrophysiol*, vol. 25, no. 4, pp. 387–394, 2014.

[63] P. Jaïs, D. C. Shah, M. Haïssaguerre, et al., "Mapping and ablation of left atrial flutters," *Circulation*, vol. 101, no. 25, pp. 2928–2934, 2000.

[64] A. M. Patel, A. d'Avila, P. Neuzil, et al., "Atrial tachycardia after ablation of persistent atrial fibrillation: identification of the critical isthmus with a combination of multielectrode activation mapping and targeted entrainment mapping," *Circulation. Arrhythmia and Electrophysiology*, vol. 1, no. 1, pp. 14–22, 2008.

[65] P. Jaïs, S. Matsuo, S. Knecht, et al., "A deductive mapping strategy for atrial tachycardia following atrial fibrillation ablation: importance of localized reentry," *J Cardiovasc Electrophysiol*, vol. 20, no. 5, pp. 480–491, 2009.

[66] L. Saghy, C. Tutuianu, and J. Szilagyi, "Atrial tachycardias following atrial fibrillation ablation," *Current Cardiology Reviews*, vol. 11, no. 2, pp. 149–156, 2015.

[67] T. A. Dewland, D. V. Glidden, and G. M. Marcus, "Healthcare utilization and clinical outcomes after catheter ablation of atrial flutter," *PloS one*, vol. 9, no. 7, p. e100509, 2014.

[68] P. Chowdhury, R. L. William, R. A. Schweikert, et al., "Ablation of atrial fibrillation: what can we tell our patients?" *Cleveland Clinical Journal of Medicine*, vol. 76, no. 9, pp. 543–550, 2009.

[69] L. A. Bokeriya, A. S. Revishvili, A. V. Kalinin, et al., "Hardware-software system for noninvasive electrocardiographic heart examination based on inverse problem of electrocardiography," *Biomedical engineering*, vol. 42, no. 6, pp. 273–279, 2008.

[70] Y. Rudy, "Noninvasive electrocardiographic imaging of arrhythmogenic substrates in humans," *Circulation Research*, vol. 112, no. 5, pp. 863–874, 2013.

[71] J. Eckstein, S. Zeemering, D. Linz, et al., "Transmural conduction is the predominant mechanism of breakthrough during atrial fibrillation: evidence from simultaneous endo-epicardial high-density activation mapping," *Circulation. Arrhythmia and Electrophysiology*, vol. 6, no. 2, pp. 334–341, 2013.

[72] S. A. Ben-Haim, D. Osadchy, I. Schuster, et al., "Nonfluoroscopic, in vivo navigation and mapping technology," *Nature Medicine*, vol. 2, no. 12, pp. 1393–1395, 1996.

[73] C. Eitel, G. Hindricks, N. Dagres, et al., "Ensite velocity cardiac mapping system: a new platform for 3D mapping of cardiac arrhythmias," *Expert Review of Medical Devices*, vol. 7, no. 2, pp. 185–192, 2010.

[74] M. Rotter, Y. Takahashi, P. Sanders, et al., "Reduction of fluoroscopy exposure and procedure duration during ablation of atrial fibrillation using a novel anatomical navigation system," *European Heart Journal*, vol. 26, no. 14, pp. 1415–1421, 2005.

[75] L. M. Ptaszek, F. Chalhoub, F. Perna, et al., "Rapid acquisition of high-resolution electroanatomical maps using a novel multielectrode mapping system," *Journal of Interventional Cardiac Electrophysiology*, vol. 36, no. 3, pp. 233–242, 2013.

[76] Y. Tanaka, M. Genet, L. Chuan Lee, et al., "Utility of high-resolution electroanatomic mapping of the left ventricle using a multispline basket catheter in a swine model of chronic myocardial infarction," *Heart Rhythm*, vol. 12, no. 1, pp. 144–154, 2015.

[77] R. J. Schilling, N. S. Peters, and D. W. Davies, "Simultaneous endocardial mapping in the human left ventricle using a noncontact catheter," *Circulation*, vol. 98, pp. 887–898, 1998.

[78] C.-T. Tai, J.-L. Huang, P.-C. Lee, et al., "High-resolution mapping around the crista terminalis during typical atrial flutter: new insights into mechanisms," *J Cardiovasc Electrophysiol*, vol. 15, no. 4, pp. 406–414, 2004.

[79] E. Rodriguez, D. C. Man, R. F. Coyne, et al., "Type I atrial flutter ablation guided by a basket catheter," *J Cardiovasc Electrophysiol*, vol. 9, no. 7, pp. 761–766, 1998.

[80] C. Schmitt, B. Zrenner, M. Schneider, et al., "Clinical experience with a novel multielectrode basket catheter in right atrial tachycardias," *Circulation*, vol. 99, pp. 2414–2422, 1999.

[81] B. Zrenner, G. Ndrepepa, M. R. Karch, et al., "Electrophysiologic characteristics of paroxysmal and chronic atrial fibrillation in human right atrium," *J Am Coll Cardiol*, vol. 38, no. 4, pp. 1143–1149, 2001.

[82] C. Schmitt, G. Ndrepepa, S. Weber, et al., "Biatrial multisite mapping of atrial premature complexes triggering onset of atrial fibrillation," *The American Journal of Cardiology*, vol. 89, no. 12, pp. 1381–1387, 2002.

[83] V. Barbaro, P. Bartolini, G. Calcagnini, et al., "Measure of synchronisation of right atrial depolarisation wavefronts during atrial fibrillation," *Medical & Biological Engineering & Computing*, vol. 40, no. 1, pp. 56–62, 2002.

[84] G. Ndrepepa, M. R. Karch, M. A. E. Schneider, et al., "Characterization of paroxysmal and persistent atrial fibrillation in the human left atrium during initiation and sustained episodes," *J Cardiovasc Electrophysiol*, vol. 13, no. 6, pp. 525–532, 2002.

[85] T. Lin, A. Rillig, T. Bucur, et al., "Focal impulse and rotor modulation using the novel 64-electrode basket catheter: electrogram characteristics of human rotors," *Europace*, vol. 17, no. 12, pp. 1791–1797, 2015.

[86] E. Anter, C. M. Tschabrunn, F. M. Contreras-Valdes, et al., "Pulmonary vein isolation using the rhythmia mapping system: Verification of intracardiac signals using the orion mini-basket catheter," *Heart Rhythm*, vol. 12, no. 9, pp. 1927–1934, 2015.

[87] J. C. Caldwell, N. Hobson, and D. Redfearn, "Voltage-directed Cavo-tricuspid isthmus ablation using novel ablation catheter mapping technology," *The Journal of Innovations in Cardiac Rhythm Management*, vol. 6, pp. 1908–1912, 2015.

[88] J. Iwasawa, S. Miyazaki, T. Takagi, et al., "Cavotricuspid isthmus ablation using a catheter equipped with mini electrodes on the 8 mm tip: a prospective comparison with an 8 mm dumbbell-shaped tip catheter and 8 mm tip cryothermal catheter," *European Society of Cardiology*, vol. 10, p. euv253, 2015.

[89] C. Schmitt, I. Deisenhofer, and B. Zrenner, Eds., *Catheter ablation of cardiac arrhythmias: A practical approach*. Springer, 2006.

[90] G. Ndrepepa, E. B. Caref, H. Yin, et al., "Activation time determination by high-resolution unipolar and bipolar extracellular electrograms in the canine heart," *J Cardiovasc Electrophysiol*, vol. 6, no. 3, pp. 174–188, 1995.

[91] T. P. Almeida, J. L. Salinet Jr., G. S. Chu, et al., "Different definitions of complex fractionated atrial electrograms do not concur with the clinical perspective," in *Computing in Cardiology*, vol. 40, pp. 1055–1058, 2013.

[92] M. Haïssaguerre, D. C. Shah, P. Jaïs, et al., "Electrophysiological breakthroughs from the left atrium to the pulmonary veins," *Circulation*, vol. 102, no. 20, pp. 2463–2465, 2000.

[93] S. Willems, H. Klemm, T. Rostock, et al., "Substrate modification combined with pulmonary vein isolation improves outcome of catheter ablation in patients with persistent atrial fibrillation: a prospective randomized comparison," *European Heart Journal*, vol. 27, no. 23, pp. 2871–2878, 2006.

[94] S. Willems and Hoffmann, "Katheterablation bei vorhofflimmern: wann bereits klinisch etabliert, wann noch experimentell?" *Herz Kardiovaskuläre Erkrankungen*, vol. 33, no. 6, pp. 402–411, 2008.

[95] M. Haïssaguerre, M. Wright, M. Hocini, et al., "The substrate maintaining persistent atrial fibrillation," *Circulation. Arrhythmia and Electrophysiology*, vol. 1, no. 1, pp. 2–5, 2008.

[96] H. Oral, A. Chugh, E. Good, et al., "Radiofrequency catheter ablation of chronic atrial fibrillation guided by complex electrograms," *Circulation*, vol. 115, no. 20, pp. 2606–2612, 2007.

[97] C. Schmitt, H. Estner, B. Hecher, et al., "Radiofrequency ablation of complex fractionated atrial electrograms (cfae): preferential sites of acute termination and regularization in paroxysmal and persistent atrial fibrillation," *J Cardiovasc Electrophysiol*, vol. 18, no. 10, pp. 1039–1046, 2007.

[98] A. L. Hodgkin and A. F. Huxley, "A quantitative description of membrane current and its application to conduction and excitation in nerve," *Journal of Physiology*, vol. 117, pp. 500–544, 1952.

[99] M. Courtemanche, R. J. Ramirez, and S. Nattel, "Ionic mechanisms underlying human atrial action potential properties: Insights from a mathematical model," *Am. J. Physiol.*, vol. 275, no. 1 Pt 2, pp. H301–H321, 1998.

[100] M. Courtemanche, R. J. Ramirez, and S. Nattel, "Ionic targets for drug therapy and atrial fibrillation-induced electrical remodeling: insights from a mathematical model," *Cardiovasc. Res.*, vol. 42, no. 2, pp. 477–489, 1999.

[101] M. W. Krueger, A. Dorn, D. U. J. Keller, et al., "In-silico modeling of atrial repolarization in normal and atrial fibrillation remodeled state," *Medical & Biological Engineering & Computing*, vol. 51, no. 10, pp. 1105–1119, 2013.

[102] G. Seemann, F. B. Sachse, M. Karl, et al., "Framework for modular, flexible and efficient solving the cardiac bidomain equation using PETSc," *Mathematics in Industry*, vol. 15, no. 2, pp. 363–369, 2010.

[103] C. S. Henriquez, "Simulating the electrical behavior of cardiac tissue using the bidomain model," *Critical Reviews ins Biomedical Engineering*, vol. 21, no. 1, pp. 1–77, 1993.

[104] M. Sermesant, E. Konukoglu, H. Delingette, et al., "An Anisotropic Multi-front Fast Marching Method for Real-Time Simulation of Cardiac Electrophysiology," *Functional Imaging and Modeling of the Heart*, vol. 4466, pp. 160–169, 2007.

[105] V. Jacquemet, "An eikonal-diffusion solver and its application to the interpolation and the simulation of reentrant cardiac activations," *Computer Methods and Programs in Biomedicine*, vol. 108, no. 2, pp. 548–558, 2012.

[106] S. K. Mitra, *Digital signal processing : A computer-based approach*. McGraw-Hill Higher Education, 2001.

[107] F. Puente León, U. Kiencke, and H. Jäkel, *Signale und systeme*. München: Oldenbourg Verlag, 2011.

[108] U. Kiencke, M. Schwarz, and T. Weickert, *Signalverarbeitung: Zeit-frequenz-analyse und schätzverfahren*. München: Oldenbourg, 2008.

[109] J. F. Kaiser, "On a simple algorithm to calculate the 'energy' of a signal," *Acoustics, Speech, and Signal Processing, 1990. ICASSP-90., 1990 International Conference on*, pp. 381–384, 1990.

[110] C. Schilling, M. P. Nguyen, A. Luik, et al., "Non-linear energy operator for the analysis of intracardial electrograms," in *IFMBE Proceedings World Congress on Medical Physics and Biomedical Engineering*, vol. 25/4, pp. 872–875, 2009.

[111] U. Kiencke and H. Jäkel, *Signale und systeme*. München: Oldenbourg-Verl., 2008.

[112] A. N. Iyer and R. A. Gray, "An experimentalist's approach to accurate localization of phase singularities during reentry," *Annals of Biomedical Engineering*, vol. 29, no. 1, pp. 47–59, 2001.

[113] M.-A. Bray and J. P. Wikswo, "Considerations in phase plane analysis for nonstationary reentrant cardiac behavior," *Physical Review. E, Statistical, Nonlinear, and Soft Matter Physics*, vol. 65, no. 5 Pt 1, p. 051902, 2002.

[114] P. Kuklik, S. Zeemering, B. Maesen, et al., "Reconstruction of instantaneous phase of unipolar atrial contact electrogram using a concept of sinusoidal recomposition and hilbert transform," *IEEE Trans Biomed Eng*, vol. 62, no. 1, pp. 296–302, 2015.

[115] M.-A. Bray, S.-F. Lin, R. R. Aliev, et al., "Experimental and theoretical analysis of phase singularity dynamics in cardiac tissue," *J Cardiovasc Electrophysiol*, vol. 12, no. 6, pp. 716–722, 2001.

[116] R. H. Clayton, E. A. Zhuchkova, and A. V. Panfilov, "Phase singularities and filaments: simplifying complexity in computational models of ventricular fibrillation," *Progress in Biophysics and Molecular Biology*, vol. 90, no. 1-3, pp. 378–398, 2006.

[117] L. J. Rantner, L. Wieser, M. C. Stuhlinger, et al., "Detection of phase singularities in triangular meshes," *Methods of Information in Medicine*, vol. 46, no. 6, pp. 646–654, 2007.

[118] P. E. H. Richard O. Duda, *Pattern classification*. New York, NY, USA: John Wiley & Sons, Inc., 2001.

[119] C. M. Bishop, *Pattern recognition and machine learning*. New York: Springer, 2007.

[120] C. H. Roney, C. D. Cantwell, N. A. Qureshi, et al., "An automated algorithm for determining conduction velocity, wavefront direction and origin of focal cardiac arrhythmias using a multipolar catheter," in *Engineering in Medicine and Biology Society Conference*, pp. 1583–1586, 2014.

[121] F. M. Weber, C. Schilling, D. Straub, et al., "Extracting clinically relevant circular mapping and coronary sinus catheter potentials from atrial simulations," in *Lecture Notes in Computer Science*, vol. 5528, pp. 30–38, 2009.

[122] D. Frisch, "Patient-specific modeling of catheter deformation to extract panoramic intracardiac electrograms during simulated atrial fibrillation," Bachelor thesis, Institute of Biomedical Engineering, Karlsruhe Institute of Technology (KIT), 2014.

[123] A. N. Pressley, *Elementary differential geometry (springer undergraduate mathematics series)*. Springer, 2010.

[124] M. Born, *Untersuchungen über die stabilität der elastischen linie in ebene und raum, unter verschiedenen grenzbedingungen*. Göttingen, 1906.

[125] J. Laughner, S. Shome, N. Child, et al., "Practical considerations of mapping persistent atrial fibrillation with whole-chamber basket catheters," *JACC: Clinical Electrophysiology*, *epub ahead of print*, 2015.

[126] B. Zrenner, G. Ndrepepa, M. Schneider, et al., "Basket catheter-guided three-dimensional activation patterns construction and ablation of common type atrial flutter," *PACE*, vol. 23, no. 9, pp. 1350–1358, 2000.

[127] H. F. Pitschner, A. Berkovic, S. Grumbrecht, et al., "Multielectrode basket catheter mapping for human atrial fibrillation," *J Cardiovasc Electrophysiol*, vol. 9, no. 8 Suppl, pp. S48–56, 1998.

[128] K. Kumagai, M. Ogawa, H. Noguchi, et al., "Electrophysiologic properties of pulmonary veins assessed using a multielectrode basket catheter," *J Am Coll Cardiol*, vol. 43, no. 12, pp. 2281–2289, 2004.

[129] T. Arentz, L. Haegeli, P. Sanders, et al., "High-density mapping of spontaneous pulmonary vein activity initiating atrial fibrillation in humans," *J Cardiovasc Electrophysiol*, vol. 18, no. 1, pp. 31–38, 2007.

[130] T. F. Kordis, E. T. Johnson, P. C. Burke, et al., "Basket style cardiac mapping catheter having a flexible electrode assembly for sensing monophasic action potentials," *US patent 20130331677 A1*, 2013.

[131] T. Baas, *ECG based analysis of the ventricular repolarisation in the human heart*, Karlsruhe Transactions on Biomedical Engineering, vol. 18. Karlsruhe: KIT Scientific Publishing, 2012.

[132] C. Schilling, *Analysis of atrial electrogram*, Karlsruhe Transactions on Biomedical Engineering, vol. 17. Karlsruhe: KIT Scientific Publishing, 2012.

[133] M. Keller, *Formation of intracardiac electrograms under physiological and pathological conditions*, Karlsruhe Transactions on Biomedical Engineering, vol. 21. Karlsruhe: KIT Scientific Publishing, 2014.

[134] G. Lenis, F. Conz, and O. Dössel, "Combining different ECG derived respiration tracking methods to create an optimal reconstruction of the breathing pattern," in *Current Directions in Biomedical Engineering*, vol. 1, no. 1, 2015, pp. 54–57.

[135] G. Lenis, N. Pilia, T. Oesterlein, et al., "P wave detection and delineation in the ECG based on the phase free stationary wavelet transform and using intracardiac atrial electrograms as reference," *Biomedizinische Technik / Biomedical Engineering*, vol. 61, no. 1, pp. 37–56, 2016.

[136] L. Sörnmo and P. Laguna, *Bioelectrical signal processing in cardiac and neurological applications*, Biomedical engineering. Amsterdam: Elsevier, 2005.

[137] T. Oesterlein, G. Lenis, A. Luik, et al., "Periodic component analysis to eliminate ventricular far field artifacts in unipolar atrial electrograms of patients suffering from atrial flutter," in *Biomedizinische Technik / Biomedical Engineering*, vol. 59, no. s1, p. 14, 2014.

[138] G. D. Clifford, F. Azuaje, and P. McSharry, *Advanced methods and tools for ECG data analysis*. Boston, Mass.[u.a.] : Artech House, 2006.

[139] T. G. Oesterlein, G. Lenis, D.-T. Rudolph, et al., "Removing ventricular far-field signals in intracardiac electrograms during stable atrial tachycardia using the periodic component analysis," *Journal of Electrocardiology*, vol. 48, no. 2, pp. 171–180, 2015.

[140] M. Keller, S. Schuler, M. Wilhelms, et al., "Characterization of radiofrequency ablation lesion development based on simulated and measured intracardiac electrograms," *IEEE Trans Biomed Eng*, vol. 61, no. 9, pp. 2467–2478, 2014.

[141] S. Huck, "Implementation and evaluation of signal preprocessing techniques for novel intracardiac high-density mapping," Bachelor thesis, Institute of Biomedical Engineering, Karlsruhe Institute of Technology (KIT), 2016.

[142] G. Lenis, T. Baas, and O. Dössel, "Ectopic beats and their influence on the morphology of subsequent waves in the electrocardiogram," *Biomedical Engineering / Biomedizinische Technik*, vol. 58, no. 2, pp. 109–119, 2013.

[143] C. Hoogendoorn, N. Duchateau, D. Sanchez-Quintana, et al., "A high-resolution atlas and statistical model of the human heart from multislice ct," *IEEE Transactions on Medical Imaging*, vol. 32, no. 1, pp. 28–44, 2013.

[144] R. Hanna, H. Barschdorf, T. Klinder, et al., "A hybrid method for automatic anatomical variant detection and segmentation," in *Functional Imaging and Modeling of the Heart*, vol. 6666, pp. 333–340, 2011.

[145] N. Konrad, "Statistical analysis of unipolar and bipolar electrograms recorded during atrial fibrillation," Master's thesis, Institute of Biomedical Engineering, Karlsruhe Institute of Technology (KIT), Karlsruhe, 2015.

[146] T. G. Oesterlein, J. Schmid, S. Bauer, et al., "Analysis and visualization of intracardiac electrograms in diagnosis and research: Concept and application of kapavie," *Computer Methods and Programs in Biomedicine*, vol. 127, pp. 165–173, 2016.

[147] J. J. Rieta, F. Hornero, R. Alcaraz, et al., "Ventricular artifacts cancellation from atrial epicardial recordings in atrial tachyarrhythmias," in *Proceedings of the 29th Annual International Conference of the IEEE EMBS*, pp. 6503–6506, 2007.

[148] F. Castells, P. Laguna, L. Sörnmo, et al., "Principal component analysis in ECG signal processing," *EURASIP J. Appl. Signal Process.*, vol. 2007, no. 1, p. 98, 2007.

[149] C. Schilling, M. Aubreville, A. Luik, et al., "Pca-based ventricular far field cancellation in intraatrial electrograms," in *Biomedizinische Technik / Biomedical Engineering*, vol. 55, no. s1, pp. 49–52, 2010.

[150] L. K. Saul and J. B. Allen, "Periodic component analysis: an eigenvalue method for representing periodic structure in speech," in *Nips*, pp. 807–813, 2000.

[151] D.-T. Rudolph, "Advanced signal processing algorithms to remove ventricular far field artifacts from intracardiac electrograms," Master's thesis, Institute of Biomedical Engineering, Karlsruhe Institute of Technology (KIT), 2014.

[152] T. Oesterlein, G. Lenis, A. Luik, et al., "Removing ventricular far field artifacts in intracardiac electrograms during stable atrial flutter using the periodic component analysis - proof of concept study," in *Proceedings 41th International Congress on Electrocardiology*, Bratislava, Slovakia, pp. 49–52, 2014.

[153] R. Sameni, C. Jutten, and M. B. Shamsollahi, "Multichannel electrocardiogram decomposition using periodic component analysis," *IEEE Trans Biomed Eng*, vol. 55, no. 8, pp. 1935–1940, 2008.

[154] R. Llinares, J. Igual, J. Miro-Borras, et al., "Atrial activity estimation using periodic component analysis," in *International Joint Conference on Neural Networks*. IEEE, pp. 1–7, 2010.

[155] M. Garibaldi and V. Zarzoso, "Exploiting intracardiac and surface recording modalities for atrial signal extraction in atrial fibrillation," *Engineering in Medicine and Biology Society Conference*, vol. 2013, pp. 6015–6018, 2013.

[156] V. Monasterio, G. D. Clifford, P. Laguna, et al., "A multilead scheme based on periodic component analysis for T-wave alternans analysis in the ECG," *Annals of Biomedical Engineering*, vol. 38, no. 8, pp. 2532–2541, 2010.

[157] M. P. Nguyen, C. Schilling, and O. Dössel, "A new approach for automated location of active segments in intracardiac electrograms," in *IFMBE Proceedings World Congress on Medical Physics and Biomedical Engineering*, vol. 25/4, pp. 763–766, 2009.

[158] F. Ravelli, M. Mase, and M. Disertori, "Mechanical modulation of atrial flutter cycle length," *Progress in Biophysics and Molecular Biology*, vol. 97, no. 2-3, pp. 417–434, 2008.

[159] G. Lenis, T. Oesterlein, and O. Dössel, "Orthogonal component analysis to remove ventricular far field in non periodic sustained atrial flutter," in *Computing in Cardiology*, vol. 42, pp. 669–672, 2015.

[160] R. H. Milad El Haddad, "Algorithmic detection of the beginning and end of bipolar electrograms: Implications for novel methods to assess local activation time during atrial tachycardia," *Biomedical Signal Processing and Control*, vol. 8, no. 6, pp. 981–991, 2012.

[161] F. M. Weber, C. Schilling, G. Seemann, et al., "Wave-direction and conduction-velocity analysis from intracardiac electrograms–a single-shot technique," *IEEE Trans Biomed Eng*, vol. 57, no. 10, pp. 2394–2401, 2010.

[162] T. G. Oesterlein, M. W. Keller, S. Schuler, et al., "Determination of local activation time in bipolar endocardial electrograms: a comparison of clinical criteria and a new method based on the non-linear energy operator," in *Journal of Electrocardiology*, vol. 46, no. 4, p. e18, 2013.

[163] J. Ng, A. H. Kadish, and J. J. Goldberger, "Technical considerations for dominant frequency analysis," *J Cardiovasc Electrophysiol*, vol. 18, no. 7, pp. 757–764, 2007.

[164] F. Atienza, J. Almendral, J. Jalife, et al., "Real-time dominant frequency mapping and ablation of dominant frequency sites in atrial fibrillation with left-to-right frequency gradients predicts long-term maintenance of sinus rhythm," *Heart Rhythm*, vol. 6, no. 1, pp. 33–40, 2009.

[165] A. Verma, D. Lakkireddy, Z. Wulffhart, et al., "Relationship between complex fractionated electrograms (cfe) and dominant frequency (df) sites and prospective assessment of adding df-guided ablation to pulmonary vein isolation in persistent atrial fibrillation (af)," *J Cardiovasc Electrophysiol*, vol. 22, no. 12, pp. 1309–1316, 2011.

[166] F. Ravelli, M. Mase, A. Cristoforetti, et al., "The logical operator map identifies novel candidate markers for critical sites in patients with atrial fibrillation," *Progress in Biophysics and Molecular Biology*, vol. 115, no. 2-3, pp. 186–197, 2014.

[167] S. M. Singh, E. K. Heist, J. S. Koruth, et al., "The relationship between electrogram cycle length and dominant frequency in patients with persistent atrial fibrillation," *J Cardiovasc Electrophysiol*, vol. 20, no. 12, pp. 1336–1342, 2009.

[168] C. Reich, "Classification of cardiac excitation patterns during atrial fibrillation using multichannel mapping data," Master's thesis, Institute of Biomedical Engineering, Karlsruhe Institute of Technology (KIT), 2015.

[169] J. Ng and J. J. Goldberger, "Understanding and interpreting dominant frequency analysis of AF electrograms," *J Cardiovasc Electrophysiol*, vol. 18, no. 6, pp. 680–685, 2007.

[170] T. F. Oostendorp, A. van Oosterom, and G. Huiskamp, "Interpolation on a triangulated 3D surface," *Journal of Computational Physics*, vol. 80, no. 2, pp. 331–343, 1989.

[171] E. Poremba, "Implementation of a fast simulation C++ framework for the computation of vulnerability to artial arrhythmias using the fast marching algorithm," Bachelor thesis, Institute of Biomedical Engineering, Karlsruhe Institute of Technology (KIT), 2013.

[172] M. W. Krueger, G. Seemann, K. Rhode, et al., "Personalization of atrial anatomy and electrophysiology as a basis for clinical modeling of radio-frequency ablation of atrial fibrillation," *IEEE Transactions on Medical Imaging*, vol. 32, no. 1, pp. 73–84, 2013.

[173] M. W. Krueger, V. Schmidt, C. Tobón, et al., "Modeling atrial fiber orientation in patient-specific geometries: a semi-automatic rule-based approach," in *Functional Imaging and Modeling of the Heart*, vol. 6666, pp. 223–232, 2011.

[174] A. Loewe, M. W. Krueger, P. G. Platonov, et al., "Left and right atrial contribution to the P-wave in realistic computational models," in *Functional Imaging and Modeling of the Heart*, no. 9126, pp. 439–447, 2015.

[175] T. Oesterlein, A. Luik, C. Schmitt, et al., "Neue möglichkeiten zur diagnose von arrhythmien durch visualisierung der zeitlichen dynamik von elektrogrammen," in *Deutsche Gesellschaft für Kardiologie 80. Jahrestagung Mannheim*, vol. 103, no. Suppl 1, p. V167, 2014.

[176] N. W. F. Linton, M. Koa-Wing, D. P. Francis, et al., "Cardiac ripple mapping: a novel three-dimensional visualization method for use with electroanatomic mapping of cardiac arrhythmias," *Heart Rhythm*, vol. 6, no. 12, pp. 1754–1762, 2009.

[177] S. Jamil-Copley, N. Linton, M. Koa-Wing, et al., "Application of ripple mapping with an electroanatomic mapping system for diagnosis of atrial tachycardias," *J Cardiovasc Electrophysiol*, vol. 24, no. 12, pp. 1361–1369, 2013.

[178] A. Nygren, C. Fiset, L. Firek, et al., "Mathematical model of a adult human atrial cell. the role of k+ currents in repolarization," *Circulation Research*, vol. 82, pp. 63–81, 1998.

[179] M. Wilhelms, H. Hettmann, M. M. C. Maleckar, et al., "Benchmarking electrophysiological models of human atrial myocytes," *Frontiers in Physiology*, vol. 3, no. 487, pp. 1–16, 2013.

[180] P. Chinchapatnam, K. S. Rhode, M. Ginks, et al., "Model-based imaging of cardiac apparent conductivity and local conduction velocity for diagnosis and planning of therapy," *IEEE Engineering in Medicine and Biology Society*, vol. 27, no. 11, pp. 1631–1642, 2008.

[181] E. Pernod, M. Sermesant, E. Konukoglu, et al., "A multi-front eikonal model of cardiac electrophysiology for interactive simulation of radio-frequency ablation," *Computers & Graphics*, vol. 35, no. 2, pp. 431–440, 2011.

[182] A. Loewe, E. Poremba, M. W. Krueger, et al., "Fast marching simulation of atrial excitation: Towards personalized ablation planning," in *TRM Forum*, 2013.

[183] F. Schenkel, T. Oesterlein, A. Luik, et al., "Detection and classification of atrial excitation patterns in intracardiac electrograms with application on biatrial basket catheter measurements," in *Biomedizinische Technik / Biomedical Engineering*, vol. 59, no. s1, pp. 166–169, 2014.

[184] J. Trächtler, T. Oesterlein, A. Loewe, et al., "Virtualizing clinical cases of atrial flutter in a fast marching simulation including conduction velocity and ablation scars," in *Current Directions in Biomedical Engineering*, vol. 1, no. 1, pp. 405–408, 2015.

[185] G. Ndrepepa, B. Zrenner, S. Weyerbrock, et al., "Activation patterns in the left atrium during counterclockwise and clockwise atrial flutter," *J Cardiovasc Electrophysiol*, vol. 12, no. 8, pp. 893–899, 2001.

[186] I. Deisenhofer, H. Estner, B. Zrenner, et al., "Left atrial tachycardia after circumferential pulmonary vein ablation for atrial fibrillation: incidence, electrophysiological characteristics, and results of radiofrequency ablation," *Europace*, vol. 8, no. 8, pp. 573–582, 2006.

[187] S. Ammar, A. Luik, G. Hessling, et al., "Ablation of perimitral flutter: acute and long-term success of the modified anterior line," *Europace*, vol. 17, no. 3, pp. 447–452, 2015.

[188] R. De Ponti, R. Verlato, E. Bertaglia, et al., "Treatment of macro-re-entrant atrial tachycardia based on electroanatomic mapping: identification and ablation of the mid-diastolic isthmus," *Europace*, vol. 9, no. 7, pp. 449–457, 2007.

[189] A. Wachter, A. Loewe, M. W. Krueger, et al., "Mesh structure-independent modeling of patient-specific atrial fiber orientation," in *Current Directions in Biomedical Engineering*, vol. 1, no. 1, pp. 409–412, 2015.

[190] A. Wachter, "Model-structure-independent, rule-based annotation of atrial fiber orientation and ablation patterns for an in silico assessment of their arrhythmogenic potential," Diplomarbeit, Institute of Biomedical Engineering, Karlsruhe Institute of Technology (KIT), 2015.

[191] S. Y. Ho and D. Sanchez-Quintana, "The importance of atrial structure and fibers," *Clinical Anatomy*, vol. 22, no. 1, pp. 52–63, 2009.

[192] D. Zöller, "Statistical analysis of propagation patterns in intracardiac panoramic mapping data," Master's thesis, Institute of Biomedical Engineering, Karlsruhe Institute of Technology (KIT), Karlsruhe, 2015.

[193] F. M. Weber, A. Luik, C. Schilling, et al., "Conduction velocity restitution of the human atrium–an efficient measurement protocol for clinical electrophysiological studies," *IEEE Trans Biomed Eng*, vol. 58, no. 9, pp. 2648–2655, 2011.

[194] G. K. Feld, M. Mollerus, U. Birgersdotter-Green, et al., "Conduction velocity in the tricuspid valve-inferior vena cava isthmus is slower in patients with type I atrial flutter compared to those without a history of atrial flutter," *J Cardiovasc Electrophysiol*, vol. 8, no. 12, pp. 1338–1348, 1997.

[195] P. Jaïs, P. Sanders, L.-F. Hsu, et al., "Flutter localized to the anterior left atrium after catheter ablation of atrial fibrillation," *J Cardiovasc Electrophysiol*, vol. 17, no. 3, pp. 279–285, 2006.

[196] C. E. Mesas, C. Pappone, C. C. Lang, et al., "Left atrial tachycardia after circumferential pulmonary vein ablation for atrial fibrillation: electroanatomic characterization and treatment," *J Am Coll Cardiol*, vol. 44, no. 5, pp. 1071–1079, 2004.

[197] L. Dang, N. Virag, Z. Ihara, et al., "Evaluation of ablation patterns using a biophysical model of atrial fibrillation," *Annals of Biomedical Engineering*, vol. 33, no. 4, pp. 465–474, 2005.

[198] M. Rotter, L. Dang, V. Jacquemet, et al., "Impact of varying ablation patterns in a simulation model of persistent atrial fibrillation," *PACE*, vol. 30, no. 3, pp. 314–321, 2007.

[199] P. Ruchat, L. Dang, J. Schlaepfer, et al., "Use of a biophysical model of atrial fibrillation in the interpretation of the outcome of surgical ablation procedures," *Eur J Cardiothorac Surg*, vol. 32, no. 1, pp. 90–95, 2007.

[200] M. Hwang, S.-S. Kwon, J. Wi, et al., "Virtual ablation for atrial fibrillation in personalized in-silico three-dimensional left atrial modeling: comparison with clinical catheter ablation," *Progress in Biophysics and Molecular Biology*, vol. 116, no. 1, pp. 40–47, 2014.

[201] C. Tobón, E. Cardona, C. Palacio, et al., "Ablation pattern guided by approximate entropy maps to prevent chronic atrial fibrillation: A simulation study," in *VI Latin American Congress on Biomedical Engineering CLAIB 2014*, vol. 49, pp. 560–563, 2014.

[202] S. Zahid, K. N. Whyte, E. L. Schwarz, et al., "Feasibility of using patient-specific models and the "minimum cut" algorithm to predict optimal ablation targets for left atrial flutter," *Heart Rhythm*, *epub ahead of print*, 2016.

[203] E. Konukoglu, J. Relan, U. Cilingir, et al., "Efficient probabilistic model personalization integrating uncertainty on data and parameters: Application to eikonal-diffusion models in cardiac electrophysiology," *Progress in Biophysics and Molecular Biology*, vol. 107, no. 1, pp. 134–146, 2011.

[204] J. Relan, P. Chinchapatnam, M. Sermesant, et al., "Coupled personalization of cardiac electrophysiology models for prediction of ischaemic ventricular tachycardia," *Interface Focus*, vol. 1, no. 3, pp. 396–407, 2011.

[205] M. Sermesant, R. Chabiniok, P. Chinchapatnam, et al., "Patient-specific electromechanical models of the heart for the prediction of pacing acute effects in CRT: A preliminary clinical validation," *Medical Image Analysis*, vol. 16, no. 1, pp. 201–215, 2012.

[206] J. Trächtler, "Analysis of electrogram morphology and parameterization of a simulation environment for clinical cases of atrial flutter," Bachelor thesis, Institute of Biomedical Engineering, Karlsruhe Institute of Technology (KIT), 2014.

[207] B. Olshansky, K. Okumura, R. W. Henthorn, et al., "Characterization of double potentials in human atrial flutter: studies during transient entrainment," *J Am Coll Cardiol*, vol. 15, no. 4, pp. 833–841, 1990.

[208] C. Schilling, M. Keller, D. Scherr, et al., "Fuzzy decision tree to classify complex fractionated atrial electrograms," *Biomedizinische Technik/ Biomedical Engineering*, vol. 60, no. 3, pp. 245–255, 2015.

[209] S. Saksena. *Interventional Cardiac Electrophysiology: A Multidisciplinary Approach. Chapter 28 - Atrial Tachycardia and Atrial Flutter*. Cardiotext Publishing, pp. 315–326, 2015.

[210] M. E. El Haddad, R. Houben, R. Tavernier, et al., "Stable reentrant circuit with spiral wave activation driving atrial tachycardia," *Heart Rhythm*, vol. 11, no. 4, pp. 716–718, 2014.

[211] P. Pascale, A. J. Shah, L. Roten, et al., "Pattern and timing of the coronary sinus activation to guide rapid diagnosis of atrial tachycardia after atrial fibrillation ablation," *Circulation. Arrhythmia and Electrophysiology*, vol. 6, no. 3, pp. 481–490, 2013.

[212] F. Akca, T. Bauernfeind, N. M. S. de Groot, et al., "The presence of extensive atrial scars hinders the differential diagnosis of focal or macroreentrant atrial tachycardias in patients with complex congenital heart disease," *Europace*, vol. 16, no. 6, pp. 893–898, 2014.

[213] S. Kapa, B. Desjardins, D. J. Callans, et al., "Contact electroanatomic mapping derived voltage criteria for characterizing left atrial scar in patients undergoing ablation for atrial fibrillation," *J Cardiovasc Electrophysiol*, vol. 25, no. 10, pp. 1044–1052, 2014.

[214] B. Olshansky, K. Okumura, P. G. Hess, et al., "Demonstration of an area slow conduction in human atrial flutter," *The American Journal of Cardiology*, vol. 16, no. 7, pp. 1639–1648, 1990.

[215] A. Kramlich, "Development and benchmarking of algorithms for the characterization of intracardiac electrograms measured during atrial flutter," Master's thesis, Institute of Biomedical Engineering, Karlsruhe Institute of Technology (KIT), Karlsruhe, 2016.

[216] G. Lenis, A. Kramlich, T. Oesterlein, et al., "Development and benchmarking of activity detection algorithms for intracardiac electrograms measured during atrial flutter," in *Proc. Workshop Biosignal 2016*, pp. 5–8, 2016.

[217] C. Schilling, A. Luik, M. W. Keller, et al., "Characterizing continuous activity with high fractionation during atrial fibrillation," in *Proc. 7th International Workshop on Biosignal Interpretation*, pp. 49–52, 2012.

[218] K. H. Kim and S. J. Kim, "A wavelet-based method for action potential detection from extracellular neural signal recording with low signal-to-noise ratio," *Biomedical Engineering, IEEE Transactions on*, vol. 50, no. 8, pp. 999–1011, 2003.

[219] T. Oesterlein, G. Lenis, A. Luik, et al., "Optimized approach for the detection of active segments in intracardiac electrograms measured during atrial flutter," in *42nd International Congress on Electrocardiology Conference Book of Abstracts*, 2015.

[220] A. Shimizu, A. Nozaki, Y. Rudy, et al., "Characterization of double potentials in a functionally determined reentrant circuit. multiplexing studies during interruption of atrial flutter in the canine pericarditis model," *J Am Coll Cardiol*, vol. 22, no. 7, pp. 2022–2032, 1993.

[221] T. Nitta, M. Wakita, Y. Watanabe, et al., "Double potential mapping: a novel technique for locating the site of incomplete ablation," *Innovations (Philadelphia, Pa.)*, vol. 7, no. 6, pp. 429–434, 2012.

[222] M. Takami, A. Yoshida, K. Fukuzawa, et al., "Utility of virtual unipolar electrogram morphologies to detect transverse conduction block and turnaround points of typical atrial flutter," *Journal of Interventional Cardiac Electrophysiology*, vol. 32, no. 2, pp. 111–119, 2011.

[223] N. V. Chawla, *Data mining and knowledge discovery handbook*. Springer US, ch. Data Mining for Imbalanced Datasets: An Overview, pp. 875–886, 2010.

[224] G. E. A. P. A. Batista, R. C. Prati, and M. C. Monard, "A study of the behavior of several methods for balancing machine learning training data," *SIGKDD Explorations*, vol. 6, no. 1, pp. 20–29, 2004.

[225] J.-E. Ban, Y.-L. Chen, H.-C. Park, et al., "Relationship between complex fractionated atrial electrograms during atrial fibrillation and the critical site of atrial tachycardia that develops after catheter ablation for atrial fibrillation," *J Cardiovasc Electrophysiol*, vol. 25, no. 2, pp. 146–153, 2014.

[226] C. D. Cantwell, C. H. Roney, F. S. Ng, et al., "Techniques for automated local activation time annotation and conduction velocity estimation in cardiac mapping," *Computers in Biology and Medicine*, vol. 65, pp. 229–42, 2015.

[227] J. P. Ugarte, A. Orozco-Duque, C. Tobón, et al., "Dynamic approximate entropy electroanatomic maps detect rotors in a simulated atrial fibrillation model," *PloS one*, vol. 9, no. 12, p. e114577, 2014.

[228] V. Barbaro, P. Bartolini, G. Calcagnini, et al., "Automated classification of human atrial fibrillation from intraatrial electrograms," *PACE*, vol. 23, no. 2, pp. 192–202, 2000.

[229] V. Kremen, L. Lhotska, M. Macas, et al., "A new approach to automated assessment of fractionation of endocardial electrograms during atrial fibrillation," *Physiological Measurement*, vol. 29, no. 12, pp. 1371–1381, 2008.

[230] G. Nollo, M. Marconcini, L. Faes, et al., "An automatic system for the analysis and classification of human atrial fibrillation patterns from intracardiac electrograms," *IEEE Trans Biomed Eng*, vol. 55, no. 9, pp. 2275–2285, 2008.

[231] R. J. Hunter, I. Diab, G. Thomas, et al., "Validation of a classification system to grade fractionation in atrial fibrillation and correlation with automated detection systems," *Europace*, vol. 11, no. 12, pp. 1587–1596, 2009.

[232] D. Cuesta-Frau, E. Cirugeda-Roldan, A. Molina Pico, et al., "Atrial electrogram complex fractionated entropy study," *Experimental & Clinical Cardiology*, vol. 20, no. 9, pp. 5566–5574, 2014.

[233] A. Orozco-Duque, S. I. Duque, J. P. Ugarte, et al., "Fractionated electrograms and rotors detection in chronic atrial fibrillation using model-based clustering," in *Engineering in Medicine and Biology Society Conference*, pp. 1579–1582, 2014.

[234] A. Orozco-Duque, J. Bustamante, and G. Castellanos-Dominguez, "Semi-supervised clustering of fractionated electrograms for electroanatomical atrial mapping," *Biomedical Engineering Online*, vol. 15, no. 1, p. 44, 2016.

[235] J. V. Tu, "Advantages and disadvantages of using artificial neural networks versus logistic regression for predicting medical outcomes," *Journal of Clinical Epidemiology*, vol. 49, no. 11, pp. 1225–1231, 1996.

[236] U. Richter, L. Faes, A. Cristoforetti, et al., "A novel approach to propagation pattern analysis in intracardiac atrial fibrillation signals," *Annals of Biomedical Engineering*, vol. 39, no. 1, pp. 310–323, 2011.

[237] U. Richter, L. Faes, F. Ravelli, et al., "Propagation pattern analysis during atrial fibrillation based on sparse modeling," *IEEE Trans Biomed Eng*, vol. 59, no. 5, pp. 1319–1328, 2012.

[238] L. A. Baccala and K. Sameshima, "Partial directed coherence: a new concept in neural structure determination," *Biological Cybernetics*, vol. 84, no. 6, pp. 463–474, 2001.

[239] L. Faes, A. Porta, and G. Nollo, "Testing frequency-domain causality in multivariate time series," *IEEE Transactions on bio-Medical Engineering*, vol. 57, no. 8, pp. 1897–1906, 2010.

[240] A. A. Schricker, G. G. Lalani, D. E. Krummen, et al., "Human atrial fibrillation initiates via organized rather than disorganized mechanisms," *Circulation. Arrhythmia and Electrophysiology*, vol. 7, no. 5, pp. 816–824, 2014.

[241] P. Kuklik, D. H. Lau, A. N. Ganesan, et al., "High-density mapping of atrial fibrillation in a chronic substrate: Evidence for distinct modes of repetitive wavefront propagation," *International Journal of Cardiology*, vol. 199, pp. 407–414, 2015.

[242] F. Schenkel, "Methoden zur detektion und klassifikation atrialer erregungsmuster in intrakardialen elektrogrammen mit anwendung auf biatriale basketkatheter messungen," Bachelor thesis, Institute of Biomedical Engineering, Karlsruhe Institute of Technology (KIT), 2014.

[243] D. Gordon, J. J. Goldberger, R. Arora, et al., "Searching for "order" in atrial fibrillation using electrogram morphology recurrence plots," *Computers in Biology and Medicine*, vol. 65, pp. 220–228, 2015.

[244] L. Faes, G. Nollo, R. Antolini, et al., "A method for quantifying atrial fibrillation organization based on wave-morphology similarity," *IEEE Trans Biomed Eng*, vol. 49, no. 12 Pt 2, pp. 1504–1513, 2002.

[245] F. Ravelli and M. Mase, "Computational mapping in atrial fibrillation: how the integration of signal-derived maps may guide the localization of critical sources," *Europace*, vol. 16, no. 5, pp. 714–723, 2014.

[246] C. L. J. Webber and J. P. Zbilut, "Dynamical assessment of physiological systems and states using recurrence plot strategies," *Journal of Applied Physiology*, vol. 76, no. 2, pp. 965–973, 1994.

[247] U. Richter, M. Stridh, D. Husser, et al., "Wavefront detection from intra-atrial recordings," in *Computers in Cardiology*, vol. 34, pp. 97–100, 2007.

[248] A. Orozco-Duque, D. Novak, V. Kremen, et al., "Multifractal analysis for grading complex fractionated electrograms in atrial fibrillation," *Physiological Measurement*, vol. 36, no. 11, pp. 2269–2284, 2015.

[249] W.-J. Rappel and S. M. Narayan, "Theoretical considerations for mapping activation in human cardiac fibrillation," *Chaos (Woodbury, N.Y.)*, vol. 23, no. 2, p. 023113, 2013.

[250] V. H. A. Kuklik P, "Technical challenges of rotor identification during atrial fibrillation using phase singularity detection," *Europace*, vol. 17, no. Supp 3, p. iii20, 2015.

[251] P. Benharash, E. Buch, P. Frank, et al., "Quantitative analysis of localized sources identified by focal impulse and rotor modulation mapping in atrial fibrillation," *Circulation. Arrhythmia and Electrophysiology*, vol. 8, no. 3, pp. 554–561, 2015.

[252] B. Zrenner, G. Ndrepepa, M. Schneider, et al., "Computer-assisted animation of atrial tachyarrhythmias recorded with a 64-electrode basket catheter," *J Am Coll Cardiol*, vol. 34, no. 7, pp. 2051–2060, 1999.

[253] H. Nakagawa, A. Ikeda, T. Sharma, et al., "Rapid high resolution electroanatomical mapping: evaluation of a new system in a canine atrial linear lesion model," *Circulation. Arrhythmia and Electrophysiology*, vol. 5, no. 2, pp. 417–424, 2012.

List of Publications and Supervised Theses

Journal Articles

- **T. G. Oesterlein**, G. Lenis, D.-T. Rudolph, A. Luik, B. Verma, C. Schmitt, O. Dössel. *Removing ventricular far-field signals in intracardiac electrograms during stable atrial tachycardia using the periodic component analysis*, Journal of Electrocardiology, 2015, 48(2):171-180
- **T. G. Oesterlein**, J. Schmid, S. Bauer, A. Jadidi, C. Schmitt, O. Dössel, A. Luik. *Analysis and visualization of intracardiac electrograms in diagnosis and research: Concept and application of KaPAVIE*, Computer Methods and Programs in Biomedicine, 2016, 127:165-173
- **T. G. Oesterlein**, D. Frisch, A. Loewe, G. Seemann, C. Schmitt, O. Dössel, A. Luik. *Basket-Type Catheters: Diagnostic Pitfalls Caused by Deformation and Limited Coverage*, *under review at time of defense, meanwhile accepted:* BioMed Research International, 2016, ID 5340574
- **T. G. Oesterlein**, G. Lenis, A. Loewe, G. Seemann, A. Luik, C. Schmitt, O. Dössel. *Morphology based Classification*, *in preparation*
- G. Lenis, N. A. Pilia, **T. Oesterlein**, A. Luik, C. Schmitt, O. Dössel. *P wave detection and delineation in the ECG based on the phase free stationary wavelet transform and using intracardiac atrial electrograms as reference*, Biomedical Engineering / Biomedizinische Technik, 2016, 61(1):37-56
- C. Schilling, M. Keller, D. Scherr, **T. Oesterlein**, M. Haïssaguerre, C. Schmitt, O. Dössel, A. Luik. *Fuzzy decision tree to classify complex fractionated atrial electrograms*, Biomedical Engineering / Biomedizinische Technik, 2015, 60(3):245-255
- O. Dössel, G. Lenis, A. Loewe, M. Rottmann, G. Seemann, **T. Oesterlein**. *Model Assisted Biosignal Analysis of Atrial Electrograms*, technisches messen, 2016, 83(2):102-111
- J. P. Ugarte, A. Orozco-Duque, C. Tobon, V. Kremen, D. Novak, J. Saiz, **T. Oesterlein**, C. Schmitt, A. Luik, J. Bustamante. *Dynamic approximate entropy electroanatomic maps detect rotors in a simulated atrial fibrillation model*, PloS one, 2014, 9(12):e114577

Refereed Conference Articles

- **T. Oesterlein**, T. Baas, H. Malberg, O. Dössel, *Multivariate AR model parameter estimation on time series extracted from the ECG of myocarditis patients*, Biomedical Engineering / Biomedizinische Technik, 2011; 56(s1)
- **T. G. Oesterlein**, A. Luik, C. Schmitt, O. Dössel, *Generating biatrial local activation time maps using the non-linear energy operator reveals arrhythmia*, Biomedical Engineering / Biomedizinische Technik, 2013; 58(s1)
- S. Schuler, M. W. Keller, **T. Oesterlein**, G. Seemann, O. Dössel, *Influence of Catheter Orientation, Tissue Thickness and Conduction Velocity on the Intracardiac Electrogram*, Biomedical Engineering /Biomedizinische Technik, 2013; 58(s1)
- M. Rottmann, **T. Oesterlein**, O. Dössel, *Local activation time based estimation of the direction of propagation of plane wave and the corresponding conduction velocity in simulated electrograms*, Biomedical Engineering / Biomedizinische Technik, 2014; 59(s1):152-155
- **T. Oesterlein**, Lenis, G., A. Luik, C. Schmitt, O. Dössel, *Periodic component analysis to eliminate ventricular far field artifacts in unipolar atrial electrograms of patients suffering from atrial flutter*, Biomedical Engineering / Biomedizinische Technik, 2014; 59(s1):14-17
- F. Schenkel, **T. Oesterlein**, A. Luik, C. Schmitt, O. Dössel, *Detection and classification of atrial excitation patterns in intracardiac electrograms with application on biatrial basket catheter measurements*, Biomedical Engineering / Biomedizinische Technik, 2014; 59(s1):166-169
- **T. Oesterlein**, G. Lenis, A. Luik, B. Verma, C. Schmitt, O. Dössel, *Removing ventricular far field artifacts in intracardiac electrograms during stable atrial flutter using the periodic component analysis - proof of concept study*, International Congress on Electrocardiology, 2014; Proceedings:49-52
- M. Rottmann, M. W. Keller, **T. Oesterlein**, G. Seemann, O. Dössel, *Comparison of different methods and catheter designs to estimate the rotor tip position - a simulation study*, Computing in Cardiology, 2014;41:133-136
- S. Bauer, **T. Oesterlein**, J. Schmid, O. Dössel, *Interactive visualization of cardiac anatomy and atrial excitation for medical diagnosis and research*, Current Directions in Biomedical Engineering, 2015;1:400-404
- J. Trächtler, **T. Oesterlein**, A. Loewe, E. Poremba, A. Luik, C. Schmitt, O. Dössel, *Virtualizing clinical cases of atrial flutter in a fast marching simulation including conduction velocity and ablation scars*, Current Directions in Biomedical Engineering, 2015;1:405-408
- G. Lenis, **T. Oesterlein**, O. Dössel, Orthogonal component analysis to remove ventricular far field in non periodic sustained atrial flutter, Computing in Cardiology, 2015;42,669-672
- B. Verma, **T. G. Oesterlein**, A. Luik, C. Schmitt, O. Dössel, *Analyzing the Atrial Depolarization Wavefront Triggered from Sinus Node and Coronary Sinus for Identification of the Arrhythmogenic Substrate*, Computing in Cardiology, 2015;42:897-900

- B. Verma, **T. G. Oesterlein**, A. Luik, C. Schmitt, O. Dössel, *Locating regions of arrhythmogenic substrate by analyzing the duration of triggered atrial activities*, Current Directions in Biomedical Engineering, 2015;1:50-53
- **T. Oesterlein**, A. Kramlich, G. Lenis, A. Luik, C. Schmitt, O. Dössel, *Automatic detection and mapping of double potentials in intracardiac electrograms*, Current Directions in Biomedical Engineering, under review for presentation in October 2016
- R. Reich, **T. Oesterlein**, M. Rottmann, G. Seemann, O. Dössel, *Classification of Cardiac Excitation Patterns during Atrial Fibrillation*, Current Directions in Biomedical Engineering, under review for presentation in October 2016
- S. Huck, **T. Oesterlein**, A. Luik, C. Schmitt, R. Wakili, O. Dössel, *Preprocessing of Unipolar Signals Acquired by a Novel Intracardiac Mapping System*, Current Directions in Biomedical Engineering, under review for presentation in October 2016

Refereed Conference Abstracts

- **T. Oesterlein**, R. Scherer, G. Müller-Putz, *Monocular Head-Mounted SSVEP based Brain-Computer Interface to Retain Situational Awareness*, Biomedizinische Technik / Biomedical Engineering, 2012;52(S1)
- A. Luik, **T. Oesterlein**, M. Merkel, A. Radzewitz, P. Hörmann, O. Dössel, et al., Biatriales Basket Mapping bei der Katheterablation von Vorhofflimmern, Clinical Research in Cardiology / Deutsche Gesellschaft für Kardiologie, Herbsttagung 2013;102
- **T. G. Oesterlein**, M. W. Keller, S. Schuler, A. Luik, G. Seemann, C. Schmitt, O. Dössel, *Determination of local activation time in bipolar endocardial electrograms: a comparison of clinical criteria and a new method based on the non-linear energy operator*, Journal of Electrocardiology, 2013;46:e18
- A. Luik, R. Wakili, **T. Oesterlein**, H. Estner, M. Merkel, G. Schymik, O. Dössel, C. Schmitt, *Biatrial basket mapping in atrial fibrillation*, Journal of Interventional Cardiac Electrophysiology, 2014:5-4 abstract 15-46
- **T. Oesterlein**, A. Luik, C. Schmitt, O. Dössel, *Neue Möglichkeiten zur Diagnose von Arrhythmien durch Visualisierung der zeitlichen Dynamik von Elektrogrammen*, Clinical Research in Cardiology / Deutsche Gesellschaft für Kardiologie, Jahrestagung 2014;103:V167
- K. Schmidt, **T. Oesterlein**, R. Wakili, H. L. Estner, A. Radzewitz, N. Horn, P. Hörmann, M. Merkel, G. Schymik, O. Dössel, C. Schmitt, A. Luik, *Abdeckungsrate der atrialen Oberfläche bei Patienten mit biatrialem Basket Mapping*, Clinical Research in Cardiology / Deutsche Gesellschaft für Kardiologie, Jahrestagung 2014;103:P1857
- B. Verma, **T. Oesterlein**, A. Luik, C. Schmitt, O. Dössel, *Analysis of local activation times and complexity in the intracardiac electrograms*, Biomedical Engineering / Biomedizinische Technik, 2014;59:s14
- A. Luik, P. Hörmann, K. Schmidt, **T. Oesterlein**, A. Radzewitz, G. Schymik, M. Merkel, C. Schmitt, *Targeting the critical isthmus in patients with atypical atrial flutter using the*

rhythmia™ mapping system, Journal of Interventional Cardiac Electrophysiology, 2016:16-15 abstract 18-27

- B. Verma, **T. Oesterlein**, A Luik, C. Schmitt, O. Dössel, *Combined analysis of unipolar and bipolar electrograms for local activation time annotation near the stimulus site of paced rhythms*, Current Directions in Biomedical Engineering, under review for presentation in October 2016

Conference Presentations

- R. Scherer, **T. Oesterlein**, M. Pröll, S. Marko, G. R. Müller-Putz, *BCI-based operation of off-the-shelf software applications: Towards a General-Purpose Application Control framework*, Fifth International Brain-Computer Interface Meeting, 2013
- A. Luik, **T. Oesterlein**, R. Wakili, K. Schmidt, H. Estner, A. Radzewitz, N. Horn, P. Hörmann, M. Merkel, G. Schymik, O. Dössel, C. Schmitt, *Coverage of the left atrial surface in patients with basket mapping for atrial fibrillation*, Heart Rhythm, 2014:5941
- B. Verma, **T. G. Oesterlein**, A. Luik, C. Schmitt, O. Dössel, *Determination of region with arrhythmogenic substrate based on local activation time and activity duration*, Gordon Research Conference, 2015
- **T. Oesterlein**, G. Lenis, A. Luik, C. Schmitt, O. Dössel, *Optimized Approach for the Detection of Active Segments in Intracardiac Electrograms Measured during Atrial Flutter*, 42nd International Congress on Electrocardiology Conference Book of Abstracts, 2015
- D. Dössel, A. Luik, **T. Oesterlein**, M. Rottmann, B. Verma, and C. Schmitt, *Computer Modeling of the Atria and Clinical Electrograms*, Annual Conference of the IEEE Engineering in Medicine and Biology Society, 2015
- **T. Oesterlein**, D. Frisch, A. Luik, C. Schmitt, O. Dössel, *An approach to model the catheter deformation in virtual cardiac anatomies for simulation of intraatrial electrogram recordings*, Jahrestagung Deutsche Gesellschaft für Biomedizinische Technik, 2015
- B. Verma, **T. Oesterlein**, A. Luik, C. Schmitt, O. Dössel, *Regional changes in intraatrial electrograms detected in sinus rhythm and with paced sequences*, Congress Atrial Signals, 2015
- M. Rottmann, **T. Oesterlein**, C. Reich, A. Luik, C. Schmitt and O. Dössel, *Characteristic Features of Electrograms of Depolarization Waves during Atrial Fibrillation*, Annual Conference of the IEEE Engineering in Medicine and Biology Society, under review for presentation in August 2016

Invited Talks

- **T. G. Oesterlein**, *Seeing is Knowing - Analysis and Visualization of Atrial Signals*, Congress Atrial Signals 2015, Karlsruhe, Germany, 2015
- **T. G. Oesterlein**, M. Rottmann, *Das Herz in 3-D*, Lecture Kinder- und Jugenduni Bretten, Bretten, Germany, 2014
- **T. G. Oesterlein**, *Computergestützte Analyse von EKGs + intrakardialen Elektrogrammen zur Unterstützung v. Diagnose und Intervention in der Kardiologie*, Kardiologisches Kolloquium, Städtisches Klinikum Karlsruhe, Karlsruhe, Germany, 2013

Supervised Student Theses

- Markus Rottmann, *Methods for Simulation based Estimation of Parameters of the Electrical Excitation Propagation in Human Atria*, Master Thesis, Institute of Biomedical Engineering, Karlsruhe Instiute of Technology, 2013.
- Fabian Schenkel, *Methoden zur Detektion und Klassifikation atrialer Erregungsmuster in intrakardialen Elektrogrammen mit Anwendung auf biatriale Basketkatheter Messungen*. Bachelor Thesis, Institute of Biomedical Engineering, Karlsruhe Instiute of Technology, 2014.
- Daniel Frisch, *Patient-specific Modeling of Catheter Deformation to Extract Panoramic Intracardiac Electrograms during Simulated Atrial Fibrillation*, Bachelor Thesis, Institute of Biomedical Engineering, Karlsruhe Instiute of Technology, 2014.
- Julia Trächtler, *Analysis of Electrogram Morphology and Parameterization of a Simulation Environment for Clinical Cases of Atrial Flutter*, Bachelor Thesis, Institute of Biomedical Engineering, Karlsruhe Instiute of Technology, 2014.
- Dan-Timon Rudolph, *Advanced Signal Processing Algorithms to Remove Ventricular Far Field Artifacts from Intracardiac Electrograms*, Master Thesis, Institute of Biomedical Engineering, Karlsruhe Instiute of Technology, 2014.
- Niko Konrad, *Statistical analysis of unipolar and bipolar electrograms recorded during atrial fibrillation*, Master Thesis, Institute of Biomedical Engineering, Karlsruhe Instiute of Technology, 2015.
- Johann Jazewitsch, *Messungen von Ausbreitungsmustern der kardialen Erregung: Aufbau einer Datenbank und Definition geeigneter Features zur Klassifikation*, Bachelor Thesis, Institute of Biomedical Engineering, Karlsruhe Instiute of Technology, 2015.
- Daniela Zöller, *Statistical Analysis of Propagation Patterns in Intracardiac Panoramic Mapping Data*, Master Thesis, Institute of Biomedical Engineering, Karlsruhe Instiute of Technology, 2015.

- Christian Reich, *Classification of Cardiac Excitation Patterns during Atrial Fibrillation using Multichannel Mapping Data*, Master Thesis, Institute of Biomedical Engineering, Karlsruhe Instiute of Technology, 2015.
- Alexander Kramlich, *Development and Benchmarking of Algorithms for the Characterization of Intracardiac Electrograms Measured during Atrial Flutter*, Master Thesis, Institute of Biomedical Engineering, Karlsruhe Instiute of Technology, 2016.
- Salina Huck, *Implementation and Evaluation of Signal Preprocessing Techniques for Novel Intracardiac High-Density Mapping*, Bachelor Thesis, Institute of Biomedical Engineering, Karlsruhe Instiute of Technology, 2016.
- Nazeline Younis, *Auswertung des Zusammenhangs von Katheterorientierung, Morphologie bipolarer Elektrogramme und Ergebnis unterschiedlicher LAT Algorithmen bei Intrakardialen Messungen*, Institute of Biomedical Engineering, Karlsruhe Instiute of Technology, Bachelor Thesis, ongoing.
- Franziska Schäuble, *Auswertung uni- und bipolarer Elektrogramme bei intrakardialen Messungen während der Ablation mittels MiFi-Ablationskatheter*, Master Thesis, Institute of Biomedical Engineering, Karlsruhe Instiute of Technology, ongoing.
- Felix Plappert, *Determining the Degree of Complexity in Electrical Conduction using Intracardiac High Density Mapping Data*, Bachelor Thesis, Institute of Biomedical Engineering, Karlsruhe Instiute of Technology, ongoing.
- Gerald Schwaderlapp, *Definition, estimation, validation and clinical value of the dominant frequency of intracardiac atrial electograms*, Bachelor Thesis, Institute of Biomedical Engineering, Karlsruhe Instiute of Technology, ongoing.
- Emanuel Poremba, *Interaktive Steuerung einer kardialen Simulationssoftware in einer VR Umgebung*, Master Thesis, Institute for Anthropomatics and Robotics, Karlsruhe Instiute of Technology, ongoing.

Student Research Projects

- Ilia Grygoryev
- Silvio Bauer
- Sophie An Xing

Awards & Grants

- Second place student competition, Workshop Biosignalverarbeitung, 2016: G. Lenis, A. Kramlich, **T. Oesterlein**, A. Luik, C. Schmitt, O. Dössel, *Development and Benchmarking of Activity Detection Algorithms for Intracardiac Electrograms Measured During Atrial Flutter*

- Third place DGBMT student competition, BMT 2014 - 48. Jahrestagung der DGBMT: **T. G. Oesterlein**, G. Lenis, A. Luik, C. Schmitt, and O. Dössel, *Periodic component analysis to eliminate ventricular far field artifacts in unipolar atrial electrograms of patients suffering from atrial flutter*
- First price Young Investigator's Award, 41. International Congress of Electrocardiology, 2014: **T. G. Oesterlein**, G. Lenis, A. Luik, B. Verma, C. Schmitt, and O. Dössel, *Removing Ventricular Far Field Artifacts in Intracardiac Electrograms during Stable Atrial Flutter using the Periodic Component Analysis - Proof of Concept Study*
- Networking Scholarship, Karlsruhe House of Young Scientists (KHYS), 2013
- Sixth place DGBMT student competition, BMT 2011 - 45. Jahrestagung der DGBMT: **T. G. Oesterlein**, T. Baas, H. Malberg, O. Dössel, *Multivariate AR model parameter estimation on time series extracted from the ECG of myocarditis patients*
- Travel Scholarship, Fulbright Commission, 2008 / 2009
- Study Exchange, Baden-Württemberg-Programm, 2008 / 2009
- IPP-Price for passing undergraduate studies with honors 2008
- Student Scholarship, Studienstiftung des Deutschen Volkes, 2008 - 2011
- Student Scholarship, Konrad-Adenauer-Stiftung, 2006 - 2012
- Student Scholarship, e-fellows.net, 2005 - 2012